DEVELOPMENT & CHARACTERIZATION OF BIO-INSPIRED EARTH-ABUNDANT METAL SYSTEMS AND EXTREME ULTRAVIOLET SPECTROSCOPY OF PRECIOUS METAL PHOTOCATALYSTS

BY

CLARE ANASTASIA LEAHY

DISSERTATION

Submitted in partial fulfillment of the requirements
for the degree of Doctor of Philosophy in Chemistry
in the Graduate College of the
University of Illinois Urbana-Champaign, 2022

Urbana, Illinois

Doctoral Committee:

Associate Professor Alison R. Fout, Chair and Director of Research
Associate Professor Josh Vura-Weis, Co-Director of Research
Professor Gregory Girolami
Assistant Professor Lisa Olshansky

ABSTRACT

Transition metal catalysis plays a vital role in a wide range of chemical transformations. Characterization of these metal catalysts and intermediates provides crucial insight into their structures, electronic manifolds, and reaction mechanisms. Overall, this thesis demonstrates the use of complementary spectroscopic techniques towards understanding the physical and electronic structures of bio-inspired earth abundant metal systems and precious metal photocatalysts.

Active sites of metalloenzymes are crucial targets for spectroscopic characterization as they are incredibly effective at performing challenging, multielectron reactions. Primary sphere coordination to the metal center and secondary sphere hydrogen-bonding interactions work together to achieve these transformations by facilitating small molecule binding & activation, stabilize reactive intermediates, and shuttle protons and electrons in the active site. Synthetic mimics integrating these enzymatic motifs can serve as useful tools in mimicking proposed intermediates and reactivity of metalloenzymes. The Fout group designed tripodal and tetrapodal scaffolds, $H_3(N(pi^{Cy})_3)$ and $Py_2Py(pi^{Cy})_2$, that incorporate biomimetic primary and secondary sphere interactions through tautomerizable arms in the ligand frameworks. The ligand arm incorporates a pyrrole-imine (pi) form that give anionic coordination to a bound metal center while providing a hydrogen-bond acceptor in the secondary sphere. Tautomerization to the azafulvene-amine (afa) form enables dative coordination to the metal while giving a hydrogen-bond donor in the secondary coordination sphere.

Early work focused on developing a new tripodal ligand scaffold that contained two tautomerizable arms and introduced a phenol group to act as the third arm, which upon deprotonation gave only anionic coordination to the metal center. A series of late 1st row transition metal(II) chloride complexes were characterized within this new framework that showed the afa

arms displaying inter- and intra-ligand hydrogen donation to the bound axial chloride and the oxygen of the phenoxy arm. The latter was found to have a dramatic impact on the geometry of the metal center and donor strength of the oxygen, not only showing the ability of hydrogen bonds from the secondary coordination sphere to stabilize axial ligands but also demonstrates a design principle for tuning geometry & reactivity at the metal center through hydrogen bonding to the ligand framework.

Later work returned to the original tripodal and tetrapodal ligand scaffolds containing three or two of the tautomerizable ligand arms, respectively. The latter $Py_2Py(pi^{Cy})_2$ was used in developing and characterizing a series of octahedral cobalt(II) complexes. The cobalt(II) bis(triflate) complex showed dioxygen activation to form a diamagnetic cobalt(III) hydroxide complex, demonstrating the use of secondary sphere hydrogen-bonds for binding & activating dioxygen. The cobalt(III) species was also found to be stable, ascribed to both hydrogen-bond donation from the afa amines stabilizing the bound axial hydroxide. Further electronic characterization of the cobalt tetrapodal system showed a strong axial ligand influence on the cobalt(II) centers' electronic structure. To explore this ligand influence, two additional cobalt(II) tetrapodal species were synthesized and characterized by structural and electronic techniques.

Additional characterization of late 1st row transition metal complexes in the $H_3(N(pi^{Cy})_3)$ scaffold was undertaken using X-ray absorption spectroscopy to both explore the impact of ligand modification in the primary and secondary coordination spheres on the electronics and further characterize the electronic manifolds of these species. Extreme ultraviolet (XUV) spectroscopy probes the $M_{2,3}$-edge of 1st row transition metals, which is sensitive oxidation, spin-state, and ligand-field. The Vura-Weis group has used this technique to examine metal-based structures and ultrafast photodynamics in several 1st row metal systems in their in-house, table-top instrument.

$M_{2,3}$-edge spectroscopy of iron(III)-oxo species in the different ligand variants of the tripodal ligand shows minor edge and pre-peak changes due to installation of an electron-withdrawing group in the ligand backbone affecting the primary sphere. The manganese(II)-hydroxo and manganese(III)-oxo tripodal species were also investigated, but the manganese(III)-oxo showed photoreduction to a manganese(II) complex. $L_{2,3}$-edge spectroscopy of the iron, manganese, and cobalt tripodal species showed good qualitative agreement with original assignment of these complexes as high-spin metal centers of the appropriate oxidation state with weak trigonal bipyramidal ligand fields. Challenges in fitting the $M_{2,3}$- and $L_{2,3}$-edges of these trigonal bipyramidal metal species precluded quantitative fitting of the spectra.

Application of XUV spectroscopy to characterizing precious metal systems was also investigated. 3rd row transition metals serve as important catalytic centers in organic transformations, particularly as photocatalysts and photosensitizers. The XUV energy region (30-100 eV) contains the $O_{2,3}$- and $N_{6,7}$-edges of 3rd row metals, but there has been little published work on the utility of XUV spectroscopy towards probing electronic structure or metal-based dynamics in these systems. Several platinum(II) and iridium(III) species were characterized at their $O_{2,3}$- and $N_{6,7}$-edges with XUV, with initial insights into changes in edge shifts from ligand field strength were obtained. Transient $N_{6,7}$-edge spectroscopy of Ir(III)ppy_3 tracking the early photodynamics showed excellent agreement with literature dynamics. Implications for current and future directions in applying XUV spectroscopy to study 3rd row metal complexes and their dynamics were discussed. Overall, using $O_{2,3}$- and $N_{6,7}$-edge XUV spectroscopy showed promise as a probe for interrogating metal structure and photodynamics of 3rd row transition metal systems.

ACKNOWLEDGEMENTS

Many amazing people have supported & guided me through the past several years in graduate school, and I would have not made it through without their sincere effort and care. My deepest appreciation goes to my advisers Drs. Alison Fout & Josh Vura-Weis for all their encouragement, advice, and conversations throughout the years. They were incredibly formative in shaping me as a scientist and always supported me through the ups and downs that research (and life!) brings. As part of two unique research groups, I have also had the wonderful privilege to work with many amazing labmates & colleagues. This includes current & former Fout group graduate members (Zack Gordon, Courtney Ford, Kenan Tokmic, Michael Drummond, Joe Nugent, Tabitha Miller, Safiyah Muhammad, Daniel Najera, Bill Darrow, Kelly Gullett, Ericka Bruske, Noah Bender, Kenai Duran, Abby Denny, Jonathan Matsuura, Jewel Moore, & Brennan Vaught), current & former Vura-Weis group members (Michaela Carlson, Liz Ryland, Max Verkamp, Kaili Zhang, Kris Benke, Aastha Sharma, Kori Sye, Yusef Shari'ati, Ryan Ash, Rachel Wallick, Jack Burke, Lauren Boedicker, Grant Barton, Justin Malme, Brandon Rassmusen, & Laura Smith), and current & former undergraduates from both groups (Nico, Ian, Eva, Nate, Ria, Steven, Brian, Sammie, Niknaz, Evan, Aryann, Michael, & Muffaddal). I'd particularly like to thank the older students for their amazing support & willingness to answer all my constant questions my first few years and beyond! Additionally, thank you to the Fout bioinorganic subgroup for all the excellent scientific discussions and early morning lab companionship. I also thank my other committee members Professor Gregory Girolami and Professor Lisa Olshansky for their advice and guidance these past five years.

I have had the opportunity to work with several colleagues on and off campus, with acknowledgements for specific collaborations in the relevant chapters. I would like to particularly

thank Drs. Danielle Gray, Toby Woods, Dean Olson, Richard Haasch, & Greg MacDougall for initial training and later advice in several techniques important in this thesis; I would be a poorer experimentalist without your support and assistance.

A huge thanks to all the staff and administration for their assistance and support – the department would fall apart, emails spontaneously disappear, and students left bereft of schedules and tasty food without you all! I'd like to particularly thank the entire IMP & A offices (Karen, Gayle, Theresa, Beth, Stacy, Katie, Lisa, Kate, Randy, and Reagan) for their efforts to keep us IMPA graduate students afloat. I greatly appreciated the opportunity to give back to the communities I was involved in the department through volunteering and committee work with the Women Chemists Committee (WCC), Joint Safety Team (JST), and Women in Chemistry Post-Doc & Grad Student Retreat Committee.

Of course, I cannot continue without mentioning my deep appreciation to all family and friends that have supported me and kept me going from day one, as I would not be anywhere near where I am today without them. To my parents, thank you so much for all your love and generosity throughout the years. To all my siblings, thanks for all your support in big and small ways (particularly for all the cute pet photos): Catharine, Sarah, Chris, Nora, Peter, Brigid, Gregory, Linus, Tabby, and Bennet! A big shout out goes to my friends and peers in the chemistry department here for their support and friendship during graduate school, and I greatly thank the Carleton crew, particularly Raul & Gaston, for all the conversations, sights, and delicious meals shared during visits, mail, and calls. Let's keep it up as the years roll on!

My cat Mochi demands thanks and treats for being an attentive group meeting member, posing cutely for photos, and always ensuring I'm awake by 6:30 AM for getting into lab.

Thank you to my partner Matt for all your support and love these past eight years – it's been a hell of a stressful ride between long-distance, moving, job hunting, cat acquisition, and a global pandemic, but I am so grateful that we have been in this together. I can always count on you to do your best to make me smile with stupid jokes, listen to my rambles as we unwind from the day, and not make too much fun of me for sucking at the crossword or looking ridiculous post-workouts. I hope in turn I've been able to show my appreciation and love for you in my own ways through a steady stream of baked goods, trying to make you laugh by (accidentally or deliberately) mispronouncing words, and listening to you rant about games. Looking forward to more fun adventures with you in the coming years!

To my family

TABLE OF CONTENTS

Chapter 1: Development and characterization of synthetic transition metal systems with earth abundant and precious metals

1.1 Spectroscopy as a probe in transition metal systems

Transition metals function as crucial catalytic centers for transformations of organic substrates in both natural and synthetic systems. Spectroscopic techniques aimed at characterizing the physical and electronic structures of these metal complexes are vital for understanding these metal centers. The aim of this work is to use a suite of spectroscopic techniques to interrogate the physical and electronic structures of bio-inspired, earth abundant metal systems developed in the Fout group towards understanding the relationship between structure & function. By extending the scope of the Vura-Weis group's table-top extreme ultraviolet (XUV) technique, this work also probed the electronic structure and dynamics of precious metal photosystems directly at the metal center.

1.2 Modeling metalloenzymatic active sites to understand and mimic biological processes

Transition metals, in the form of metalloenzymes, serve as powerful catalysts for challenging transformations in biological processes, with classic examples including heme-based systems such as cytochrome P450 monooxygenases,[1,2] non-heme enzymes like α-ketoglutarate-dependent hydroxylases,[3,4] and non-iron enzymes such as copper-based tyrosinases.[5–7] Key enzymatic motifs play important roles in facilitating reactions at the metal cofactor. Primary sphere coordination to the metal center by amino acid ligands and substrates enforces a particular ligand field geometry, directly controlling the valence d-orbital manifold, and determines the metal's Lewis acidity.[8–12] Secondary sphere interactions provide additional control over reactivity, primarily through hydrogen-bonding networks from nearby amino acids.[13–15] These interactions

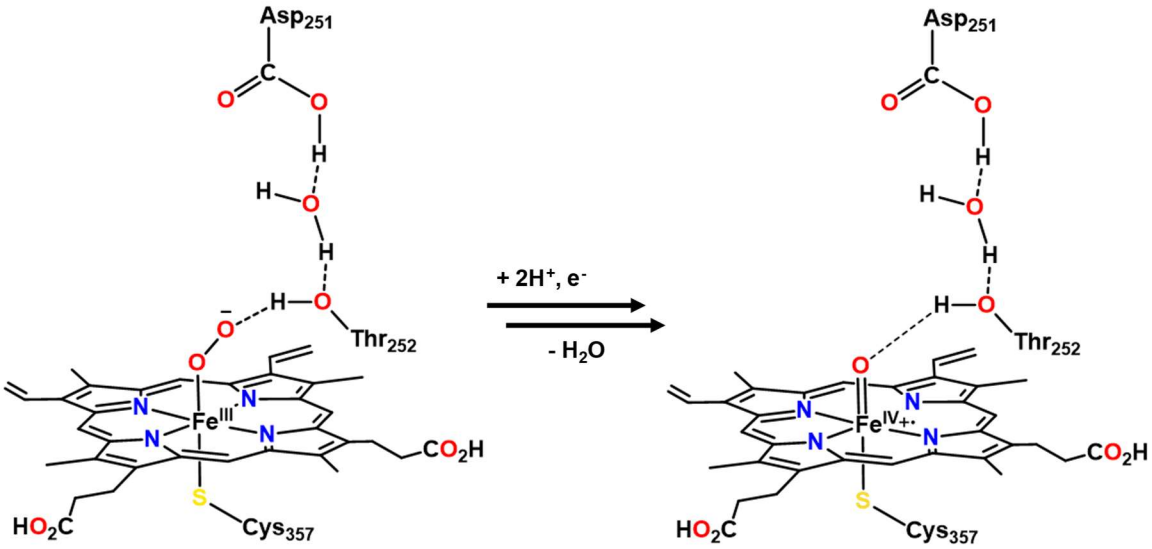

Figure 1.1 Secondary coordination sphere hydrogen-bonding network as a proton relay in cytochrome c p450 to form the reactive iron(IV)-oxo compound-I.

control substrate coordination and selectivity, stabilize reactive intermediates, and tune donor strength at the metal center, changing the metal redox potential.[16,17] The importance of these hydrogen-bonding interactions can clearly be observed in the cytochrome P450 superfamily (Fig. 1.1), which uses a heme cofactor for hydroxylation of substrates.[2,9,10,18,19] Upon dioxygen binding, the iron donates an electron to form an iron(III)-peroxide species (Fig. 1.1, left). A proton relay comprised of a network of amino acid residues Thr-252, Asp-251, Lys-178, and Arg-186 (the latter two omitted from Fig. 1.1 for clarity) then allows for rapid, controlled protonation to form the reactive iron(IV)-oxo porphyrin π-cation radical species (Compound-I, Fig. 1.1 right).[9,10,18–20] Through the cooperation of both primary and secondary coordination spheres, metalloenzymes facilitate challenging transformations selectively and effectively with high turnover numbers and frequencies.[14,21,22] However, it can be challenging to understand the mechanisms of these processes and interpret the cooperative relationship between the metal and greater protein scaffold due to the large protein size, dynamic scaffold, and challenges in isolating intermediate species.

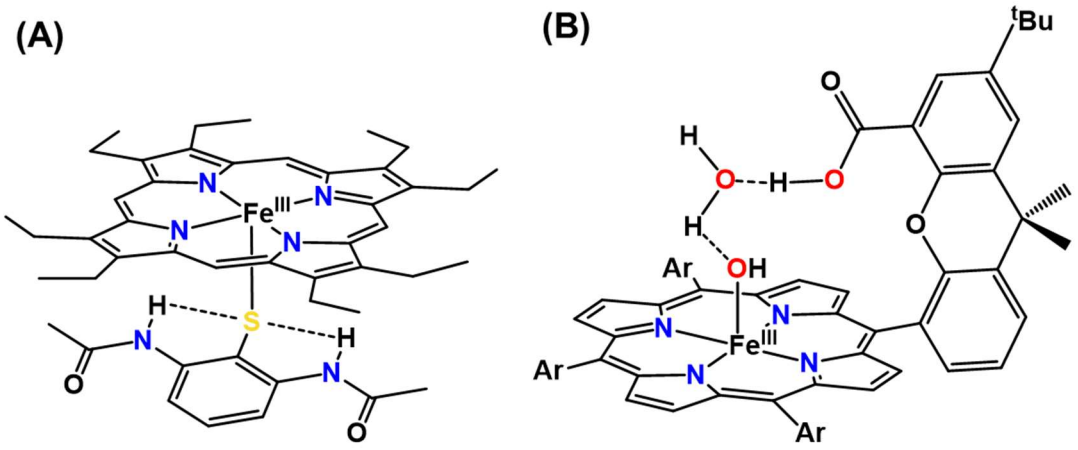

Figure 1.2 (A) Hydrogen-bond donation to bound sulfur of ferric octaethylporphyrin as mimics for tuning donor strength for control of iron redox potential in P540s; (B) Hangman porphyrin with pendant aldehyde group showing hydrogen-bonding network to axial hydroxide of ferric porphyrin.

Synthetic systems incorporating both primary and secondary sphere enzymatic motifs into ligand scaffolds have been developed to understand the metalloenzymatic systems and mimic their reactivity.[5,11–15,20,21,23–61] By developing synthetic models of proposed intermediates and characterizing their physical and electronic structures, we can gain insight into these processes using pared-down examples and develop spectroscopic references that can be used to identify key intermediates in complicated systems. For example, synthetic systems incorporating both primary and secondary enzymatic motifs, such as hydrogen bond donors or acceptors, can begin to explore how metal active sites and the greater protein network cooperate to enable reactivity, particularly with small molecules such as dioxygen,[5,23,25,47,53,62,63] peroxides & hydroxides,[33,46,57,64,65] and oxyanions.[32,54,55,58,60]

Iron porphyrin systems incorporating secondary sphere hydrogen-bonding networks have been a common target for spectroscopic characterization efforts and reactivity studies as biomimics of heme enzymes. Early examples were a series of ferric hemes with bound aryl- or akylthiolate ligands that had varied hydrogen bonds (0-2) to the sulfur, where increased hydrogen bond donation resulted in an increase in the iron(II/III) redox couple by tuning of the sulfur bond

donation (Fig. 1.2A).[8,26,36,38] More recent work using ferric heme nitric oxide model complexes bound with an axial thiolate bearing a tunable hydrogen-bond donor has shown similar impact on the Fe-NO and N-O stretching frequencies.[66] EPR studies of a similar series of low-spin ferric hemes bearing a tunable hydrogen-bond to the bound thiolate show direct correlation between hydrogen-bond strength and g-value dispersion in the rhombic EPR signal.[67] Other examples are "picket fence" or "hangman" porphyrins where an aldehyde or imidazole hangs over the iron center via installation of a spacer group (Fig. 1.2B), stabilizing peroxide & dioxygen binding and facilitating activation through inter-ligand hydrogen-bonding.[23,34,68–72]

Non-heme model systems incorporating enzymatic primary and secondary sphere designs using three-fold symmetric or trigonal bipyramidal ligand scaffolds have received much attention over the past few decades.[13,21,60] These have been found to stabilize reactive intermediates relevant

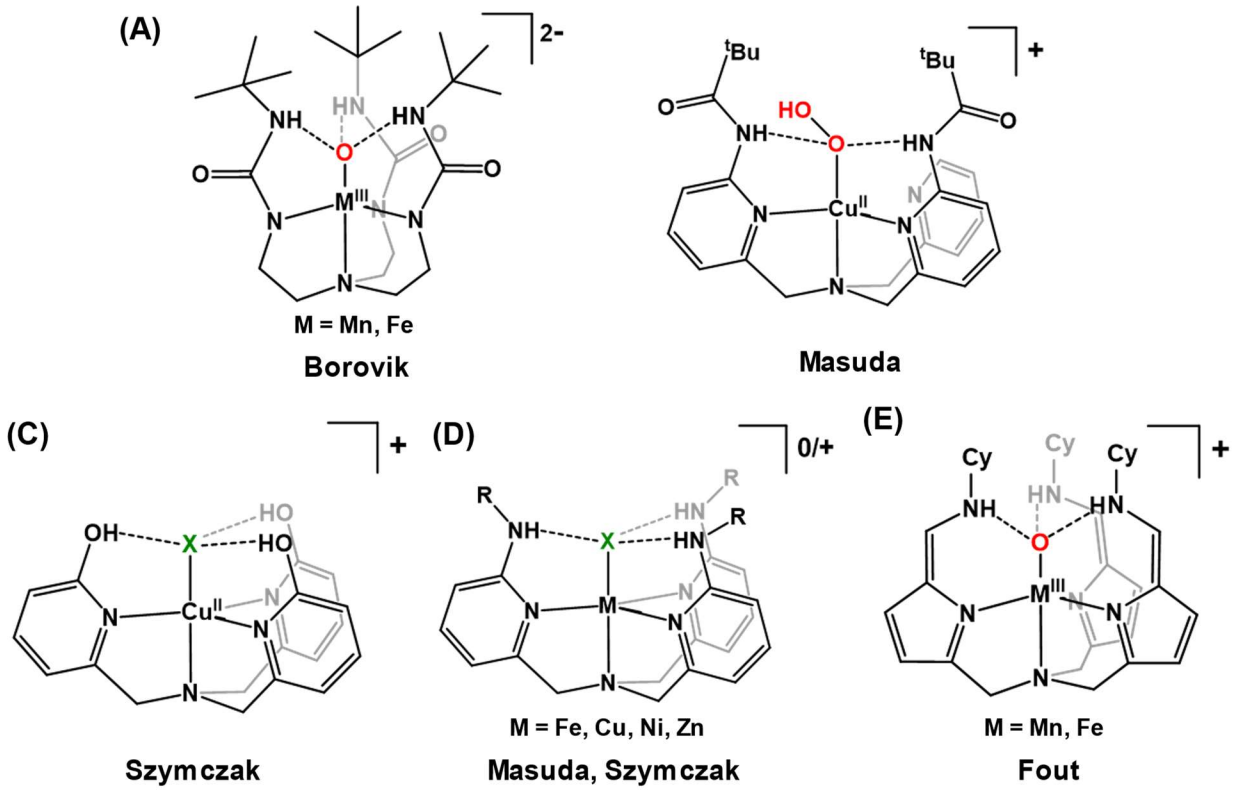

Figure 1.3 Select examples of synthetic model complexes in trigonal bipyramidal ligands with secondary sphere hydrogen-bonding interactions.

in biological processes, such as high-valent metal-oxos and -peroxos, and incorporate pendant hydrogen-bond donors or acceptors near the bound metal to facilitate mimicry of enzymatic secondary sphere hydrogen-bonding networks.[51–53,55,56,58,63] Several groups including Borovik,[42,45,48,49,62,73–84] Szymczak,[25,32,33,35,61,85] Masuda,[24,65,86,87] and Fout[51–53,55,56,58,63] have described the development of these tripodal ligand scaffolds in conjunction with mid-to-late 1st row transition metals for modeling enzymatic active sites and small molecule activation (Fig. 1.3A-E). These have included structural characterization of metal-oxo & peroxo species stabilized by hydrogen-bonding interactions, such as structural characterization of a copper(II)-OOH complex by Masuda and coworkers (Fig. 1.3B);[65] small molecule activation to form these species including stable metal(III)-oxos (Fig. 1.3A,E)[48,51,53,54,58,62,63,76,80,81] or other hydroxide or aqua species from halide staring materials (Fig. 1.3C-D);[25,30,33,35,61,65,85] and electronic characterization of these systems[82,88–90] to gain insight into the interplay between primary sphere coordination and secondary sphere hydrogen-bonding on the metal center.

1.3 Flexible tripodal and tetrapodal ligand scaffolds with earth abundant metals

The Fout group has developed a trigonal bipyramidal ligand platform inspired by prior work with secondary coordination sphere hydrogen-bonding interactions (as described *vide supra*)

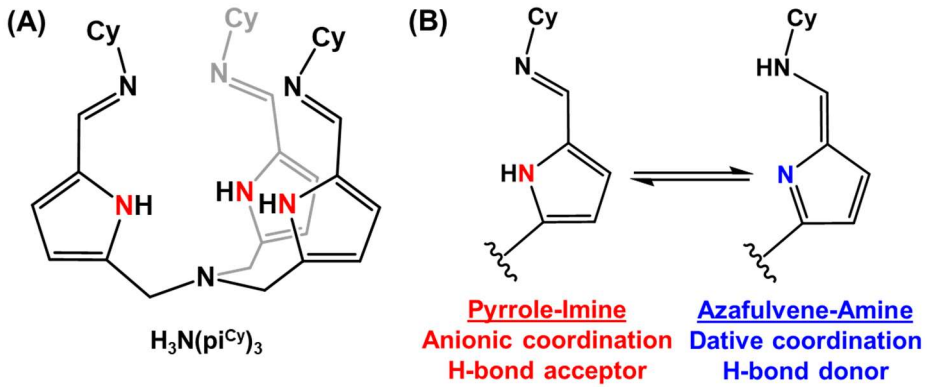

Figure 1.4 (A) Fout group tripodal ligand scaffold $H_3N(pi^{Cy})_3$; (B) Pyrrole-imine and azafulvene-amine tautomeric forms of the ligand arm.

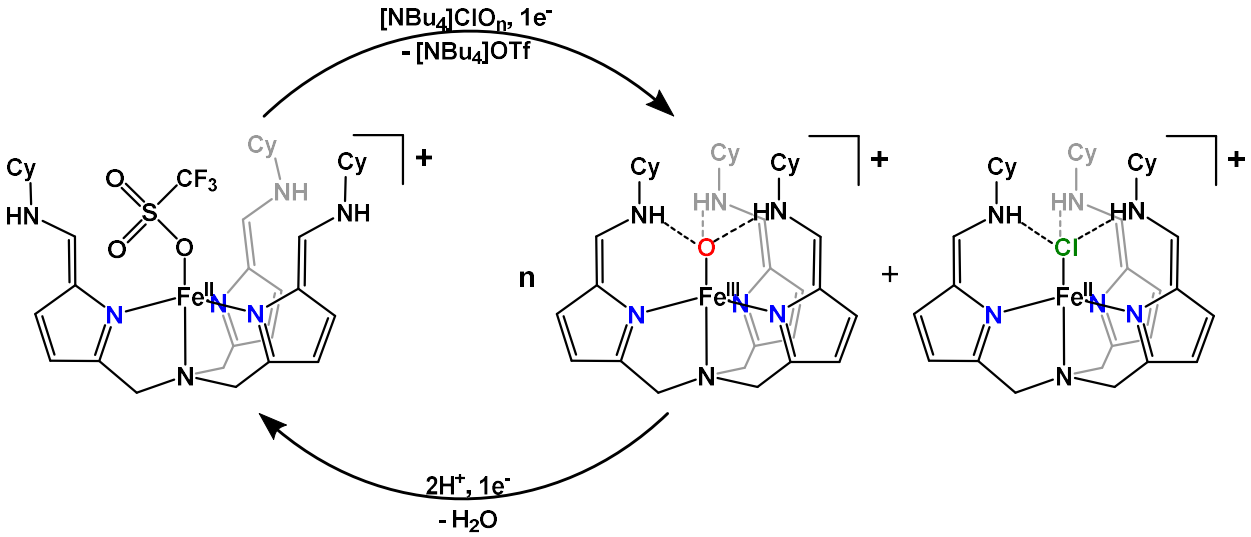

Figure 1.5 Perchlorate oxyanion reduction by the iron system with the tripodal N(pi^{Cy})$_3$ scaffold.

and a ligand scaffold with pyrrole-imine basis.[91,92] This ligand, tris(5-cyclohexylimino-pyrrol-2-ylmethyl)amine ($H_3N(pi^{Cy})_3$, Fig. 1.4A), has three ligand arms which can individually tautomerize from a pyrrole-imine (pi) tautomer to an azafulvene-amine (afa) tautomer (Figure 1.4B).[52] The pi tautomer provides an anionic ligand for a metal center and a hydrogen bond acceptor in the secondary coordination sphere, while the afa tautomer serves as a dative ligand and provides a hydrogen bond donor in the secondary coordination sphere. This scaffold has been successful in developing manganese and iron systems capable of mimicking biological activation of small molecules such as dioxygen[53,63] and oxyanions[51,54,58] (Figure 1.5) and modeling biologically relevant metal(II/III)-oxo species[52,90] (Figures 1.3E & 1.5). Additional investigations have been undertaken with manganese, iron, and cobalt in this ligand scaffold with anionic, axial substrates to determine their influence on ligand coordination and non-covalent hydrogen-bonding interactions of the secondary coordination sphere.[55] To provide additional insight into the electronic structure of these tripodal systems, x-ray absorption (XAS) spectroscopy was pursued at the respective metal transitions and qualitative analysis was undertaken as part of this work (Chapter 4).

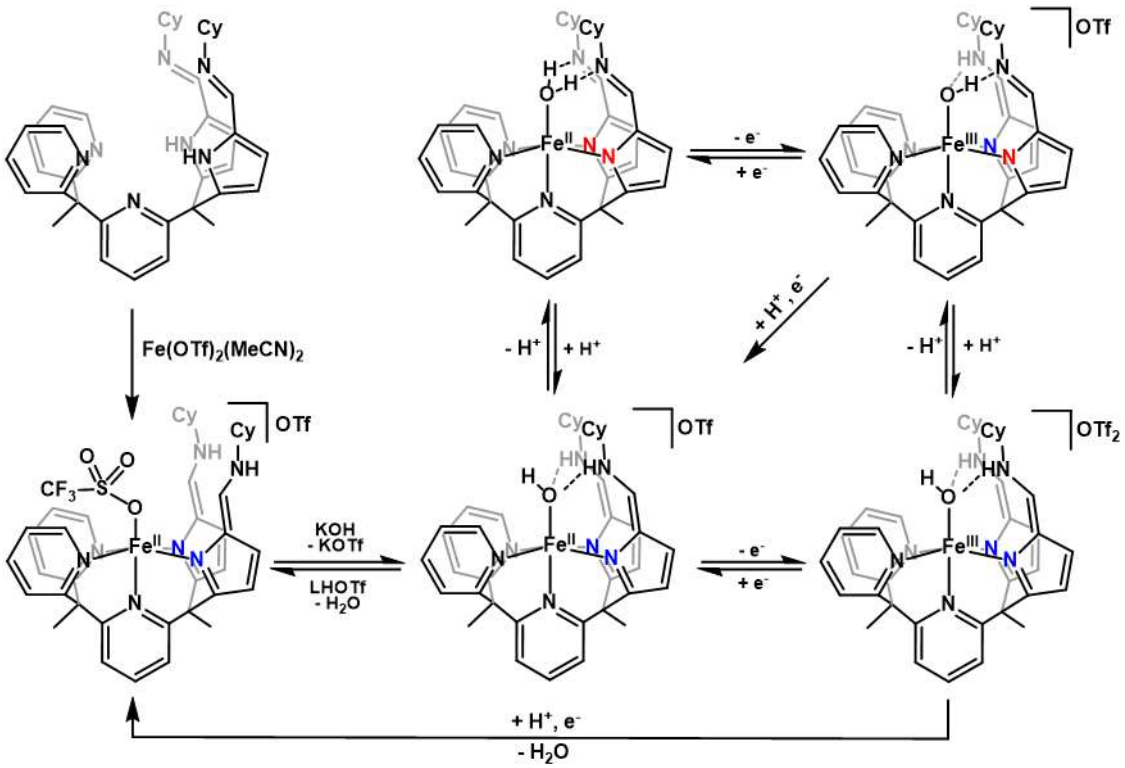

Figure 1.6 Iron(II/III) system with the tetrapodal ligand scaffold $Py_2Py(pi^{Cy})_2$.

While there has been much success in modeling metalloenzymatic intermediates with 3-fold symmetric ligand scaffolds, tripodal synthetic complexes that do not feature C_3-symmetric ligands but also incorporate hydrogen bonding motifs are less developed. Recent results[59] are detailed (Chapter 2) in this work describing the synthesis of a C_s-symmetric tripodal scaffold that retained two flexible ligand arms with secondary sphere hydrogen-bonding and allowed for observations of intra-ligand hydrogen-bonding effects with late 1st row transition metal binding. There have also been significantly fewer non-heme model systems that impose an octahedral (O_h) geometry at a metal center with secondary sphere hydrogen bonding, despite displaying similar activity and modeling of biological processes such as dioxygen (O_2) activation and O-atom transfer to their tri-fold counterparts.[23,24,70–72,80] The Fout group recently showed the development of a tetrapodal ligand scaffold, 2,2',2'-methylbis-pyridyl-6-(2,2',2'-methylbis-5-cyclo-hexyliminopyrrol)-pyridine ($Py_2Py(pi^{Cy})_2$, Fig. 1.6) that incorporates both secondary sphere

hydrogen-bonding and octahedral primary coordination environment for a bound metal.[57] It was found to be successful in generating a series of iron(II) and iron(III) complexes (Fig. 1.6), and the system achieved biomimetic radical rebound hydroxylation[57] and oxyanion reduction.[93] Part of this work (Chapter 3) expands on exploration of this ligand scaffold with another late 1st row transition metal, cobalt, describing O_2 activation by a cobalt bis(triflate) complex and providing insight into ligand influence on the metal electronic structure through characterization of a series of cobalt(II) species in this ligand framework and further comparison with the iron system.

1.4 Soft X-ray absorption spectroscopies towards targeting precious metal systems

While the biomimetic systems described above tend to focus on earth-abundant metals such as iron and cobalt, precious metal centers such as gold, platinum, and iridium also serve as important catalytic centers in synthetic chemical transformations.[94–101] Moreover, the strong spin-orbit coupling and intense visible-light absorption inherent in 3rd row transition metal complexes has led to their dominance in photocatalysis and photosensitization; for example, iridium(III) complexes with phenylpyridine-based ligands are commonly used in photocatalysis of organic substrates, with recent interest focused on their application in asymmetric transformations (Figure 1.7A-B)[100,102–109] and photosensitizers paired with other metal catalysts such as nickel in cross-coupling reactions (Figure 1.7C-D).[110–113] Additionally, these 3rd row metal centers are commonly used as dopants in organic light-emitting diodes (OLEDs).[114,115] Despite their successes, these systems can still undergo deactivation through off-pathway reactivity or relaxation dynamics. It thus remains important to have experimental tools that can identify and track metal behavior during catalysis, providing insight into on- and off-cycle pathways, and inform the development of better systems designed to promote desired reactivity and disfavor off-cycle activity towards more efficient use of these precious metals.

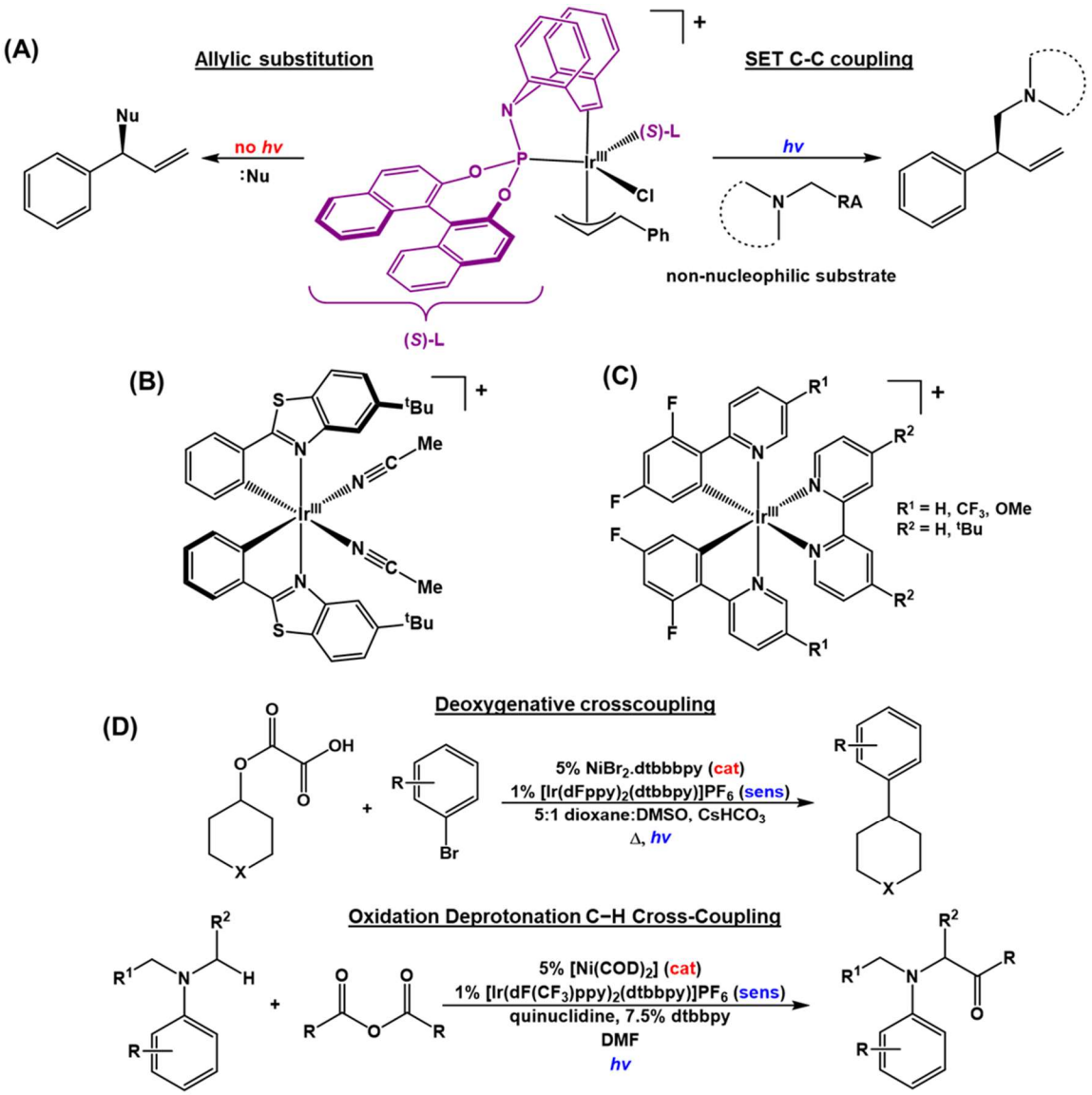

Figure 1.7 Select iridium examples of the use of 3rd row metal photocatalysts and sensitizers in organic transformations; (A) and (B) show recent examples of iridium(III) with chiral ligands (A) and chiral-at-metal iridium(III) (B) photocatalysts for asymmetric transformations, while (C) shows iridium(III) in a fluorinated, modifiable ligand scaffold that is commonly used for C-C cross-coupling reactions (D).

Synchrotron-based X-ray absorption spectroscopy (XAS) provides a powerful tool to probe these metal centers directly. X-ray absorption near-edge structure (XANES) and extended X-ray absorption fine structure (EXAFS) have shown great use in probing structure & coordination at transition metal centers and important chemical and electronic dynamics.[116–120] For 3rd row transition metals, XAS has been used to examine the structure and dynamics at primarily their metal $L_{2,3}$-edges, which are the dipole-allowed transitions from the spin-orbit coupling split 2p

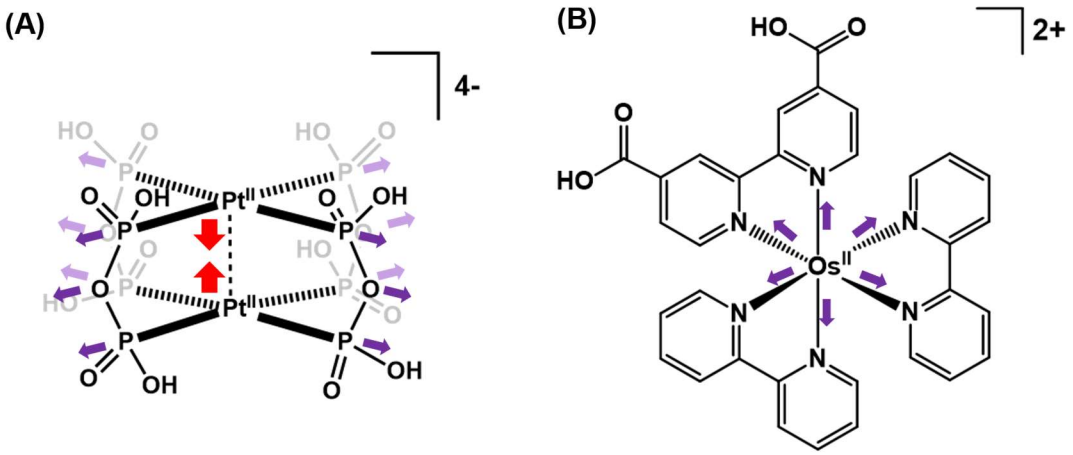

Figure 1.8 Select complexes studied by transient L_3-edge XAS with arrows indicating observed structural distortions in the triplet excited state for (A) $[Pt_2(P_2O_5H_2)_4]^{4-}$ & (B) $[Os^{II}(bpy)_2(pby)](PF_6)_2$.

core orbitals ($2p_{1/2}$ and $2p_{3/2}$) to the valence 5d orbitals. These transitions are highly sensitive to oxidation, spin-states, and ligand field changes, and temporal resolutions can reach as low as the tens of picoseconds.[116,119,121–125] This has allowed for examination of static characterization of 3rd row metal centers, including measuring metal-bond covalency,[126–135] and key excited state electronic and structural changes during photodynamics.[121–125,130,136,137] These have included examining structural changes of platinum(II) dimers in their triplet excited state, where there has been observed contraction of the Pt-Pt bond and elongation in the Pt-P bond in Pt by both transient XANES and EXAFS (Fig. 1.8A).[124,136] Similar elongations of metal-ligand bonds have also been observed in the triplet metal-to-ligand charge transfer excited states of osmium(II) polypyridyl complexes (Fig. 1.8B).[123]

Recent advances in high-harmonic generation (HHG) have allowed for the development of table-top soft X-ray instruments that can reach femtosecond temporal resolution, allowing for examination of ultrafast dynamics at transition metal centers.[116,138] HHG has shown to be particularly useful for generation of extreme ultraviolet (XUV) photons in the 10-100 eV range.[138,139] Work from several groups[140–148] have used XUV spectroscopy to primarily probe various 1st row transition metal systems and their photo- or chemical dynamics at the $M_{2,3}$-edges

(3p → valence 3d orbital transitions) in this energy region. The XUV energy range also includes the $O_{2,3}$- and $N_{6,7}$-edges of 3rd row transition metals (5p → valence 5d & 4f → valence 5d transitions, respectively) but has been much less explored relative to their 1st row counterparts, primarily limited to simple atomic or free ion plasma cases.[149–156] Part of this work (Chapter 5) describes efforts in characterizing the $O_{2,3}$- and $N_{6,7}$-edges of several 3rd row transition metal coordination complexes and tracks charge transfer dynamics of an iridium(III) photosensitizer with transient $N_{6,7}$-edge spectroscopy, showing XUV spectroscopy as a promising in-lab technique for characterization and probe for ultrafast metal-based dynamics of 3rd row metal centers.

1.5 Conclusions

Spectroscopy provides insight into electronic effects and structure at transition metal centers capable of performing challenging transformations. For example, active sites of metalloenzymes are crucial targets for spectroscopic characterization as they are incredibly effective at performing challenging, multielectron reactions. However, they can prove challenging to interrogate directly due to the large, dynamic protein scaffold. Synthetic systems that incorporate motifs important in these active sites, such as secondary sphere hydrogen-bonding coordination, are crucial for modeling enzymatic systems. Such model complexes will contribute to better understanding how more complicated biological systems work and facilitate mimicking their reactivities; chapters 2 through 4 are focused on this. Chapter 2 describes work in developing a new ligand scaffold that has secondary sphere H-bonding coordination and C_s-symmetrical primary sphere, detailing success with forming and characterizing late 1st row transition metal(II) chlorides. Chapter 3 looks at taking a known tetrapodal ligand, originally used in an iron system, and developing an understanding of the analogous cobalt system in terms of O_2 activity and characterization of the electronic structure. Chapter 4 touches on X-ray absorption characterization

of a series of trigonal bipyramidal 1st row metal complexes to understand the effect of ligand modifications on the metal electronic structure and characterize the ground state of a bimetallic trigonal system. Additionally, as synthetic precious metal systems also play key roles in chemical and photo-catalysis, Chapter 5 details initial efforts in using XUV spectroscopy to characterize the electronic structures of 3rd row transition metal coordination complexes, primarily with iridium and platinum centers, and demonstrate photodynamics occurring at the metal centers through transient $N_{6,7}$-edge XANES spectroscopy. Overall, these show the power of complementary spectroscopic techniques towards understanding the interplay between physical and electronic structures of transition metal systems.

1.6 References

(1) Wang, W.; Liang, A. D.; Lippard, S. J. Coupling Oxygen Consumption with Hydrocarbon Oxidation in Bacterial Multicomponent Monooxygenases. *Acc. Chem. Res.* **2015**, *48* (9), 2632–2639.

(2) Meunier, B.; de Visser, S. P.; Shaik, S. Mechanism of Oxidation Reactions Catalyzed by Cytochrome P450 Enzymes. *Chem. Rev.* **2004**, *104* (9), 3947–3980.

(3) Solomon, E. I.; Goudarzi, S.; Sutherlin, K. D. O2 Activation by Non-Heme Iron Enzymes. *Biochemistry* **2016**, *55* (46), 6363–6374.

(4) Kovaleva, E. G.; Lipscomb, J. D. Versatility of Biological Non-Heme Fe(II) Centers in Oxygen Activation Reactions. *Nat. Chem. Biol.* **2008**, *4* (3), 186–193.

(5) Fontecave, M.; Pierre, J. L. Oxidations by Copper Metalloenzymes and Some Biomimetic Approaches. *Coord. Chem. Rev.* **1998**, *170* (1), 125–140.

(6) Mirica, L. M.; Ottenwaelder, X.; Stack, T. D. P. Structure and Spectroscopy of Copper-Dioxygen Complexes. *Chem. Rev.* **2004**, *104* (2), 1013–1045.

(7) Lewis, E. A.; Tolman, W. B. Reactivity of Dioxygen-Copper Systems. *Chem. Rev.* **2004**, *104* (2), 1047–1076.

(8) Dey, A.; Jiang, Y.; De Montellano, P. O.; Hodgson, K. O.; Hedman, B.; Solomon, E. I. S K-Edge XAS and DFT Calculations on Cytochrome P450: Covalent and Ionic Contributions to the Cysteine-Fe Bond and Their Contribution to Reactivity. *J. Am. Chem. Soc.* **2009**, *131* (22), 7869–7878.

(9) Shaik, S.; Cohen, S.; Wang, Y.; Chen, H.; Kumar, D.; Thiel, W. P450 Enzymes: Their Structure, Reactivity, and Selectivity - Modeled by QM/MM Calculations. *Chem. Rev.*

2010, *110* (2), 949–1017.

(10) Denisov, I. G.; Makris, T. M.; Sligar, S. G.; Schlichting, I. Structure and Chemistry of Cytochrome P450. *Chem. Rev.* **2005**, *105* (6), 2253–2277.

(11) Costas, M.; Mehn, M. P.; Jensen, M. P.; Que, L. Dioxygen Activation at Mononuclear Nonheme Iron Active Sites: Enzymes, Models, and Intermediates. *Chem. Rev.* **2004**, *104* (2), 939–986.

(12) Solomon, E. I.; Light, K. M.; Liu, L. V.; Srnec, M.; Wong, S. D. Geometric and Electronic Structure Contributions to Function in Non-Heme Iron Enzymes. *Acc. Chem. Res.* **2013**, *46* (11), 2725–2739.

(13) de Visser, S. P. Second-Coordination Sphere Effects on Selectivity and Specificity of Heme and Nonheme Iron Enzymes. *Chem. - A Eur. J.* **2020**, *26* (24), 5308–5327.

(14) Lu, Y.; Pfister, T. D. Beyond Heme-Thiolate Interactions: Roles of the Secondary Coordination Sphere in Cytochrome P450 Systems. *Met. Ions Life Sci.* **2007**, *3*, 267–284.

(15) Zhao, M.; Wang, H. B.; Ji, L. N.; Mao, Z. W. Insights into Metalloenzyme Microenvironments: Biomimetic Metal Complexes with a Functional Second Coordination Sphere. *Chem. Soc. Rev.* **2013**, *42* (21), 8360–8375.

(16) Davydov, R.; Im, S.; Shanmugam, M.; Gunderson, W. A.; Pearl, N. M.; Hoffman, B. M.; Waskell, L. Role of the Proximal Cysteine Hydrogen Bonding Interaction in Cytochrome P450 2B4 Studied by Cryoreduction, Electron Paramagnetic Resonance, and Electron-Nuclear Double Resonance Spectroscopy. *Biochemistry* **2016**, *55* (6), 869–883.

(17) Pardillo, A. D.; Morozov, A. N.; Chatfield, D. C. Proximal Pocket Hydrogen Bonds Significantly Influence the Mechanism of Chloroperoxidase Compound i Formation. *J. Phys. Chem. B* **2015**, *119* (39), 12590–12602.

(18) Gerber, N. C.; Sligar, S. G. Catalytic Mechanism of Cytochrome P-450: Evidence for a Distal Charge Relay. *Journal of the American Chemical Society*. 1992, pp 8742–8743.

(19) Vidakovic, M.; Sligar, S. G.; Li, H.; Poulos, T. L. Understanding the Role of the Essential Asp251 in Cytochrome P450cam Using Site-Directed Mutagenesis, Crystallography, and Kinetic Solvent Isotope Effect. *Biochemistry* **1998**, *37* (26), 9211–9219.

(20) Hohenberger, J.; Ray, K.; Meyer, K. The Biology and Chemistry of High-Valent Iron–Oxo and Iron–Nitrido Complexes. *Nat. Commun.* **2012**, *3* (1), 720.

(21) Shook, R. L.; Borovik, A. S. Role of the Secondary Coordination Sphere in Metal-Mediated Dioxygen Activation. *Inorg. Chem.* **2010**, *49* (8), 3646–3660.

(22) Hosseinzadeh, P.; Lu, Y. Design and Fine-Tuning Redox Potentials of Metalloproteins Involved in Electron Transfer in Bioenergetics. *Biochim. Biophys. Acta - Bioenerg.* **2016**, *1857* (5), 557–581.

(23) Yeh, C.; Chang, C. J.; Nocera, D. G. “Hangman” Porphyrins for the Assembly of a Model Heme Water Channel. *J. Am. Chem. Soc.* **2001**, *123* (7), 1513–1514.

(24) Widger, L. R.; Davies, C. G.; Yang, T.; Siegler, M. A.; Troeppner, O.; Jameson, G. N. L.;

Ivanović-Burmazović, I.; Goldberg, D. P. Dramatically Accelerated Selective Oxygen-Atom Transfer by a Nonheme Iron(IV)-Oxo Complex: Tuning of the First and Second Coordination Spheres. *J. Am. Chem. Soc.* **2014**, *136* (7), 2699–2702.

(25) Dahl, E. W.; Kiernicki, J. J.; Zeller, M.; Szymczak, N. K. Hydrogen Bonds Dictate O2 Capture and Release within a Zinc Tripod. *J. Am. Chem. Soc.* **2018**, *140* (32), 10075–10079.

(26) Suzuki, N.; Higuchi, T.; Urano, Y.; Kikuchi, K.; Uekusa, H.; Ohashi, Y.; Uchida, T.; Kitagawa, T.; Nagano, T. Novel Iron Porphyrin−Alkanethiolate Complex with Intramolecular NH···S Hydrogen Bond: Synthesis, Spectroscopy, and Reactivity. *J. Am. Chem. Soc.* **1999**, *121* (49), 11571–11572.

(27) Bediako, D. K.; Solis, B. H.; Dogutan, D. K.; Roubelakis, M. M.; Maher, A. G.; Lee, C. H.; Chambers, M. B.; Hammes-Schiffer, S.; Nocera, D. G. Role of Pendant Proton Relays and Proton-Coupled Electron Transfer on the Hydrogen Evolution Reaction by Nickel Hangman Porphyrins. *Proc. Natl. Acad. Sci. U. S. A.* **2014**, *111* (42), 15001–15006.

(28) Dogutan, D. K.; Bediako, D. K.; Graham, D. J.; Lemon, C. M.; Nocera, D. G. Proton-Coupled Electron Transfer Chemistry of Hangman Macrocycles: Hydrogen and Oxygen Evolution Reactions. *J. Porphyr. Phthalocyanines* **2015**, *19* (01–03), 1–8.

(29) Jasniewski, A. J.; Que, L. Dioxygen Activation by Nonheme Diiron Enzymes: Diverse Dioxygen Adducts, High-Valent Intermediates, and Related Model Complexes. *Chem. Rev.* **2018**, *118* (5), 2554–2592.

(30) Ogo, S.; Wada, S.; Watanabe, Y.; Iwase, M.; Wada, A.; Harata, M.; Jitsukawa, K.; Masuda, H.; Einaga, H. Synthesis, Structure, and Spectroscopic Properties of [Fe(III)(Tnpa)(OH)(PhCOO)ClO4: A Model Complex for an Active Form of Soybean Lipoxygenase-1. *Angew. Chemie - Int. Ed.* **1998**, *37* (15), 2102–2104.

(31) Dahl, E. W.; Szymczak, N. K. Hydrogen Bonds Dictate the Coordination Geometry of Copper: Characterization of a Square-Planar Copper(I) Complex. *Angew. Chemie - Int. Ed.* **2016**, *55* (9), 3101–3105.

(32) Moore, C. M.; Szymczak, N. K. Nitrite Reduction by Copper through Ligand-Mediated Proton and Electron Transfer. *Chem. Sci.* **2015**, *6* (6), 3373–3377.

(33) Dahl, E. W.; Dong, H. T.; Szymczak, N. K. Phenylamino Derivatives of Tris(2-Pyridylmethyl)Amine: Hydrogen-Bonded Peroxodicopper Complexes. *Chem. Commun.* **2018**, *54* (8), 892–895.

(34) Ly, H. K.; Wrzolek, P.; Heidary, N.; Götz, R.; Horch, M.; Kozuch, J.; Schwalbe, M.; Weidinger, I. M. 2nd Coordination Sphere Controlled Electron Transfer of Iron Hangman Complexes on Electrodes Probed by Surface Enhanced Vibrational Spectroscopy. *Chem. Sci.* **2015**, *6* (12), 6999–7007.

(35) Wilson, J. R.; Zeller, M.; Szymczak, N. K. Hydrogen-Bonded Nickel(i) Complexes. *Chem. Commun.* **2021**, *57* (6), 753–756.

(36) Ueyama, N.; Nishikawa, N.; Yamada, Y.; Okamura, T. A.; Oka, S.; Sakurai, H.; Nakamura, A. Synthesis and Properties of Octaethylporphinato(Arenethiolato)Iron(III)

Complexes with Intramolecular NH···S Hydrogen Bond: Chemical Function of the Hydrogen Bond. *Inorg. Chem.* **1998**, *37* (10), 2415–2421.

(37) Dey, A.; Okamura, T. A.; Ueyama, N.; Hedman, B.; Hodgson, K. O.; Solomon, E. I. Sulfur K-Edge XAS and DFT Calculations on P450 Model Complexes: Effects of Hydrogen Bonding on Electronic Structure and Redox Potentials. *J. Am. Chem. Soc.* **2005**, *127* (34), 12046–12053.

(38) Ueyama, N.; Nishikawa, N.; Yamada, Y.; Okamura, T. A.; Nakamura, A. Cytochrome P-450 Model (Porphinato)(Thiolato)Iron(III) Complexes with Single and Double NH···S Hydrogen Bonds at the Thiolate Site. *J. Am. Chem. Soc.* **1996**, *118* (50), 12826–12827.

(39) Lehnert, N.; Kim, E.; Dong, H. T.; Harland, J. B.; Hunt, A. P.; Manickas, E. C.; Oakley, K. M.; Pham, J.; Reed, G. C.; Alfaro, V. S. The Biologically Relevant Coordination Chemistry of Iron and Nitric Oxide: Electronic Structure and Reactivity. *Chem. Rev.* **2021**, *121* (24), 14682–14905.

(40) Srnec, M.; Wong, S. D.; Matthews, M. L.; Krebs, C.; Bollinger, J. M.; Solomon, E. I. Electronic Structure of the Ferryl Intermediate in the α-Ketoglutarate Dependent Non-Heme Iron Halogenase SyrB2: Contributions to H Atom Abstraction Reactivity. *J. Am. Chem. Soc.* **2016**, *138* (15), 5110–5122.

(41) Miller, D. L.; Siedschlag, R. B.; Clouston, L. J.; Young, V. G.; Chen, Y. S.; Bill, E.; Gagliardi, L.; Lu, C. C. Redox Pairs of Diiron and Iron-Cobalt Complexes with High-Spin Ground States. *Inorg. Chem.* **2016**, *55* (19), 9725–9735.

(42) Jones, J. R.; Ziller, J. W.; Borovik, A. S. Modulating the Primary and Secondary Coordination Spheres within a Series of CoII-OH Complexes. *Inorg. Chem.* **2017**, *56* (3), 1112–1120.

(43) Kubin, M.; Kern, J.; Gul, S.; Kroll, T.; Chatterjee, R.; Löchel, H.; Fuller, F. D.; Sierra, R. G.; Quevedo, W.; Weniger, C.; Rehanek, J.; Firsov, A.; Laksmono, H.; Weninger, C.; Alonso-Mori, R.; Nordlund, D. L.; Lassalle-Kaiser, B.; Glownia, J. M.; Krzywinski, J.; Moeller, S.; Turner, J. J.; Minitti, M. P.; Dakovski, G. L.; Koroidov, S.; Kawde, A.; Kanady, J. S.; Tsui, E. Y.; Suseno, S.; Han, Z.; Hill, E.; Taguchi, T.; Borovik, A. S.; Agapie, T.; Messinger, J.; Erko, A.; Föhlisch, A.; Bergmann, U.; Mitzner, R.; Yachandra, V. K.; Yano, J.; Wernet, P. Soft X-Ray Absorption Spectroscopy of Metalloproteins and High-Valent Metal-Complexes at Room Temperature Using Free-Electron Lasers. *Struct. Dyn.* **2017**, *4* (5), 054307.

(44) Guo, M.; Corona, T.; Ray, K.; Nam, W. Heme and Nonheme High-Valent Iron and Manganese Oxo Cores in Biological and Abiological Oxidation Reactions. *ACS Cent. Sci.* **2019**, *5* (1), 13–28.

(45) Barman, S. K.; Jones, J. R.; Sun, C.; Hill, E. A.; Ziller, J. W.; Borovik, A. S. Regulating the Basicity of Metal-Oxido Complexes with a Single Hydrogen Bond and Its Effect on C-H Bond Cleavage. *J. Am. Chem. Soc.* **2019**, *141* (28), 11142–11150.

(46) Yamaguchi, S.; Nagatomo, S.; Kitagawa, T.; Funahashi, Y.; Ozawa, T.; Jitsukawa, K.; Masuda, H. Copper Hydroperoxo Species Activated by Hydrogen-Bonding Interaction with Its Distal Oxygen. *Inorg. Chem.* **2003**, *42* (22), 6968–6970.

(47) Rohde, J.-U.; In, J.-H.; Lim, M. H.; Brennessel, W. W.; Bukowski, M. R.; Stubna, A.; Münck, E.; Nam, W.; Que, L. Crystallographic and Spectroscopic Characterization of a Nonheme Fe(IV)=O Complex. *Science (80-.).* **2003**, *299* (5609), 1037–1039.

(48) Lucas, R. L.; Zart, M. K.; Mukherjee, J.; Sorrell, T. N.; Powell, D. R.; Borovik, A. S. A Modular Approach toward Regulating the Secondary Coordination Sphere of Metal Ions: Differential Dioxygen Activation Assisted by Intramolecular Hydrogen Bonds. *J. Am. Chem. Soc.* **2006**, *128* (3), 15476–15489.

(49) Lacy, D. C.; Gupta, R.; Stone, K. L.; Greaves, J.; Ziller, J. W.; Hendrich, M. P.; Borovik, A. S. Formation, Structure, and EPR Detection of a High Spin FeIV-Oxo Species Derived from Either an FeIII-Oxo or FeIII-OH Complex. *J. Am. Chem. Soc.* **2010**, *132* (35), 12188–12190.

(50) Hong, S.; Sutherlin, K. D.; Park, J.; Kwon, E.; Siegler, M. A.; Solomon, E. I.; Nam, W. Crystallographic and Spectroscopic Characterization and Reactivities of a Mononuclear Non-Haem Iron(III)-Superoxo Complex. *Nat. Commun.* **2014**, *5*.

(51) Matson, E. M.; Park, Y. J.; Fout, A. R. Facile Nitrite Reduction in a Non-Heme Iron System: Formation of an Iron(III)-Oxo. *J. Am. Chem. Soc.* **2014**, *136* (50), 17398–17401.

(52) Matson, E. M.; Bertke, J. A.; Fout, A. R. Isolation of Iron(II) Aqua and Hydroxyl Complexes Featuring a Tripodal H-Bond Donor and Acceptor Ligand. *Inorg. Chem.* **2014**, *53* (9), 4450–4458.

(53) Park, Y. J.; Matson, E. M.; Nilges, M. J.; Fout, A. R. Exploring Mn–O Bonding in the Context of an Electronically Flexible Secondary Coordination Sphere: Synthesis of a Mn(III)–Oxo. *Chem. Commun.* **2015**, *51* (25), 5310–5313.

(54) Ford, C. L.; Park, Y. J.; Matson, E. M.; Gordon, Z.; Fout, A. R. A Bioinspired Iron Catalyst for Nitrate and Perchlorate Reduction. *Science (80-.).* **2016**, *354* (6313), 741–743.

(55) Matson, E. M.; Park, Y. J.; Bertke, J. a.; Fout, A. R. Synthesis and Characterization of M(II) (M = Mn, Fe and Co) Azafulvene Complexes and Their X_3^- Derivatives. *Dalt. Trans.* **2015**, *44* (22), 10377–10384.

(56) Gordon, Z.; Drummond, M. J.; Matson, E. M.; Bogart, J. A.; Schelter, E. J.; Lord, R. L.; Fout, A. R. Tuning the Fe(II/III) Redox Potential in Nonheme Fe(II)-Hydroxo Complexes through Primary and Secondary Coordination Sphere Modifications. *Inorg. Chem.* **2017**, *56* (9), 4852–4863.

(57) Drummond, M. J.; Ford, C. L.; Gray, D. L.; Popescu, C. V.; Fout, A. R. Radical Rebound Hydroxylation Versus H-Atom Transfer in Non-Heme Iron(III)-Hydroxo Complexes: Reactivity and Structural Differentiation. *J. Am. Chem. Soc.* **2019**, *141* (16), 6639–6650.

(58) Drummond, M. J.; Miller, T. J.; Ford, C. L.; Fout, A. R. Catalytic Perchlorate Reduction Using Iron: Mechanistic Insights and Improved Catalyst Turnover. *ACS Catal.* **2020**, *10* (5), 3175–3182.

(59) Leahy, C. A.; Drummond, M. J.; Vura-Weis, J.; Fout, A. R. Synthesis of a Series of M(Ii) (M = Mn, Fe, Co) Chloride Complexes with Both Inter- And Intra-Ligand Hydrogen

Bonding Interactions. *Dalt. Trans.* **2021**, *50* (35), 12088–12092.

(60) Reed, C. J.; Lam, Q. N.; Mirts, E. N.; Lu, Y. Molecular Understanding of Heteronuclear Active Sites in Heme-Copper Oxidases, Nitric Oxide Reductases, and Sulfite Reductases through Biomimetic Modelling. *Chem. Soc. Rev.* **2021**, *50* (4), 2486–2539.

(61) Moore, C. M.; Quist, D. A.; Kampf, J. W.; Szymczak, N. K. A 3-Fold-Symmetric Ligand Based on 2-Hydroxypyridine: Regulation of Ligand Binding by Hydrogen Bonding. *Inorg. Chem.* **2014**, *53* (7), 3278–3280.

(62) MacBeth, C. E.; Golombek, A. P.; Young, V. G.; Yang, C.; Kuczera, K.; Hendrich, M. P.; Borovik, A. S. O 2 Activation by Nonheme Iron Complexes: A Monomeric Fe(III)-Oxo Complex Derived From O 2. *Science (80-.).* **2000**, *289* (5481), 938–941.

(63) Gordon, Z.; Miller, T. J.; Leahy, C. A.; Matson, E. M.; Burgess, M.; Drummond, M. J.; Popescu, C. V.; Smith, C. M.; Lord, R. L.; Rodríguez-López, J.; Fout, A. R. Characterization of Terminal Iron(III)-Oxo and Iron(III)-Hydroxo Complexes Derived from O2 Activation. *Inorg. Chem.* **2019**, *58* (23), 15801–15811.

(64) Huang, X.; Groves, J. T. Oxygen Activation and Radical Transformations in Heme Proteins and Metalloporphyrins. *Chem. Rev.* **2018**, *118* (5), 2491–2553.

(65) Wada, A.; Harata, M.; Hasegawa, K.; Jitsukawa, K.; Masuda, H.; Mukai, M.; Kitagawa, T.; Einaga, H. Structural and Spectroscopic Characterization of a Mononuclear Hydroperoxo-Copper(II) Complex with Tripodal Pyridylamine Ligands. *Angew. Chemie - Int. Ed.* **1998**, *37* (6), 798–799.

(66) Hunt, A. P.; Samanta, S.; Dent, M. R.; Milbauer, M. W.; Burstyn, J. N.; Lehnert, N. Model Complexes Elucidate the Role of the Proximal Hydrogen-Bonding Network in Cytochrome P450s. *Inorg. Chem.* **2020**, *59* (12), 8034–8043.

(67) Dent, M. R.; Milbauer, M. W.; Hunt, A. P.; Aristov, M. M.; Guzei, I. A.; Lehnert, N.; Burstyn, J. N. Electron Paramagnetic Resonance Spectroscopy as a Probe of Hydrogen Bonding in Heme-Thiolate Proteins. *Inorg. Chem.* **2019**, *58* (23), 16011–16027.

(68) Nehrkorn, J.; Bonke, S. A.; Aliabadi, A.; Schwalbe, M.; Schnegg, A. Examination of the Magneto-Structural Effects of Hangman Groups on Ferric Porphyrins by EPR. *Inorg. Chem.* **2019**, *58* (20), 14228–14237.

(69) Rosenthal, J.; Chng, L. L.; Fried, S. D.; Nocera, D. G. Stereochemical Control of H2O2 Dismutation by Hangman Porphyrins. *Chem. Commun.* **2007**, No. 25, 2642.

(70) Chng, L. L.; Chang, C. J.; Nocera, D. G. Catalytic O-O Activation Chemistry Mediated by Iron Hangman Porphyrins with a Wide Range of Proton-Donating Abilities. *Org. Lett.* **2003**, *5* (14), 2421–2424.

(71) Margarit, C. G.; Asimow, N. G.; Gonzalez, M. I.; Nocera, D. G. Double Hangman Iron Porphyrin and the Effect of Electrostatic Nonbonding Interactions on Carbon Dioxide Reduction. *J. Phys. Chem. Lett.* **2020**, *11* (5), 1890–1895.

(72) Graham, D. J.; Dogutan, D. K.; Schwalbe, M.; Nocera, D. G. Hangman Effect on Hydrogen Peroxide Dismutation by Fe(III) Corroles. *Chem. Commun.* **2012**, *48* (35),

4175–4177.

(73) Lee, J. L.; Ross, D. L.; Barman, S. K.; Ziller, J. W.; Borovik, A. S. C-H Bond Cleavage by Bioinspired Nonheme Metal Complexes. *Inorg. Chem.* **2021**, *60* (18), 13759–13783.

(74) Mukherjee, J.; Lucas, R. L.; Zart, M. K.; Powell, D. R.; Day, V. W.; Borovik, A. S. Synthesis, Structure, and Physical Properties for a Series of Monomeric Iron(III) Hydroxo Complexes with Varying Hydrogen-Bond Networks. *Inorg. Chem.* **2008**, *47* (13), 5780–5786.

(75) Taguchi, T.; Gupta, R.; Lassalle-Kaiser, B.; Boyce, D. W.; Yachandra, V. K.; Tolman, W. B.; Yano, J.; Hendrich, M. P.; Borovik, A. S. Preparation and Properties of a Monomeric High-Spin Mn V-Oxo Complex. *J. Am. Chem. Soc.* **2012**, *134* (4), 1996–1999.

(76) Sickerman, N. S.; Peterson, S. M.; Ziller, J. W.; Borovik, A. S. Synthesis, Structure and Reactivity of FeII/III-NH3 Complexes Bearing a Tripodal Sulfonamido Ligand. *Chem. Commun.* **2014**, *50* (19), 2515–2517.

(77) Gupta, R.; Lacy, D. C.; Bominaar, E. L.; Borovik, A. S.; Hendrich, M. P. Electron Paramagnetic Resonance and Mössbauer Spectroscopy and Density Functional Theory Analysis of a High-Spin Fe IV-Oxo Complex. *J. Am. Chem. Soc.* **2012**, *134* (23), 9775–9784.

(78) Oswald, V. F.; Weitz, A. C.; Biswas, S.; Ziller, J. W.; Hendrich, M. P.; Borovik, A. S. Manganese–Hydroxido Complexes Supported by a Urea/Phosphinic Amide Tripodal Ligand. *Inorg. Chem.* **2018**, *57* (21), 13341–13350.

(79) Hill, E. A.; Weitz, A. C.; Onderko, E.; Romero-Rivera, A.; Guo, Y.; Swart, M.; Bominaar, E. L.; Green, M. T.; Hendrich, M. P.; Lacy, D. C.; Borovik, A. S. Reactivity of an FeIV-Oxo Complex with Protons and Oxidants. *J. Am. Chem. Soc.* **2016**, *138* (40), 13143–13146.

(80) MacBeth, C. E.; Gupta, R.; Mitchell-Koch, K. R.; Young, V. G.; Lushington, G. H.; Thompson, W. H.; Hendrich, M. P.; Borovik, A. S. Utilization of Hydrogen Bonds to Stabilize M-O(H) Units: Synthesis and Properties of Monomeric Iron and Manganese Complexes with Terminal Oxo and Hydroxo Ligands. *J. Am. Chem. Soc.* **2004**, *126* (8), 2556–2567.

(81) Gupta, R.; Borovik, A. S. Monomeric MnIII/II and FeIII/II Complexes with Terminal Hydroxo and Oxo Ligands: Probing Reactivity via O-H Bond Dissociation Energies. *J. Am. Chem. Soc.* **2003**, *125* (43), 13234–13242.

(82) Dey, A.; Hocking, R. K.; Larsen, P.; Borovik, A. S.; Hodgson, K. O.; Hedman, B.; Solomon, E. I. X-Ray Absorption Spectroscopy and Density Functional Theory Studies of [(H3buea)FeIII-X]n- (X = S2-, O 2-, OH-): Comparison of Bonding and Hydrogen Bonding in Oxo and Sulfido Complexes. *J. Am. Chem. Soc.* **2006**, *128* (30), 9825–9833.

(83) Oswald, V. F.; Lee, J. L.; Biswas, S.; Weitz, A. C.; Mittra, K.; Fan, R.; Li, J.; Zhao, J.; Hu, M. Y.; Alp, E. E.; Bominaar, E. L.; Guo, Y.; Green, M. T.; Hendrich, M. P.; Borovik, A. S. Effects of Noncovalent Interactions on High-Spin Fe(IV)-Oxido Complexes. *J. Am. Chem. Soc.* **2020**, *142* (27), 11804–11817.

(84) Sun, C.; Oswald, V. F.; Hill, E. A.; Ziller, J. W.; Borovik, A. S. Investigation of Iron-Ammine and Amido Complexes within a: C 3-Symmetrical Phosphinic Amido Tripodal Ligand. *Dalt. Trans.* **2021**, *50* (32), 11197–11205.

(85) Moore, C. M.; Szymczak, N. K. Redox-Induced Fluoride Ligand Dissociation Stabilized by Intramolecular Hydrogen Bonding. *Chem. Commun.* **2015**, *51* (25), 5490–5492.

(86) Fujii, T.; Yamaguchi, S.; Hirota, S.; Masuda, H. H-Atom Abstraction Reaction for Organic Substrates via Mononuclear Copper(ii)-Superoxo Species as a Model for DβM and PHM. *Dalt. Trans.* **2008**, No. 1, 164–170.

(87) Wada, A.; Honda, Y.; Yamaguchi, S.; Nagatomo, S.; Kitagawa, T.; Jitsukawa, K.; Masuda, H. Steric and Hydrogen-Bonding Effects on the Stability of Copper Complexes with Small Molecules. *Inorg. Chem.* **2004**, *43* (18), 5725–5735.

(88) Gupta, R.; Taguchi, T.; Lassalle-Kaiser, B.; Bominaar, E. L.; Yano, J.; Hendrich, M. P.; Borovik, A. S. High-Spin Mn-Oxo Complexes and Their Relevance to the Oxygen-Evolving Complex within Photosystem II. *Proc. Natl. Acad. Sci. U. S. A.* **2015**, *112* (17), 5319–5324.

(89) Weitz, A. C.; Hill, E. A.; Oswald, V. F.; Bominaar, E. L.; Borovik, A. S.; Hendrich, M. P.; Guo, Y. Probing Hydrogen Bonding Interactions to Iron-Oxido/Hydroxido Units by 57Fe Nuclear Resonance Vibrational Spectroscopy. *Angew. Chemie - Int. Ed.* **2018**, *57* (49), 16010–16014.

(90) Gordon, Z.; Drummond, M. J.; Matson, E. M.; Bogart, J. A.; Schelter, E. J.; Lord, R. L.; Fout, A. R. Tuning the Fe(II/III) Redox Potential in Nonheme Fe(II)–Hydroxo Complexes through Primary and Secondary Coordination Sphere Modifications. *Inorg. Chem.* **2017**, *56* (9), 4852–4863.

(91) Hart, J. S.; White, F. J.; Love, J. B. Donor-Extended Tripodal Pyrroles: Encapsulation, Metallation, and H-Bonded Tautomers. *Chem. Commun.* **2011**, *47* (20), 5711–5713.

(92) Zeini Jahromi, E.; Gailer, J. Probing Bioinorganic Chemistry Processes in the Bloodstream to Gain New Insights into the Origin of Human Diseases. *Dalt. Trans.* **2010**, *39* (2), 329–336.

(93) Drummond, M. Bio-Inspired Iron and Cobalt Complexes Featuring a Secondary Coordination Sphere: Ligand Design, Complexation, and Modeling of Enzymatic Processes, University of Illinois at Urbana-Champaign, 2019.

(94) Fürstner, A. Gold and Platinum Catalysis—a Convenient Tool for Generating Molecular Complexity. *Chem. Soc. Rev.* **2009**, *38* (11), 3208–3221.

(95) Meister, T. K.; Riener, K.; Gigler, P.; Stohrer, J.; Herrmann, W. A.; Kühn, F. E. Platinum Catalysis Revisited-Unraveling Principles of Catalytic Olefin Hydrosilylation. *ACS Catal.* **2016**, *6* (2), 1274–1284.

(96) Schrock, R. R.; Hoveyda, A. H. Molybdenum and Tungsten Imido Alkylidene Complexes as Efficient Olefin-Metathesis Catalysts. *Angew. Chemie - Int. Ed.* **2003**, *42* (38), 4592–4633.

(97) Freyschlag, C. G.; Madix, R. J. Precious Metal Magic: Catalytic Wizardry. *Mater. Today* **2011**, *14* (4), 134–142.

(98) Hoque, M. E.; Hassan, M. M. M.; Chattopadhyay, B. Remarkably Efficient Iridium Catalysts for Directed C(Sp2)-H and C(Sp3)-H Borylation of Diverse Classes of Substrates. *J. Am. Chem. Soc.* **2021**, *143* (13), 5022–5037.

(99) Cadu, A.; Andersson, P. G. Iridium Catalysis: Application of Asymmetric Reductive Hydrogenation. *Dalt. Trans.* **2013**, *42* (40), 14345–14356.

(100) Peters, B. B. C.; Zheng, J.; Birke, N.; Singh, T.; Andersson, P. G. Iridium-Catalyzed Enantioconvergent Hydrogenation of Trisubstituted Olefins. *Nat. Commun.* **2022**, *13* (1), 1–8.

(101) Archer, S.; Weinstein, J. A. Charge-Separated Excited States in Platinum(II) Chromophores: Photophysics, Formation, Stabilization and Utilization in Solar Energy Conversion. *Coord. Chem. Rev.* **2012**, *256* (21–22), 2530–2561.

(102) Genzink, M. J.; Kidd, J. B.; Swords, W. B.; Yoon, T. P. Chiral Photocatalyst Structures in Asymmetric Photochemical Synthesis. *Chem. Rev.* **2022**, *122* (2), 1654–1716.

(103) Zheng, J.; Dong, X.; Yoon, T. P. Divergent Photocatalytic Reactions of α-Ketoesters under Triplet Sensitization and Photoredox Conditions. *Org. Lett.* **2020**, *22* (16), 6520–6525.

(104) Zhang, X.; Qin, J.; Huang, X.; Meggers, E. One-Pot Sequential Photoredox Chemistry and Asymmetric Transfer Hydrogenation with a Single Catalyst. *European J. Org. Chem.* **2018**, *2018* (4), 571–577.

(105) Huo, H.; Shen, X.; Wang, C.; Zhang, L.; Röse, P.; Chen, L. A.; Harms, K.; Marsch, M.; Hilt, G.; Meggers, E. Asymmetric Photoredox Transition-Metal Catalysis Activated by Visible Light. *Nature* **2014**, *515* (7525), 100–103.

(106) Huo, H.; Wang, C.; Harms, K.; Meggers, E. Enantioselective, Catalytic Trichloromethylation through Visible-Light-Activated Photoredox Catalysis with a Chiral Iridium Complex. *J. Am. Chem. Soc.* **2015**, *137* (30), 9551–9554.

(107) Chapman, S. J.; Swords, W. B.; Le, C. M.; Guzei, I. A.; Toste, F. D.; Yoon, T. P. Cooperative Stereoinduction in Asymmetric Photocatalysis. *J. Am. Chem. Soc.* **2022**, *144* (9), 4206–4213.

(108) Skubi, K. L.; Kidd, J. B.; Jung, H.; Guzei, I. A.; Baik, M. H.; Yoon, T. P. Enantioselective Excited-State Photoreactions Controlled by a Chiral Hydrogen-Bonding Iridium Sensitizer. *J. Am. Chem. Soc.* **2017**, *139* (47), 17186–17192.

(109) Crisenza, G. E. M.; Faraone, A.; Gandolfo, E.; Mazzarella, D.; Melchiorre, P. Catalytic Asymmetric C–C Cross-Couplings Enabled by Photoexcitation. *Nat. Chem.* **2021**, *13* (6), 575–580.

(110) Chan, A. Y.; Perry, I. B.; Bissonnette, N. B.; Buksh, B. F.; Edwards, G. A.; Frye, L. I.; Garry, O. L.; Lavagnino, M. N.; Li, B. X.; Liang, Y.; Mao, E.; Millet, A.; Oakley, J. V.; Reed, N. L.; Sakai, H. A.; Seath, C. P.; MacMillan, D. W. C. Metallaphotoredox: The

Merger of Photoredox and Transition Metal Catalysis. *Chem. Rev.* **2022**, *122* (2), 1485–1542.

(111) Holmberg-Douglas, N.; Nicewicz, D. A. Photoredox-Catalyzed C–H Functionalization Reactions. *Chem. Rev.* **2022**, *122* (2), 1925–2016.

(112) Zhang, X.; MacMillan, D. W. C. Alcohols as Latent Coupling Fragments for Metallaphotoredox Catalysis: Sp3-Sp2 Cross-Coupling of Oxalates with Aryl Halides. *J. Am. Chem. Soc.* **2016**, *138* (42), 13862–13865.

(113) Joe, C. L.; Doyle, A. G. Direct Acylation of C(Sp3)-H Bonds Enabled by Nickel and Photoredox Catalysis. *Angew. Chemie - Int. Ed.* **2016**, *55* (12), 4040–4043.

(114) Gildea, L. F.; Williams, J. A. G. *Iridium and Platinum Complexes for OLEDs*; Woodhead Publishing Limited, 2013.

(115) Evans, R. C.; Douglas, P.; Winscom, C. J. Coordination Complexes Exhibiting Room-Temperature Phosphorescence: Evaluation of Their Suitability as Triplet Emitters in Organic Light Emitting Diodes. *Coord. Chem. Rev.* **2006**, *250* (15–16), 2093–2126.

(116) Kraus, P. M.; Zürch, M.; Cushing, S. K.; Neumark, D. M.; Leone, S. R. The Ultrafast X-Ray Spectroscopic Revolution in Chemical Dynamics. *Nat. Rev. Chem.* **2018**, *2* (6), 82–94.

(117) Smolentsev, G.; Sundström, V. Time-Resolved X-Ray Absorption Spectroscopy for the Study of Molecular Systems Relevant for Artificial Photosynthesis. *Coord. Chem. Rev.* **2015**, *304–305*, 117–132.

(118) Milne, C. J.; Penfold, T. J.; Chergui, M. Recent Experimental and Theoretical Developments in Time-Resolved X-Ray Spectroscopies. *Coord. Chem. Rev.* **2014**, *277–278*, 44–68.

(119) Vogt, M.; Smolentsev, G. Time-Resolved X-Ray Spectroscopy to Study Luminophores with Relevance for OLEDs. *ChemPhotoChem* **2022**, e202100180.

(120) Macmillan, S. N.; Lancaster, K. M. X-Ray Spectroscopic Interrogation of Transition-Metal-Mediated Homogeneous Catalysis: Primer and Case Studies. *ACS Catal.* **2017**, *7* (3), 1776–1791.

(121) Smolentsev, G.; Van Vliet, K. M.; Azzaroli, N.; Van Bokhoven, J. A.; Brouwer, A. M.; De Bruin, B.; Nachtegaal, M.; Tromp, M. Pump-Probe XAS Investigation of the Triplet State of an Ir Photosensitizer with Chromenopyridinone Ligands. *Photochem. Photobiol. Sci.* **2018**, *17* (7), 896–902.

(122) Gawelda, W.; Johnson, M.; De Groot, F. M. F.; Abela, R.; Bressler, C.; Chergui, M. Electronic and Molecular Structure of Photoexcited [RuII(Bpy) 3]2+ Probed by Picosecond X-Ray Absorption Spectroscopy. *J. Am. Chem. Soc.* **2006**, *128* (15), 5001–5009.

(123) Zhang, X.; Canton, S. E.; Smolentsev, G.; Wallentin, C. J.; Liu, Y.; Kong, Q.; Attenkofer, K.; Stickrath, A. B.; Mara, M. W.; Chen, L. X.; Wärnmark, K.; Sundström, V. Highly Accurate Excited-State Structure of [Os(Bpy)2dcbpy] 2+ Determined by X-Ray Transient

Absorption Spectroscopy. *J. Am. Chem. Soc.* **2014**, *136* (24), 8804–8809.

(124) Weingartz, N. P.; Mara, M. W.; Roy, S.; Hong, J.; Chakraborty, A.; Brown-Xu, S. E.; Phelan, B. T.; Castellano, F. N.; Chen, L. X. Excited-State Bond Contraction and Charge Migration in a Platinum Dimer Complex Characterized by X-Ray and Optical Transient Absorption Spectroscopy. *J. Phys. Chem. A* **2021**, *125* (40), 8891–8898.

(125) Göries, D.; Dicke, B.; Roedig, P.; Stübe, N.; Meyer, J.; Galler, A.; Gawelda, W.; Britz, A.; Geßler, P.; Sotoudi Namin, H.; Beckmann, A.; Schlie, M.; Warmer, M.; Naumova, M.; Bressler, C.; Rübhausen, M.; Weckert, E.; Meents, A. Time-Resolved Pump and Probe x-Ray Absorption Fine Structure Spectroscopy at Beamline P11 at PETRA III. *Rev. Sci. Instrum.* **2016**, *87* (5).

(126) Hoffman, A. S.; Sokaras, D.; Zhang, S.; Debefve, L. M.; Fang, C. Y.; Gallo, A.; Kroll, T.; Dixon, D. A.; Bare, S. R.; Gates, B. C. High-Energy-Resolution X-Ray Absorption Spectroscopy for Identification of Reactive Surface Species on Supported Single-Site Iridium Catalysts. *Chem. - A Eur. J.* **2017**, *23* (59), 14760–14768.

(127) Pan, G.; Hu, C.; Hong, S.; Li, H.; Yu, D.; Cui, C.; Li, Q.; Liang, N.; Jiang, Y.; Zheng, L.; Jiang, L.; Liu, Y. Biomimetic Caged Platinum Catalyst for Hydrosilylation Reaction with High Site Selectivity. *Nat. Commun.* **2021**, *12* (1), 1–9.

(128) Griffith, K. J.; Wiaderek, K. M.; Cibin, G.; Marbella, L. E.; Grey, C. P. Niobium Tungsten Oxides for High-Rate Lithium-Ion Energy Storage. *Nature* **2018**, *559* (7715), 556–563.

(129) Choy, J. H.; Kim, D. K.; Hwang, S. H.; Demazeau, G.; Jung, D. Y. XANES and EXAFS Studies on the Ir–O Bond Covalency in Ionic Iridium Perovskites. *J. Am. Chem. Soc.* **1995**, *117* (33), 8557–8566.

(130) Britz, A.; Bokarev, S. I.; Assefa, T. A.; Bajnóczi, È. G.; Németh, Z.; Vankó, G.; Rockstroh, N.; Junge, H.; Beller, M.; Doumy, G.; March, A. M.; Southworth, S. H.; Lochbrunner, S.; Kühn, O.; Bressler, C.; Gawelda, W. Site-Selective Real-Time Observation of Bimolecular Electron Transfer in a Photocatalytic System Using L-Edge X-Ray Absorption Spectroscopy**. *ChemPhysChem* **2021**, *22* (7), 693–700.

(131) Jayarathne, U.; Chandrasekaran, P.; Greene, A. F.; Mague, J. T.; Debeer, S.; Lancaster, K. M.; Sproules, S.; Donahue, J. P. X-Ray Absorption Spectroscopy Systematics at the Tungsten L-Edge. *Inorg. Chem.* **2014**, *53* (16), 8230–8241.

(132) Li, L.; Yang, J.; Ali-Löytty, H.; Weng, T. C.; Toma, F. M.; Sokaras, D.; Sharp, I. D.; Nilsson, A. Operando Observation of Chemical Transformations of Iridium Oxide during Photoelectrochemical Water Oxidation. *ACS Appl. Energy Mater.* **2019**, *2* (2), 1371–1379.

(133) Monteseguro, V.; Sans, J. A.; Cuartero, V.; Cova, F.; Abrikosov, I. A.; Olovsson, W.; Popescu, C.; Pascarelli, S.; Garbarino, G.; Jönsson, H. J. M.; Irifune, T.; Errandonea, D. Phase Stability and Electronic Structure of Iridium Metal at the Megabar Range. *Sci. Rep.* **2019**, *9* (1), 1–9.

(134) Clancy, J. P.; Chen, N.; Kim, C. Y.; Chen, W. F.; Plumb, K. W.; Jeon, B. C.; Noh, T. W.; Kim, Y.-J. Spin-Orbit Coupling in Iridium-Based 5d Compounds Probed by x-Ray Absorption Spectroscopy. *Phys. Rev. B* **2012**, *86* (19), 195131.

(135) Laguna-Marco, M. A.; Kayser, P.; Alonso, J. A.; Martínez-Lope, M. J.; Van Veenendaal, M.; Choi, Y.; Haskel, D. Electronic Structure, Local Magnetism, and Spin-Orbit Effects of Ir(IV)-, Ir(V)-, and Ir(VI)-Based Compounds. *Phys. Rev. B - Condens. Matter Mater. Phys.* **2015**, *91* (21), 1–9.

(136) Van Der Veen, R. M.; Milne, C. J.; Nahhas, A. El; Lima, F. A.; Pham, V. T.; Best, J.; Weinstein, J. A.; Borca, C. N.; Abela, R.; Bressler, C.; Chergui, M. Structural Determination of a Photoehemieally Active Diplatinum Molecule by Time-Resolved EXAFS Spectroscopy. *Angew. Chemie - Int. Ed.* **2009**, *48* (15), 2711–2714.

(137) El Nahhas, A.; Van Der Veen, R. M.; Penfold, T. J.; Pham, V. T.; Lima, F. A.; Abela, R.; Blanco-Rodriguez, A. M.; Záliš, S.; Vlček, A.; Tavernelli, I.; Rothlisberger, U.; Milne, C. J.; Chergui, M. X-Ray Absorption Spectroscopy of Ground and Excited Rhenium-Carbonyl- Diimine Complexes: Evidence for a Two-Center Electron Transfer. *J. Phys. Chem. A* **2013**, *117* (2), 361–369.

(138) Geneaux, R.; Marroux, H. J. B.; Guggenmos, A.; Neumark, D. M.; Leone, S. R. Transient Absorption Spectroscopy Using High Harmonic Generation: A Review of Ultrafast X-Ray Dynamics in Molecules and Solids. *Philos. Trans. R. Soc. A Math. Phys. Eng. Sci.* **2019**, *377* (2145), 20170463.

(139) Scutelnic, V.; Leone, S. R. Elucidation of Molecular Dynamics by Extreme Ultraviolet and Soft X-Ray Transient-Absorption Spectroscopy. *ACS Symp. Ser.* **2021**, *1398*, 1–14.

(140) Cirri, A.; Husek, J.; Biswas, S.; Baker, L. R. Achieving Surface Sensitivity in Ultrafast XUV Spectroscopy: M2,3-Edge Reflection-Absorption of Transition Metal Oxides. *J. Phys. Chem. C* **2017**, *121* (29), 15861–15869.

(141) Sandhu, A. S.; Tong, X. M. Femtosecond and Attosecond Spectroscopy in the Xuv Regime. *IEEE J. Sel. Top. Quantum Electron.* **2012**, *18* (1), 351–362.

(142) Vura-Weis, J.; Jiang, C. M.; Liu, C.; Gao, H.; Lucas, J. M.; De Groot, F. M. F.; Yang, P.; Alivisatos, A. P.; Leone, S. R. Femtosecond M2,3-Edge Spectroscopy of Transition-Metal Oxides: Photoinduced Oxidation State Change in α-Fe2O3. *J. Phys. Chem. Lett.* **2013**, *4* (21), 3667–3671.

(143) Ryland, E. S.; Lin, M.-F.; Verkamp, M. A.; Zhang, K.; Benke, K.; Carlson, M.; Vura-Weis, J. Tabletop Femtosecond M-Edge X-Ray Absorption Near-Edge Structure of FeTPPCl: Metalloporphyrin Photophysics from the Perspective of the Metal. *J. Am. Chem. Soc.* **2018**, *140* (13), 4691–4696.

(144) Shari'Ati, Y.; Vura-Weis, J. Ballistic Δ: S = 2 Intersystem Crossing in a Cobalt Cubane Following Ligand-Field Excitation Probed by Extreme Ultraviolet Spectroscopy. *Phys. Chem. Chem. Phys.* **2021**, *23* (47), 26990–26996.

(145) Zhang, K.; Ash, R.; Girolami, G. S.; Vura-Weis, J. Tracking the Metal-Centered Triplet in Photoinduced Spin Crossover of Fe(Phen)32+ with Tabletop Femtosecond M-Edge X-Ray Absorption Near-Edge Structure Spectroscopy. *J. Am. Chem. Soc.* **2019**, *141* (43), 17180–17188.

(146) Ryland, E. S.; Zhang, K.; Vura-Weis, J. Sub-100 Fs Intersystem Crossing to a Metal-

Centered Triplet in Ni(II)OEP Observed with M-Edge XANES. *J. Phys. Chem. A* **2019**, *123* (25), 5214–5222.

(147) Zhang, K.; Lin, M. F.; Ryland, E. S.; Verkamp, M. A.; Benke, K.; De Groot, F. M. F.; Girolami, G. S.; Vura-Weis, J. Shrinking the Synchrotron: Tabletop Extreme Ultraviolet Absorption of Transition-Metal Complexes. *J. Phys. Chem. Lett.* **2016**, *7* (17), 3383–3387.

(148) Britz, A.; Attar, A. R.; Zhang, X.; Chang, H.-T.; Nyby, C.; Krishnamoorthy, A.; Park, S. H.; Kwon, S.; Kim, M.; Nordlund, D.; Sainio, S.; Heinz, T. F.; Leone, S. R.; Lindenberg, A. M.; Nakano, A.; Ajayan, P.; Vashishta, P.; Fritz, D.; Lin, M.-F.; Bergmann, U. Carrier-Specific Dynamics in 2H-MoTe 2 Observed by Femtosecond Soft x-Ray Absorption Spectroscopy Using an x-Ray Free-Electron Laser. *Struct. Dyn.* **2021**, *8* (1), 014501.

(149) Haensel, R.; Radler, K.; Sonntag, B.; Kunz, C. Optical Absorption Measurements of Tantalum, Tungsten, Rhenium and Platinum in the Extreme Ultraviolet. *Solid State Commun.* **1969**, *7* (20), 1495–1497.

(150) Dietz, R. E.; McRae, E. G.; Weaver, J. H. Core-Electron Excitation Edges in Metallic Ni, Cu, Pt, and Au. *Phys. Rev. B* **1980**, *21* (6), 2229–2247.

(151) Costello, J. T.; Kennedy, E. T.; Sonntagi, B. F.; Cromer, C. L. Xuv Photoabsorption of Laser-Generated w and Pt Vapours. *J. Phys. B At. Mol. Opt. Phys.* **1991**, *24* (24), 5063–5069.

(152) Sladeczek, P.; Martins, M.; Richter, M.; Selbmann, K. H.; Zimmermann, P. Photoionization Experiments on Atomic Pt in the Range 40-90 Ev. *J. Phys. B At. Mol. Opt. Phys.* **1994**, *27* (18), 4123–4131.

(153) Martins, M.; Sladeczek, P.; Tiedtke, K.; Zimmermann, P. Vacuum Ultraviolet Photoionization of the 5d Elements in the Region of the 5p and 4f Excitation. *Eur. Phys. J. D - At. Mol. Opt. Phys.* **1998**, *1* (1), 47–52.

(154) Kennedy, E. T.; Costello, J. T.; Mosnier, J. P.; Van Kampen, P. VUV/EUV Ionising Radiation and Atoms and Ions: Dual Laser Plasma Investigations. *Radiat. Phys. Chem.* **2004**, *70* (1–3), 291–321.

(155) Su, M. G.; Dong, C. Z.; Murphy, N.; O'Sullivan, G. Analysis of the Xuv Photoabsorption Spectrum of Au2+, Au3+, and Au4+. *Phys. Rev. A - At. Mol. Opt. Phys.* **2009**, *79* (4), 1–8.

(156) Chang, H. T.; Guggenmos, A.; Chen, C. T.; Oh, J.; Géneaux, R.; Chuang, Y. De; Schwartzberg, A. M.; Aloni, S.; Neumark, D. M.; Leone, S. R. Coupled Valence Carrier and Core-Exciton Dynamics in WS2 Probed by Few-Femtosecond Extreme Ultraviolet Transient Absorption Spectroscopy. *Phys. Rev. B* **2021**, *104* (6), 1–14.

Chapter 2: Synthesis of a series of M(II) chloride complexes with inter- and intra-ligand hydrogen bonding interactions

2.1 Hydrogen-bonding in synthetic metal systems

Hydrogen bonding networks found within metalloproteins play an essential role in the structure and function of enzymes. Intermolecular hydrogen bonds are responsible for positioning and stabilizing substrate at the active site while intramolecular hydrogen bonds between amino acids can function to change the metal's ligand field, reduction potential, and geometry within the metalloprotein (Fig. 2.1A).[1–4] While these interactions are ubiquitous throughout enzymatic systems, modelling both intra- and intermolecular hydrogen bonding interactions in synthetic systems is difficult.[5]

Many reported examples of hydrogen bonding in synthetic complexes use C_3-symmetric ligands with three ligand arms capable of providing or receiving hydrogen bonds from a ligand bound to a metal. Examples by Borovik,[6–12] Szymczak,[13,14] Scarborough,[15] and Fout[16–19] have all

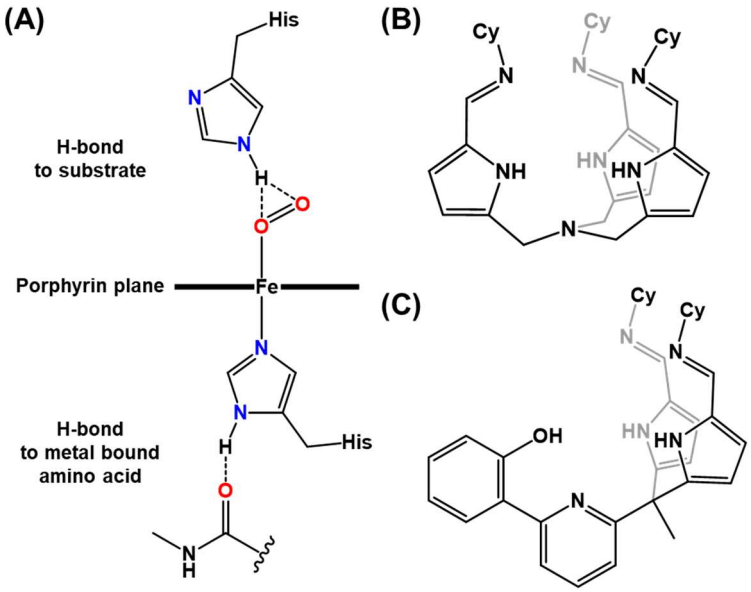

Figure 2.1 (A) Hydrogen bonding to bound substrate and amino acid residues characterized in heme proteins. (B) Ligand used in previous studies with C_3 symmetry. (C) Ligand used in this study with approximate C_S symmetry.

used ligands which incorporate hydrogen bond donors or acceptors in the secondary coordination sphere of a metal to model biological systems.

Less developed are synthetic complexes that do not feature C_3-symmetric ligands but also incorporate hydrogen bonding motifs.[20–23] Most of these complexes are designed to interact with a metal-bound extrinsic ligand via inter-ligand hydrogen bonds, such as hydrogen bond donation to O_2 or oxyanions prior to (or during) reaction with those species.[23–30] Synthetic heme systems have focused on trying to incorporate hydrogen bonds to ligands that are meant to act as amino acid mimics and demonstrate how protein scaffolds can also use intramolecular hydrogen bonds to tune metal reactivity patterns.[31,32]

This chapter describes work[33] on the synthesis of metal (M = Mn, Fe, Co) chloride complexes that exhibit both intra- and inter-ligand hydrogen bonds with a new biomimetic ligand scaffold (Figure 2.1C). The intra-ligand hydrogen bonds are shown to have a profound effect on the coordination geometry of the metal center, while maintaining a separate inter-ligand hydrogen bond with an axially bound chloride ligand.

2.2 Synthesis of the ligand $^{Ph}OPy(pi^{Cy})_2$

Our group has previously reported the use of a C_3-symmetric tripodal ligand, ($N(pi^{Cy})_3$) (Figure 2.1B), and its complexation with late first row metals (M = Mn, Fe, Co, Zn).[16–18] One of the unique features of this ligand system is the ability of the pyrrole-imine (pi) functionalities to tautomerize to an azafulvene-amine (afa) tautomer upon binding of a metal. The tautomerization allows for the ligand arms to present as either a hydrogen bond donor or acceptor for axially bound ligands, as well as alternating between anionic or dative coordination of the metal center.

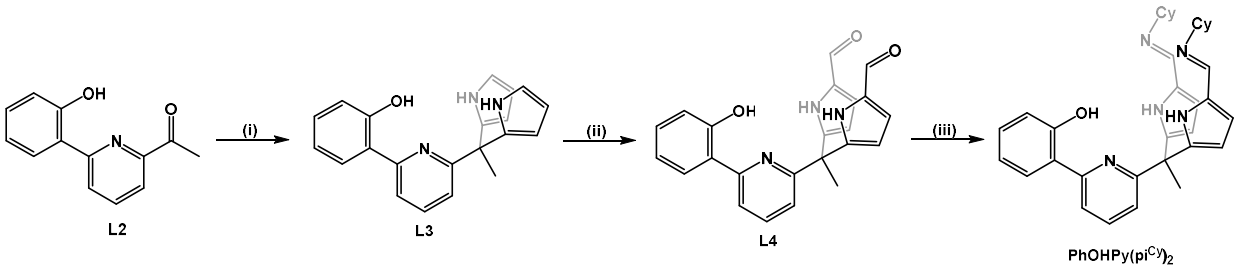

Figure 2.2 Synthesis of ^{Ph}OHPy(pi^{Cy})$_2$.(i) Pyrrole, cat. trifluoroacetic acid (TFA), 18 h, room temperature (r.t.) (ii) 2.1 equiv. $POCl_3$, dimethylformamide (DMF) /dichloromethane (DCM), r.t. to 40 °C, 2 h; sat. sodium acetate (aq), 45 °C, 1 h (iii) 2.2 cyclohexylamine (H_2N-Cy), 18 h, r.t. DCM.

As many metalloproteins have a non-symmetric ligand field around the metal center, we sought to desymmetrize the chelating ligand field through the replacement of an axial pyrrole-imine ligand arm with a tyrosine-like ligand in the form of a phenoxide. The incorporation of the phenoxide arm with the pyrrole-imine arms was accomplished in the synthesis of the new ligand 2-(6-(1,1-bis(5-(cyclohexylimino)methyl)-pyrrol-2-yl)ethyl)pyridin-2-yl)phenol, ^{Ph}OHPy(pi^{Cy})$_2$ (Figure 2.1C). The ligand was prepared from a previously reported precursor,[34] 2-hydroxyphenol-6-actylpyridine (**L1**), over three steps (Figure 2.2). **L1** was reacted with an excess of pyrrole in the presence of catalytic amounts of trifluoroacetic acid (TFA) overnight; the reaction mixture was subsequently neutralized, extracted with dichloromethane, and the organic fractions combined for solvent removal to afford the crude product as a brown oil. This was purified by precipitating out the desired product as a light tan powder using diethyl ether and collecting on a frit in good yield (76%). **L2** underwent a modified Vilsmeier-Haack formulation with N,N-dimethylformamide (DMF) in dichloromethane (DCM) to give the desired product **L3** as a yellow film in good yield (81%), which was thoroughly dried under high vacuum to remove unreacted DMF. To form the final ligand ^{Ph}OHPy(pi^{Cy})$_2$, L3 underwent an imine condensation with cyclohexylamine (3.01 equivalents) in DCM at room temperature overnight. The resulting reaction solution had solvents removed *in vacuo*, and the dark red-brown oil was dissolved in a minimal amount of Et_2O to precipitate out the desired product as an off-white-to-tan powder in great yield (81%). The ligand

was dried under high vacuum overnight, brought under inert atmosphere, and dried thoroughly by adding 4Å sieves to a DCM solution of the ligand and let sit for a minimum of 24 hours. The ligand was checked by ^{1}H NMR spectroscopy for water prior to use in metalations.

2.3 Synthesis of first-row metal(II) chloride complexes (M = Mn, Fe, Co)

The synthesis of the metal complexes PhOPy(afa^{Cy})$_2$MCl (Mn = **1**, Fe = **2**, Co = **3**) was successfully accomplished by treating PhOHPy(pi^{Cy})$_2$ with potassium hydride (KH) in tetrahydrofuran, followed by addition of the corresponding metal dichloride salts (MCl_2 = Mn, Fe, Co; 1 eq, Figure 2.3). The resulting solutions were stirred overnight, and volatiles removed *in vacuo*. Metal complexes were subsequently dissolved in dichloromethane and filtered through diatomaceous earth to remove insoluble salts. Analytically pure samples were recrystallized from concentrated solutions of metal complex in dichloromethane with vapor diffusion of diethyl ether. Nickel and copper metalations were attempted using the corresponding metal halide ($NiCl_2$, CuX and CuX_2; X = Cl or Br); however, no reaction occurred with the nickel salt, and copper also showed no reactivity (CuX) or an intractable mess of products (CuX_2).

Examination of **1-3** using IR spectroscopy (Table 1, Figures 2.20-2.22) revealed that ligand arms with hydrogen bonding functionality had tautomerized to the azafulvene-amine tautomer, based on the C=N stretching energies compared with previously characterized complexes (1635-

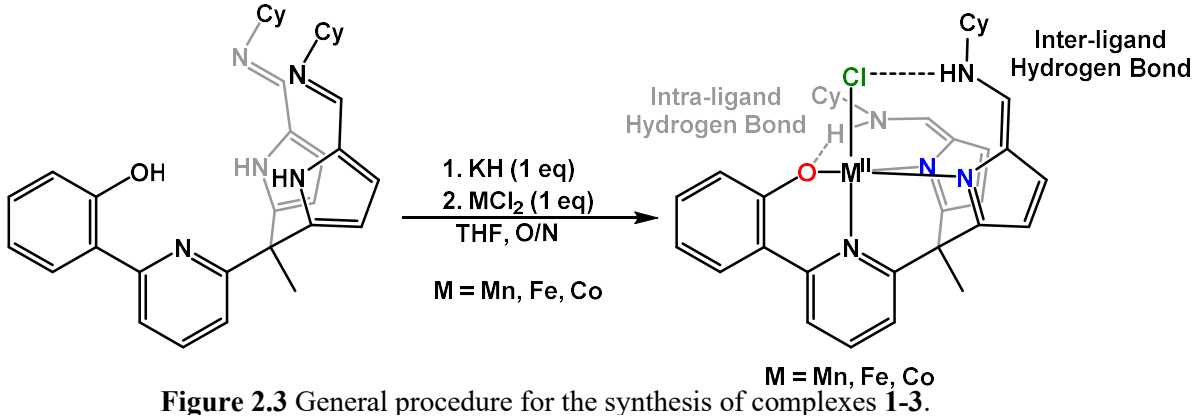

Figure 2.3 General procedure for the synthesis of complexes **1-3**.

Table 2.1 Spectroscopic characterization of complexes **1-3**.

Complex	$\nu_{C=N}$ (cm^{-1})	ν_{N-H} (cm^{-1})	μ_{eff} (μ_B)
1	1640	3284	6.10(22)
2	1638	3250	5.26(12)
3	1654	3183	4.62(16)

1655 cm^{-1}).[16-17] Each complex also displayed what were assigned as N-H stretches above 3200 cm^{-1}, with **3** displaying multiple N-H stretching modes (*vide infra*). Compounds **1-3** were found to adopt high-spin states at ambient temperature based on paramagnetic ^{1}H NMR spectra (Figures 2.13-2.14) and characterization of the complexes using Evan's method (Table 2.1).

Crystals appropriate for single crystal X-ray diffraction studies were grown using the same solvent system as for bulk purification and the solid-state structures of **1-3** were characterized. The manganese analogue, **1**, refined as a pseudo-square pyramidal complex (Table 2.2, Figure 2.4A) with an equatorial plane consisting of anionic coordination from the deprotonated phenoxy arm, and tautomerization of the ligand arms from the initial pyrrole-imine motif to the azafulvene-amine motif, as suggested by IR spectroscopy. Interestingly, hydrogen bonding interactions are observed from the ligand arms to both the bound chloride (inter-ligand), and the coordinated phenoxy arm (intra-ligand), in analogy to hydrogen bonding interactions observed in metalloprotein scaffolds. The corresponding iron complex, **2**, displayed a similar coordination geometry and hydrogen bonding interactions (Table 2.2, Figure 2.4B).

As a contrast to **1** and **2**, the cobalt derivative, **3**, presented an asymmetric unit cell with two unique molecules that are differentiated by their hydrogen bonding interactions. One complex (**3a**) was isostructural to **1** and **2** with both intra- and inter-ligand hydrogen bonding interactions, whereas the other cobalt complex (**3b**) presented with only one inter-ligand hydrogen bond to the chloride atom (Table 2.2, Figure 2.4 C & D) with the other ligand arm not engaging in hydrogen bonding.

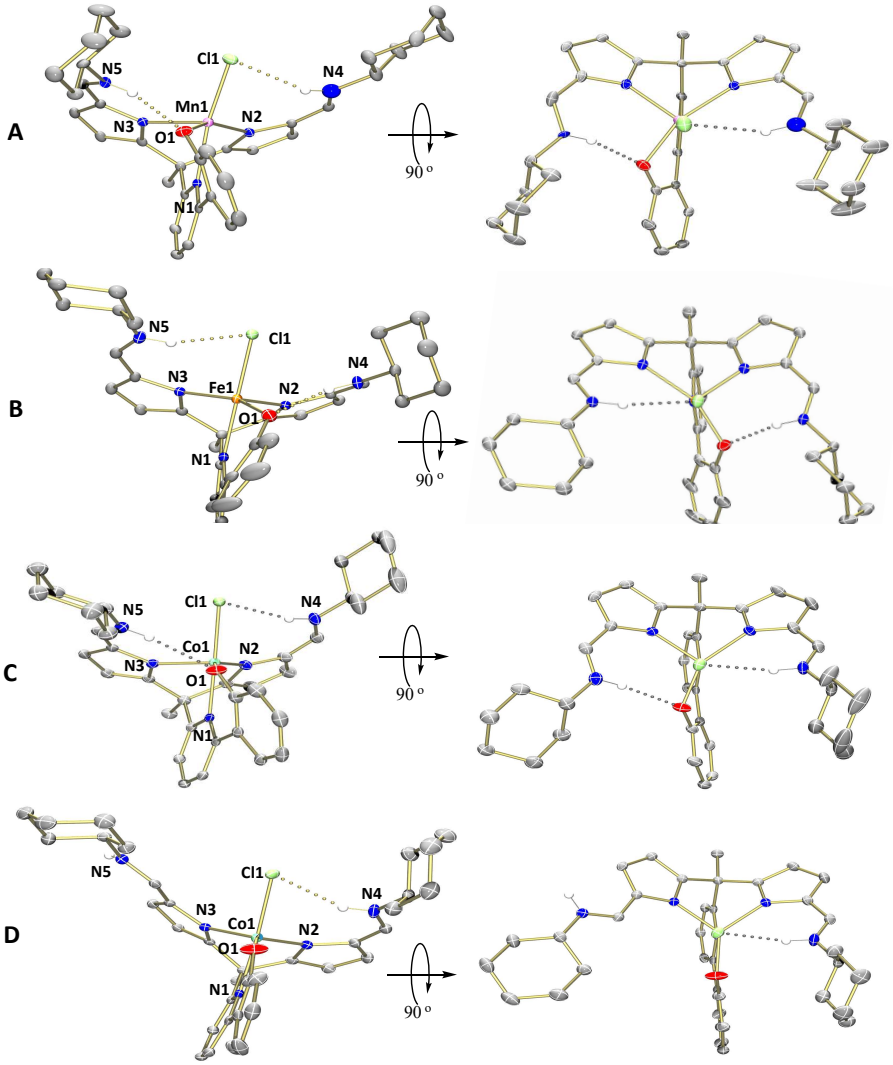

Figure 2.4 Structural characterization of complexes **1-3**. The solid-state structures of **1** (Mn, A) and **2** (Fe, B) displayed both inter- and intra-ligand hydrogen bonds, whereas the cobalt analogue displayed one isostructural complex **3a** (C), and **3b** with only an inter-ligand hydrogen bond (D). Corresponding bond lengths, angles, and τ_5 values can be found in Table 2.2.

The inter-ligand hydrogen bonds observed in complexes **1-3** had N-H---Cl distances of 3.0938(16) - 3.1786(15) Å and H---Cl bond lengths of 2.26-2.31 Å, while the intra-ligand hydrogen bonds had N-H---O distances of 2.804(14) - 3.155(3) Å and H---O bond lengths of 2.01-2.15 Å. These values are consistent for expected hydrogen bonding interactions, with the inter-ligand hydrogen bond distances slightly weaker in comparison to similar characterized complexes with the $N(pi^{Cy})_3$ ligand framework.[17] Interestingly, upon the loss of the inter-ligand hydrogen

Table 2.2 Selected bond lengths and angles of complexes **1-3.**

Bond length (Å)	1 (Mn)	2 (Fe)	3a (Co, arm in)	3b (Co, arm out)
M1-O1	**2.0304(1)**	**1.9378(1)**	**1.9203(16)**	**1.8751(17)**
M1-Cl1	**2.4355(5)**	**2.4518(5)**	**2.4357(6)**	**2.4712(6)**
M1-N1	**2.3083(1)**	**2.2358(2)**	**2.2238(18)**	**2.2249(18)**
M1-N2	**2.1240(1)**	**2.0549(2)**	**2.0275(18)**	**2.0244(18)**
M1-N3	**2.1337(1)**	**2.0766(2)**	**2.0142(18)**	**2.0047(18)**
N#-H---Cl (# = 4 or 5)	**3.1786(15)**	**3.0938(16)**	**3.116(2)**	**3.129(2)**
N#-H---O (# = 4 or 5)	**2.804(14)**	**2.922(2)**	**3.155(3)**	**--**
Bond Angles (degrees)				
O1-M1-N2 or –N3 (α)	**154.62(5)**	**154.10(6)**	**148.33(8)**	**132.73(8)**
N1-M1-Cl1 (β)	**171.04(3)**	**178.32(5)**	**176.54(5)**	**175.44(5)**
N2-M1-N3	**95.17(7)**	**96.26(7)**	**97.05(7)**	**96.46(7)**
N2-M1-O1	**154.62(6)**	**105.74(7)**	**148.33(7)**	**132.73(7)**
N3-M1-O1	**100.38(7)**	**154.10(7)**	**111.98(7)**	**129.12(7)**
τ_5	**0.27**	**0.40**	**0.47**	**0.71**

bond from **3a** to **3b**, there is an approximate 0.045 Å contraction of the Co-O bond length and 0.036 Å elongation of the Co-Cl bond length (Table 2.2). This suggests that the inter-ligand hydrogen bond tunes the donor ability of the phenolic oxygen by making it a poorer electron donor.

To further understand how the hydrogen bonding interactions effected the geometry of **1-3**, each complex was analyzed using the structural parameter τ_5 (Equation 2.1).[35] The analysis identifies whether the geometry of a five-coordinate species is closer to being trigonal bipyramidal

$$\tau_5 = \frac{\beta - \alpha}{60°} \qquad (Eq. 2.1)$$

($\tau_5 = 1$) or square pyramidal ($\tau_5 = 0$), where β and α (β > α) are the two greatest valence angles of the metal center.

Complex **1** has the lowest τ_5 value ($\tau_5 = 0.27$), indicating its structure is best described as distorted square pyramidal, whereas complexes **2** and **3** have τ_5 values of $\tau_5 = 0.40$ and $\tau_5 = 0.47$, respectively, showing an intermediate geometry (calculations in Eq. 2.2-2.5). Interestingly, **3b** has a τ_5 value of 0.71, indicating it is best described as distorted trigonal bipyramidal. While the metal(II) ion size contributes the ligand conformation, the comparison of **3a** and **3b** highlights how the presence or absence of a hydrogen bond to a bound ligand can greatly affect the geometry of the metal center. The increased τ_5 value of **3b** upon the loss of the inter-ligand hydrogen bond from **3a** to the phenol oxygen to reflect a more trigonal pyramidal structure suggests that this could be used to control substrate coordination to the metal center by favoring or disfavoring an open face *cis* to the axial ligand.

Complexes **1-3** demonstrate a break from the trend of 5-coordinate complexes with a secondary coordination sphere being best describes as trigonal bipyramidal. The introduction of the intramolecular hydrogen bond to the phenoxy ligand arm causes a change in geometry of the metal center and creates a potential binding site on the more square pyramidal complexes. It is possible this change in geometry could lead to better synthetic models for enzymes, such as non-heme iron halogenases that activate dioxygen and go through a number of 5-coordinate intermediates during catalytic turnover.[36,37] Furthermore, the tuning of the oxygen donor ability by the inter-ligand hydrogen bond as evidenced by structures **3a** and **3b** could be used to influence reactivity at the axial position . This system showcases the ability of hydrogen bonds from the secondary coordination sphere as a way to not only bond to axial ligands but also as a new design

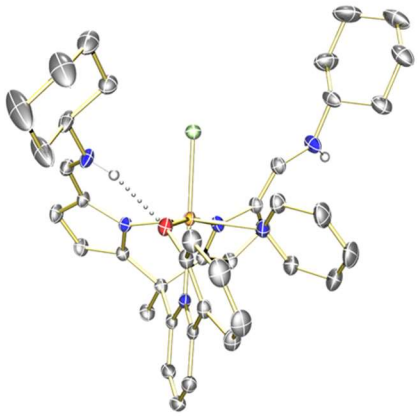

Bond length (Å)	4 (Fe)
M1-O1	1.929(2)
M1-Cl1	2.3206(8)
M1-N1	2.208(2)
M1-N2	2.084(2)
M1-N3	2.066(2)
M1-N6	2.211(2)
N5-H---O1	2.819(3)

Figure 2.5 Solid state structure of complex **4** with select bond parameters; non-heteroatomic hydrogens and outer sphere counter anion removed for clarity.

principle for future complexes that seek to tune a metal center's geometry through hydrogen bonding to the ligand framework.

Cyclic voltammetry of the metal(II) chloride species suggested oxidation to a metal(III) species was possible (Fig. 2.25-2.27). A reaction of silver triflate (AgOTf) to complex **2** in the dark resulted in a dark brown mixture that filtered off Ag^0. We speculated that this was the iron(III) chloride species, $[^{Ph}OPy(afa^{Cy})_2Fe^{III}Cl]OTf$ (**4**). Crystals suitable for preliminary crystallographic characterization were grown from vapor diffusion of diethyl ether into a concentrated solution of **4** in acetonitrile with a drop of pyridine. Without an L-type coordinator such as pyridine or acetonitrile around, crystallization attempts proved fruitless and gave only non-diffracting crystalline material. Refinement showed that complex **4** is the anticipated iron(III) chloride (Figure 2.5), where there is a contraction of the Fe-Cl bond compared to complex **2** and an outer sphere triflate anion. Pyridine is also observed to coordinate with the metal center in the site opened by the inter-ligand hydrogen bond to the phenoxy, supporting the use of intra-ligand hydrogen bond as a source for controlling coordination to the metal center and thus reactivity.

Attempts at reacting the iron(II) and iron(III) chloride species to either transfer the chloride or introduce an O-based species were unsuccessful. While the pyridine structure showed that

substrate coordination could occur to the open face of the metal species, attempts at replacing this by reacting the iron(III) complex with dioxygen or O-based species resulted in messy paramagnetic ^{1}H NMR spectra and no isolable products. Based on prior work with a similar trigonal bipyramidal ligand,[30] the chloride is likely too tightly bound to the metal center to function as a useful halogenation agent or catalyst. Using a more loosely bound ligand such as triflate or tetrafluoroborate could prove a more reactive species for small molecule activation, akin to the bistriflate tripodal and tetrapodal metal species discussed later in this thesis (Chapters 4 and 3, respectively).

2.4 An alternative binding pocket - PhOHPy(afa^{Cy})$_2$ZnCl$_2$

An alternative binding pocket was observed with zinc metalation. The formation of a zinc(II) dichloride complex was accomplished by performing a similar metalation procedure to the other mid- to late first row metals; after the ligand was deprotonated, the zinc salt was added to the solution and allowed to stir overnight. Shifts in the diamagnetic peaks in the ^{1}H NMR spectrum and the C=N IR stretch increasing to 1646 cm^{-1} indicated that the metalation had successfully occurred; however, a proton peak in the phenolic region appeared, indicative that there was

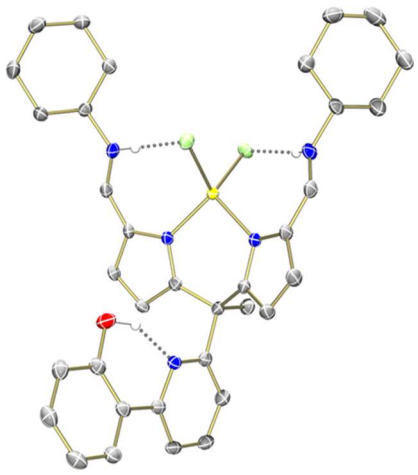

Bond length (Å)	5 (Zn)
Zn1-Cl1	2.2713(5)
Zn1-Cl2	2.2686(5)
Zn1-N2	1.9879(15)
Zn1-N3	1.9903(15)
O1-H---N1	2.619(2)
N4-H---Cl2	3.4305(17)
N5-H---Cl1	3.3131(16)

Figure 2.6 Solid state structure of complex **6** with select structural parameters.

protonation of the phenol group. Upon refinement, the solid-state structure was shown to be of $^{PhOHPy}(afa^{Cy})_2ZnCl_2$ (**5**, Figure 2.6), where the zinc does not sit in the expected binding pocket but sits between the azafulvene-amine arms in a tetrahedral geometry. Both chlorides are still present with the amine on the nearest ligand arm pointing towards it, but the N-H---Cl distance is too long to be a strong hydrogen bonding interaction. The re-protonated phenol group hydrogen bonds to the pyridine backbone. This "scorpion"-like structure is akin to the metal(II) dichloride (M = Fe, Cu) species from prior work with our group's dipodal ligand system,[38] where the binding pocket is the tautomeric arms. Unlike the iron or copper chloride dipodal species, the zinc(II) exhibits tetrahedral coordination instead of pseudo trigonal bipyramidal, and both ligand arms are each weakly hydrogen-bonding with the bound chlorides. It is suspected that ligand re-protonation occurs during the reaction in THF overnight, so an aprotic solvent mixture could furnish the zinc(II) monochloride species analogous to complexes **1-3**.

2.5 Conclusions

We have reported the synthesis of a new ligand platform $^{PhOH}Py(pi^{Cy})_2$ that upon complexation with mid to late first row transition metal chloride salts demonstrates both intra- and inter-ligand hydrogen bonding interactions. The intra-ligand hydrogen bonding interactions with the phenoxy ligand arm are shown to have a profound effect on the geometry of the metal center and coordination to the metal. This provides a new design principle for future biomimetic complexes that incorporate hydrogen bonding motifs.

2.6 Experimental

General Considerations. All manipulations were carried out in the absence of water and dioxygen using standard Schlenk techniques or in an MBraun inert atmosphere drybox under a dinitrogen

atmosphere except where specified otherwise. All glassware was oven- dried for a minimum of 8 h and cooled in an evacuated antechamber prior to use in the drybox. Solvents were dried and deoxygenated on a Glass Contour System (SG Water USA, Nashua, NH) and stored over 4 Å molecular sieves purchased from Strem following literature procedure prior to use.

2-bromo-6-acetylpyridine was synthesized using the same procedure as previously reported.[22] 2-phenol-6-acetylpyridine (**L1**) was synthesized according to a modified literature procedure.[33] NMR spectra were recorded at room temperature on a Varian spectrometer operating at 400 MHz or 500 MHz (^{1}H NMR) and 126 MHz (^{13}C NMR) and referenced to the residual solvent resonance (δ in parts per million and J in Hz). For paramagnetic molecules, the ^{1}H NMR data are reported with the chemical shift referenced to solvent peaks. Solid-state infrared spectra were recorded using a PerkinElmer Frontier FT-IR spectrophotometer equipped with a KRS5 thallium bromide/iodide universal attenuated total reflectance accessory. Elemental analyses were performed by the University of Illinois at Urbana−Champaign (UIUC) School of Chemical Sciences Microanalysis Laboratory in Urbana, IL. Samples submitted for elemental analyses were dried under vacuum for a minimum of 12 hours; solvates were confirmed by ^{1}H NMR. High-resolution mass spectra were recorded by the University of Illinois at Urbana-Champaign Mass Spectrometry Laboratory. Voltammograms were collected with a sweep rate of 0.1 V/s with 1 mM solutions in acetonitrile with 0.1 M [^{n}Bu][PF_6] as a supporting electrolyte and were referenced to ferrocene (Fc).

2-phenol-6-acetyl-pyridine (L1). A modified literature procedure was used.[39] A 250 mL round-bottom flask was charged with 2-bromo-6-acetyl-pyridine (0.500 g, 2.50 mmol), 2-hydroxyphenylboronic acid (1.4 eq, 0.483 g, 3.50 mmol), $Pd(OAc)_2$ (0.010 g, 0.0445 mmol), triphenylphosphine (PPh_3, 0.027 g, 0.103 mmol), a solution of toluene:ethanol (2:1, total volume

15 mL) and 2 M K_2CO_3 (2.5 mL), and the reaction mixture was heated at 90 ºC for 16 h. The resulting black reaction mixture was cooled to room temperature, H_2O_2 (0.25 mL, 30% in water) was added, and the mixture was stirred at room temperature in air for 30 minutes. The reaction mixture was then transferred to a separatory funnel and the organic portion collected. The aqueous portion was extracted with more toluene (4 x 10 mL) and the organic extractions combined and washed with brine (15 mL) and water (4 x 10 mL). The organic phase was finally dried with magnesium sulfate and filtered to removed solids. Volatiles were removed *in vacuo*, and the subsequent brown film was dissolved in a minimal amount of methanol. The resulting mixture was stirred for 1 hour, and the desired product was collected as a powdery yellow precipitate via filtration. Yield, ^{1}H NMR, and IR data agreed with literature values.

^{Ph}OHPy(pi^{H})$_2$ (L2). A 20 mL scintillation vial was charged with 2-phenol-6-acetyl-pyridine (L1, 0.500 g, 2.34 mmol), pyrrole (0.5 mL, 7.21 mmol), and tetrahydrofuran (3 mL). While stirring, trifluoroacetic acid (20 drops) was added dropwise to the dark yellow-brown solution. The solution was stirred at room temperature for 24 h. Subsequently, the black solution was neutralized with saturated aqueous sodium bicarbonate solution and transferred to a separatory funnel. The aqueous portion was extracted with dichloromethane (3 x 10 mL), and the combined organic fractions were washed with brine (1 x 10 mL) and water (2 x 10 mL). Volatiles were removed *in vacuo*, resulting in a dark brown residue. The residue was dissolved in diethyl ether, precipitating out a light tan powder that was separated by filtering the mixture using a frit to give a light-tan powder and a dark orange-brown filtrate that may be discarded. The powder was dried of trace solvents *in vacuo*, giving the desired product as a light tan powder (0.588 g, 1.79 mmol, 76%). ^{1}H NMR ($CDCl_3$, 22 °C): δ = 13.41 (s, Ph-OH, 1H), 8.07 (bs, pyrr-NH, 2H), 7.77 (m, py & Ph, 3H), 7.28 (m, py, 1H), 7.11 (dd, J= 2.90 & 5.80 Hz, 1H), 6.97 (dd, J = 1.15 & 8.28 Hz, Ph, 1H), 6.90 (m, Ph, 1H),

6.73 (m, pyrr-H, 2H), 6.20 (m, pyrr-H, 2H), 5.99 (m, pyrr-H, 2H), 2.17 (s, -CH_3, 3H). ^{13}C NMR ($CDCl_3$, 22 °C): δ = 163.0, 159.5, 157.1, 138.5, 135.7, 131.6, 126.6, 119.7, 119.3, 119.0, 118.7, 117.7, 117.5, 108.6, 106.7, 46.7, 27.4. IR = 3288 cm^{-1} (N−H), 3412 cm^{-1} (O-H). ESI-MS: calculated $[C_{21}H_{20}N_3O]^+$: 330.1606, found: 330.1599.

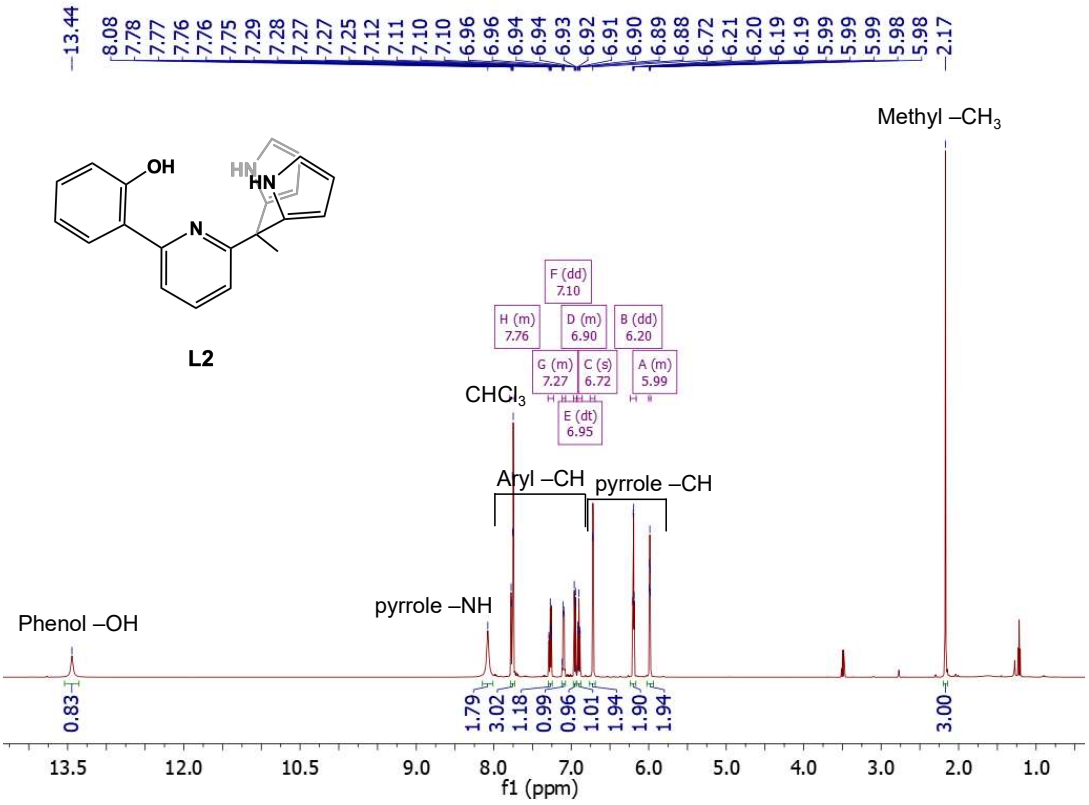

Figure 2.7 ^{1}H NMR spectrum of **L2** in d_1-$CHCl_3$.

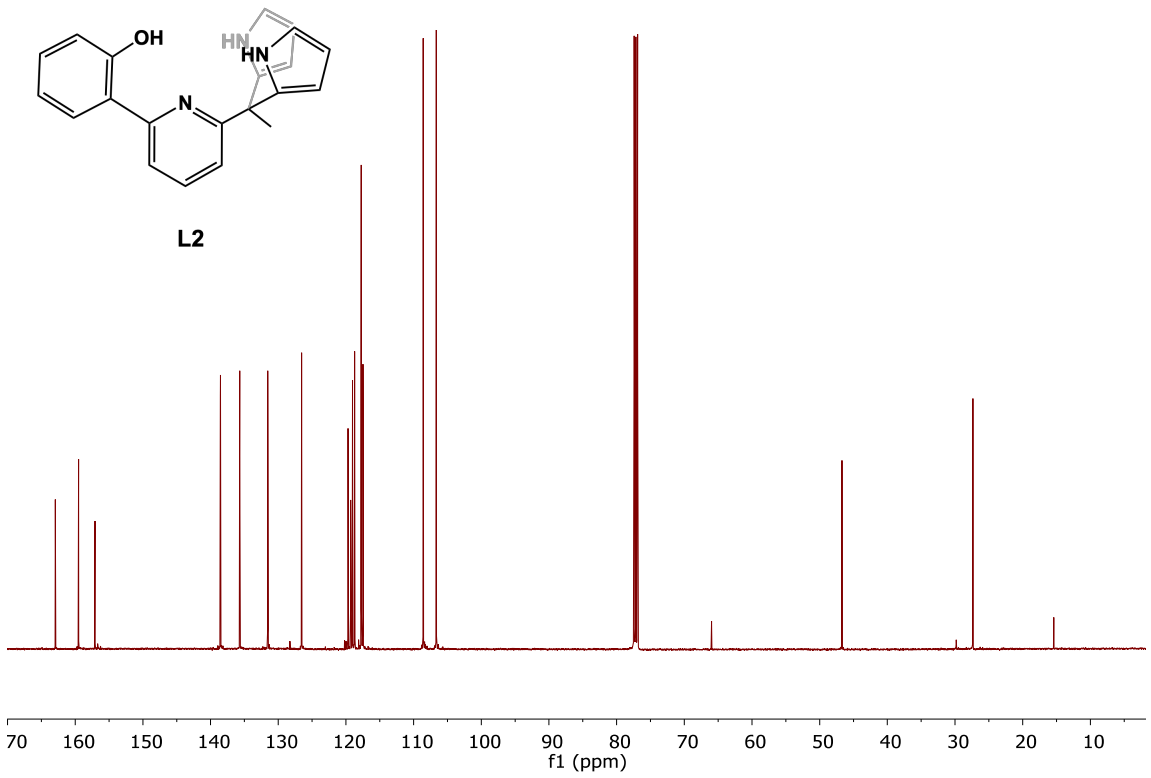

Figure 2.8 ^{13}C NMR spectrum of **L2** in d_1-$CHCl_3$.

^{Ph}OHPy(pi^{COH})$_2$ (L3). A 250 mL Schlenk flask was charged with **L2** (0.550 g, 1.67 mmol), dichloromethane (40 mL) and dimethylformamide (10 mL) and topped with an addition funnel. A solution of $POCl_3$ (2.5 eq, 0.640 g, 4.17 mmol) in dichloromethane (10 mL) was added to the addition funnel. The entire system was purged with nitrogen for 10 min. The $POCl_3$ solution was added dropwise over the course of 5 min while stirring vigorously, and the reaction solution was heated at reflux for 2 h. Sodium acetate (8 eq, 1.10 g, 13.4 mmol) in water was then added to the brown reaction solution, and the mixture was heated at 40°C for 1 h. The dark brown reaction mixture was cooled to room temperature, neutralized with saturated sodium bicarbonate, and separated. The aqueous portion was extracted with dichloromethane (3 x 15 mL), and the combined organics were washed with brine (1 x 15 mL), and water (1 x 15 mL). The organic solution was subsequently dried with magnesium sulfate and filtered. Solvents were removed *in*

vacuo, and the desired product was acquired as a yellow film (0.521 g, 1.35 mmol, 81%). ^{1}H NMR ($CDCl_3$, 25 °C): δ = 13.43 (s, OH, 1H), 10.91 (bs, pyrr-NH, 2H), 9.11 (s, COH, 2H), 7.80-7.75 (m, Ph, 3H), 7.28 (m, *p*-pyr-H, 1H), 7.15 (d(d), J= 7.3 Hz (0.8 Hz), *m*-pyr-H, 1H), 6.95 (d(d), J = 8.23 Hz (0.8 Hz), *m*-pyr-H, 1H), 6.91 (m, Ph, 1H), 6.88 (dd, J = 3.7 & 2.3 Hz, pyrr-H, 2H), 6.16 (dd, J = 3.5 & 2.6 Hz, pyrr-H, 2H), 2.23 (s, -CH_3, 3H). ^{13}C NMR ($CDCl_3$,25 °C): δ = 179.2, 160.4, 159.6, 157.2, 144.7, 138.8, 133.0, 131.8, 126.6, 122.1, 120.9, 119.1, 118.9, 118.7, 118.0, 111.0, 47.9, 27.4. IR = 1650 cm^{-1} (C=O), 3216, 3278 cm^{-1} (N-H). ESI-MS: calculated $[C_{23}H_{20}N_3O_3]^+$: 386.1505, found: 386.1502.

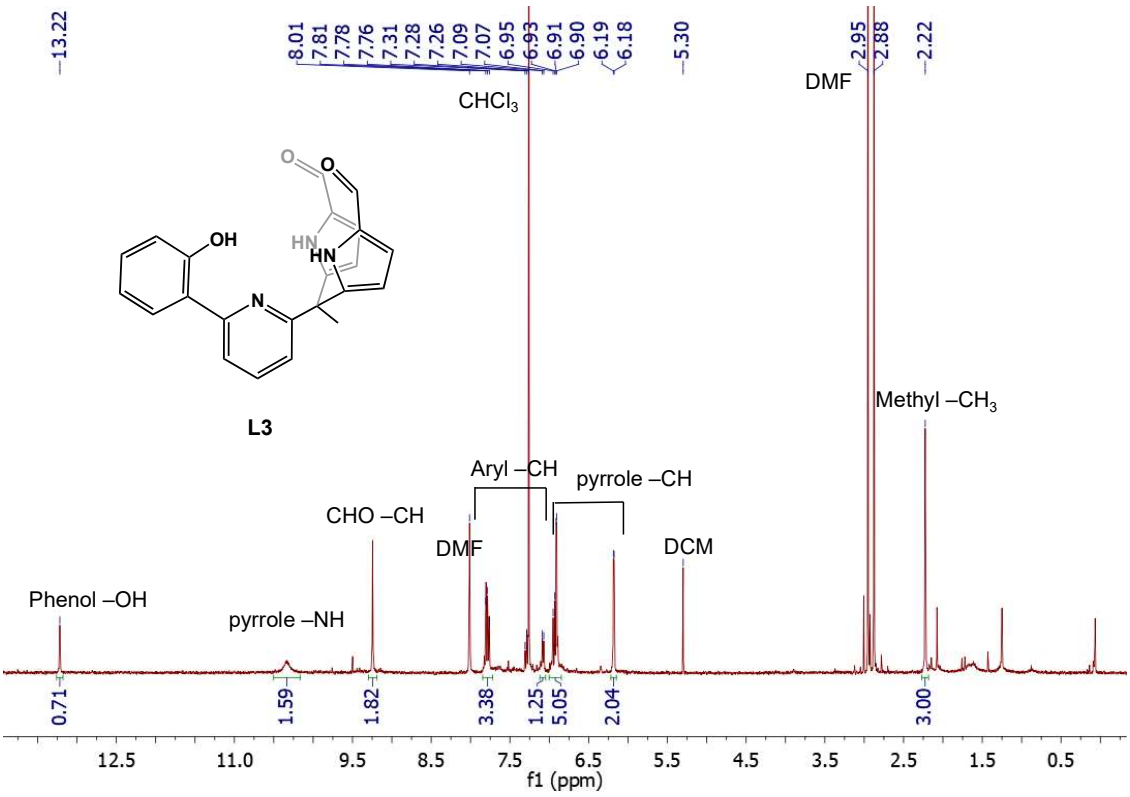

Figure 2.9 ^{1}H NMR spectrum of **L3** in d_1-$CHCl_3$.

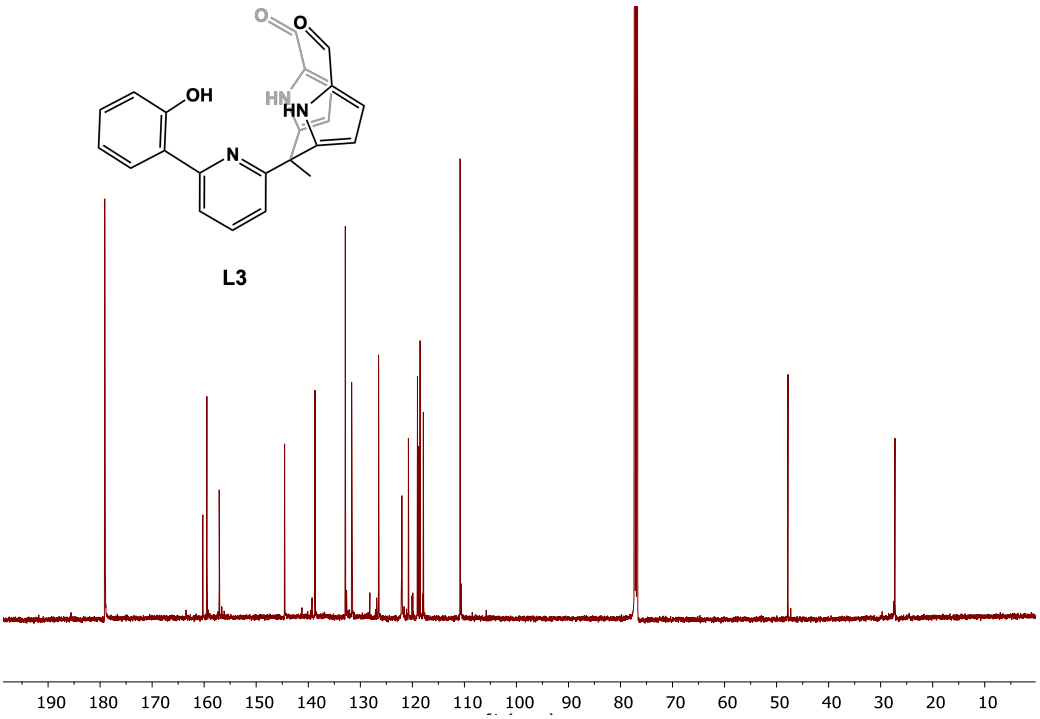

Figure 2.10 ^{13}C NMR spectrum of **L3** in d_1-$CHCl_3$.

^{Ph}OHPy(pi^{Cy})$_2$. A 20 mL scintillation vial was charged with **L3** (0.520 g, 1.35 mmol), dichloromethane (5 mL), and cyclohexylamine (0.500 mL, 4.36 mmol). The dark red-brown solution was stirred overnight, and solvents were removed *in vacuo*. The resulting dark red film was dissolved in a small amount of diethyl either and left to sit for 20 min, precipitating out an off-white powder. This precipitate was collected by filtration and dried overnight under vacuum. The desired product was produced as a white-to-tan powder (0.599 g, 1.09 mmol, 81%). Prior to use in metal chemistry ^{Ph}OHPy(pi^{Cy})$_2$ was brought into a glovebox, dissolved in dichloromethane and left to sit over 4Å molecular sieves for at least 18 h. Analysis for $C_{35}H_{41}N_5O$•$0.6C_6H_{13}N$•$0.1CH_2Cl_2$ (calc., found): C (75.49, 75.51), H (8.02, 8.00), N (12.74, 12.70). ^{1}H NMR ($CDCl_3$, 25 °C): δ = 7.98 (bs, pyrr-NH, 2H), 7.76-7.73 (m, Ph, 3H), 7.25 (m, Ph 1H), 6.94 (dd, J= 8.3 & 1.0 Hz, Ph, 1H), 6.87 (m, Ph, 1H), 6.44 (d, J = 1.7 Hz, pyrr-H, 2H), 6.17 (dd, J = 3.6 Hz, pyrr-H, 2H), 3.06 (bm, Cy-CH, 2H), 2.16 (s, -CH_3, 3H), 1.82-0.99 (m, Cy, 20H).

^{13}C NMR ($CDCl_3$, 25 °C): δ = 163, 159, 157, 150, 139, 139, 131, 127, 119.6, 119.6, 118.9, 117.7, 115, 109, 68.8, 47.3, 34.8, 27.0, 25.8, 25.0. IR = 1634 cm^{-1} (C=N), 3245 cm^{-1} (N−H), 3425 cm^{-1} (O-H).

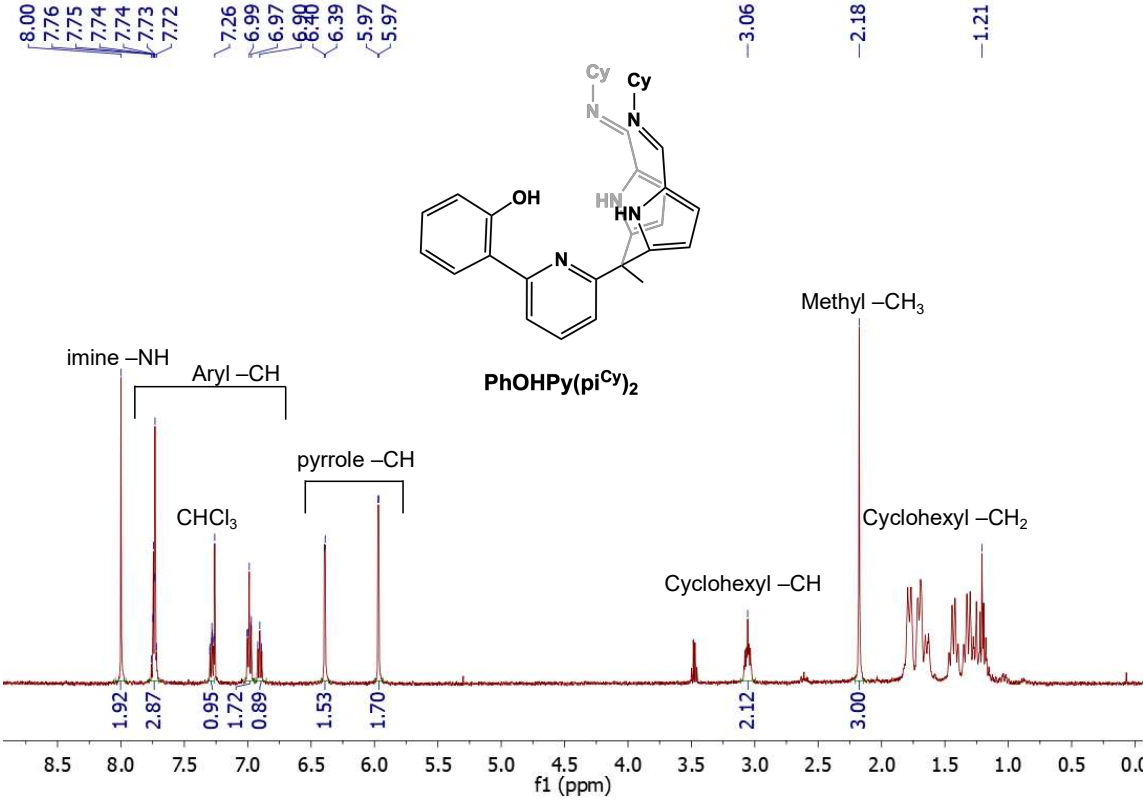

Figure 2.11 ^{1}H NMR spectrum of ^{Ph}OHPy(pi^{Cy})$_2$ in d_1-$CHCl_3$.

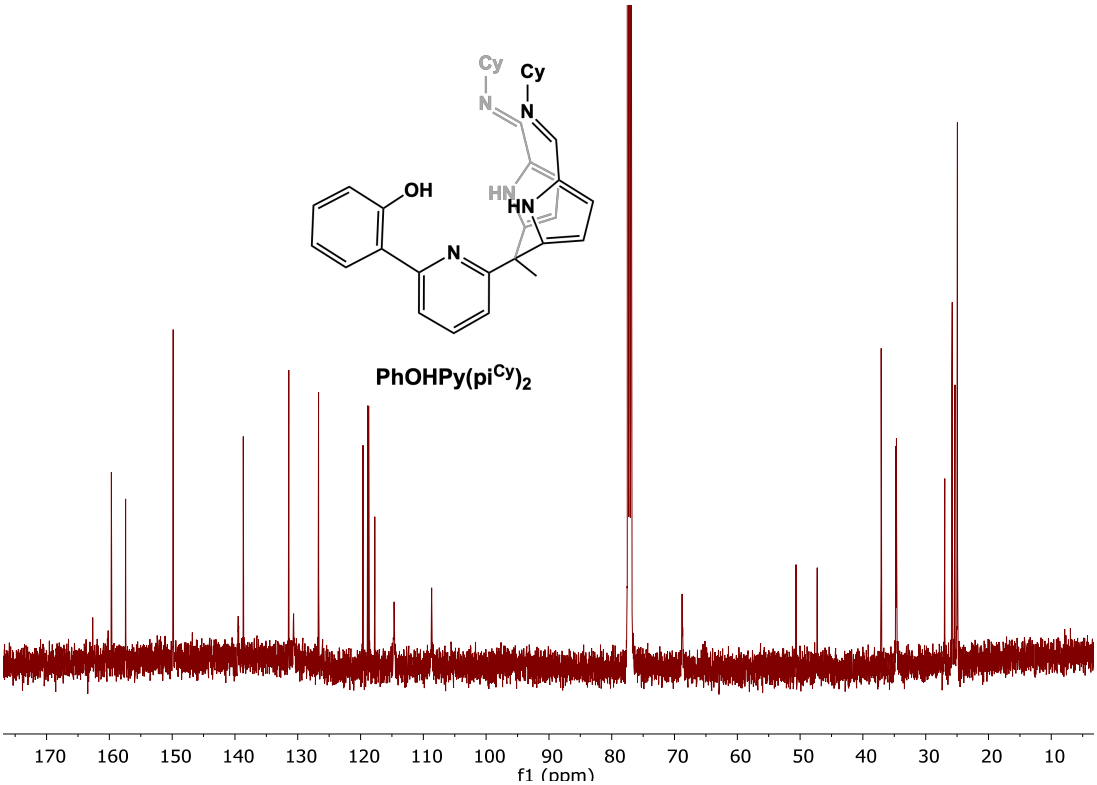

Figure 2.12 ^{13}C NMR spectrum of ^{Ph}OHPy(pi^{Cy})$_2$ in d_1-CHCl$_3$.

General metalation procedure. A 20 mL scintillation vial was charged with ^{Ph}OHPy(pi^{Cy})$_2$ (27.0 mg, 0.049 mmol) and tetrahydrofuran (8 mL). While stirring, potassium hydride (2.0 mg, 0.050 mmol) was added. The reaction mixture was stirred for 10 min and filtered to remove excess potassium hydride, resulting in a light-yellow solution. The metal dichloride salt (1 equiv., 0.049 mmol) was added, and the reaction was left to stir at room temperature for 18 h before work-up (described *vide infra*).

^{Ph}OPy(afa^{Cy})$_2$MnCl (1). After following the general procedure of complexation of MCl$_2$ salts (*vide supra*), the dark orange-yellow reaction solution had volatiles removed, and the remaining orange solids were dissolved in dichloromethane. This mixture was filtered through Celite™, and the filtrate collected. Solvents were removed *in vacuo*, and the desired product was collected as an orange film (28.4 mg, 0.0445 mmol, 91%). Dark orange crystals suitable for X-ray crystallography

were grown from a vapor diffusion of diethyl ether into a concentrated solution of the product in dichloromethane. Analysis for $C_{35}H_{40}N_5OClMn$•0.1 CH_2Cl_2 (calc., found): C (65.30, 65.18), H (6.28, 6.22), N (10.85, 10.72). This complex presented as ^{1}H NMR silent. IR: 1640 cm^{-1} (C=N), 3161 (N-H). μ_{eff} = 6.10(22) μ_B.

^{Ph}OPy(afa^{Cy})$_2$FeCl (2). After following the general procedure of complexation of MCl_2 salts (*vide supra*), the dark red reaction solution was filtered through Celite™, with volatiles removed from the filtrate. The resulting dark red-brown solid was dissolved in dichloromethane, filtered through Celite™, and solvents were removed in vacuo. The desired product was collected as a dark red solid (30.7 mg, 0.048 mmol, 98%). Red crystals suitable for X-ray crystallography were grown from a vapor diffusion of diethyl ether into a concentrated solution of the product in dichloromethane. Analysis for $C_{35}H_{40}N_5OClFe$•0.75CH_2Cl_2 (calc., found): C (61.19, 61.50), H (5.96, 6.35), N (9.98, 10.26). ^{1}H NMR (d_2-CD_2Cl_2, 500 MHz, 21°C): 45, 43, 40, 39, 38, 35, 32, 29, 24, 8.8, 2.0, 1.5-0.9, 0.2, -1.2, -1.6, -3.5, -4.7, -6.3, -6.5, -8.6, -14, -15, -16, -18, -21, -22, -23, -25 ppm. IR: 1639 cm-1 (C=N), 3242 (broad, N-H). μ_{eff} = 5.26(12) μ_B.

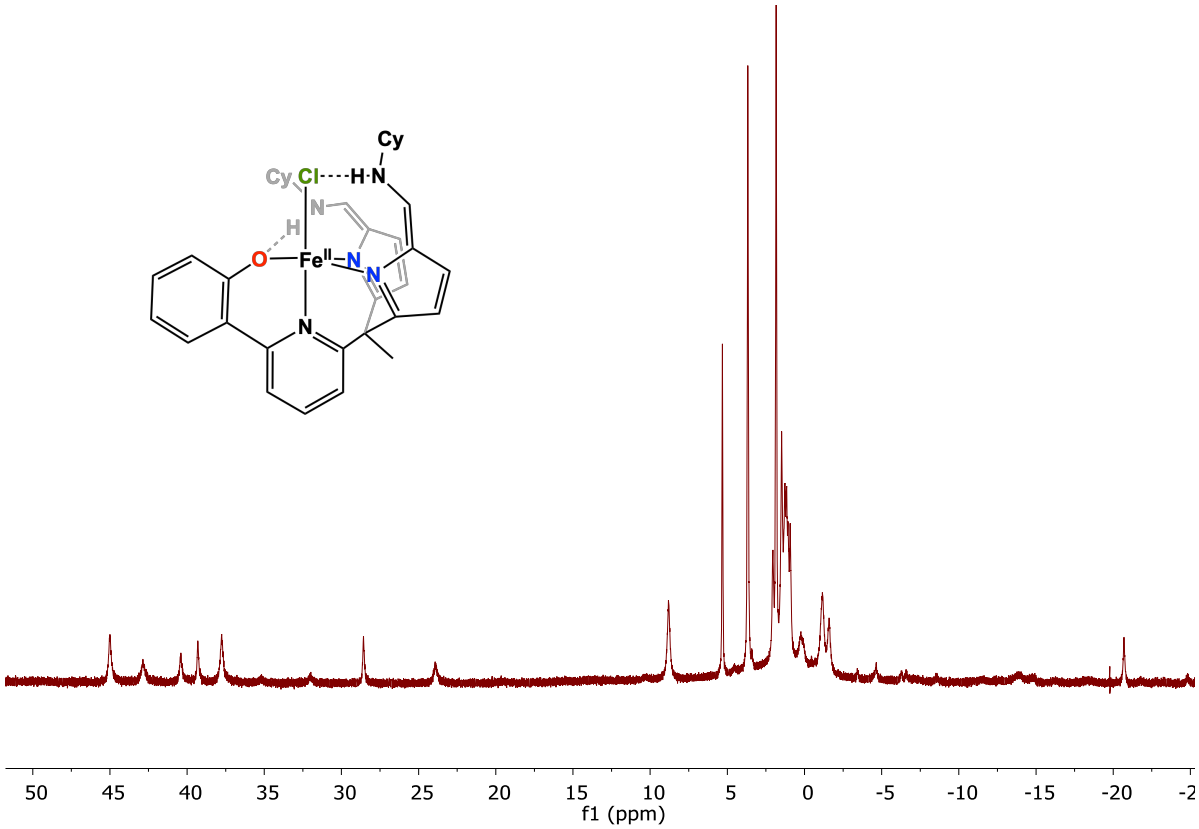

Figure 2.13 ^{1}H NMR spectrum for **2** in d_2-CH_2Cl_2.

^{Ph}OPy(afa^{Cy})$_2$CoCl (3). After following the general procedure of complexation of MCl_2 salts (*vide supra*), the dark green solution was filtered through Celite™, and the filtrate had volatiles removed. The resulting dark green film was dissolved in a minimal amount of dichloromethane, filtered through Celite, and solvents removed *in vacuo*. The desired product was collected as a dark green solid (29.7 mg, 0.0434 mmol, 89%). Dark green-brown crystals suitable for X-ray crystallography were grown from a vapor diffusion of diethyl ether into a concentrated solution of the product in dichloromethane. Analysis for $C_{35}H_{40}N_5OClCo$•$0.25CH_2Cl_2$ (calc., found): C (63.92, 63.70), H (6.16, 6.12), N (10.57, 10.61). ^{1}H NMR (d_2-CD_2Cl_2, 500 MHz, 21°C): 59.7, 53.5, 43.9, 43.4, 38.0, 29.5, 13.3, 10.8, 9.4, 6.3, 5.4, 4.3, 3.9, 3.8, 3.3, 2.1, 1.4, 1.2, 0.6, 0.4, -2.4, -14.8, -19.4 ppm IR: 1641 cm-^{1} (C=N), 3183 (N-H). μ_{eff} = 4.62(16) μ_B.

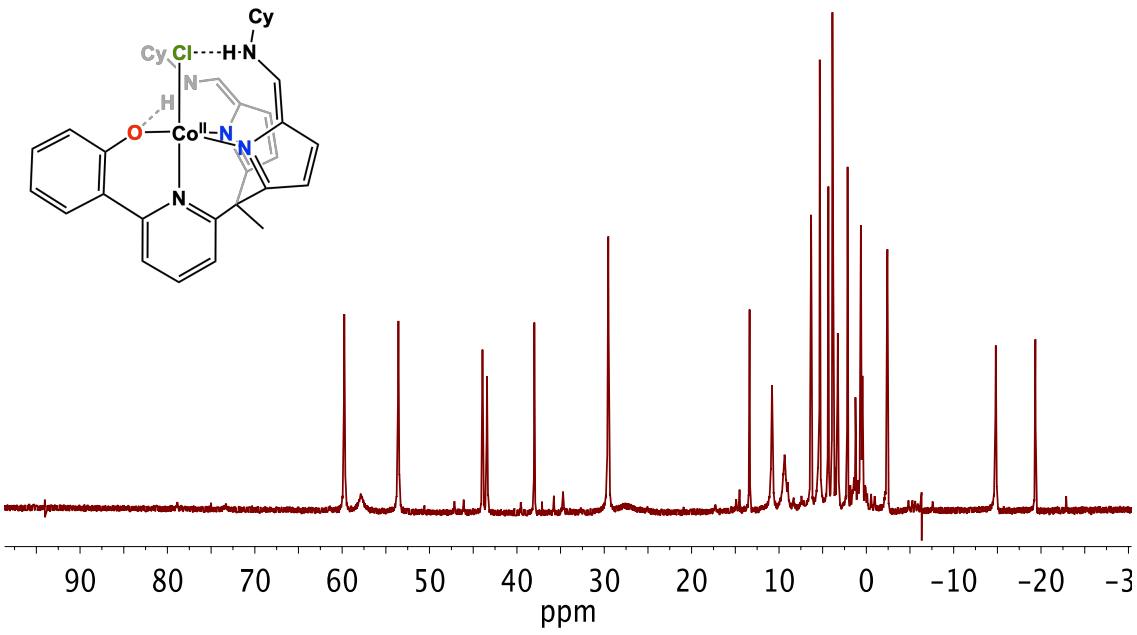

Figure 2.14 ^{1}H NMR spectrum for **3** in d_2-CH_2Cl_2.

[^{Ph}OPy(afa^{Cy})$_2$FeCl]OTf (4). Complex **2** (6.5 mg, 0.01 mmol) was added to a 20 ml scintillation vial wrapped in electrical tape in addition to 4 mL dichloromethane. AgOTf (1.05 equiv., 2.7 mg, 0.0105 mmol) was added, and the reaction was allowed to stir in the dark at room temperature for 1 hour. The dark green reaction mixture was filtered through Celite to remove Ag^0, and the filtrate had its solvents removed *in vacuo* to give the desired product as a dark brown-red powder (6.8 mg, 0.0086, 86%). Crystals suitable for x-ray crystallography were grown from a vapor diffusion of diethyl ether into a concentrated solution in 1:1 DCM:MeCN.

^{Ph}OHPy(afa^{Cy})$_2$ZnCl$_2$ (5). After following the general procedure of complexation of MCl_2 salts (*vide supra*), the orange solution was filtered through Celite™, and the filtrate had volatiles removed. The resulting orange film was dissolved in a minimal amount of dichloromethane, filtered through Celite, and solvents removed *in vacuo*. The desired product was collected as a light orange powder (31.2 mg, 0.045 mmol, 93%). Colorless crystals suitable for X-ray

crystallography were grown from a vapor diffusion of diethyl ether into a concentrated solution of the product in dichloromethane. ^{1}H NMR (d_2-CD_2Cl_2, 500 MHz, 21°C): δ = 13.58, 9.44, 7.78, 7.74, 7.69, 7.52, 7.25, 7.12, 6.87, 6.31, 3.44, 2.17, 2.11-0.99. IR = 1646 cm^{-1} (C=N), 3186 (N-H).

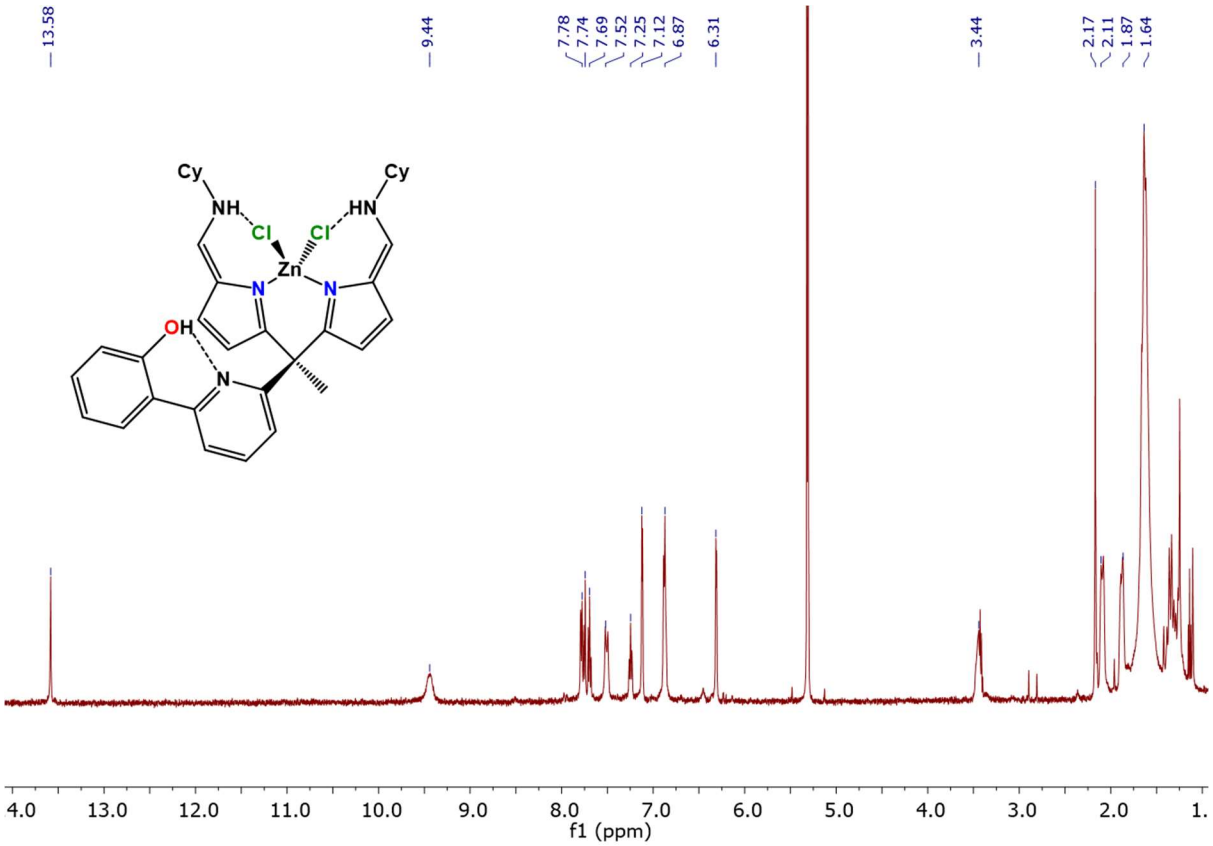

Figure 2.15 ^{1}H NMR spectrum of complex **5** in CD_2Cl_2 (22°C).

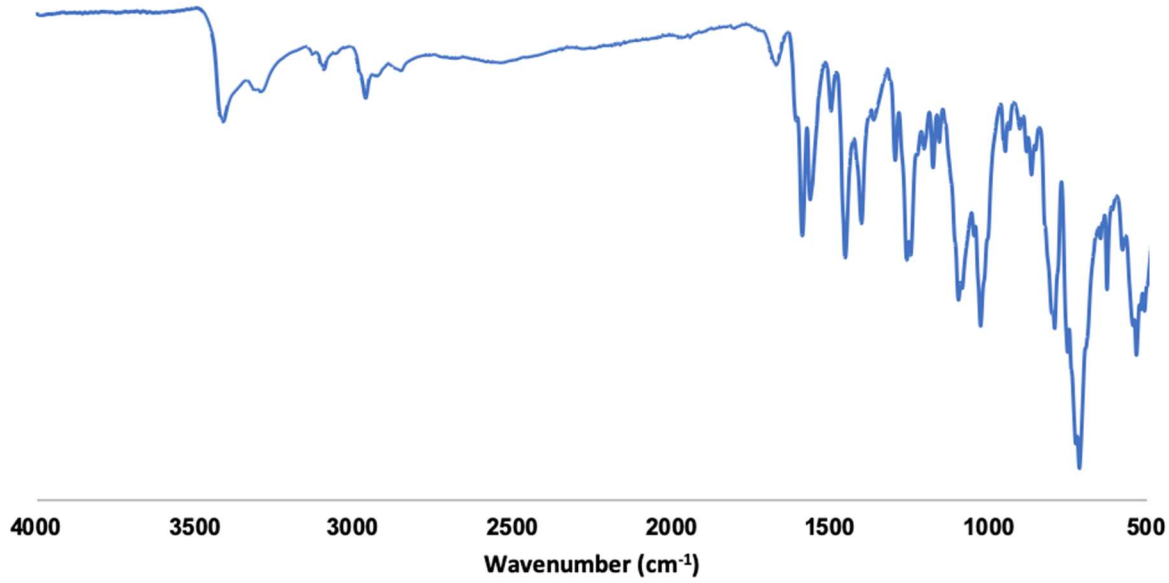

Figure 2.16 FT-IR spectrum for **L2**.

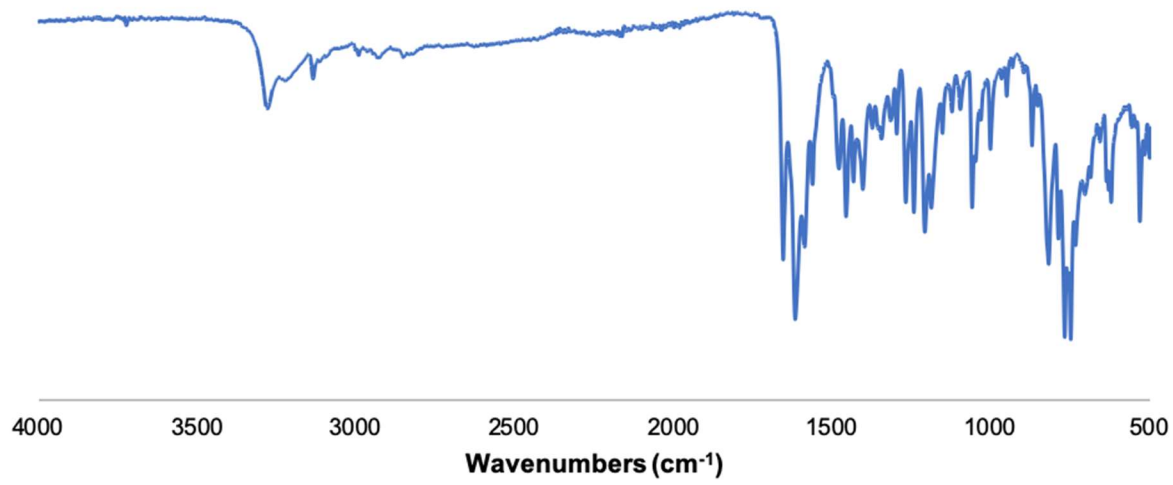

Figure 2.17 FT-IR spectrum for **L3**.

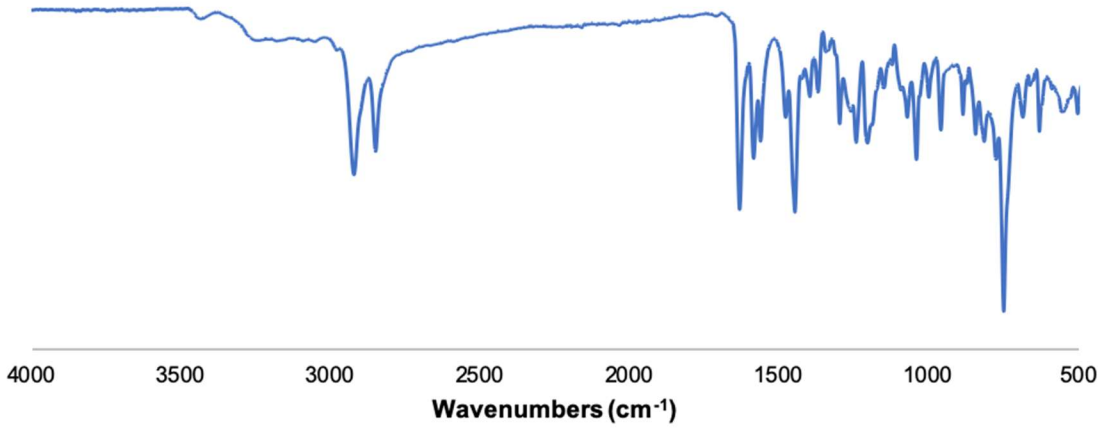

Figure 2.18 FT-IR spectrum for ^{Ph}OHPy(pi^{Cy})$_2$.

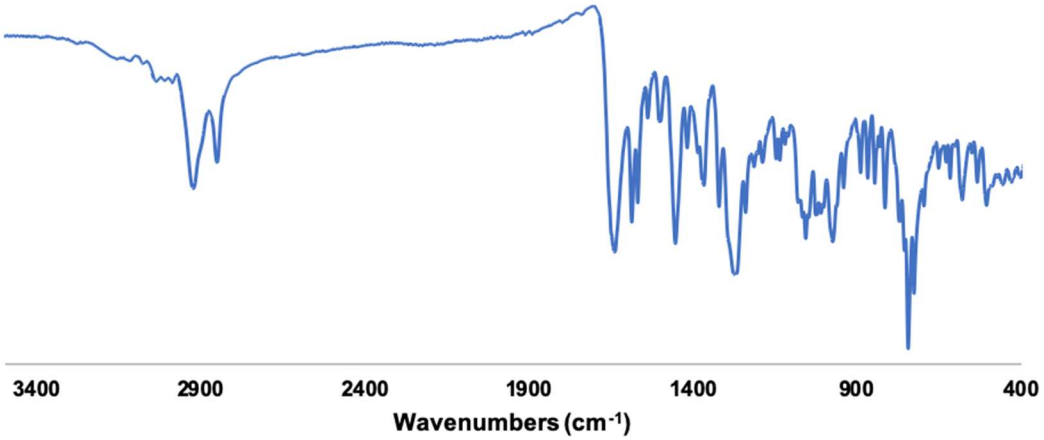

Figure 2.19 FT-IR spectrum for complex **1**.

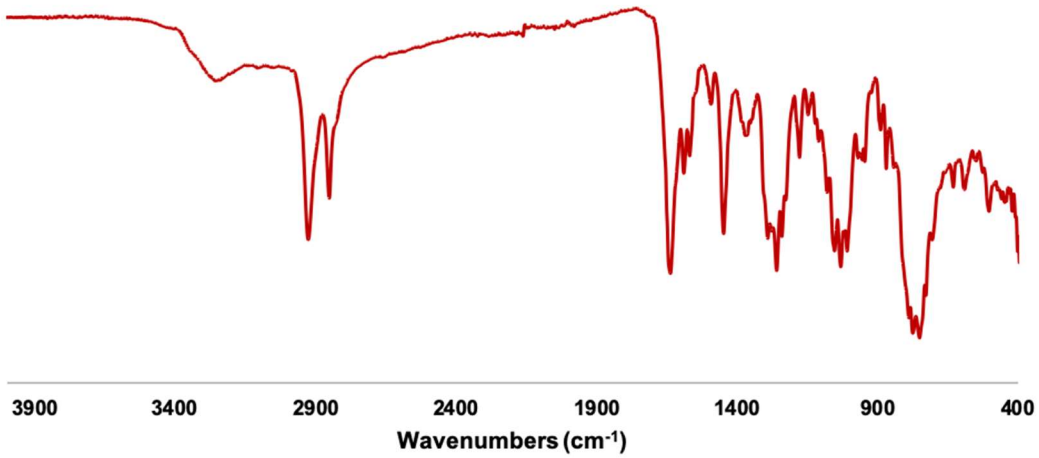

Figure 2.20 FT-IR spectrum for complex **2**.

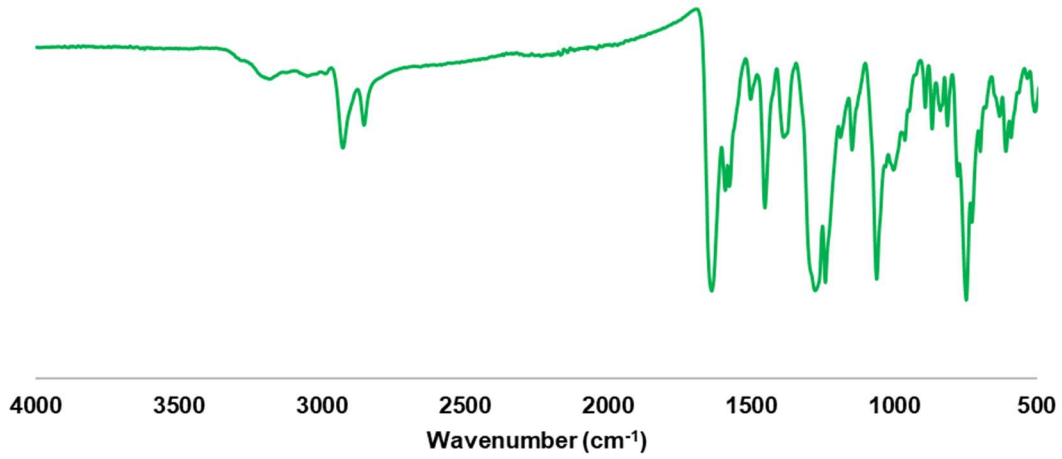

Figure 2.21 FT-IR spectrum for complex **3**.

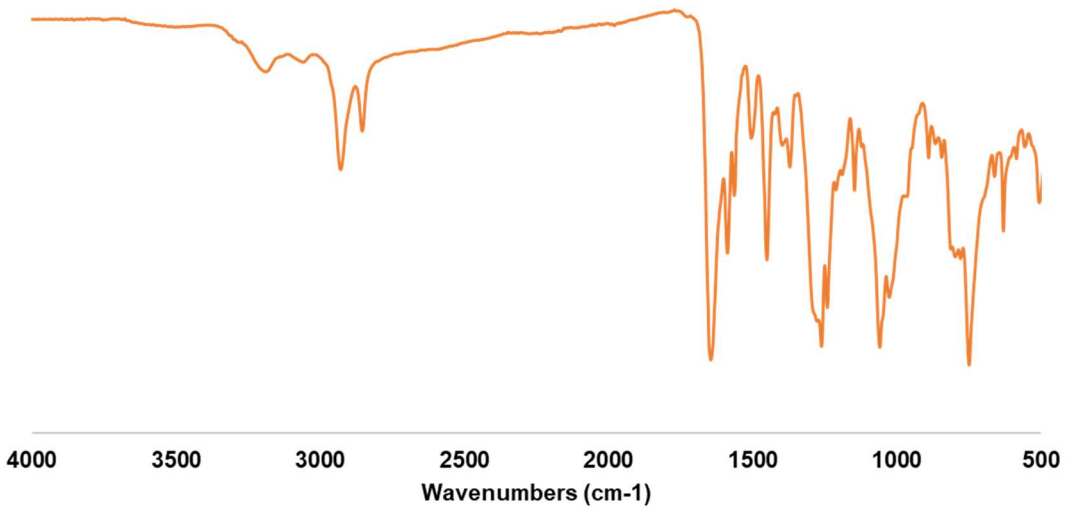

Figure 2.22 FT-IR spectrum for complex **5.**

$$\tau_5 = \frac{\beta - \alpha}{60°} = \frac{171.03° - 154.62°}{60°} = \frac{16.41°}{60°} = 0.27$$

Equation 2.2 Calculation of τ_5 for **1.**

$$\tau_5 = \frac{\beta - \alpha}{60°} = \frac{178.32° - 154.10°}{60°} = \frac{24.22°}{60°} = 0.40$$

Equation 2.3 Calculation of τ_5 for **2.**

$$\tau_5 = \frac{\beta - \alpha}{60°} = \frac{176.54° - 148.33°}{60°} = \frac{28.21°}{60°} = 0.47$$

Equation 2.4 Calculation of τ_5 for **3a.**

$$\tau_5 = \frac{\beta - \alpha}{60°} = \frac{175.44° - 132.73°}{60°} = \frac{42.71°}{60°} = 0.71$$

Equation 2.5 Calculation of τ_5 for **3b.**

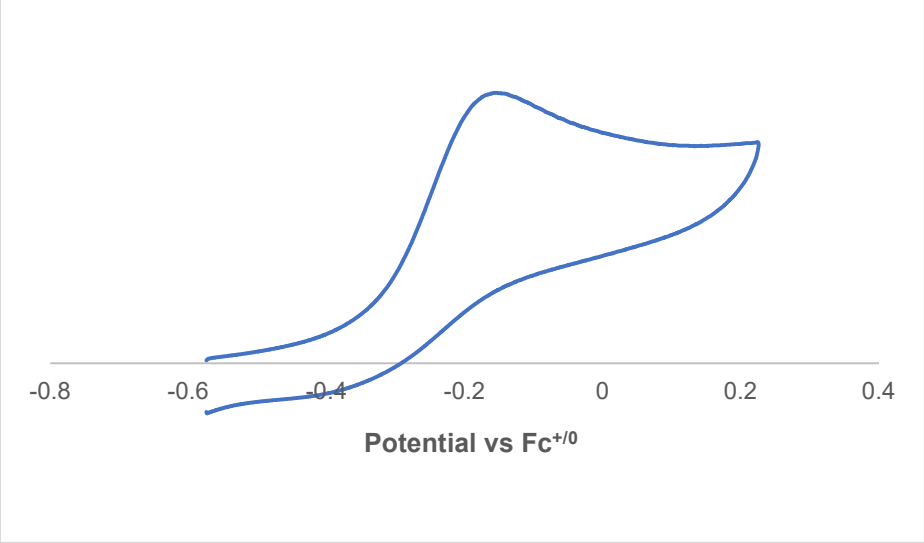

Figure 2.23 Cyclic voltammogram of irreversible Mn(II/III) oxidation observed in complex **1**.

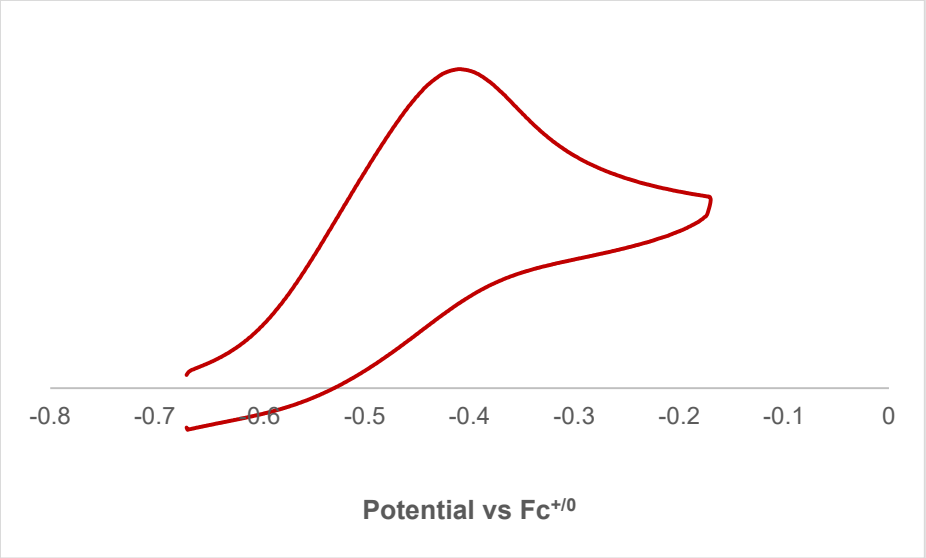

Figure 2.24 Cyclic voltammograms of irreversible Fe(II/III) oxidation observed in complex **2**.

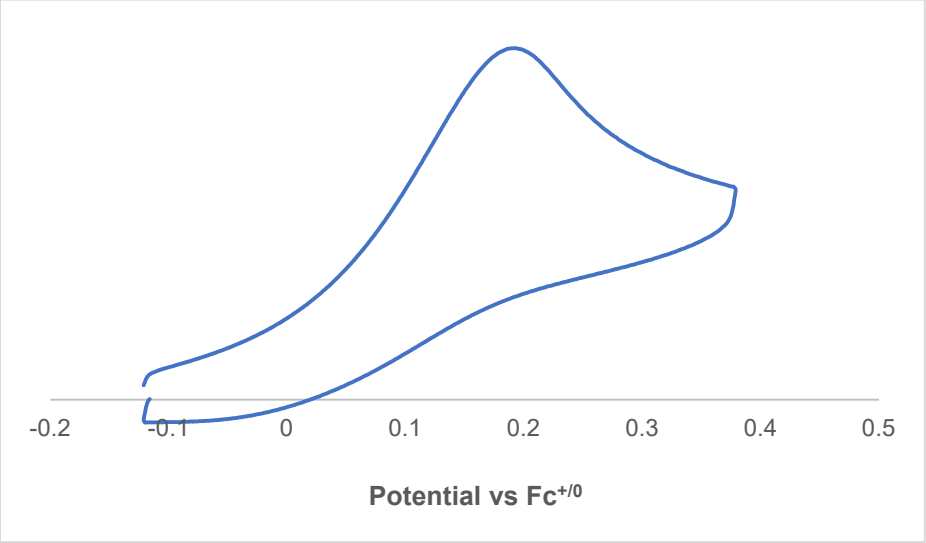

Figure 2.25 Cyclic voltammograms of irreversible Co(II/III) oxidation observed in complex **3**.

Table 2.3 Crystallographic parameters for complexes **1-3** (CCDC 2101168-2101170).

	^{Ph}OPy(afa^{Cy})$_2$MnCl (1) dd68n	**^{Ph}OPy(afa^{Cy})$_2$FeCl (2) dm30h**	**^{Ph}OPy(afa^{Cy})$_2$CoCl (3a,b) dd29n**
Empirical Formula	$C_{35}H_{40}ClMnN_5O$	C35H40ClFeN5O	$C_{71}H_{82}Cl_4Co_2N_{10}O_2$
Formula Weight	637.11 g/mol	638.02 g/mol	1367.12
Temperature	100.01 K	100.15 K	100.02
Wavelength	MoKα (λ = 0.71073)	MoKα (λ = 0.71073)	MoKα (λ = 0.71073)
Crystal System	Triclinic	Triclinic	Triclinic
Space Group	P-1	P-1	P-1
a (Å)	8.2117(2)	8.2743(3)	12.8543(4)
b (Å)	13.3475(4)	14.0697(5)	13.1875(4)
c (Å)	14.2019(4)	16.2126(6)	21.8904(7)
α (°)	98.8761(9)	107.625(2)	93.4590(10)
β (°)	95.6991(9)	99.068(2)	91.0240(10)
γ (°)	92.0161(9)	106.032(2)	106.6890(10)
Volume (Å^3)	1528.34(7)	1667.83(11)	3545.59(19)
Z	2	2	2
Reflections Collected	45633	24340	175399
Independent Reflections	5609	8309	13068
Goodness-of-fit on F2	1.098	1.053	1.064
Final R indices [I>2σ(I)]	R_1 = 0.0291, wR_2 = 0.0723	R_1 = 0.0417, wR_2 = 0.1140	R_1 = 0.0386, wR_2 = 0.0856
Final R indices [all data]	R_1 = 0.0337, wR_2 = 0.0751	R1 = 0.0532, wR2 = 0.1225	R_1 = 0.0450, wR_2 = 0.0892

Table 2.4 Crystallographic parameters for complexes **4-5.**

	[^{Ph}OPy(afa^{Cy})$_2$FeCl]OTf (4) dd52k	**^{PhOHPy}(afa^{Cy})$_2$ZnCl$_2$ (5) dd22o**
Empirical formula	$C_{41}H_{45}ClF_3FeN_6O_4S$	$C_{35}H_{41}Cl_2N_5OZn$
Formula weight	866.19	684.03
Temperature/K	99.99	99.99
Crystal system	Monoclinic	Monoclinic
Space group	$P2_1/c$	$P2_1/c$
a/Å	14.7191(6)	15.3092(3)
b/Å	16.1676(6)	17.2491(4)
c/Å	18.7281(8)	12.4701(3)
α/°	90	90
β/°	95.9390(10)	100.0900(10)
γ/°	90	90
Volume/Å^3	4432.9(3)	3242.05(13)
Z	4	4
Reflections collected	160690	82790
Independent reflections	11025 [R_{int} = 0.0482, R_{sigma} = 0.0184]	5961 [R_{int} = 0.0368, R_{sigma} = 0.0135]
Goodness-of-fit on F^2	1.045	1.091
Final R indexes [I>=2σ (I)]	R_1 = 0.0426, wR_2 = 0.1019	R_1 = 0.0271, wR_2 = 0.0641
Final R indexes [all data]	R_1 = 0.0528, wR_2 = 0.1089	R_1 = 0.0310, wR_2 = 0.0661

2.7 References

(1) Bertini, I.; Gray, H. B.; Stiefel, E. I.; Valentine, J. *Biological Inorganic Chemistry: Structure and Reactivity*; University Science Books: Sausalito, 2007.

(2) Goodin, D. B.; McRee, D. E. The Asp-His-Fe Triad of Cytochrome c Peroxidase Controls the Reduction Potential, Electronic Structure, and Coupling of the Tryptophan Free Radical to the Hemet. *Biochemistry* **1993**, *32* (13), 3313–3324.

(3) Krest, C. M.; Silakov, A.; Rittle, J.; Yosca, T. H.; Onderko, E. L.; Calixto, J. C.; Green,

M. T. Significantly Shorter Fe-S Bond in Cytochrome P450-I Is Consistent with Greater Reactivity Relative to Chloroperoxidase. *Nat. Chem.* **2015**, *7* (9), 696–702.

(4) Mitchell, A. J.; Dunham, N. P.; Martinie, R. J.; Bergman, J. A.; Pollock, C. J.; Hu, K.; Allen, B. D.; Chang, W.; Silakov, A.; Bollinger, J. M.; Krebs, C.; Boal, A. K. Visualizing the Reaction Cycle in an Iron(II) and 2-(Oxo)-Glutarate- Dependent Hydroxylase. *J. Am. Chem. Soc.* **2017**, *139*, 13830–13836.

(5) Cook, S. A.; Hill, E. A.; Borovik, A. S. Lessons from Nature: A Bio-Inspired Approach to Molecular Design. *Biochemistry* **2015**, *54* (27), 4167–4180.

(6) Hammes, B. S.; Young, V. G.; Borovik, A. S. Hydrogen-Bonding Cavities about Metal Ions : A Redox Pair of Coordinatively Unsaturated Paramagnetic Co-OH Complexes. *Angew. Chemie - Int. Ed.* **1999**, *12* (5), 666–669.

(7) MacBeth, C. E.; Gupta, R.; Mitchell-Koch, K. R.; Young, V. G.; Lushington, G. H.; Thompson, W. H.; Hendrich, M. P.; Borovik, A. S. Utilization of Hydrogen Bonds to Stabilize M-O(H) Units: Synthesis and Properties of Monomeric Iron and Manganese Complexes with Terminal Oxo and Hydroxo Ligands. *J. Am. Chem. Soc.* **2004**, *126* (8), 2556–2567.

(8) Lacy, D. C.; Gupta, R.; Stone, K. L.; Greaves, J.; Ziller, J. W.; Hendrich, M. P.; Borovik, A. S. Formation, Structure, and EPR Detection of a High Spin Fe^{IV}-Oxo Species Derived from Either an Fe^{III}-Oxo or Fe^{III}-OH Complex Preparative Routes to the Fe^{IV}-Oxo Complex. *J. Am. Chem. Soc.* **2010**, *132*, 12188–12190.

(9) Parsell, T. H.; Behan, R. K.; Green, M. T.; Hendrich, M. P.; Borovik, A. S. Preparation and Properties of a Monomeric MnIV-Oxo Complex. *J. Am. Chem. Soc.* **2006**, *128* (27), 8728–8729.

(10) Cook, S. A.; Ziller, J. W.; Borovik, A. S. Iron(II) Complexes Supported by Sulfonamido Tripodal Ligands: Endogenous versus Exogenous Substrate Oxidation. *Inorg. Chem.* **2014**, *53* (20), 11029–11035.

(11) Usharani, D.; Lacy, D. C.; Borovik, A. S.; Shaik, S. Dichotomous Hydrogen Atom Transfer vs Proton-Coupled Electron Transfer During Activation of X−H Bonds (X = C, N, O) by Nonheme Iron−Oxo Complexes of Variable Basicity. *J. Am. Chem. Soc.* **2013**, *135*, 17090–17104.

(12) Cook, S. A.; Borovik, A. S. Molecular Designs for Controlling the Local Environments around Metal Ions. *Acc. Chem. Res.* **2015**, *48* (8), 2407–2414.

(13) Moore, C. M.; Szymczak, N. K. Redox-Induced Fluoride Ligand Dissociation Stabilized by Intramolecular Hydrogen Bonding. *Chem. Commun.* **2015**, *51* (25), 5490-5492.

(14) Dahl, E. W.; Dong, H. T.; Szymczak, N. K. Phenylamino Derivatives of Tris(2-Pyridylmethyl)Amine: Hydrogen-Bonded Peroxodicopper Complexes. *Chem. Commun.* **2018**, *54* (8), 892–895.

(15) Wallen, C. M.; Bacsa, J.; Scarborough, C. C. Hydrogen Peroxide Complex of Zinc. *J. Am. Chem. Soc.* **2015**, *137*, 14606–14609.

(16) Matson, E. M.; Bertke, J. A.; Fout, A. R. Isolation of Iron(II) Aqua and Hydroxyl Complexes Featuring a Tripodal H-Bond Donor and Acceptor Ligand. *Inorg. Chem.* **2014**, *53* (9), 4450–4458.

(17) Matson, E. M.; Park, Y. J.; Bertke, J. A.; Fout, A. R. Synthesis and Characterization of M(II) (M = Mn, Fe and Co) Azafulvene Complexes and Their X_3^- Derivatives. *Dalt. Trans.* **2015**, *44* (22), 10377–10384.

(18) Park, Y. J.; Matson, E. M.; Nilges, M. J.; Fout, A. R. Exploring Mn–O Bonding in the Context of an Electronically Flexible Secondary Coordination Sphere: Synthesis of a Mn(III)–Oxo. *Chem. Commun.* **2015**, *51* (25), 5310–5313.

(19) Gordon, Z.; Drummond, M. J.; Matson, E. M.; Bogart, J. A.; Schelter, E. J.; Lord, R. L.; Fout, A. R. Tuning the Fe(II/III) Redox Potential in Nonheme Fe(II)-Hydroxo Complexes through Primary and Secondary Coordination Sphere Modifications. *Inorg. Chem.* **2017**, *56* (9), 4852–4863.

(20) Soo, H. Sen; Komor, A. C.; Lavarone, A. T.; Chang, C. J. A Hydrogen-Bond Facilitated Cycle for Oxygen Reduction by an Acid- and Base-Compatible Iron Platform. *Inorg. Chem.* **2009**, *48* (21), 10024–10035.

(21) Kendall, A. J.; Zakharov, L. N.; Gilbertson, J. D. Synthesis and Stabilization of a Monomeric Iron(II) Hydroxo Complex via Intra Molecular Hydrogen Bonding in the Secondary Coordination Sphere. *Inorg. Chem.* **2010**, *49* (19), 8656–8658.

(22) Drummond, M. J.; Ford, C. L.; Gray, D. L.; Popescu, C. V; Fout, A. R. Radical Rebound Hydroxylation Versus H-Atom Transfer in Non-Heme Iron(III)-Hydroxo Complexes: Reactivity and Structural Differentiation. *J. Am. Chem. Soc.* **2019**, *141* (16), 6639–6650.

(23) Yadav, V.; Gordon, J. B.; Siegler, M. A.; Goldberg, D. P. Dioxygen-Derived Nonheme Mononuclear Fe^{III} (OH) Complex and Its Reactivity with Carbon Radicals. *J. Am. Chem. Soc.* **2019**, *141* (26), 10148–10153.

(24) MacBeth, C. E.; Golombek, A. P.; Young, V. G.; Yang, C.; Kuczera, K.; Hendrich, M. P.; Borovik, A. S. O-2 Activation by Nonheme Iron Complexes: A Monomeric Fe(III)- Oxo Complex Derived from O-2. *Science (80-.).* **2000**, *289* (5481), 938–941.

(25) Gordon, Z.; Miller, Tabitha, J.; Leahy, C. A.; Matson, E. M.; Burgess, M.; Drummond, M. J.; Popescu, C. V; Smith, C. M.; Lord, R. L.; Rodriguez-Lopez; Fout, A. R. Characterization of Terminal Iron(III)-Oxo and Iron(III)-Hydroxo Complexes Derived from O_2 Activation. *Inorg. Chem.* **2019**, *58* (23), 15801–15811.

(26) Moore, C. M.; Szymczak, N. K. Nitrite Reduction by Copper through Ligand Mediated Proton and Electron Transfer. *Chem. Sci.* **2015**, *6*, 3373–3377.

(27) Matson, E. M.; Park, Y. J.; Fout, A. R. Facile Nitrite Reduction in a Non-Heme Iron System: Formation of an Iron(III)-Oxo. *J. Am. Chem. Soc.* **2014**, *136* (50), 17398–17401.

(28) Ford, C. L.; Park, Y. J.; Matson, E. M.; Gordon, Z.; Fout, A. R. A Bioinspired Iron Catalyst for Nitrate and Perchlorate Reduction. *Science (80-.).* **2016**, *354*, 741–743.

(29) Kwon, Y. M.; Delgado, M.; Zakharov, L. N.; Seda, T.; Gilbertson, J. D. Nitrite Reduction

by a Pyridinediimine Complex with a Proton-Responsive Secondary Coordination Sphere. *Chem. Commun.* **2016**, *214* (1), 11016–11019.

(30) Drummond, M. J.; Miller, T. J.; Ford, C. L.; Fout, A. R. Catalytic Perchlorate Reduction Using Iron: Mechanistic Insights and Improved Catalyst Turnover. *ACS Catal.* **2020**, *10* (5), 3175–3182.

(31) Ueyama, N.; Nishikawa, N.; Yamada, Y.; Okamura, T.; Nakamura, A. Cytochrome P-450 Model (Porphinato)(Thiolato)Iron(III) Complexes with Single and Double NH···S Hydrogen Bonds at the Thiolate Site. *J. Am. Chem. Soc.* **1996**, *118* (50), 12826–12827.

(32) Dey, A.; Okamura, T. A.; Ueyama, N.; Hedman, B.; Hodgson, K. O.; Solomon, E. I. Sulfur K-Edge XAS and DFT Calculations on P450 Model Complexes: Effects of Hydrogen Bonding on Electronic Structure and Redox Potentials. *J. Am. Chem. Soc.* **2005**, *127* (34), 12046–12053.

(33) Leahy, C. A.; Drummond, M. J.; Vura-Weis, J.; Fout, A. R. Synthesis of a Series of M(Ii) (M = Mn, Fe, Co) Chloride Complexes with Both Inter- And Intra-Ligand Hydrogen Bonding Interactions. *Dalt. Trans.* **2021**, *50* (35), 12088–12092.

(34) Zong, R.; Wang, D.; Hammitt, R.; Thummel, R. P. Synthetic Approaches to Polypyridyl Bridging Ligands with Proximal Multidentate Binding Sites. *J. Org. Chem.* **2006**, *71* (1), 167–175.

(35) Addison, A. W.; Rao, T. N. Synthesis, Structure, and Spectroscopic Properties of Copper(II) Compounds Containing Nitrogen-Sulphur Donor Ligands; the Crystal and Molecular Structure of Aqua[1,7-Bis(N-Methylbenzimidazol-2'-Yl)-2,6-Dithiaheptane]Copper(II) Perchlorate. *J. Chem. Soc. Dalt. Trans.* **1984**, 1349–1356.

(36) Mitchell, A. J.; Dunham, N. P.; Bergman, J. A.; Wang, B.; Zhu, Q.; Chang, W.; Liu, X.; Boal, A. K. Structure-Guided Reprogramming of a Hydroxylase To Halogenate Its Small Molecule Substrate. *Biochemistry* **2017**, *56*, 441–444.

(37) Yadav, V.; Rodriguez, R. J.; Siegler, M. A.; Goldberg, D. P. Determining the Inherent Selectivity for Carbon Radical Hydroxylation versus Halogenation with FeIII(OH)(X) Complexes: Relevance to the Rebound Step in Non-heme Iron Halogenases. *J. Am. Chem. Soc.* **2020**, *142* (16), 7259–7264.

(38) Matson, E. M.; Gordon, Z.; Lin, B.; Nilges, M. J.; Fout, A. R. Meridional vs. Facial Coordination Geometries of a Dipodal Ligand Framework Featuring a Secondary Coordination Sphere. *Dalt. Trans.* **2014**, *43* (45), 16992–16995.

(39) Wright, L. A.; Hope, E. G.; Solan, G. A.; Cross, W. B.; Singh, K. *O* , *N* , *N* -Pincer Ligand Effects on Oxidatively Induced Carbon–Chlorine Coupling Reactions at Palladium. *Dalt. Trans.* **2015**, *44* (13), 6040–6051.

Chapter 3: Activation of O_2 by a cobalt(II) bistriflate complex and electronic characterization of the cobalt and iron tetrapodal systems

3.1 Dioxygen activation by cobalt in biological and synthetic model systems

Dioxygen (O_2) activation by metalloenzymes is crucial in biological processes as O_2 serves as an oxygen-atom and oxidant in these transformations.[1–7] Synthetic efforts towards achieving similar transformations have mainly focused on using iron or copper in ligand scaffolds inspired by enzymatic motifs,[2,5,14–21,6–13] as these are commonly found as the metal center in cofactors of dioxygenase metalloenzymes. However, non-heme metalloenzymes with other first row metals, have been found to activate O_2 successfully.[22–26] For example, cobalt substituted as the metal center in certain zinc dioxygenases has shown O_2 binding and activation and can perform other types of small molecule activation,[22–24,27,28] indicating that cobalt can serve as a competent metal center in biomimetic models investigating biological activity such as O_2 activation.

While less prevalent compared to synthetic iron or copper systems, cobalt in bio-inspired ligand scaffolds have become more common for performing synthetic small molecule activation using O_2. Reversible binding of O_2 by cobalt has been known for decades in several systems such as porphyrins, tetraazamacrocyclic, and salen ligands to form a variety of adducts.[23,29–33] Reinaud and Theopold reported O_2 binding by a tris(pyrrazol)cobalt(II) complex (Fig. 3.1A) and explored the stability and activity of the formed superoxide species.[34–36] In 2004, Meyer and coworkers developed a tripodal, polydentate non-heterocyclic carbene (NHC) ligand with cobalt as the metal center that reacts with O_2 to form a κ_2-peroxo bound species (Fig. 3.1B),[37] while Goldberg that same year found that a cobalt corrolazine species reversibly formed a superoxo species upon exposure to O_2 (Fig. 3.1C).[38] While not through O_2 activation, Anderson and coworkers have recently generated high-valent cobalt(III)-oxo species and cobalt(IV) species from oxidizing

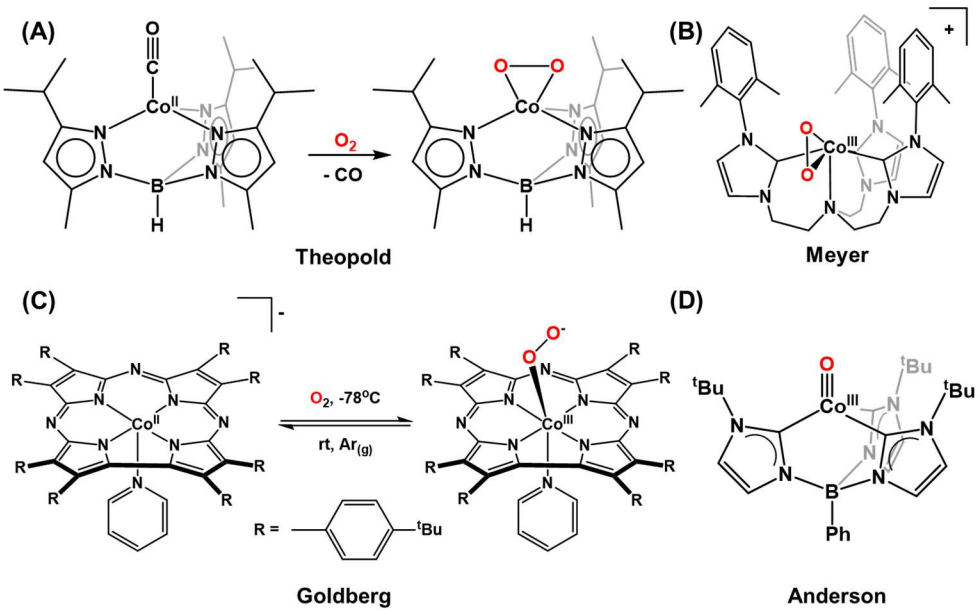

Figure 3.1 Select examples of synthetic cobalt systems that activate O_2 or access high-valent cobalt(III).

cobalt(II)-hydroxide complexes, and these are capable of cleaving moderate to strong aliphatic C-H bonds akin to enzymatic systems (Fig. 3.1D).[39–41] Others have also reported the generation of high-valent cobalt centers through other routes, such as peroxide or hydroxide addition, towards achieving catalytic transformations.[31,33,42–44]

Cobalt systems containing bio-inspired secondary sphere hydrogen-bonding capabilities have been shown to be effective at activating small molecules like dioxygen but are less explored compared to their iron analogues. Borovik and co-workers were the first to report the use of cobalt in a ligand system containing hydrogen bond donors in the secondary coordination sphere.[45] Using modified versions of the rigid, C_3-symmetric tripodal ligand $(H_3buea)^{3-}$ (shown in Fig. 3.2A), they examined the impact of secondary sphere hydrogen-bonding on the activation of dioxygen with cobalt.[45] The authors found that with three or two hydrogen-bonds donors in the secondary sphere, O_2 activation occurred and resulted in a formation of an isolable cobalt(III)-hydroxide (Fig. 3.2A). However, an excess of O_2 had to be added to achieve activation for the single hydrogen-bond cobalt(II) species to form the corresponding cobalt(III)-hydroxide, and no activation occurred at

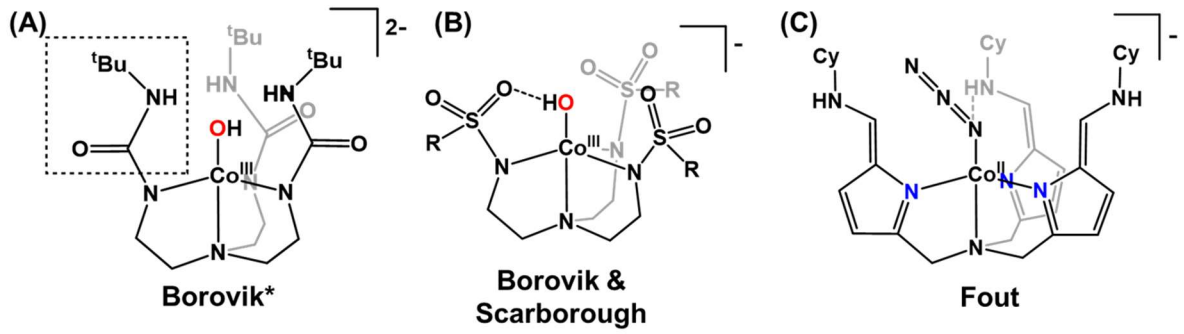

* Reported complexes has 0–3 hydrogen bonds; donator (boxed) swapped with ^{i}Pr group

Figure 3.2 Cobalt systems with secondary coordination sphere hydrogen-bonding from prior studies.

all with no hydrogen-bond donors. Additionally, only the cobalt(III)-hydroxide with three hydrogen-bonds was stable in solution at room temperature; the one and two hydrogen-bonding cobalt(III)-hydroxides gradually decayed in solution overtime, with the single hydrogen-bond cobalt(III)-hydroxide decaying more quickly compared to the double hydrogen-bond cobalt(III) complex. They suggested that the increased activation and stability of the resultant cobalt(III)-hydroxide complex arose from the increased number of H-bonds providing (a) improved binding of O_2 to the metal center and (b) stabilization through reducing the nucleophilicity of the hydroxide and providing a more rigid cavity, making it more challenging for outside molecules to interact with the OH moiety.[45]

Borovik's work has broadened to include examples of complexes with homo- and hetero-bimetallic cobalt along with hydrogen-bond accepting sulfonamide functionalities (Fig. 3.2B).[3,12,46] The Scarborough group expanded upon this work with the cobalt(II) trisulfonamido complex towards *in situ* detection of a cobalt(II)-peroxide adducts.[47] A recent report by Nam and coworkers shows activation of dioxygen by a cobalt(II) tripodal species only in the presence of hydrogen atom donor substrates to form a cobalt(II)-alkylperoxide intermediate that converts to a high-valent cobalt(IV)-oxo adduct upon addition of coordinating scandium tristriflate.[43] The Fout group has used a flexible tripodal ligand framework with secondary sphere H-bonding in

conjunction with cobalt to form a series of X_3^- complexes (Fig. 3.2C),[48] and current work in our group is focused on expanding the use of cobalt in the tripodal ligand framework towards small molecule activation such as O_2 through accessing cobalt(III) centers.

Recently, our group reported the synthesis and characterization of a family of iron complexes supported by the electronically flexible tetrapodal ligand platform, $Py_2Py(pi^{Cy})_2$ (Fig. 3.3).[49] The ligand arms can tautomerize between the azafulvene-amine (afa) or pyrrole-imine (pi) form to give flexible donation in both the primary and secondary sphere (Fig. 3.3 inset); the primary coordination pocket also provides an octahedral environment for the metal center. This ligand been successful in forming a series of iron(II/III) octahedral complexes, and the iron(II) bistriflate complex can activate small molecules such as oxyanions and weak C-H bonds.[49] In this chapter, recent work is summarized that shows the development of the analogous cobalt system with the tetrapodal ligand $Py_2Py(pi^{Cy})_2$ and the formation of a stable cobalt(III)-hydroxo complex from activation of O_2 by the cobalt(II) bistriflate complex. Furthermore, electronic characterization of the cobalt tetrapodal system in conjunction with computational work from collaborators has shown that the cobalt(II) species exhibit unusual character in the electronic ground state. This behavior is proposed to arise from the tetrapodal backbone only weakly coordinating to the metal center, with the degree of this character influenced by the axial ligand. Syntheses of new cobalt(II) tetrapodal species and their characterizations were undertaken to examine the axial ligand influence on the electronic structure, with computational efforts still ongoing. Finally, supplemental electronic structure characterization of the iron tetrapodal system is detailed for comparison to the analogous cobalt species.

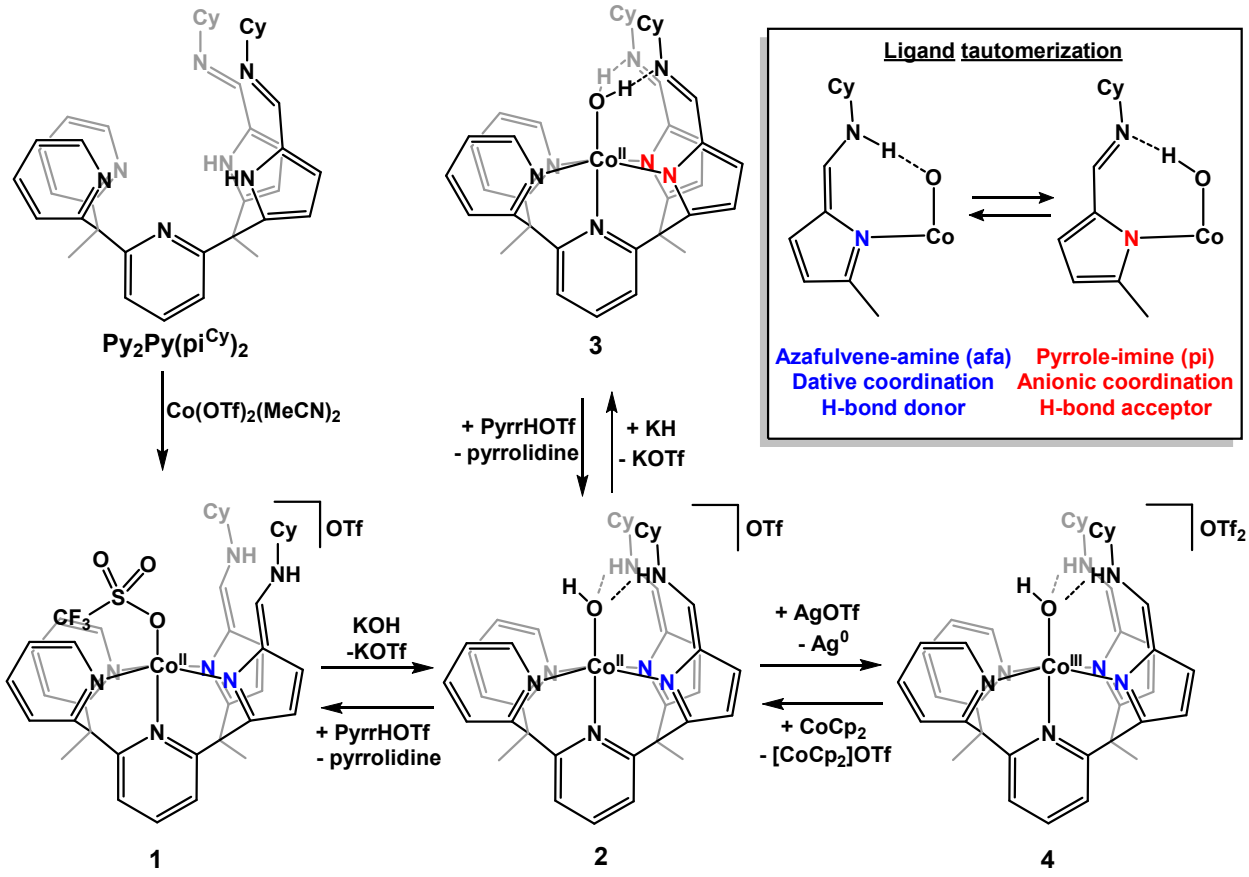

Figure 3.3 Synthesis of cobalt tetrapodal system; inset shows tautomers of ligand arm that provides flexible primary coordination to a metal center and secondary sphere hydrogen bonds.

3.2 Synthesis of Cobalt Complexes.

The syntheses of the cobalt tetrapodal species have been prior described[50] but are summarized here with modifications. $[(Py_2Py(afa^{Cy})_2)Co^{II}OTf]OTf$ (**1**) was generated by reacting one equivalent of cobalt(II) bistriflate bis(acetonitrile) with one equivalent of the tetrapodal ligand $Py_2Py(pi^{Cy})_2$ in tetrahydrofuran (THF), resulting in the precipitation of an orange powder over the course of an hour. This powder was isolated and identified as complex **1** (88% yield) by crystallography and IR spectroscopy, though its poor solubility precluded characterization by ^1H NMR spectroscopy.

Formation of the cobalt(II)-hydroxide tetrapodal complex was accomplished through the addition of potassium hydroxide (KOH) to **1** in acetonitrile. The reaction mixture had solvents

removed after one hour, upon which the light orange film was redissolved in dichloromethane and filtered through Celite to remove unreacted material. The filtrate was pumped down to give the desired product as a light-sensitive, light orange film (95% yield). Characterization by ^{1}H NMR and IR spectroscopies as well as crystallography showed that the hydroxide ligand had been installed to form the complex [($Py_2Py(afa^{Cy})_2$)Co^{II}OH]OTf (**2,** Fig. 3.3). **2** shows both azafulvene-amine arms of the secondary coordination sphere donating hydrogen bonds to the bound hydroxo ligand, and an acetonitrile solvate molecule was observed acting as a hydrogen bond acceptor for the hydroxide ligand. A new high-spin cobalt(II) species formed as a bright yellow-orange precipitate from the addition of lithium oxide (Li_2O) to an acetonitrile solution of **1**, which was found to be the cobalt(II)-aqua species **(**$Py_2Py(pi^{Cy})_2$)$Co^{II}OH_2$ (**3**) by crystallography and supported by IR spectroscopy (yield 89%); akin to complex **1**, its poor solubility in everything but DMA prevented characterization by ^{1}H NMR spectroscopy. Crystallographic data confirmed that **3** is the aqueous cobalt(II) complex (Fig. 3.3), with the pyrrole-imine arms pointing inward to act as hydrogen bond acceptors for the aqua hydrogens; IR stretches of 1617 cm^{-1} confirmed assignment of the ligand arms as the pyrrole-imine tautomer.

Interconversion with these complexes could be achieved in overall good yields (Fig. 3.3). **3** could be converted back to **2** by addition of pyrrolidinium triflate to a solution of **3** in DMA in the dark and allowing to stir for 2 hours. Removal of volatiles gave a light orange film, which was dissolved in DCM and filtered over Celite to remove any unreacted starting material. This dark orange filtrate had its solvent removed *in vacuo*, giving complex **2** as the expected light orange film in excellent yield (87%) and was confirmed by ^{1}H NMR spectroscopy. Complex **3** could be formed by deprotonating **2** with potassium hydride (KH) in acetonitrile, allowing the reaction to stir overnight, and isolating the bright yellow-orange precipitate as **3** (85% yield); due to its

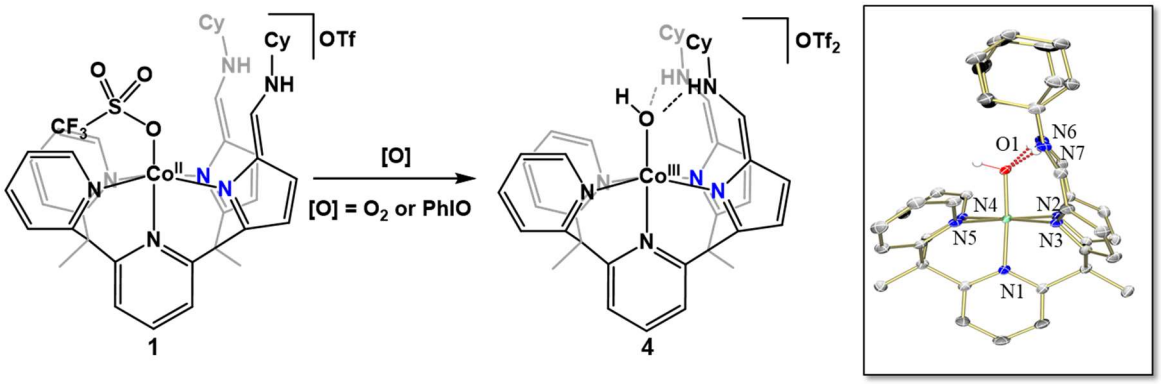

Figure 3.4 Formation of a cobalt(III)-hydroxide (**4**) via O_2 activation or O-atom transfer; inset is the solid-state structure of complex **4** (solvent and outer sphere anions removed for clarity).

insolubility, its identity was confirmed via X-ray crystallography and supported by IR spectroscopy. Regeneration of **1** could be achieved from **2** by the addition of pyrrolidinium triflate in good yield (75%) and confirmed by IR and crystallography.

3.3 Activation of O_2 by Cobalt(II)-Triflate Complex.

Intriguingly, complex **1** was found to form new diamagnetic species when exposed to dioxygen. Upon exposure to either O_2 or ambient atmosphere, an orange solution of **1** in MeCN turned dark brown-purple over the course of 3 hours. Examining the crude ^{1}H NMR spectrum showed solely diamagnetic products, with no visible paramagnetic resonances remaining. The major product was isolated via crystallographic purification. After dissolving the crude residue with DCM and filtering over Celite to remove any unreacted complex **1**, dark red-purple crystals (74% crystalline yield) suitable for X-ray diffraction formed from dissolving the dried dark crude residue with MeCN and allowing diethyl ether to slowly diffuse into the concentrated solution. The refined crystallographic data showed an octahedral cobalt(III)-hydroxide complex ($[(Py_2Py(afa^{Cy})_2)\,Co^{III}OH](OTf)_2$), **4**; Fig. 3.4 inset), isostructural to complex **2**, with a contraction of the Co-O bond and an additional outer sphere triflate counteranion present. Complex **4** was further characterized by ^{1}H NMR and IR spectroscopies. The ^{1}H NMR spectrum showed a single

diamagnetic species, indicative of a low-spin cobalt(III) center, while the IR spectrum showed a C=N stretching frequency at 1668 cm^{-1}, confirming the azafulvene-amine tautomeric form of the ligand. There was also a broad stretch observed at 3365 cm^{-1} in the IR spectrum that was tentatively assigned as an O–H stretch. Complex **4** could also be formed by reacting complex **1** the hypervalent iodide O-atom transfer reagent iodosobenzene (PhIO), which upon addition of PhIO immediately turned a dark magenta that gradually turned dark purple over the course of an hour. The resulting reaction solution had solvents removed *in vacuo*, and the dark red-purple film showed the sole formation of complex **4** in near-quantitative yield (96%). Complex **4** could also be independently synthesized in excellent yield (90%) via another synthetic route through oxidation of complex **2** with silver triflate (AgOTf) in the dark, filtering off the remaining Ag^0, and removing solvents *in vacuo* (Fig. 3.3).

The reaction of the cobalt(II) bistriflate complex **1** with O_2 shows a still unusual example of a cobalt(II) species activating dioxygen to form a cobalt(III)-hydroxide. As described *vide supra*, cobalt(II) species have generally exhibited reversible binding of O_2 or the formation of super-oxide or -peroxide species. Borovik and coworkers showed that hydrogen-bonding in the secondary coordination sphere for their cobalt trigonal bipyramidal system helps to bind and activate dioxygen and stabilize the resulting cobalt(III)-hydroxide complex.[45] In our tetrapodal ligand platform, the tautomerizable arms allow for providing the supportive hydrogen-bonding network in the secondary sphere needed for coordinating and activating dioxygen, in addition to providing flexible dative/anion coordination to the metal center directly. Furthermore, the generated cobalt(III)-hydroxide is remarkably stable, existing for weeks in solution without noticeable degradation by ^1H NMR spectroscopy. In comparison, the analogous tripodal Borovik cobalt(III)-hydroxide complex with two hydrogen-bonding arms is less stable, exhibiting decay to

an unknown cobalt species with a half-life of 13 hours.[45] The stability of complex **4** can be ascribed to both the stabilizing influence of the hydrogen-bond donation to the hydroxide in the secondary sphere and the octahedral geometry providing an ideal d-orbital manifold for generating a low-spin, d^6 species. This showcases the importance of considering both the primary and secondary sphere for catalysis and stabilization of intermediates and products.

3.4 Electronic Characterization of Cobalt Tetrapodal Complexes.

To supplement physical characterization, electronic structure characterization of the cobalt tetrapodal complexes were undertaken. X-band EPR spectra of complexes **1-3** were acquired in 1:1 DMA:toluene frozen solution and shown in Figure 3.5 alongside their simulations. Cobalt(II) is a d^7 system, leading to configurations with possible spin states of S = ½ (low-spin) or 3/2 (high-spin) in an octahedral ligand field. Based on the observed unequal g-values greater than 2, this indicates that these are rhombic high-spin (S = 3/2) cobalt(II) systems. Simulations with predicted

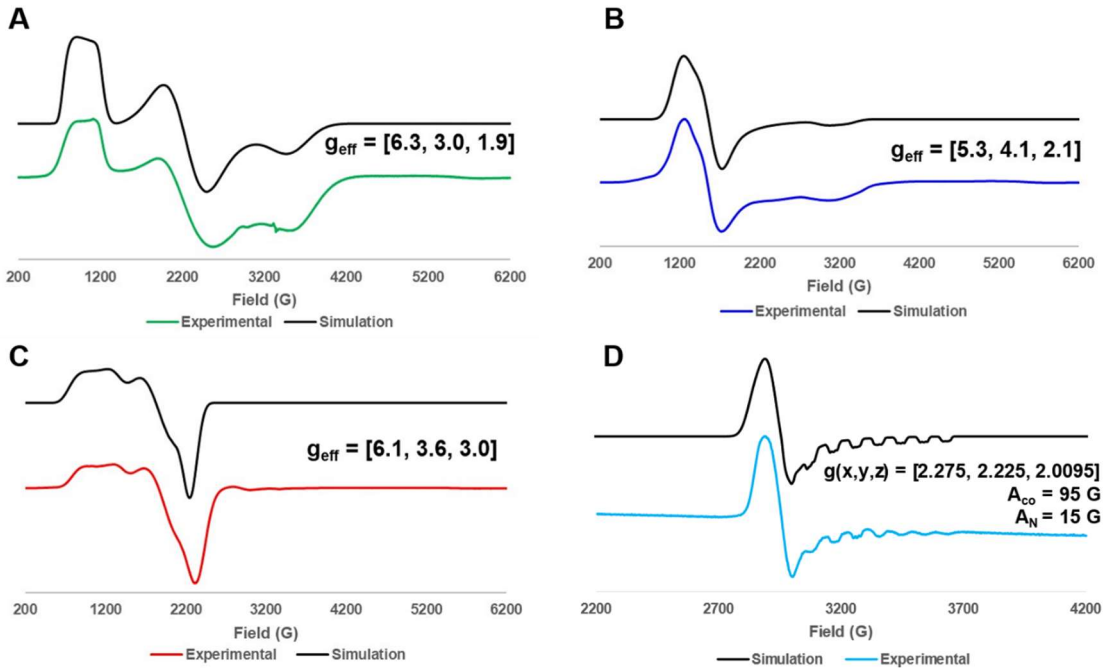

Figure 3.5 X-band EPR spectra of complexes **1** (A, green), **2** (B, blue), **3** (C, red), and **LS-2** (D, cyan); experimental conditions 10 mM 1:1 DMA:tol at 5K (A-C) and 10 mM 1:1 MeCN:tol at 5K (D). Black lines are the simulated spectra with the g_{eff} values found for each complex.

effective g-values reflect these for all three species (Fig. 3.5A-C); their different g_{eff}-values imply that there are changes in the electronic structure based on the different axial ligands. Complex **4** is diamagnetic and exhibits no EPR signal accordingly.

Interestingly, while complexes **1** and **3** show only minor differences in their EPR spectra upon solvent changes, complex **2** in a 1:1 acetonitrile:toluene (MeCN:tol) shows a dramatic shift to a low-spin, S = ½ system with distinct cobalt hyperfine and nitrogen superhyperfine coupling (Figure 3.5D). This allowed for a more descriptive picture of the d-orbital manifold (Scheme 3.1). ^{1}H NMR spectra of complex **2** after exposure to the same EPR solvent mixture remain consistent with the original ^{1}H NMR spectrum of complex **2**. While the source of this "spin-switch" yet remains unclear, the crystal structure of complex **2** shows that acetonitrile can hydrogen-bond with the hydroxide moiety, indicating that other potential hydrogen-bond acceptors such as trace water in the solvent could interact similarly in a stronger manner with the hydroxide. This suggests that a strong hydrogen-bond acceptor could "trigger" a spin-switch on the cobalt. Acetonitrile itself is not likely the source of the switch, as examining the UV-Vis spectra in the presence of other nitriles and freshly dried acetonitrile show the high-spin, S = 3/2 cobalt(II)-hydroxide behavior. This also is likely not reflected in the ^{1}H NMR spectra of these complexes, as the unique paramagnetic signals remain relatively consistent with only minor shifts when the compound is dissolved in acetonitrile-d_3 or dichloromethane-d_2.

In addition to EPR and UV-Vis spectroscopies, magnetic susceptibility studies were also acquired. Poor solubility of complexes **1** and **3** precluded Evan's method for determining μ_{eff} values, but complex **2** was found to have μ_{eff} = 4.6(1) at room temperature in dichloromethane, indicating an expected high-spin S = 3/2 system predicted from EPR and similar in value to other cobalt(II) systems in prior work from our group. Magnetic susceptibility measurements on solid-

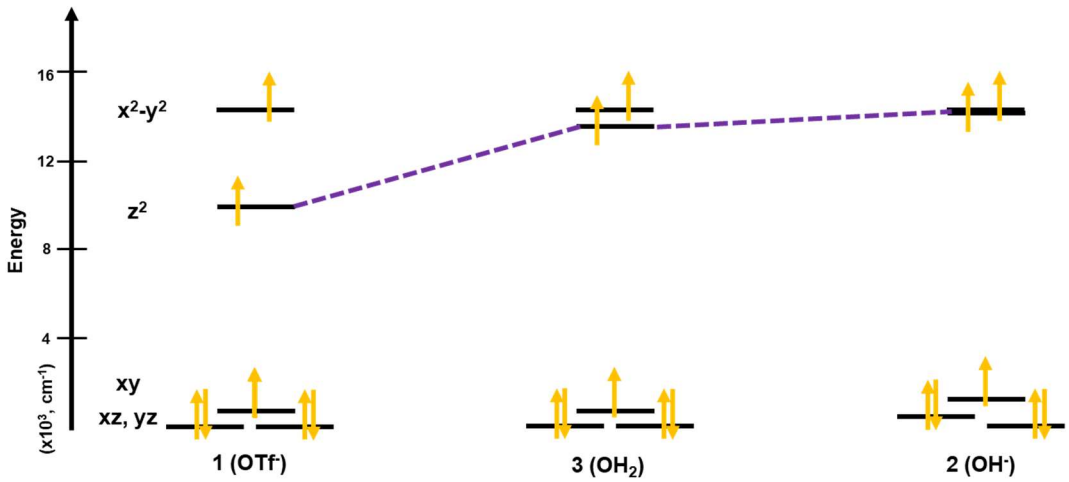

Figure 3.6 Calculated valence d-orbital manifolds for complexes **1-3**. Calculations performed using Kestrel as described in reference 71.

state samples of complexes **1-4** were collected by Ekaterina Lapsheva (Schelter Group, U. Penn.) and detailed in a prior work;[50] all the cobalt(II) complexes gave high-spin, S=3/2 χT values at room temperature with only weak temperature dependence observed for complexes **1** and **3**. The difference in magnetic moment between the Evan's method and SQUID measurements can be attributed to the difference in matrix, as Evan's method is performed in solutions while SQUID magnetic data were acquired on solid samples. Complex **4** was found to be diamagnetic, again as expected for a cobalt(III) d^6 low spin configuration. UV-Vis spectra were also acquired[50] and gave strong, primarily ligand-based bands in the UV region with only minor d-d bands visible between 400-500 nm as is typical for this tetrapodal ligand system.[50]

Initial computational work by George Nunn (Walton Group) suggested that there may be bulk magnetic behavior due to intermixing of excited non-Aufbau states with the expected Aufbau electronic ground state by the cobalt(II) species, though this work is still under investigation. This is predicted based on the tetrapodal ligand only weakly binding to the metal center, potentially decreasing enough ligand field quenching of these states to lead to measurable orbital angular momentum and thus non-Aufbau states.[51–53] Based on current electronic characterization, the

identity of the axial ligand appears to predominantly control the resulting electronic ground state and was confirmed by calculations of the valence d-orbital manifold for complexes **1-3** (Fig. 3.6), indicating variations in the d_{z2} orbital energy based on axial ligand strength. To test the presence of non-Aufbau character in the ground state electronic structure, magnetic hysteresis experiments were undertaken. Magnetic hysteresis has been observed in non-Aufbau cobalt d^7 systems[51–53] and can be used as a measure of the magnetic anisotropy of the complex. Preliminary magnetic hysteresis experiments were performed at various temperatures (2K, 5K, 50K, 77K, 100K) on the cobalt(II) bistriflate complex, as this has the highest degree of non-Aufbau character of the species predicted by calculations. However, no hysteresis was observed at any temperature. Instead, the curvature indicates predominantly paramagnetic behavior in the bulk material (see Fig. 3.15 for example at 2K), indicating that the presence of the non-Aufbau state is too low to be measured and thus useful for applications.

3.5 Development of Other Cobalt(II) Tetrapodal Complexes.

To expand the range of axial ligands in this system to determine the influence of the axial identity on the electronic structure and investigate avenues of reactivity, additional cobalt(II) tetrapodal species were developed and characterized. The targets were X-based and N-based axial ligands, as prior work in the cobalt tripodal system[48] suggested that these would form the desired axial-bound cobalt(II) tetrapodal complexes analogous to complexes **1-3**.

Aimed at developing a primarily solvent-bound (aka a "loose" axial ligand) complex for characterization, a cobalt(II) bis(tetraphenylborate) species $[(Py_2Py(afa^{Cy})_2)Co^{II}](BPh_4)_2$, **5**; Fig. 3.7) was synthesized by reacting two equivalents of sodium tetraphenylborate with a suspension of **1** in THF, where dissolution of the starting complex and a color change from light orange to dark orange-red occurred over the course of 1 hour. The resulting reaction solution had solvents

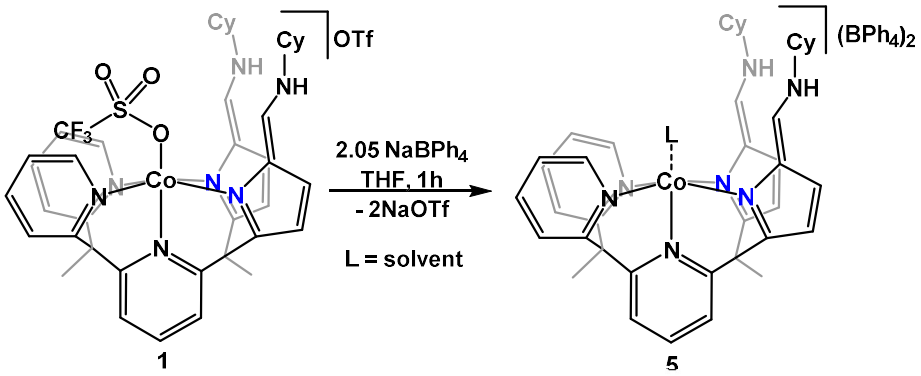

Figure 3.7 Synthesis of complex **5** with proposed structure.

removed *in vacuo* to give a light red-orange film. This film was dissolved in a minimal amount of DCM and filtered to remove sodium triflate, and the filtrate was pumped down to give the desired product as a dark orange-red film (95% yield). ^{1}H NMR spectroscopy showed a unique paramagnetic spectrum, and ^{19}F and ^{11}B NMR spectra showed that no triflate remained and was completely replaced by the tetraphenylborate. IR spectroscopy showed a 1658 cm^{-1} C=N stretch, corresponding to the afa tautomer of the ligand arms. Attempts at growing diffractable crystals provided only oils or powders; additionally, if left in solution, this complex readily reacts with trace amounts of water to form the cobalt(II) hydroxide complex over the course of several days. Without the crystallographic structure we cannot definitively say that there is a particular solvent bound in complex **5**; prior work with the tetraphenylborate salts with these ligand frameworks has shown that these species preferentially keep the BPh_4 anion in the outer sphere rather than bound due to the anion not fitting into the available binding pocket.

Halides were targeted as axial ligands to provide a predicted weaker field ligand relative to the aqua and hydroxide complex based on the spectrochemical series.[54] Unfortunately, attempts at characterizing a halide-bound cobalt(II) tetrapodal species were unsuccessful. Directly metalating the tetrapodal ligand with the corresponding cobalt(II) halide resulted in insoluble salts, and presumably the dihalide cobalt(II) tetrapodal complex. Performing axial ligand exchanges with either the triflate or tetraphenylborate cobalt(II) complex using the addition of one equivalent

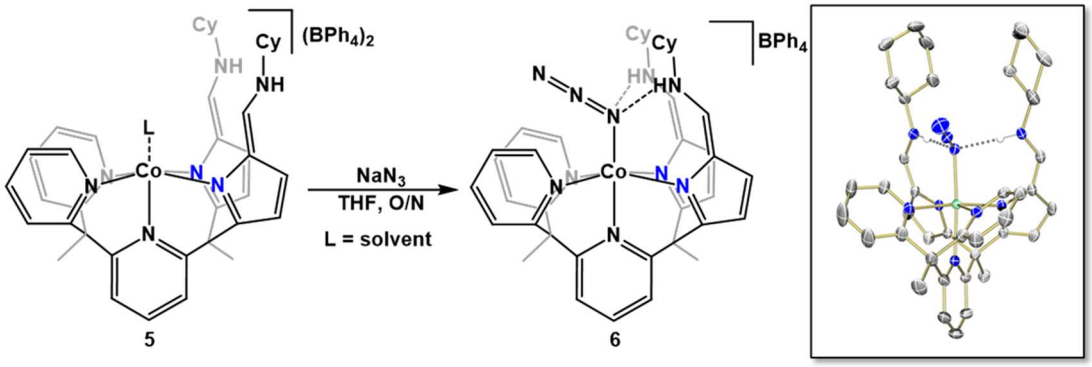

Figure 3.8 Synthesis of complex **6** from complex **5**; inset is solid state structure of complex **6**, solvent and outer sphere anion removed for clarity.

of various sodium or potassium halides generally resulted in a mixture of unconsumed starting material and the insoluble (presumably dihalide) salts or an intractable mixture of paramagnetic products.

However, more success was achieved with azides. When sodium azide was added to a solution of complex **5** (Fig. 3.8), a slow color change was observed over the course of several hours from dark red to light orange. The isolated light orange product (81% yield) from this reaction gave a new, distinctive paramagnetic ^{1}H NMR spectrum. The IR spectrum showed stretches at 1648 cm^{-1}, indicating the presence of afa tautomer arms on the ligand backbone, and 2049 cm^{-1}, corresponding to an N=N=N stretch; this suggested to us that this was $[(Py_2Py(afa^{Cy})_2)Co^{II}N_3]BPh_4$, (**6**). While near-identical ^{1}H NMR and IR spectra (minus BPh_4 and added OTf signals) were achieved when reacting sodium azide with complex **1** in an identical manner, crystallizations of the purported cobalt-azide with an outer sphere triflate only provided feathery plates or powders of poor quality for characterization. Instead, dark red-orange crystallographic-quality crystals were grown from a vapor diffusion of diethyl ether into a concentrated solution of the orange tetraphenylborate product in DCM in the dark, and the solid-state structure was characterized. Refinement revealed the anticipated azide-bound cobalt complex **6** (Fig. 3.8 inset, select structural parameters in Table 3.2) as a pseudo-octahedral structure at the

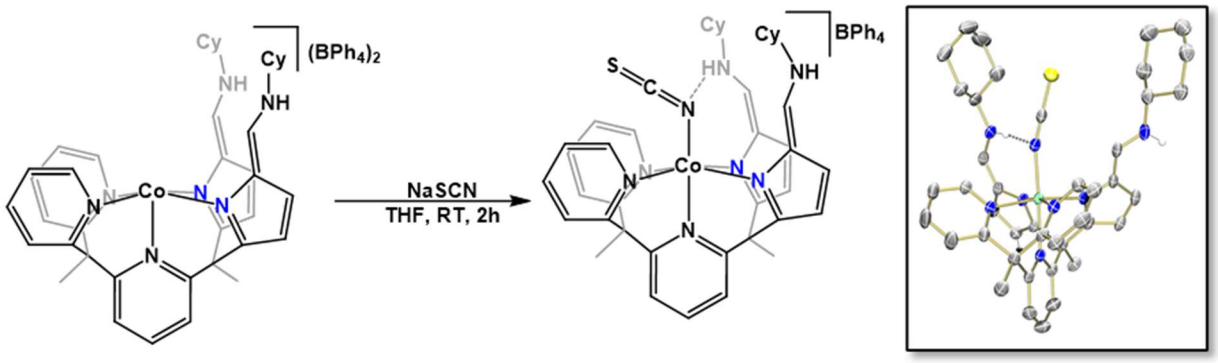

Figure 3.9 Synthesis of isothiocyanate complex **7** from complex **5**; inset is solid state structure of complex **6**, outer sphere anion removed for clarity.

metal center, with the equatorial plane consisting of anionic coordination to the amine nitrogen of the afa tautomeric arm and dative coordination to the pyridyl nitrogens. Both ligand arms rotate inward to give a H-bonding interaction between the amino moiety of the secondary coordination sphere and the bound nitrogen atom of the azide, unlike the analogous cobalt(II)-azide in the tripodal ligand system which only exhibits one inter-ligand hydrogen-bonding interaction.

Additional success with isothiocyanates was achieved. Addition of potassium thiocyanate to a solution of complex **5** resulted in an immediate color change to dark yellow (Fig. 3.9). The solution was allowed to stir for 1 hour to ensure full consumption of the starting materials before solvent was removed and a light-yellow-orange powder was isolated (91% yield). This powder gave a distinctive, paramagnetic ^{1}H NMR spectrum and IR stretches at 1661 and 2041cm^{-1}, corresponding to the afa-tautomer C=N stretch and S=C=N stretch respectively, suggestive that we had formed an isothiocyanate cobalt species $[(Py_2Py(afa^{Cy})_2)Co^{II}(NCS)]BPh_4$ (**7**). Light yellow-orange crystals suitable for crystallography were grown from a vapor diffusion of diethyl ether into a concentrated solution of the target compound in DCM in the dark. Refinement of the data provided the isothiocyanate cobalt(II) **7** as a pseudo-octahedral complex (Fig. 3.9 inset, see Table 3.2 for select parameters). The isothiocyanate is bound through the nitrogen atom, and one

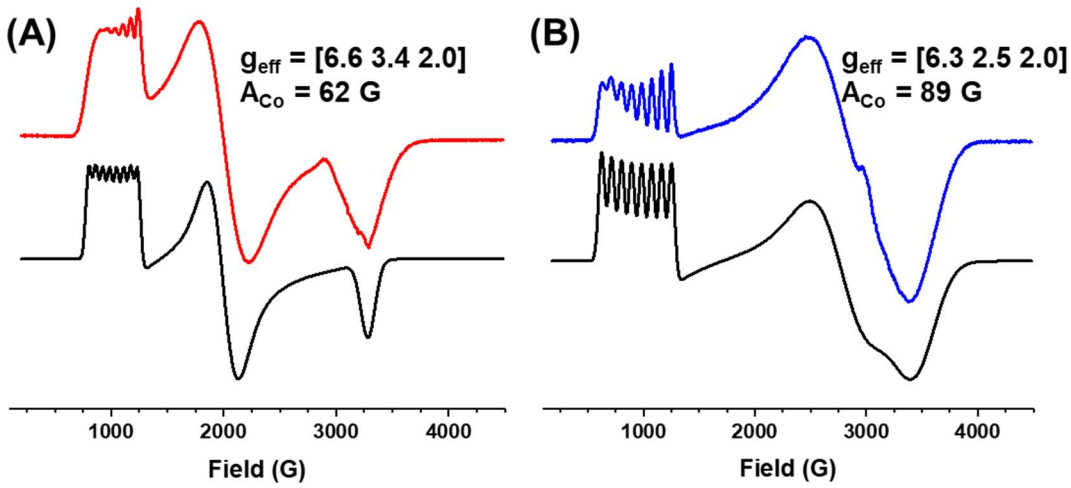

Figure 3.10 X-band EPR of cobalt(II) tetrapodal complexes **6** (A, 2 mM, 15K) and **7** (B, 5 mM, 5K) in 1:1 DMA:toluene; initial simulations are shown in black and effective g-values listed.

of the ligand arms has again rotated inward to hydrogen-bond with the bound nitrogen atom of the substrate.

Characterization was undertaken of complexes **6** and **7** for comparison with the other cobalt(II) species. Based on the spectrochemical series, it is anticipated that azide will be a weaker field ligand and isothiocyanate (N-bound) a stronger field ligand relative to both hydroxide and aqua axial ligands,[54] though the hydrogen-bonding from the ligand arms may tune this donor strength as observed in biological and synthetic model systems.[3,46,55–59] UV-Vis of the two species (Fig. 3.23-24) show primarily ligand-based transitions in the ultraviolet region, with small d-d bands present at $\lambda > 400$ nm, as expected from the other cobalt tetrapodal species. X-band EPR data acquired for these two species show distinct differences based on the axial ligand akin to the other cobalt(II) species (Fig. 3.10). For complex **7**, the results give a rhombic spectrum with g-values greater than 2 indicating a high-spin, d^7 metal center, with preliminary simulations assigning these resonances at g_{eff} at 6.3, 2.5, & 2.0. Hyperfine coupling to the cobalt center is observed for $g_{eff,z}$ at 89 G. Likewise, Complex **6** gives a rhombic EPR spectrum indicative of a high-spin Co(II) rhombic system with three g_{eff} values with visible hyperfine coupling (62 G) at

$g_{eff,z}$ = 6.3. In both cases, significant line broadening (~100-450 G for $g_{eff,x}$ & $g_{eff,y}$ and 50-55 G) made simulating these as effective S = ½ systems to acquire g_{eff} values challenging, akin to initial attempts at effective S = ½ simulations of the EPR spectra of complexes **1-3** in Figure 3.5A-C (though satisfactory parameters for those spectra were eventually determined). Generally, EPR resonances from high-spin cobalt(II) centers can be broadened by excited state character mixing into the ground state, large g-anisotropy, sizable spin–orbit coupling, or a combination of these effects.[27,60,61] Given calculations of complexes **1-3** that noted excited state mixing into the ground state electronic character, complexes **6** and **7** may demonstrate this same mixing in their ground states as well based on their broadened resonances. More representative simulations are underway to better account for this broadening and determine their g-values and rhombicity terms. Computational calculations and magnetic susceptibility measurements towards understanding the axial ligand effect on the electronic structure are still ongoing for these species. Overall, these initial characterizations of complexes **6** & **7** alongside complexes **1-3** show that the axial ligand plays a key role in the electronic structure at the metal center.

3.6 Additional Characterization of Electronic Structure of Iron Tetrapodal Complexes.

To determine if the same effects were observed in the analogous iron system, the electronics of the analogous iron tetrapodal **8-12**[62] (identities shown in Figure 3.11) were further characterized by SQUID, attempted M-edge X-ray absorption spectroscopy (XAS), and X-ray photoelectron spectroscopy (XPS). While prior characterization had acquired EPR, Mossbauer, and UV-Vis of the iron tetrapodal system, no comparison of their electronic structures to cobalt has been done.

Solid state magnetic susceptibility from 4K to room temperature (300K) were acquired for the iron complexes **8-12** (see Figure 3.12), with the iron species synthesized and characterized

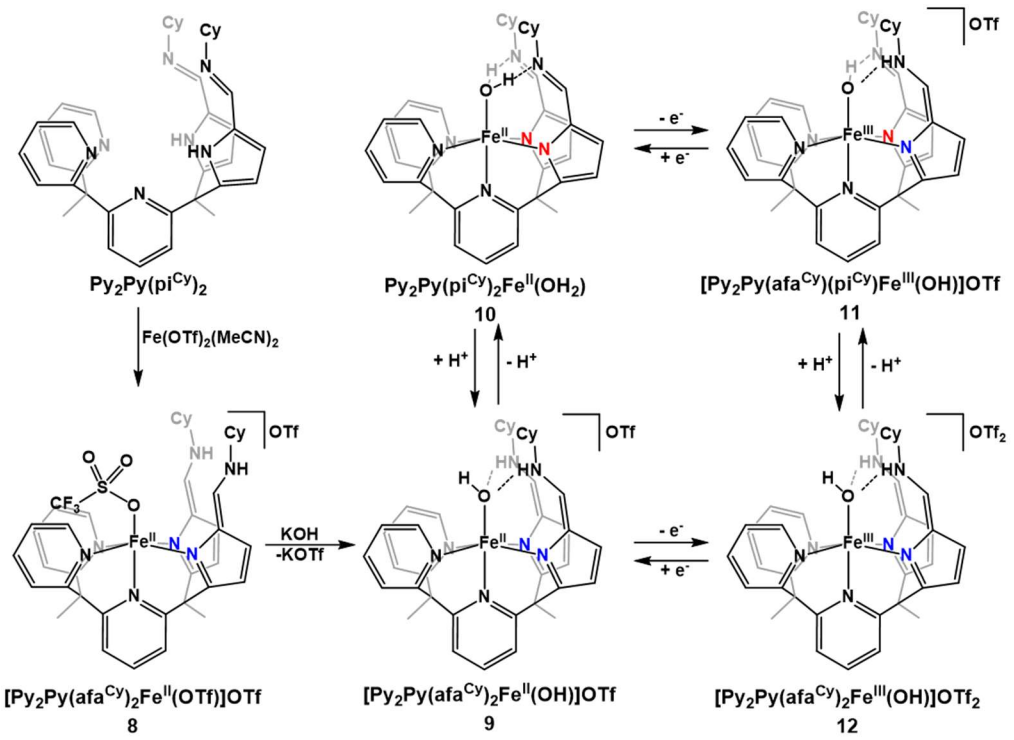

Figure 3.11 Simplified synthetic scheme for complexes **8-12**; synthesis and physical characterization of the iron tetrapodal system described in reference 62.

according to literature procedure.[62] The iron(II) species exhibit similar magnetic character at room temperature. At 300 K, complex **8** has χT of 3.07 emu*K*mol^{-1}, complex **9** of 3.36 emu*K*mol^{-1}, and complex **10** of 3.19 emu*K*mol^{-1}; this corresponds to u_{eff} of 4.96 μ_B, 5.18 μ_B, and 5.05 μ_B, respectively, indicating that at room temperature these are high-spin, d^6 iron(II) centers. Complex **8** and **10** experience a weak temperature dependence between 300 K and 150 K (**8**) or 50 K (**10**). The iron (II)-hydroxide **9** showed that $\chi_M T$ is only slightly dependent on the temperature in the range of 150 to 25 K, exhibiting a sharper decrease below 25 K. Values of χT and μ_{eff} at 4 K for complexes **8-10** were 1.93 emu*K*mol^{-1} & 3.92 μ_B, 2.59 emu*K*mol^{-1} & 4.55 μ_B, and 2.51 emu*K*mol^{-1} & 4.48 μ_B, respectively. There appears to be a similar axial ligand dependence on the electronic structure akin to the cobalt system, where the more loosely bound triflate and aqua complex show a stronger temperature dependence than the hydroxide complex.

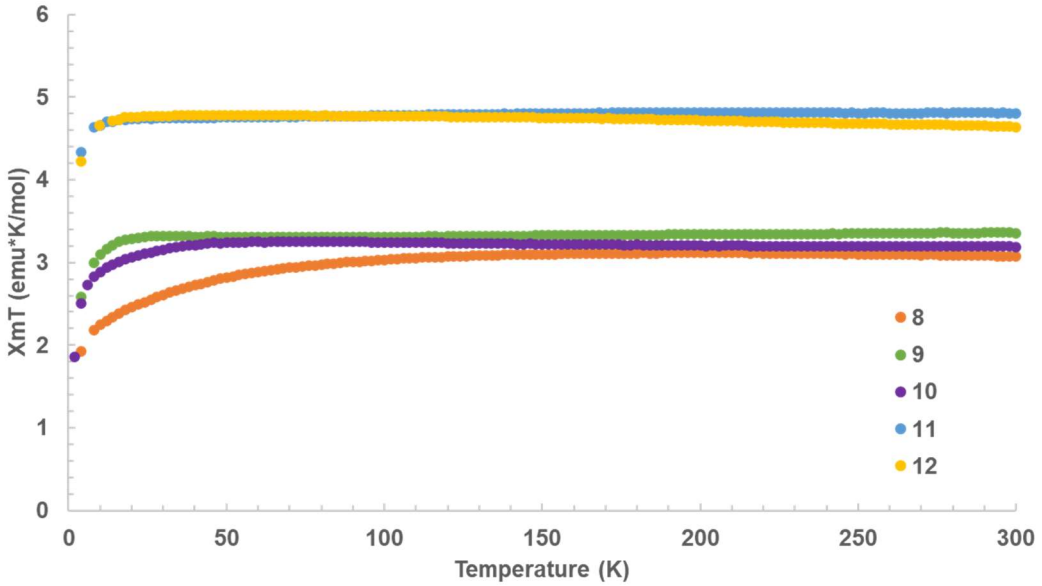

Figure 3.12 Temperature dependence of χT values of complex **8** (orange), **9** (green), **10** (purple), **11** (blue), and **12** (yellow) at 1.0 T field from 2 K to 300 K.

For the iron(III)-hydroxide afa (**12**) and mixed arm (**11**) species, their χT curves were similar and showed weak to little dependence on temperature from 300 K to 20K, below which χT rapidly drops. Their room temperature magnetic susceptibilities were 4.81 emu*K*mol^{-1} for complex **11** and 4.64 emu*K*mol^{-1} for complex **12** at 300 K; these correspond to μ_{eff} of 6.20 μ_B and 6.09 μ_B, respectively, indicating these species are high-spin, S = 5/2 iron(III) systems and match well with μ_{eff} values acquired by Evan's method. At 4K, χT were 4.34 emu*K*mol^{-1} & 5.89 μ_B and 4.33 emu*K*mol^{-1} & 5.81 μ_B, respectively, for complex **11** and **12**, indicating that even at low temperatures these complexes remain generally high-spin, S=5/2 iron(III) systems. These values are similar to what has been collected for other iron(III) high-spin compounds in these ligand systems.[63,6465]

X-ray absorption spectroscopy is ideal for determining electronic structure, particularly at the L- and M-edge due to its sensitivity to oxidation state, ligand field, and spin-state.[66–68] To provide more detail on the electronic structure, thin-film samples of the various iron and cobalt tetrapodal species were attempted on silicon nitride substrate and polymer substrate via drop-

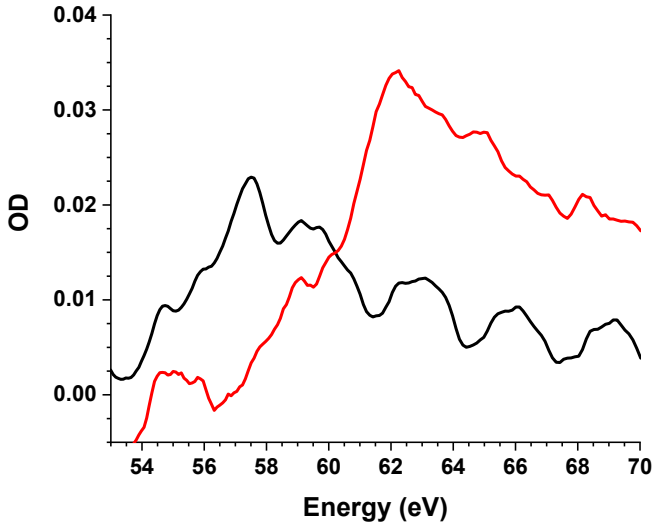

Figure 3.13 $M_{2,3}$-edge spectra of bistriflate metal(II) complexes **1** (cobalt, red) and **8** (iron, black).

casting, spin-coating, or embedment (polymer only) of the complexes for $M_{2,3}$-edge spectroscopy of the metal centers. Compound aggregation unfortunately precluded data collection in most cases, as the samples proved too inhomogeneous for M-edge spectroscopy with the available XUV instrumentation. However, sufficient sample quality was achieved for the iron(II) and cobalt(II) bistriflate complexes (**8** and **1**, respectively) for M-edge spectral acquisition (shown in Figure 3.13). Iron complex **8** shows a broad, single peak feature centered at 57.5 eV anticipated for a high-spin octahedral iron(II).[66,69] The M-edge of cobalt complex **1** appears primarily as a broad, single peak centered at 62.1 eV with a slight shoulder at ~59.5 eV, likewise indicative of a high-spin cobalt(II) center.[66,70]

Given the difficulties with sample preparation for $M_{2,3}$-edge spectroscopy by XUV, XPS data were acquired of the iron 3p core energies of complexes **8-12** to determine if any possible differentiation could be achieved between the known iron complexes with a core orbital-level technique for future potential XUV or XAS-based experiments. Samples of complexes **8-12** were prepared on Au-coated Si substrate to ensure sufficient conductivity for XPS. Table 3.1 displays the Fe 3p binding energy and FWHM fit for these complexes. We found that generally the iron(II)

Table 3.1 - XPS of iron 3p orbital binding energies of complexes **8-12.**

Complex	Binding energy (eV)	FWHM (eV)
8	54.5	3.0
9	54.3	2.8
10	55	2.9
11	55.5	4.5
12	56.7	4

and iron(III) species could be differentiated based on their binding energy and broadness; complexes **8-10** could be found at lower binding energies (~54.5 eV) and gave narrower FWHM (2.5-3 eV) than the higher oxidation state iron(III) complexes **11-12** (~56 eV and 4-4.5 eV, respectively). This means that future $M_{2,3}$-edge spectroscopy could differentiate these iron tetrapodal complexes based on their oxidation state at a minimum, but it is uncertain if clear differences will be apparent between the complexes of the same oxidation state at the $M_{2,3}$-edge (as these are dependent on both iron 3p and 3d orbital manifolds).[66] The Fe 2p binding energies were also collected and showed similar energy shift trends between the iron(II) and iron(III) complexes, but due to the high-spin nature of the species, complicated multiplet splitting was present that precluded quantitative fitting. However, these XPS data show that future XAS experiments of the iron tetrapodal system will likely be fruitful for differentiating between the various complexes or intermediate species in investigating their processes.

These magnetic susceptibilities and XPS features in combination with the already collected EPR and Mössbauer data showcase that these iron tetrapodal complexes have unique electronic structure. It is proposed for the iron(III)-hydroxo tetrapodal complexes that the noncovalent interactions in the secondary coordination sphere and oxidizing potential of the metal center influences the reactivity,[62] which are reflected in the d-orbital manifolds of the complexes and seen in the tripodal iron system (see Chapter 4 and in reference 64). Like the cobalt(II) species, the

iron(II) species show differences in their electronic structure based on their axial ligand identity, suggestive that these ligand effects play a similar role in controlling the electronic structures of the two metal systems.

3.7 Conclusions

Cobalt complexes for dioxygen activation are less explored in comparison to their iron counterparts. Prior work has shown that secondary coordination sphere hydrogen-bonding networks can be used to help activate small molecules like dioxygen and stabilize the generated cobalt(III)-axial bound products. We have shown the synthesis of a series of cobalt tetrapodal complexes that contain secondary coordination sphere hydrogen bonding. The cobalt(II) bistriflate complex can activate dioxygen to form a stable cobalt(III)-hydroxide complex. This stability is proposed to come from the combination of the secondary sphere H-bonding to the bound hydroxide and the octahedral coordination environment stabilizing a low-spin, d^6 complex. The characterization of the cobalt system has determined that the cobalt(II) species are high-spin S = 3/2 species, with the axial ligand dominating the electronic structure. Synthesis and characterization of other cobalt(II) species with X_3^- axial ligands were also described, indicating that other X-type ligands can be accessed in this system for potential reactivity and control of the electronic structure. Additional characterization of the analogous iron tetrapodal system was also described for further comparison to the cobalt tetrapodal system and show similar dependence on ligand identity in the electronic structure.

Acknowledgements: This project was done in collaboration with several people. Dr. Michael Drummond performed initial synthesis and physical characterization of the complexes, while Kenai Duran and Xin Ying (Sammie) Guo assisted in yield replications with the updated synthetic preparations. We thank Ekaterina Lapsheva (Shelter Group, U. Pennsylvania) for performing

magnetic susceptibility measurements of complexes **1-3**. We deeply thank George Nunn (Walton Group, U. York) for performing computational calculations of the cobalt(II) tetrapodal complexes and to both George and Paul Walton for fruitful discussions throughout this work.

3.8 Experimental

General Considerations. All manipulations of air- and moisture-sensitive metal compounds were carried out in the absence of water and dioxygen using a MBraun inert atmosphere drybox under a dinitrogen atmosphere. All glassware was oven-dried for a minimum of 8 h and cooled in an evacuated antechamber prior to use in the drybox. Solvents were dried and deoxygenated on a Glass Contour System (SG Water USA, Nashua, NH) and stored over 4 Å molecular sieves (3 Å in the case of acetonitrile) purchased from Strem prior to use. Dichloromethane-d_2 and acetonitrile-d_3 were purchased from Cambridge Isotope Laboratories and stored over 4 and 3 Å molecular sieves, respectively, prior to use. Lithium oxide (Sigma-Aldrich), silver triflate (Strem), potassium hydride (Sigma-Aldrich), triflic acid (Sigma-Aldrich), potassium hydroxide (Fischer Scientific), pyrrolidine (Sigma-Aldrich), were purchased from the vendor listed and used as received. Pyrrolidinium triflate (PyrHOTf) was prepared according to literature procedures. The ligand was synthesized and dried according to literature procedure, and the iron tetrapodal species (complexes **8-12**) were likewise prepared and characterized as described by literature procedures. Celite^{TM} 545 was dried in Schlenk flasks for 24 hour under a dynamic vacuum while heating to at least 150 °C prior to use in a drybox.

Physical Methods. NMR spectra were recorded on a Varian spectrometer at 500 MHz (^{1}H NMR). All ^{1}H chemical shifts (ppm) are reported relative to the resonance of the residual solvent. Solid-state infrared spectra were recorded using a PerkinElmer Frontier FT-IR spectrophotometer equipped with a KRS5 thallium bromide/iodide universal attenuated total reflectance accessory. UV-visible spectra were recorded on an Agilent 8453 Spectrophotometer with accompanying software. All samples were prepared at the specified concentration in a drybox containing a dinitrogen atmosphere in quartz cuvettes with a 1 cm pathlength and capped with a rubber septum or gas-tight screw cap. EPR samples were prepared as dilute solutions in 1:1 [dimethylacetamide (DMA) or acetonitrile (MeCN)]:toluene solvent mix at 10 mM (complexes **1-3**), 5 mM (complex **7**) or 2 mM concentration (complex **6**) under dinitrogen atmosphere in a drybox. These were then

frozen using liquid nitrogen to generate frozen glasses of the sample. EPR spectra were recorded on a Varian E-line 12 Century series X-band CW spectrometer (complexes **1-3**) or Bruker 10" EMXPlus X-band Continuous Wave EPR spectrometer (complexes **6-7**), and the spectra were simulated using the programs WinEPR and Simfonia, with thanks to the Mirica group (UIUC) for training. Magnetic susceptibility samples were purified and thoroughly dried before use to ensure sample homogeneity. Small amounts (c.a. 10-20 mg) of the target complex were placed in sample capsules and secured with dried eicosane. Data were collected on a Quantum Design MPMS3 SQUID Magnetometer at the Materials Research Laboratory (MRL) Central Research Facilities at 1 T from 2-300 K. Magnetic hysteresis experiments were implemented at set temperatures with the hysteresis mode of the MPMS magnetometer with a sweep rate of 50 Oe/s and settling at each field before measurement was acquired. Data were collected in a range of from -10,000 to 10,000 Oes (-1.0 to 1.0 T). The authors acknowledge the use of facilities and instrumentation at the Materials Research Laboratory Central Research Facilities, University of Illinois, partially supported by NSF through the University of Illinois Materials Research Science and Engineering Center DMR-1720633. Kestrel calculations on complexes **1-3** were performed by G. Nunn as described in prior work.[71]

$M_{2,3}$-edge samples were prepared by spincasting 2-3 drops of a concentrated, filtered solution of either complex **1** or **8** in MeCN onto dried 100 nm Si_3N_4 substrate under dinitrogen atmosphere in a drybox. Data were collected on the home-built XUV instrumentation in the Vura-Weis group at UIUC using HHG generation of XUV photons as described in prior works and Chapter 5 using Ar (40 torr) and Ne (100 torr) harmonics with resolution averaging ~0.35-0.4 eV. XPS samples were prepared by spincasting 2-3 drops of a concentrated, filtered solution in MeCN (**8-9, 11-12**) or DMA (**10**) of the target compound onto dried Au-coated Si substrate (provided by A. Sharma) under dinitrogen atmosphere in a drybox. Samples were run courtesy of Dr. Richard Haasch on the Kratos Axis ULTRA XPS spectrometer at the Materials Research Laboratory Central Research Facilities at the University of Illinois at Urbana-Champaign.

[($Py_2Py(afa^{Cy})_2$)$Co^{II}OTf$]OTf (1). To a 20 mL scintillation vial was added $Py_2Py(pi^{Cy})_2$ (0.032 g, 0.050 mmol), a stir bar, and 2 mL of tetrahydrofuran. After dissolution, $Co(OTf)_2(MeCN)_2$ (0.0242 g, 0.055 mmol, 1.1 eq) was added to the solution. An immediate color change to dark red orange was observed, followed by the formation of an orange precipitate over the course of 1 h. The

reaction was filtered over Celite^{TM}, and the orange solid was washed with THF (0.5-1 mL). The powder was eluted with six, 1 mL portions of acetonitrile or until no visible orange solid remained on filter. Volatiles were removed under reduced pressure to give an orange powder (0.044 g, 0.44 mmol, 88%). Crystals suitable for X-ray analysis were grown from the vapor diffusion of diethyl ether into a concentrated solution of the target molecule in acetonitrile at room temperature. The poor solubility of the complex precluded its characterization by ^{1}H NMR spectroscopy and Evan's method. μ_{eff} (SQUID): 4.92 μ_B (300 K). IR ν_{max}: 1635 cm^{-1} (C=N), 3215, 3283 cm^{-1} (N-H).

[(Py$_2$Py(afa^{Cy})$_2$)Co^{II}OH]OTf (2). To a 20 mL scintillation vial covered with black electrical tape was added complex **1** (0.044 g, 0.044 mmol), a stir bar, and 4 mL of acetonitrile. KOH (0.0040 g, 0.071 mmol, 1.6 eq) was added to the orange suspension and a dark orange solution formed over 1 h. After the removal of volatiles under reduced pressure, the orange residue was dissolved in dichloromethane and filtered over a pad of Celite^{TM} to remove unreacted KOH and KOTf byproduct. The volatiles were again removed under reduced pressure, yielding an orange powder (0.0361 g, 0.042 mmol, 95%). Crystals suitable for X-ray analysis were grown from vapor diffusion of diethyl ether into a concentrated solution of the target molecule in acetonitrile at room temperature in the dark. Bulk crystallization was performed by a vapor diffusion of diethyl ether into a concentrated solution in dichloromethane in the dark. ^{1}H NMR (d_3-CD_3CN, 21 ^{o}C): -16.7, -0.8, 1.1, 1.8, 2.9, 3.4, 4.8, 4.9, 5.4, 6.9, 7.8, 9.6, 10.0, 13.6, 15.2, 17.1, 17.8, 21.3, 22.1, 25,7 47.4, 50.0, 54.2, 59.9, 60.2, 66.5. μ_{eff} (Evan's): = 4.6(1) (300 K), μ_{eff} (SQUID): 4.52 μ_B (300K). IR ν_{max}: 1661 cm^{-1} (C=N), 3585 cm^{-1} (O-H).

(Py$_2$Py(pi^{Cy})$_2$)Co^{II}OH$_2$ (3). To a 20 mL scintillation vial was added complex **1** (0.0440 g, 0.044 mmol), a stir bar, and 2 mL of acetonitrile. Li_2O (0.003 g, 0.10 mmol, 2.3 eq) was added to the solution. The solution changed from orange to light orange over the course of 1 h, followed by the precipitation of a bright orange solid over the course of 18 h. The suspension was filtered, and the precipitate was washed with 1 mL of acetonitrile. The solid was eluted with dimethylacetamide (DMA). Crystals suitable for X-ray analysis were grown from the vapor diffusion of diethyl ether and dichloromethane into a concentrated solution of the target complex in dimethylacetamide at room temperature (0.0279 g, 89%). The poor solubility of the complex precluded its characterization by ^{1}H NMR spectroscopy and Evan's method. μ_{eff} (SQUID): 4.79 μ_B (300K). IR ν_{max}: 1617 cm^{-1} (C=N).

[($Py_2Py(afa^{Cy})_2$)$Co^{III}OH$](OTf)$_2$ (4). To a 20 mL scintillation vial wrapped in black electrical tape was added complex **2** (0.0350 g, 0.041 mmol), 4 mL of dichloromethane, and a stir bar. AgOTf (0.0104 g, 0.041 mmol) was added to the solution, and the reaction was allowed to stir at room temperature for 1 h. The mixture was filtered over Celite^{TM} revealing the presence of grey Ag^0 precipitate, and the dark purple filtrate was dried under reduced pressure, producing a dark purple-red powder (0.0373 g, 0.037 mmol, 90%). Crystals suitable for X-ray analysis were grown from vapor diffusion of diethyl ether into a concentrated solution in acetonitrile at room temperature. Bulk crystallization was performed by a vapor diffusion of diethyl ether in a concentrated solution in dichloromethane at room temperature. ^{1}H NMR (d_3-CD_3CN, 500 MHz, 21 ^{0}C): 1.06 – 1.87 (m, 3H), 2.22 (dd, *J* = 49.0, 12.2 Hz, 5H), 2.44 (s, 3H), 2.74 (s, 3H), 3.41 (q, J = 7.1 Hz, 1H), 3.62 (td, *J* = 11.5, 6.1 Hz, 2H), 6.63 (d, *J* = 4.4 Hz, 2H), 7.26 (d, *J* = 4.3 Hz, 2H), 7.65 (t, *J* = 6.7 Hz, 2H), 8.08 – 7.90 (m, 6H), 8.10 (q, *J* = 8.9, 8.5 Hz, 3H), 9.19 (d, *J* = 6.3 Hz, 2H), 13.85 (d, *J* = 12.0 Hz, 2H). IR ν_{max}: 1668 cm^{-1} (C=N), 3365 cm^{-1} (O-H).

Formation of 4 via PhIO. To a 20 mL scintillation vial was added complex **1** (0.040 g, 0.040 mmol), 4 mL of acetonitrile, and a stir bar. PhIO (0.0090 g, 0.041 mmol, 1.02 eq) was added to the reaction vial, and an immediate color change from orange to dark pink-red. The reaction was allowed to stir at room temperature for 1 hour, with the solution changing from a dark pink-red to dark purple. Volatiles were removed, and the residue was washed with diethyl ether. This resulted in the final product complex **4** as a dark red-purple film (0.0194 g, 0.0192 mmol, 96% yield). Crystals of **4** were grown from the layered purple solution (0.0221 g, 0.022 mmol, 54% yield) and confirmed by ^{1}H NMR spectroscopy.

Formation of 4 via O_2 activation. To a 20 mL scintillation vial was added complex **1** (0.040 g, 0.040 mmol), 4 mL of acetonitrile, and a stir bar. Vacuum was pulled on the solution for ~1 min to remove most dissolved gas from the solution. The vial was capped with a rubber septum and removed from the dry box. A balloon filled with dried O_2 and fitted with a needle was injected into the atmosphere of the reaction vial. The solution changed from orange to purple over the course of 30 min and was allowed to stir for a total of 3 hours to fully consume starting material. Volatiles were removed from the reaction, leaving behind a dark purple-red residue (91% crude). The residue was brought back into the drybox, dissolved in acetonitrile, and layered with diethyl

ether. Crystals of **4** were grown from the layered purple solution (0.030 g, 0.030 mmol, 74% yield) and confirmed by XRD and ^{1}H NMR spectroscopy.

Formation of 3 via 2. To a 20 mL scintillation vial wrapped in electrical tape was added complex **2** (0.0280 g, 0.032 mmol), 3 mL of acetonitrile, and a stir bar. KH (0.0015 g, 0.037 mmol, 1.15 eq) was added, and the solution was allowed to stir at room temperature overnight, resulting in a bright orange precipitate. The reaction mixture was filtered over Celite, washed with an additional 1 mL of acetonitrile, and the isolated light orange powder was eluted off the filter with dimethylacetamide (3 x 0.75 mL). Solvents were removed *in vacuo*, resulting in a light orange film (0.0200 mg, 0.028 mmol, 87% yield). This was confirmed to be **3** by IR spectroscopy and XRD.

Formation of 2 via 3. To a 20 mL scintillation vial wrapped in electrical tape was added complex **3** (0.0220 g, 0.031 mmol), 2 mL of dimethylacetamide, and a stir bar. Pyrrolidinium triflate (6.9 mg, 0.031 mmol, 1 eq) was added, and the solution was allowed to stir at room temperature for 2 h, resulting in a dark red-orange solution. Volatiles were removed *in vacuo*, and the resulting dark orange powder was dissolved in dichloromethane and filtered over Celite to remove any unreacted starting material. Solvents were removed *in vacuo*, resulting in a light orange film (0.0227 g, 0.026 mmol, 85% yield). This was confirmed to be **2** by ^{1}H NMR spectroscopy.

Formation of 2 via 4. To a 20 mL scintillation vial wrapped in electrical tape was added complex **4** (0.0320 mg, 0.032 mmol), 4 mL of acetonitrile, and a stir bar. $CoCp_2$ (6.1 mg, 0.032 mmol, 1 eq) was added, and the solution was allowed to stir at room temperature for 1 h, resulting in a dark red-orange solution. Volatiles were removed *in vacuo*. The resulting dark orange powder was washed with diethyl ether, then dissolved in dichloromethane and filtered over Celite. Solvents were removed *in vacuo*, resulting in a light orange film (0.0199 g, 0.023 mmol, 73% yield). This was confirmed to be **2** by ^{1}H NMR spectroscopy.

Formation of 1 via 2. To a 20 mL scintillation vial wrapped in electrical tape was added complex **2** (0.0320 g, 0.037 mmol), 4 mL of acetonitrile, and a stir bar. Pyrrolidinium triflate (8.2 mg, 0.037 mmol, 1 eq) was added, and the solution was allowed to stir at room temperature for 2 h, resulting in an orange solution. Volatiles were removed *in vacuo*, and the resulting orange powder was washed with diethyl ether and dried under vacuum. This powder was confirmed to be **1** (0.0277 g, 0.028 mmol, 75% yield) by IR spectroscopy and XRD.

[($Py_2Py(afa^{Cy})_2$)Co^{II}](BPh_4)$_2$ (5). To a suspension of complex **1** (0.0440 g, 0.044 mmol) in 4 mL THF was added anhydrous sodium tetraphenylborate (2.05 eq., 0.0902 mmol, 0.0309 g). The reaction was allowed to stir for 1 hour at room temperature, resulting in the dissolution of **1** and formation of a dark orange-red solution. Solvents were removed from the reaction mixture to give a streaky light orange/dark red-orange film. A minimal amount of dichloromethane was added to dissolve the dark red-orange film, and the mixture was filtered through Celite. Volatiles were removed from the filtrate, washed with diethyl ether (3 x 1 mL) to remove any unreacted $NaBPh_4$, and then dried to give the desired product as a dark red-orange film (0.0564 g, 0.042 mmol, 95% yield). ^{1}H NMR (d_3-CD_3CN, 500 MHz, 22 ^{0}C): -22.89, -15.33, -14.18, -11.22, -10.84, -9.56, -9.00, -8.74, -5.68, -5.32, -4.55, 6.99, 7.05, 7.41, 29.48, 31.75, 50.36, 72.51, 77.43, 93.13. IR ν_{max}: 1658 cm^{-1} (C=N).

[($Py_2Py(afa^{Cy})_2$)$Co^{II}N_3$](BPh_4) (6). To a solution of complex **5** (0.056 g, 0.042 mmol) in 4 mL THF was added sodium azide (1.05 eq., 0.044 mmol, 0.0029 g); *SAFETY NOTE – sodium azide is shock-sensitive; manipulate with non-conductive plastics, use caution, and never use more than 10 mg at a time.* The reaction was allowed to stir overnight at room temperature, resulting in a light orange solution. Solvents were removed from the reaction mixture to give a flaky light orange film. A minimal amount of dichloromethane was added to dissolve the film, and the mixture was filtered through Celite. Volatiles were removed from the filtrate to give the desired product as a light red-orange film (0.034 mmol, 0.0359 g, 81%). Note this complex is slightly light sensitive, so recommended long-term storage should be in the dark. Crystals suitable for XRD were grown from vapor diffusion of diethyl ether into a concentrated solution of **6** in dichloromethane in the dark. ^{1}H NMR (d_3-CD_3CN, 500 MHz, 21 ^{0}C): -21.84,-20.18, -11.62, -9.20, -4.86, -2.78, -0.59, 0.75, 1.11, 1.55, 1.78, 3.41, 5.44, 6.49, 6.73, 6.88, 7.20, 16.02, 26.90, 33.45, 52.72,53.72, 54.90, 62.34, 76.38. IR ν_{max}: 1648 cm^{-1} (C=N), 2049 (N=N).

[($Py_2Py(afa^{Cy})_2$)Co^{II}NCS](BPh_4) (7). To a solution of complex **5** (0.056 g, 0.042 mmol) in 4 mL THF was added sodium thiocyanate (1.05 eq., 0.044 mmol, 0.0036 g). The reaction was allowed to stir for 1 hour at room temperature, resulting in a light yellow-tan solution. Solvents were removed from the reaction mixture to give a flaky light yellowish film. A minimal amount of dichloromethane was added to dissolve the film, and the mixture was filtered through Celite. Volatiles were removed from the filtrate to give the desired product as a light red-orange film

(0.038 mmol, 0.0411 g, 91%). Crystals suitable for XRD were grown from vapor diffusion of diethyl ether into a concentrated solution of **6** in dichloromethane in the dark. ^{1}H NMR (d_3-CD_2Cl_2, 500 MHz, 22 ^{0}C): -74.49, -61.61, -58.68, -24.70, -16.34, -14.91, -14.64, -14.20, -12.71, -10.72, -8.50, -6.56, -5.55, -4.07, -3.47, -2.44, -2.12, 0.06, 1.79, 3.63, 6.27, 6.37, 7.02, 17.98, 20.58, 22.10, 27.11, 28.81, 32.75, 34.59, 35.25, 42.48, 45.35, 50.31, 52.90, 54.56, 56.59, 59.69, 72.42, 72.80, 79.38, 86.08. IR ν_{max}: 1661 (C=N), 2041 (N=C=S), 3323 (N-H) cm^{-1}.

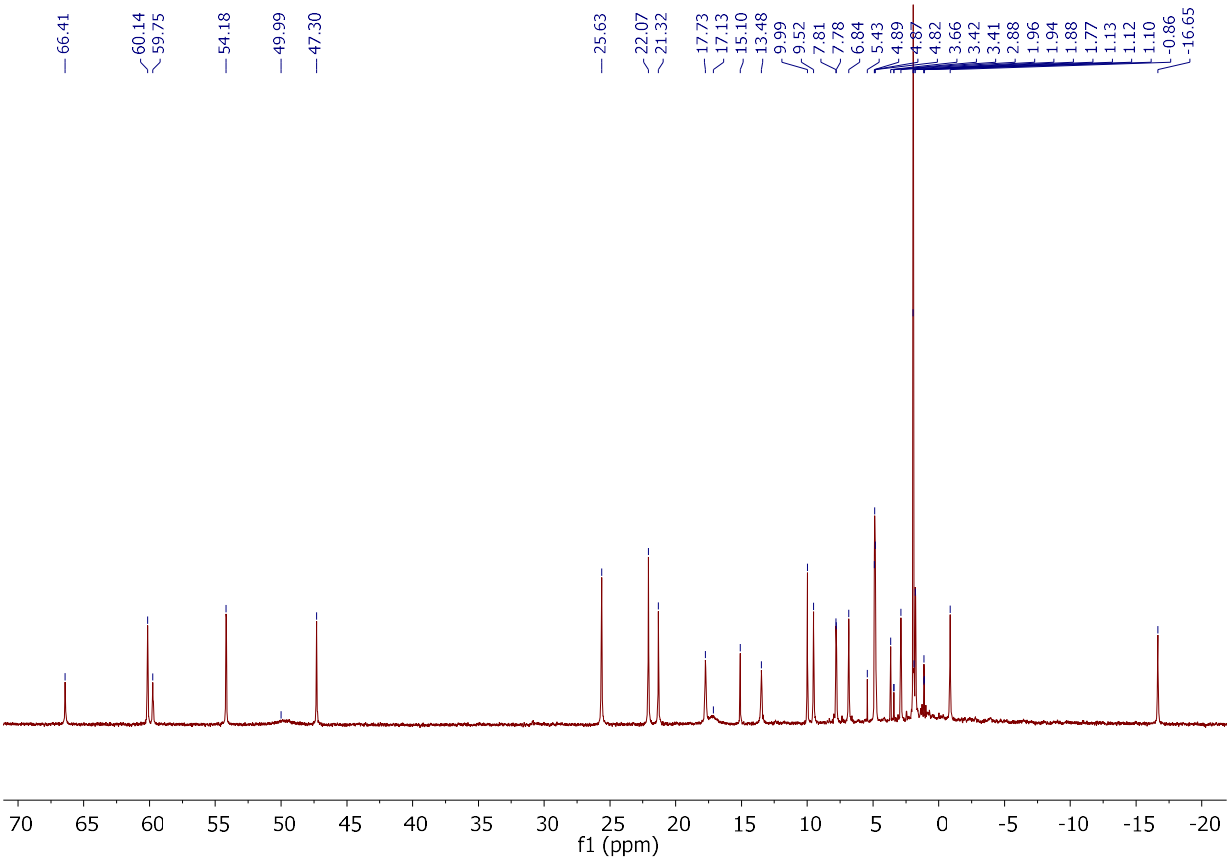

Figure 3.14 ^{1}H NMR of complex **2** in MeCN-d_3 (22ºC).

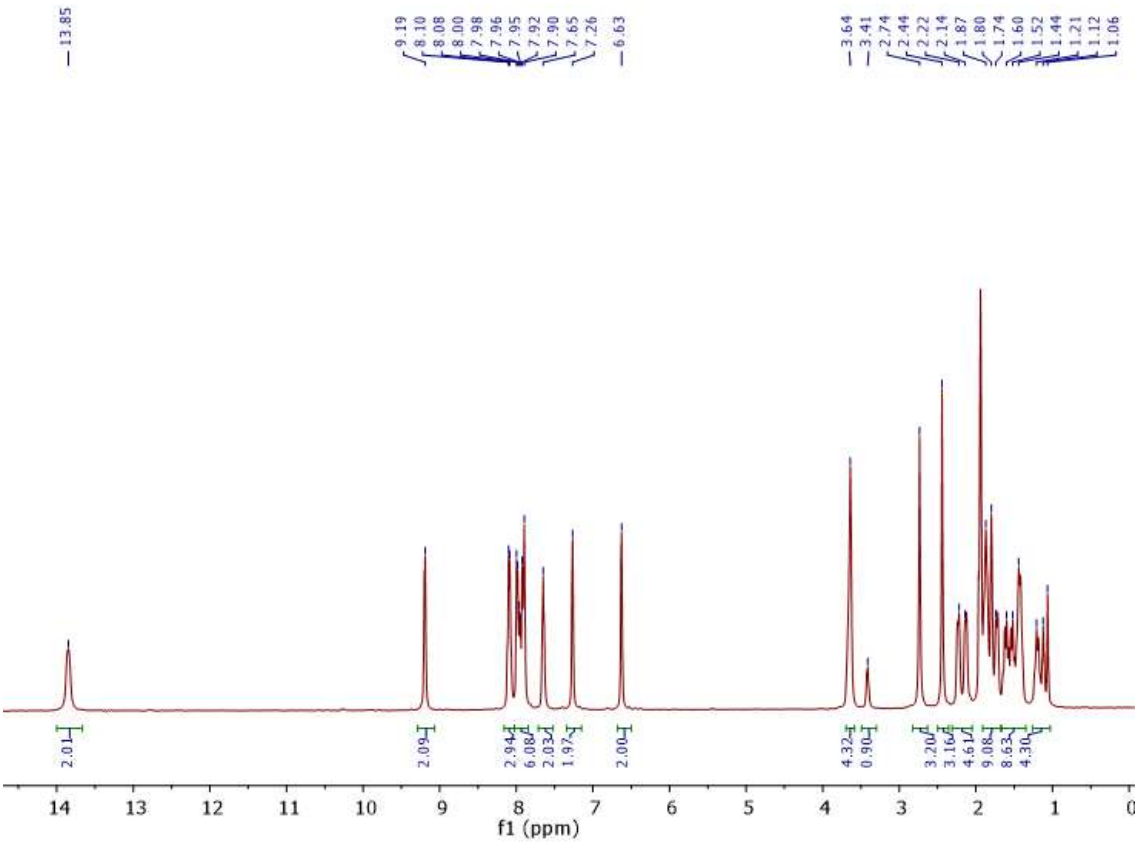

Figure 3.15 ^{1}H NMR of complex **4** in MeCN-d_3 (20°C).

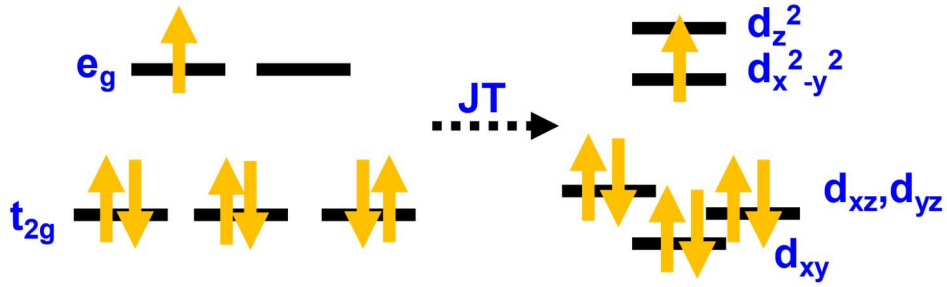

Scheme 3.1 Valence d-orbital manifold estimated for complex **2-LS** based on EPR Fig. 3.5D, where there is distortion from the perfect O_h crystal field by axial contraction (evidenced by g_x,g_y > g_z) and additional Jahn-Teller (JT) distortion to give a rhombic EPR spectrum.

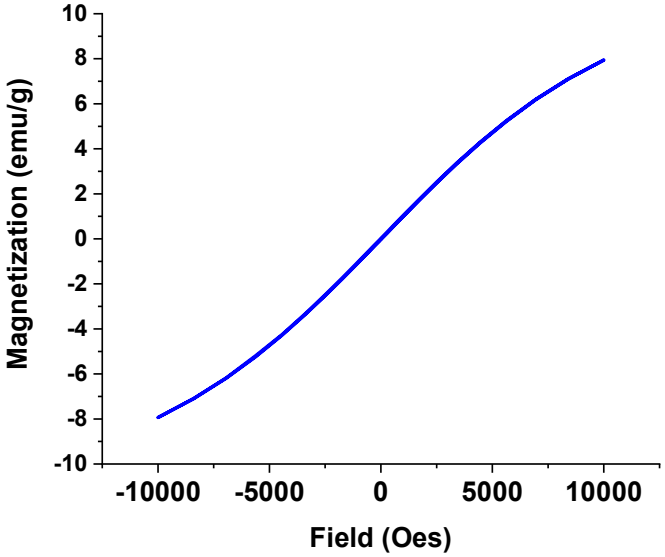

Figure 3.16 Magnetic hysteresis of complex **1** at 2K, with sweep rate 50 Oes/s.

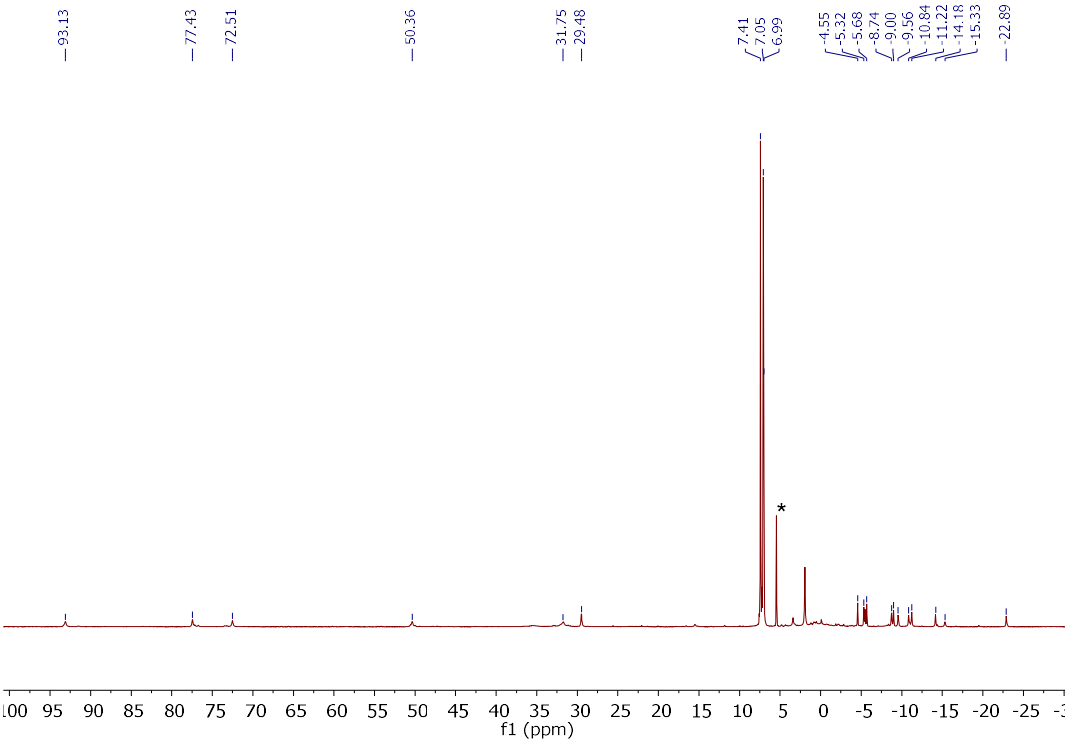

Figure 3.17 ^{1}H NMR spectrum of complex **5** in MeCN-d_3 (20°C); *DCM solvent from work-up.

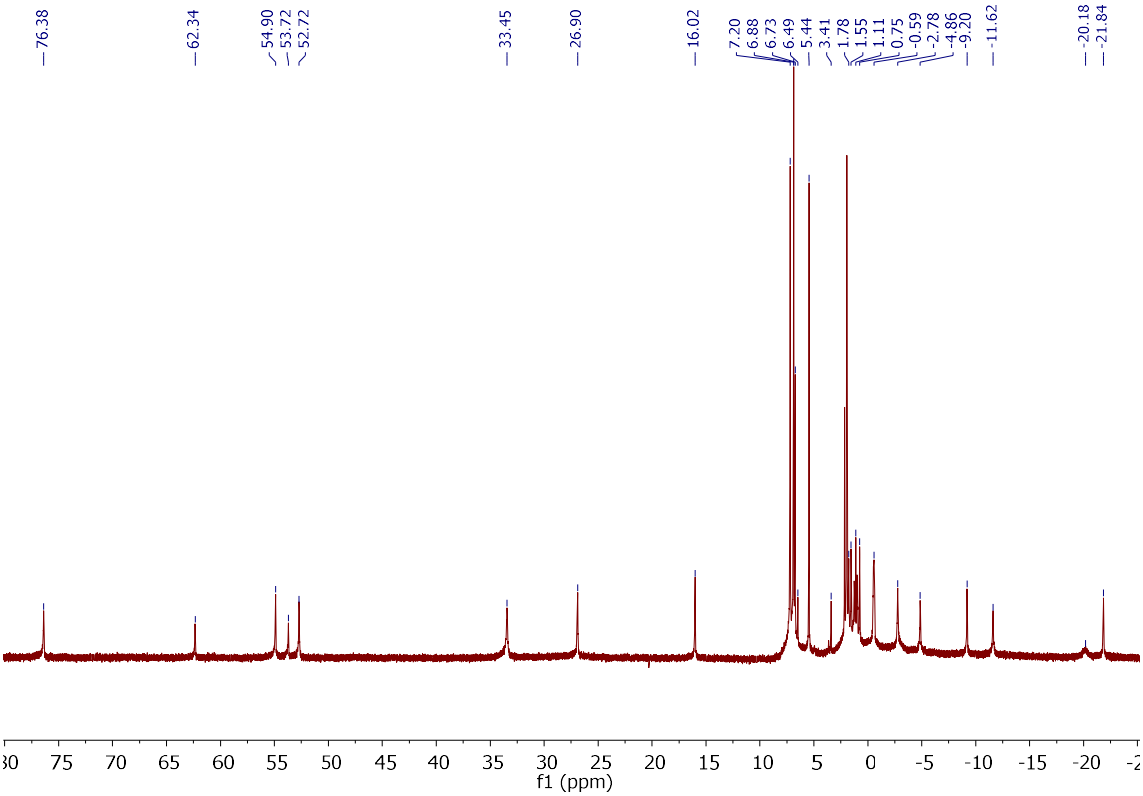

Figure 3.18 ^{1}H NMR spectrum of complex **6** in MeCN-d_3 (21°C).

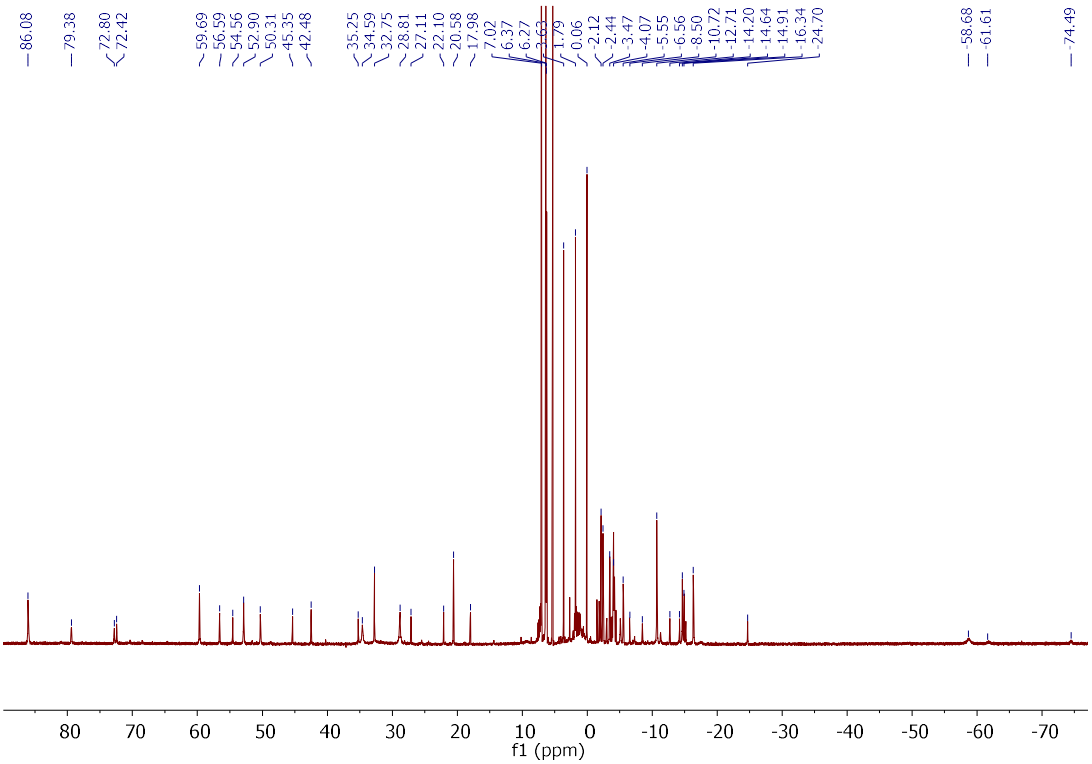

Figure 3.19 ^{1}H NMR spectrum of complex **7** in DCM-d_2 (21°C).

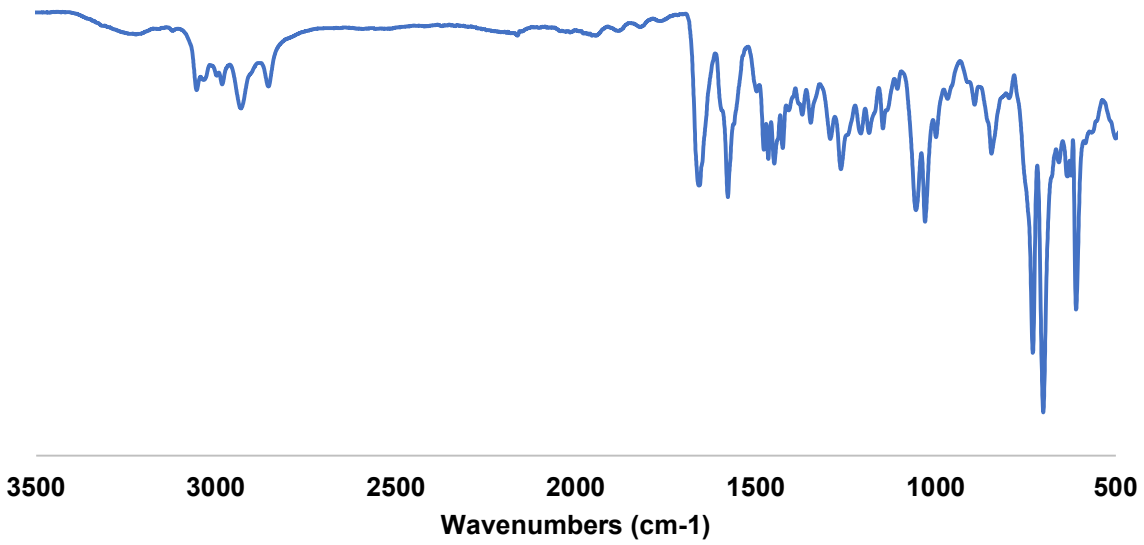

Figure 3.20 FT-IR of complex **5.**

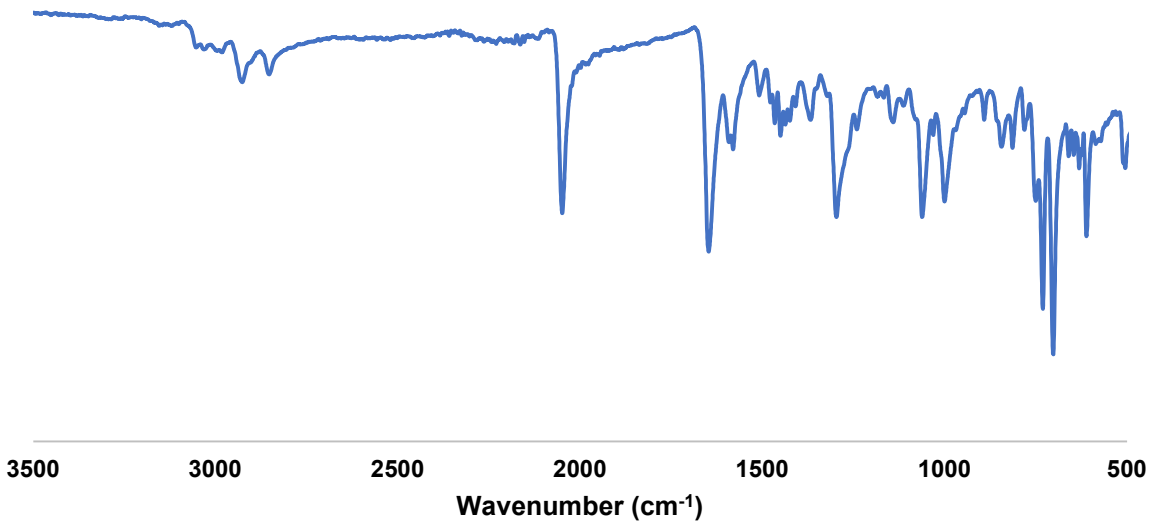

Figure 3.21 FT-IR of complex **6.**

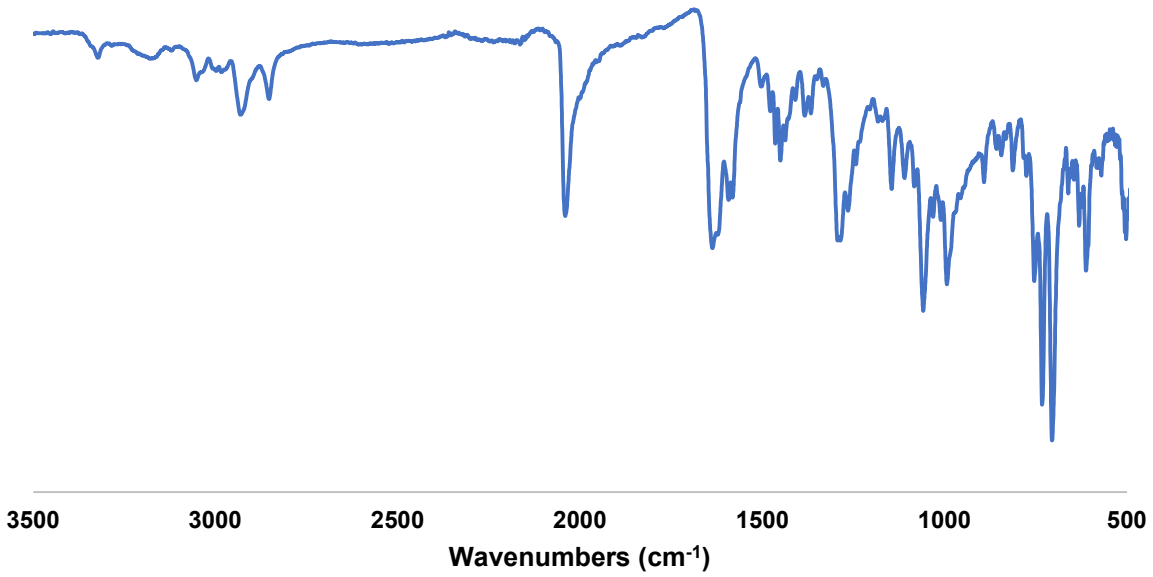

Figure 3.22 FT-IR of complex **7.**

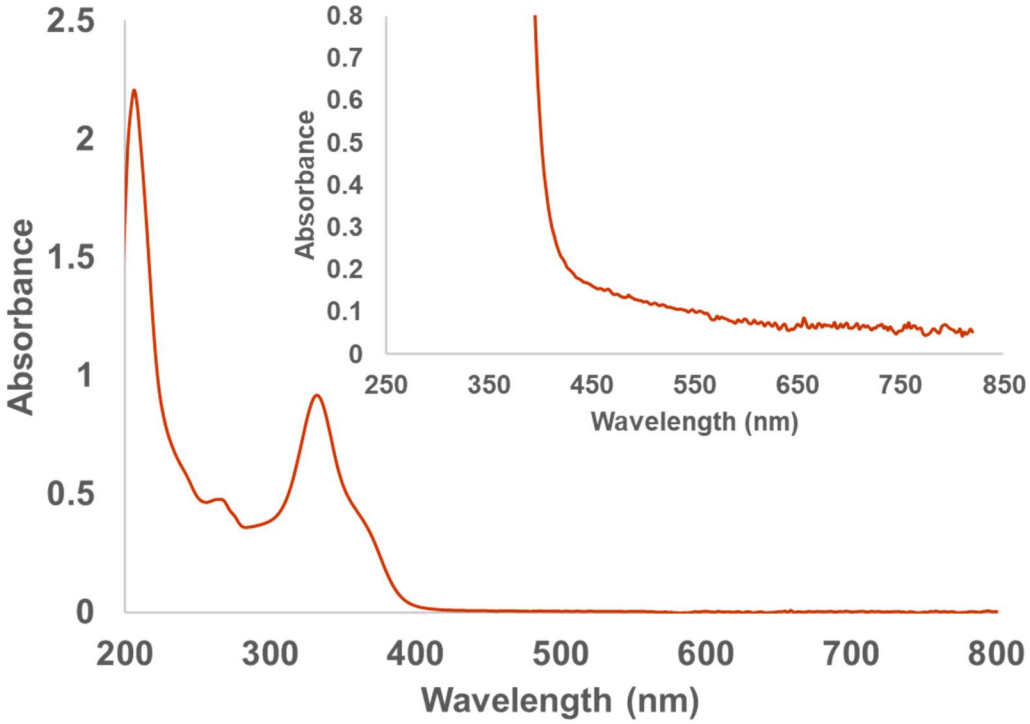

Figure 3.23 UV-Vis spectra of complex **6** in MeCN (0.02 mM, inset 0.5 mM).

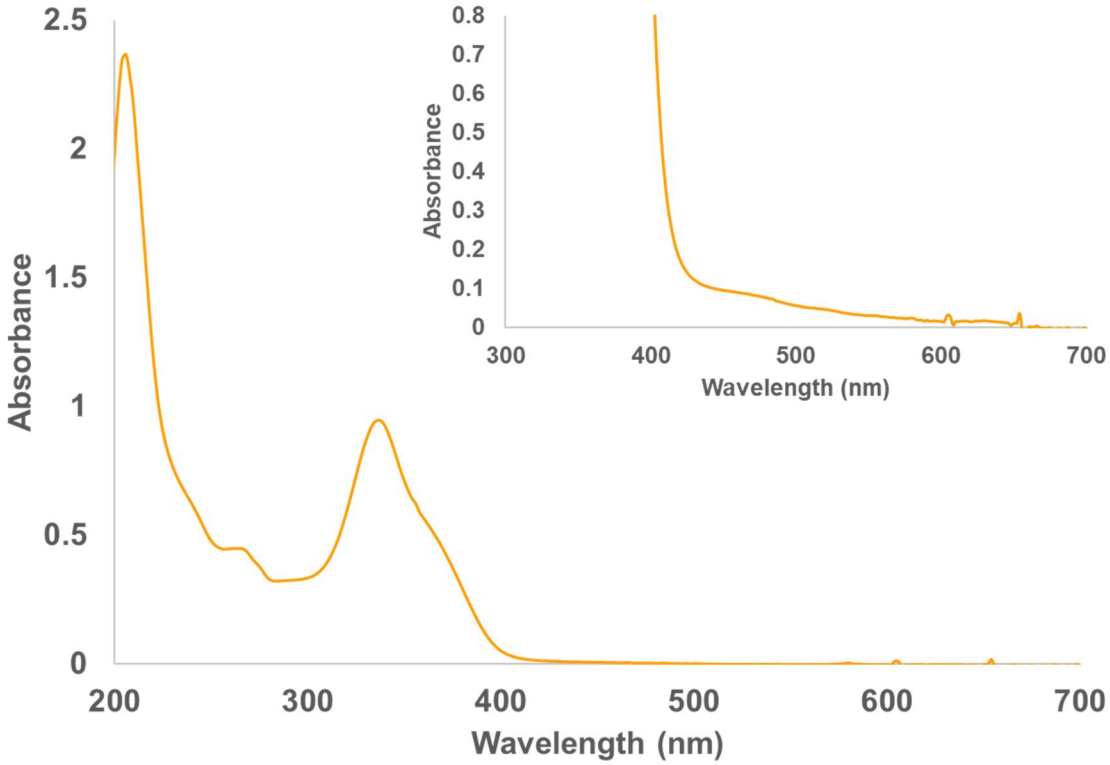

Figure 3.24 UV-Vis spectra of complex **7** in MeCN (0.02 mM, inset 0.5 mM).

Table 3.2 Selected structural parameters & IR stretches of complexes **6** & **7.**

	6 (N_3)	**7 (NCS)**
Co-N8 (Å)	2.112(6)	2.085(4)
Co-N3 (Å)	2.169(6)	2.194(4)
Co-$N_{afa,4}$ (Å)	2.135(5)	2.171(4)
Co-$N_{afa,6}$ (Å)	2.146(5)	2.115(4)
Co-$py_{(1/2)}$ (Å, avg)	2.161(6)	2.167(8)
N=X=X (Å)	1.213(8) (N8-N9) 1.144(9) (N9-N10)	1.164(6) (N8-C41) 1.619(5) (C41-S1)
N_{afa}(H)···N8 (Å, avg)	2.834(8)	3.001(2)
$\nu_{C=N}$ (cm^{-1})	1648	1661
$\nu_{N=[N=N,\ 6/C=S,\ 7]}$ (cm^{-1})	2049	2041

Table 3.3 Crystallographic parameters for complexes **6** & **7**.

	[($Py_2Py(afa^{Cy})_2$)$Co^{II}N_3$]BPh_4 (6)	**[($Py_2Py(afa^{Cy})_2$)Co^{II}NCS]BPh_4 (7)**
Empirical formula	$C_{65}H_{67}BCoN_{10}$	$C_{70}H_{77}BCoN_8OS$
Formula weight	1058.02	1148.19
Temperature (K)	100	99.99
Wavelength	MoKα (λ = 0.71073)	MoKα (λ = 0.71073)
Crystal system	Monoclinic	Triclinic
Space group	$P2_1/c$	P-1
a/Å	17.7128(9)	13.7706(3)
b/Å	20.5461(10)	13.9744(3)
c/Å	19.6499(10)	19.1666(5)
α/°	90	104.9970(10)
β/°	93.675(2)	100.8220(10)
γ/°	90	102.1260(10)
Volume/$Å^3$	7136.5(6)	3366.80(14)
Z	4	2
Reflections collected	138560	132590
Independent reflections	13094 [R_{int} = 0.0446, R_{sigma} = 0.0201]	12351 [R_{int} = 0.0609, R_{sigma} = 0.0280]
Data/restraints/parameters	13094/0/696	12351/36/827
Goodness-of-fit on F^2	1.147	1.029
Final R indexes [I≥2σ (I)]	R_1 = 0.0673, wR_2 = 0.1817	R_1 = 0.0419, wR_2 = 0.0937
Final R indexes [all data]	R_1 = 0.0732, wR_2 = 0.1853	R_1 = 0.0528, wR_2 = 0.0989

3.9 References

(1) Denisov, I. G.; Makris, T. M.; Sligar, S. G.; Schlichting, I. Structure and Chemistry of Cytochrome P450. *Chem. Rev.* **2005**, *105* (6), 2253–2277.

(2) Fontecave, M.; Pierre, J. L. Oxidations by Copper Metalloenzymes and Some Biomimetic Approaches. *Coord. Chem. Rev.* **1998**, *170* (1), 125–140.

(3) Shook, R. L.; Borovik, A. S. Role of the Secondary Coordination Sphere in Metal-Mediated Dioxygen Activation. *Inorg. Chem.* **2010**, *49* (8), 3646–3660.

(4) Hohenberger, J.; Ray, K.; Meyer, K. The Biology and Chemistry of High-Valent Iron–Oxo and Iron–Nitrido Complexes. *Nat. Commun.* **2012**, *3* (1), 720.

(5) Solomon, E. I.; Goudarzi, S.; Sutherlin, K. D. O2 Activation by Non-Heme Iron Enzymes. *Biochemistry* **2016**, *55* (46), 6363–6374.

(6) Reed, C. J.; Lam, Q. N.; Mirts, E. N.; Lu, Y. Molecular Understanding of Heteronuclear Active Sites in Heme-Copper Oxidases, Nitric Oxide Reductases, and Sulfite Reductases

through Biomimetic Modelling. *Chem. Soc. Rev.* **2021**, *50* (4), 2486–2539.

(7) Zhang, X. P.; Chandra, A.; Lee, Y. M.; Cao, R.; Ray, K.; Nam, W. Transition Metal-Mediated O-O Bond Formation and Activation in Chemistry and Biology. *Chem. Soc. Rev.* **2021**, *50* (8), 4804–4811.

(8) Hong, S.; Lee, Y.-M.; Ray, K.; Nam, W. Dioxygen Activation Chemistry by Synthetic Mononuclear Nonheme Iron, Copper and Chromium Complexes. *Coord. Chem. Rev.* **2017**, *334*, 25–42.

(9) Gunay, A.; Theopold, K. H. C-H Bond Activations by Metal Oxo Compounds. *Chem. Rev.* **2010**, *110* (2), 1060–1081.

(10) Ray, K.; Pfaff, F. F.; Wang, B.; Nam, W. Status of Reactive Non-Heme Metal-Oxygen Intermediates in Chemical and Enzymatic Reactions. *J. Am. Chem. Soc.* **2014**, *136* (40), 13942–13958.

(11) Bediako, D. K.; Solis, B. H.; Dogutan, D. K.; Roubelakis, M. M.; Maher, A. G.; Lee, C. H.; Chambers, M. B.; Hammes-Schiffer, S.; Nocera, D. G. Role of Pendant Proton Relays and Proton-Coupled Electron Transfer on the Hydrogen Evolution Reaction by Nickel Hangman Porphyrins. *Proc. Natl. Acad. Sci. U. S. A.* **2014**, *111* (42), 15001–15006.

(12) Shook, R. L.; Peterson, S. M.; Greaves, J.; Moore, C.; Rheingold, A. L.; Borovik, A. S. Catalytic Reduction of Dioxygen to Water with a Monomeric Manganese Complex at Room Temperature. *J. Am. Chem. Soc.* **2011**, *133* (15), 5810–5817.

(13) Rosenthal, J.; Chng, L. L.; Fried, S. D.; Nocera, D. G. Stereochemical Control of H2O2 Dismutation by Hangman Porphyrins. *Chem. Commun.* **2007**, No. 25, 2642.

(14) Zeini Jahromi, E.; Gailer, J. Probing Bioinorganic Chemistry Processes in the Bloodstream to Gain New Insights into the Origin of Human Diseases. *Dalt. Trans.* **2010**, *39* (2), 329–336.

(15) Mirica, L. M.; Ottenwaelder, X.; Stack, T. D. P. Structure and Spectroscopy of Copper-Dioxygen Complexes. *Chem. Rev.* **2004**, *104* (2), 1013–1045.

(16) Lewis, E. A.; Tolman, W. B. Reactivity of Dioxygen-Copper Systems. *Chem. Rev.* **2004**, *104* (2), 1047–1076.

(17) Costas, M.; Mehn, M. P.; Jensen, M. P.; Que, L. Dioxygen Activation at Mononuclear Nonheme Iron Active Sites: Enzymes, Models, and Intermediates. *Chem. Rev.* **2004**, *104* (2), 939–986.

(18) Lee, J. L.; Ross, D. L.; Barman, S. K.; Ziller, J. W.; Borovik, A. S. C-H Bond Cleavage by Bioinspired Nonheme Metal Complexes. *Inorg. Chem.* **2021**, *60* (18), 13759–13783.

(19) Chng, L. L.; Chang, C. J.; Nocera, D. G. Catalytic O-O Activation Chemistry Mediated by Iron Hangman Porphyrins with a Wide Range of Proton-Donating Abilities. *Org. Lett.* **2003**, *5* (14), 2421–2424.

(20) Rohde, J.-U.; In, J.-H.; Lim, M. H.; Brennessel, W. W.; Bukowski, M. R.; Stubna, A.; Münck, E.; Nam, W.; Que, L. Crystallographic and Spectroscopic Characterization of a

Nonheme Fe(IV)=O Complex. *Science (80-.).* **2003**, *299* (5609), 1037–1039.

(21) MacBeth, C. E.; Golombek, A. P.; Young, V. G.; Yang, C.; Kuczera, K.; Hendrich, M. P.; Borovik, A. S. O 2 Activation by Nonheme Iron Complexes: A Monomeric Fe(III)-Oxo Complex Derived From O 2. *Science (80-.).* **2000**, *289* (5481), 938–941.

(22) Vallee, W. M. B. L. Cobalt as Probe and Label of Proteins. *Methods Enzymol.* **1993**, *226* (C), 52–71.

(23) Fiedler, A. T.; Fischer, A. A. Oxygen Activation by Mononuclear Mn, Co, and Ni Centers in Biology and Synthetic Complexes. *J. Biol. Inorg. Chem.* **2017**, *22* (2–3), 407–424.

(24) Fielding, A. J.; Lipscomb, J. D.; Que, L. Characterization of an O 2 Adduct of an Active Cobalt-Substituted Extradiol-Cleaving Catechol Dioxygenase. *J. Am. Chem. Soc.* **2012**, *134* (2), 796–799.

(25) Emerson, J. P.; Kovaleva, E. G.; Farquhar, E. R.; Lipscomb, J. D.; Que, L. Swapping Metals in Fe- and Mn-Dependent Dioxygenases: Evidence for Oxygen Activation without a Change in Metal Redox State. *Proc. Natl. Acad. Sci. U. S. A.* **2008**, *105* (21), 7347–7352.

(26) Rice, D. B.; Massie, A. A.; Jackson, T. A. Manganese-Oxygen Intermediates in O-O Bond Activation and Hydrogen-Atom Transfer Reactions. *Acc. Chem. Res.* **2017**, *50* (11), 2706–2717.

(27) Bennett, B. EPR of Cobalt-Substituted Zinc Enzymes. In *Metals in Biology. Biological Magnetic Resonance*; Hanson, G., Berliner, L., Eds.; Springer US: New York, NY, 2010; Vol. 29, pp 345–370.

(28) Kobayashi, M.; Shimizu, S. Cobalt Proteins. *Eur. J. Biochem.* **1999**, *261* (1), 1–9.

(29) Corona, T.; Padamati, S. K.; Acuña-Parés, F.; Duboc, C.; Browne, W. R.; Company, A. Trapping of Superoxido Cobalt and Peroxido Dicobalt Species Formed Reversibly from CoII and O2. *Chem. Commun.* **2017**, *53* (86), 11782–11785.

(30) Busch, D. H.; Alcock, N. W. Iron and Cobalt "Lacunar" Complexes as Dioxygen Carriers. *Chem. Rev.* **1994**, *94* (3), 585–623.

(31) Kim, D.; Cho, J.; Lee, Y. M.; Sarangi, R.; Nam, W. Synthesis, Characterization, and Reactivity of Cobalt(III)-Oxygen Complexes Bearing a Macrocyclic N-Tetramethylated Cyclam Ligand. *Chem. - A Eur. J.* **2013**, *19* (42), 14112–14118.

(32) Martell, A. E.; Motekaitis, R. J. Binding and Activation of Molecular Oxygen Within the Cavity of the Dinuclear Cobalt Bisdien Macrocyclic Complex; Reactions with Bridging Coordinated Bifunctional Reducing Substrates. In *Studies in Surface Science and Catalysis*; 1991; Vol. 66, pp 331–336.

(33) Wang, C. C.; Chang, H. C.; Lai, Y. C.; Fang, H.; Li, C. C.; Hsu, H. K.; Li, Z. Y.; Lin, T. S.; Kuo, T. S.; Neese, F.; Ye, S.; Chiang, Y. W.; Tsai, M. L.; Liaw, W. F.; Lee, W. Z. A Structurally Characterized Nonheme Cobalt-Hydroperoxo Complex Derived from Its Superoxo Intermediate via Hydrogen Atom Abstraction. *J. Am. Chem. Soc.* **2016**, *138* (43), 14186–14189.

(34) Reinaud, O. M.; Theopold, K. H. Hydrogen Tunneling in the Activation of Dioxygen by a Tris(Pyrazolyl)Borate Cobalt Complex. *J. Am. Chem. Soc.* **1994**, *116* (15), 6979–6980.

(35) Theopold, K. H.; Reinaud, O. M.; Doren, D.; Konecny, R. Dioxygen Activation with Sterically Hindered Tris(Pyrazolyl)Borate Cobalt Complexes. *Stud. Surf. Sci. Catal.* **1997**, *110* (1), 1081–1088.

(36) Reinaud, O. M.; Yap, G. P. A.; Rheingold, A. L.; Theopold, K. H. Novel Binuclear Cobalt Dioxygen Complex—A Step on the Path to Dioxygen Activation. *Angew. Chemie Int. Ed. English* **1995**, *34* (18), 2051–2052.

(37) Hu, X.; Castro-Rodriguez, I.; Meyer, K. Dioxygen Activation by a Low-Valent Cobalt Complex Employing a Flexible Tripodal N-Heterocyclic Carbene Ligand. *J. Am. Chem. Soc.* **2004**, *126* (41), 13464–13473.

(38) Ramdhanie, B.; Telser, J.; Caneschi, A.; Zakharov, L. N.; Rheingold, A. L.; Goldberg, D. P. An Example of O2 Binding in a Cobalt(II) Corrole System and High-Valent Cobalt-Cyano and Cobalt-Alkynyl Complexes. *J. Am. Chem. Soc.* **2004**, *126* (8), 2515–2525.

(39) Goetz, M. K.; Hill, E. A.; Filatov, A. S.; Anderson, J. S. Isolation of a Terminal Co(III)-Oxo Complex. *J. Am. Chem. Soc.* **2018**, *140* (41), 13176–13180.

(40) Goetz, M. K.; Anderson, J. S. Experimental Evidence for p Ka-Driven Asynchronicity in C-H Activation by a Terminal Co(III)-Oxo Complex. *J. Am. Chem. Soc.* **2019**, *141* (9), 4051–4062.

(41) Goetz, M. K.; Schneider, J. E.; Filatov, A. S.; Jesse, K. A.; Anderson, J. S. Enzyme-Like Hydroxylation of Aliphatic C-H Bonds from an Isolable Co-Oxo Complex. *J. Am. Chem. Soc.* **2021**, *143* (49), 20849–20862.

(42) Nguyen, A. I.; Hadt, R. G.; Solomon, E. I.; Tilley, T. D. Efficient C-H Bond Activations via O2 Cleavage by a Dianionic Cobalt(Ii) Complex. *Chem. Sci.* **2014**, *5* (7), 2874–2878.

(43) Malik, D. D.; Chandra, A.; Seo, M. S.; Lee, Y. M.; Farquhar, E. R.; Mebs, S.; Dau, H.; Ray, K.; Nam, W. Formation of Cobalt-Oxygen Intermediates by Dioxygen Activation at a Mononuclear Nonheme Cobalt(Ii) Center. *Dalt. Trans.* **2021**, *50* (34), 11889–11898.

(44) Hikichi, S.; Komatsuzaki, H.; Akita, M.; Moro-oka, Y. Aliphatic C-H Bond Oxygenation by the Co(II)OOX Species with the Hindered Hydrotris(Pyrazolyl)Borate Ligand (X = Co(II), Alkyl, H). *J. Am. Chem. Soc.* **1998**, *120* (19), 4699–4710.

(45) Lucas, R. L.; Zart, M. K.; Mukherjee, J.; Sorrell, T. N.; Powell, D. R.; Borovik, A. S. A Modular Approach toward Regulating the Secondary Coordination Sphere of Metal Ions: Differential Dioxygen Activation Assisted by Intramolecular Hydrogen Bonds. *J. Am. Chem. Soc.* **2006**, *128*, 15476–15489.

(46) Jones, J. R.; Ziller, J. W.; Borovik, A. S. Modulating the Primary and Secondary Coordination Spheres within a Series of CoII-OH Complexes. *Inorg. Chem.* **2017**, *56* (3), 1112–1120.

(47) Wallen, C. M.; Palatinus, L.; Bacsa, J.; Scarborough, C. C. Hydrogen Peroxide Coordination to Cobalt(II) Facilitated by Second-Sphere Hydrogen Bonding. *Angew.*

Chemie - Int. Ed. **2016**, *55* (39), 11902–11906.

(48) Matson, E. M.; Park, Y. J.; Bertke, J. a.; Fout, A. R. Synthesis and Characterization of M(II) (M = Mn, Fe and Co) Azafulvene Complexes and Their X_3^- Derivatives. *Dalt. Trans.* **2015**, *44* (22), 10377–10384.

(49) Drummond, M. J.; Ford, C. L.; Gray, D. L.; Popescu, C. V; Fout, A. R. Radical Rebound Hydroxylation Versus H-Atom Transfer in Non-Heme Iron(III)-Hydroxo Complexes: Reactivity and Structural Differentiation. *J. Am. Chem. Soc.* **2019**, *141* (Iii), 6639–6650.

(50) Drummond, M. Bio-Inspired Iron and Cobalt Complexes Featuring a Secondary Coordination Sphere: Ligand Design, Complexation, and Modeling of Enzymatic Processes, University of Illinois at Urbana-Champaign, 2019.

(51) Atanasov, M.; Aravena, D.; Suturina, E.; Bill, E.; Maganas, D.; Neese, F. First Principles Approach to the Electronic Structure, Magnetic Anisotropy and Spin Relaxation in Mononuclear 3d-Transition Metal Single Molecule Magnets. *Coord. Chem. Rev.* **2015**, *289–290* (1), 177–214.

(52) Kazin, P. E.; Zykin, M. A.; Trusov, L. A.; Eliseev, A. A.; Magdysyuk, O. V.; Dinnebier, R. E.; Kremer, R. K.; Felser, C.; Jansen, M. A Co-Based Single-Molecule Magnet Confined in a Barium Phosphate Apatite Matrix with a High Energy Barrier for Magnetization Relaxation. *Chem. Commun.* **2017**, *53* (39), 5416–5419.

(53) Bunting, P. C.; Atanasov, M.; Damgaard-Møller, E.; Perfetti, M.; Crassee, I.; Orlita, M.; Overgaard, J.; Van Slageren, J.; Neese, F.; Long, J. R. A Linear Cobalt(II) Complex with Maximal Orbital Angular Momentum from a Non-Aufbau Ground State. *Science (80-.).* **2018**, *362* (6421), 1–41.

(54) Yersin, H. *Highly Efficient OLEDs with Phosphorescent Materials*, 1st ed.; WILEY-VCH Verlag GmbH & Co. KGaA, 2008.

(55) Ueyama, N.; Nishikawa, N.; Yamada, Y.; Okamura, T. A.; Nakamura, A. Cytochrome P-450 Model (Porphinato)(Thiolato)Iron(III) Complexes with Single and Double NH···S Hydrogen Bonds at the Thiolate Site. *J. Am. Chem. Soc.* **1996**, *118* (50), 12826–12827.

(56) Vidakovic, M.; Sligar, S. G.; Li, H.; Poulos, T. L. Understanding the Role of the Essential Asp251 in Cytochrome P450cam Using Site-Directed Mutagenesis, Crystallography, and Kinetic Solvent Isotope Effect. *Biochemistry* **1998**, *37* (26), 9211–9219.

(57) Suzuki, N.; Higuchi, T.; Urano, Y.; Kikuchi, K.; Uekusa, H.; Ohashi, Y.; Uchida, T.; Kitagawa, T.; Nagano, T. Novel Iron Porphyrin−Alkanethiolate Complex with Intramolecular NH···S Hydrogen Bond: Synthesis, Spectroscopy, and Reactivity. *J. Am. Chem. Soc.* **1999**, *121* (49), 11571–11572.

(58) Ueyama, N.; Nishikawa, N.; Yamada, Y.; Okamura, T. A.; Oka, S.; Sakurai, H.; Nakamura, A. Synthesis and Properties of Octaethylporphinato(Arenethiolato)Iron(III) Complexes with Intramolecular NH···S Hydrogen Bond: Chemical Function of the Hydrogen Bond. *Inorg. Chem.* **1998**, *37* (10), 2415–2421.

(59) Leahy, C. A.; Drummond, M. J.; Vura-Weis, J.; Fout, A. R. Synthesis of a Series of M(Ii) (M = Mn, Fe, Co) Chloride Complexes with Both Inter- And Intra-Ligand Hydrogen

Bonding Interactions. *Dalt. Trans.* **2021**, *50* (35), 12088–12092.

(60) Marts, A. R.; Greer, S. M.; Whitehead, D. R.; Woodruff, T. M.; Breece, R. M.; Shim, S. W.; Oseback, S. N.; Papish, E. T.; Jacobsen, F. E.; Cohen, S. M.; Tierney, D. L. Dual Mode EPR Studies of a Kramers Ion: High-Spin Co(II) in 4-, 5- and 6-Coordination. *Appl. Magn. Reson.* **2011**, *40* (4), 501–511.

(61) Bennett, B. EPR of Co(II) as a Structural and Mechanistic Probe of Metalloprotein Active Sites: A Review of Studies on Aminopeptidase. *Curr. Top. Biophys.* **2002**, *26* (1), 49–57.

(62) Drummond, M. J.; Ford, C. L.; Gray, D. L.; Popescu, C. V.; Fout, A. R. Radical Rebound Hydroxylation Versus H-Atom Transfer in Non-Heme Iron(III)-Hydroxo Complexes: Reactivity and Structural Differentiation. *J. Am. Chem. Soc.* **2019**, *141* (16), 6639–6650.

(63) Matson, E.; Park, Y.; Fout, A. Facile Nitrite Reduction in a Non-Heme Iron System: Formation of an Iron (III)-Oxo. *J. Am. Chem. Soc.* **2014**, *136* (Iii), 17398.

(64) Gordon, Z.; Drummond, M. J.; Matson, E. M.; Bogart, J. A.; Schelter, E. J.; Lord, R. L.; Fout, A. R. Tuning the Fe(II/III) Redox Potential in Nonheme Fe(II)–Hydroxo Complexes through Primary and Secondary Coordination Sphere Modifications. *Inorg. Chem.* **2017**, *56* (9), 4852–4863.

(65) Gupta, R.; Borovik, A. S. Monomeric MnIII/II and FeIII/II Complexes with Terminal Hydroxo and Oxo Ligands: Probing Reactivity via O-H Bond Dissociation Energies. *J. Am. Chem. Soc.* **2003**, *125* (43), 13234–13242.

(66) Zhang, K.; Lin, M. F.; Ryland, E. S.; Verkamp, M. A.; Benke, K.; De Groot, F. M. F.; Girolami, G. S.; Vura-Weis, J. Shrinking the Synchrotron: Tabletop Extreme Ultraviolet Absorption of Transition-Metal Complexes. *J. Phys. Chem. Lett.* **2016**, *7* (17), 3383–3387.

(67) Macmillan, S. N.; Lancaster, K. M. X-Ray Spectroscopic Interrogation of Transition-Metal-Mediated Homogeneous Catalysis: Primer and Case Studies. *ACS Catal.* **2017**, *7* (3), 1776–1791.

(68) Kowalska, J. K.; Lima, F. A.; Pollock, C. J.; Rees, J. A.; DeBeer, S. A Practical Guide to High-Resolution X-Ray Spectroscopic Measurements and Their Applications in Bioinorganic Chemistry. *Isr. J. Chem.* **2016**, *56* (9–10), 803–815.

(69) Zhang, K.; Ash, R.; Girolami, G. S.; Vura-Weis, J. Tracking the Metal-Centered Triplet in Photoinduced Spin Crossover of Fe(Phen)32+ with Tabletop Femtosecond M-Edge X-Ray Absorption Near-Edge Structure Spectroscopy. *J. Am. Chem. Soc.* **2019**, *141* (43), 17180–17188.

(70) Ash, R.; Zhang, K.; Vura-Weis, J. Photoinduced Valence Tautomerism of a Cobalt-Dioxolene Complex Revealed with Femtosecond M-Edge XANES. *J. Chem. Phys.* **2019**, *151* (10), 104201.

(71) Comba, P.; Nunn, G.; Scherz, F.; Walton, P. H. Intermediate-Spin Iron(Iv)-Oxido Species with Record Reactivity. *Faraday Discuss.* **2022**, *234*, 232–244.

Chapter 4: Electronic structure characterization of trigonal bipyramidal late first row transition metal complexes using soft X-ray absorption spectroscopy

4.1 Bio-inspired C_3-symmetric First Row Transition Metal Species

Metalloenzymes in nature are used to perform challenging multi-electron transformations of small molecules. Examples of these are oxidation,[1–4] halogenation,[5–7] and oxyanion reduction.[8,9] Key intermediates proposed for these transformations are high-valent metal-oxygen (-oxo or -hydroxo) species, typically featuring a first-row transition metal such as iron, manganese, or cobalt.[2] Investigations of the active metal center in metalloenzymes have shown that primary and secondary sphere interactions are crucial for achieving these species.[10,11] The primary sphere interactions directly impact electronic structure and reactivity of the metal center, while secondary sphere interactions such as hydrogen-bonding (H-bonding) networks influence substrate selectivity, intermediate metal-oxo stability, and the redox potential of the metal center.

There has been immense interest in modeling the reactivity and structure of the intermediate metal-oxygen species involved in these transformations. Synthetic systems[12–20] with C_3-symmetric ligands have been developed that incorporate key primary and secondary structural motifs from metalloenzyme active sites towards accessing the metal-oxygen (M-O) species. These complexes allow for developing and modulating the metal-ligand structure, isolation of proposed M-O intermediates, and understanding of spectroscopic signatures from enzymatic systems. These improve understanding of the biological processes and aid in developing better synthetic systems for achieving desirable small molecule transformations.

The Fout group has developed ligand systems (Figure 4.1) that have secondary sphere H-bonding, analogous to enzymatic systems with extensive H-bonding networks. The tripodal ligand

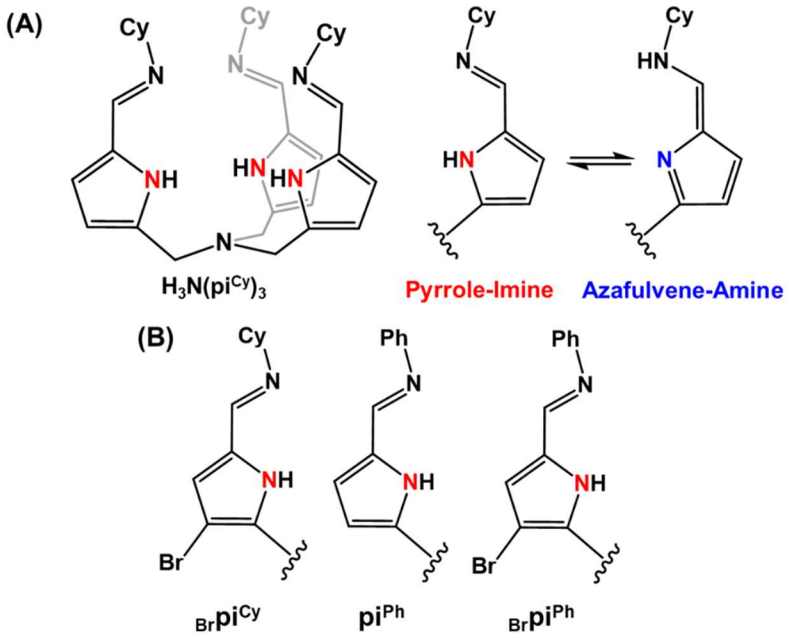

Figure 4.1 (A) Tripodal ligand scaffold $H_3N(pi^{Cy})_3$ with tautomeric arms; (B) backbone ligand modifications at either the capping group or at the 3-position on the pyrrole.

$H_3[N(pi^{Cy})_3]$ has three ligand arms capable of H-bonding to an axially bound substrate to the metal center.[12] The arms of the ligand are capable of tautomerizing from the pyrrole-imine (pi) form to the azafulvene-amine (afa) form (Figure 4.1A). These ligands can coordinate various first-row transition metal complexes, and these have been found to form metal-oxo[21] and -hydroxo species that are of interest towards mimicking the structure and activities of the enzymatic metal centers, particularly with dioxygen activation and biomimetic reduction of oxyanions such as perchlorate and nitrate.[12,19,20,22–26]

While the reactivity for these tripodal complexes is well-explored, what's less well known is their detailed electronic structure and its impact on their observed reactivity. This work sought to characterize the metal electronic structure of the metal-oxygen tripodal complexes from the Fout group at the metal centers directly towards improving our understanding of their structure, reactivities and accessing high-valent metal-oxygen species. Data were collected on the tripodal metal-hydroxo and -oxo complexes (manganese, iron, and cobalt) using soft X-ray absorption

spectroscopy (XAS) at the respective $M_{2,3}$- and $L_{2,3}$-edges of the metal centers. This was used to examine the static electronic structure of the species and assisted in the identification of the electronic state of a bimetallic cobalt-manganese complex.

4.2 $M_{2,3}$- and $L_{2,3}$-edge XAS of trigonal bipyramidal iron system

Our initial interest was examining the impact of primary and secondary sphere ligand modifications on the electronic structure in the iron tripodal system. The tripodal ligand scaffold can be easily modified at two positions: the pyrrole 3-position and the amine R-group in the secondary coordination sphere (ligand arm variants shown in Fig. 4.1B). Bromination at the 3-position or altering the capping group of the amine from cyclohexyl to phenyl each result in a 200 mV positive shift in the Fe(II/III) reduction potential.[23] While it is challenging to separate out the effect of primary and secondary modifications, UV-Vis and computational calculations show that the phenyl group extends the π-system, allowing for further electron density delocalization and destabilization of the lowest unoccupied molecular orbital (LUMO), and causes its amino moieties to act as stronger hydrogen bond donors, tuning the donor strength of the bound hydroxo/oxo ligand and thus determining the electronics of the iron center. Similarly, in calculations examining the original (pi^{Cy}) and modified ligand arms ($_{Br}pi^{Cy}$ and pi^{Ph}), introduction of an electron-withdrawing group (EWG) at the 3-pyrrole position resulted in the stabilization of the highest-occupied molecular orbital (HOMO) and LUMO and only causing a minimal shift in energy for the π- π* transition, as observed in the experimental redox potentials and UV-Vis spectra.[23]

Towards probing the metal electronic structure directly, we examined the iron(III)-oxo complexes with the different ligand variants by $M_{2,3}$-edge x-ray absorption spectroscopy. The $M_{2,3}$-edge ($3p_{1/2,3/2} \rightarrow 3d$) XANES for 1st row transition metals is in the extreme ultraviolet (XUV) energy region (30-100 eV). The $M_{2,3}$-edge is element-, oxidation state-, spin state-, and ligand

field-specific, which provide useful information on the metal center and its chemical environment.[27] $M_{2,3}$-edge XANES has been used to examine the ground electronic states and femtosecond-to-nanosecond photochemical dynamics of various 1st row metal complexes such as iron porphyrins[28] and iron & cobalt spin-crossover complexes.[29–31]

Initial $M_{2,3}$-edge characterization focused on the iron tripodal system using the original $H_3[N(pi^{Cy})_3]$ ($_HL^{Cy}$) scaffold, comparing the iron(III)-oxo $[(N(afa^{Cy})_3)Fe^{III}O]OTf$ (**1**) to the iron(II)-hydroxo $(N(afa^{Cy})_2(pi^{Cy}))Fe^{II}OH$ (**2**) species. Samples of the iron(II)-hydroxide were prepared via spin-casting onto 100 nm Si_3N_4 substrate, while the iron(III)-oxo samples could be prepared similarly by spin-casting on Si_3N_4 substrate or through embedment in polystyrene film as described in prior work.[32] The $M_{2,3}$-edge spectra of complexes **1** and **2** are shown in Figure 4.2. The iron(III)-oxo **1** shows a single, broad peak at 57.5 eV, matching prior studies of high-spin iron(III) systems[28] and was expected based on prior spectroscopic characterization.[21] In comparison, the iron(II)-hydroxide rises in at lower energy (starting at ~53.5 eV) and has an two-

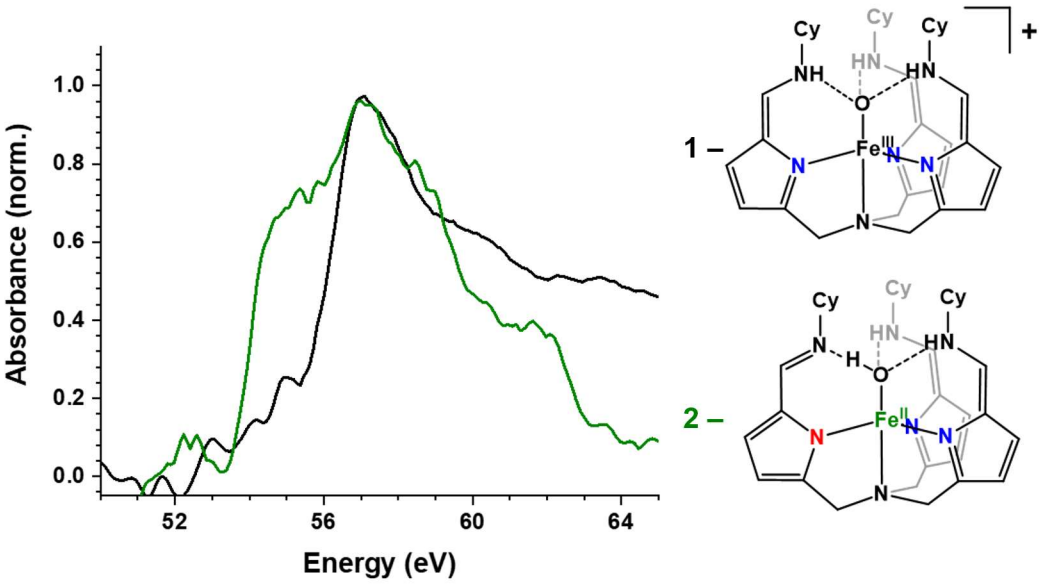

Figure 4.2 $M_{2,3}$-edge spectra of iron(III)-oxo complex **1** (black) and iron(II)-hydroxide complex **2** (green) in the unmodified ligand scaffold $N(pi^{Cy})_3$.

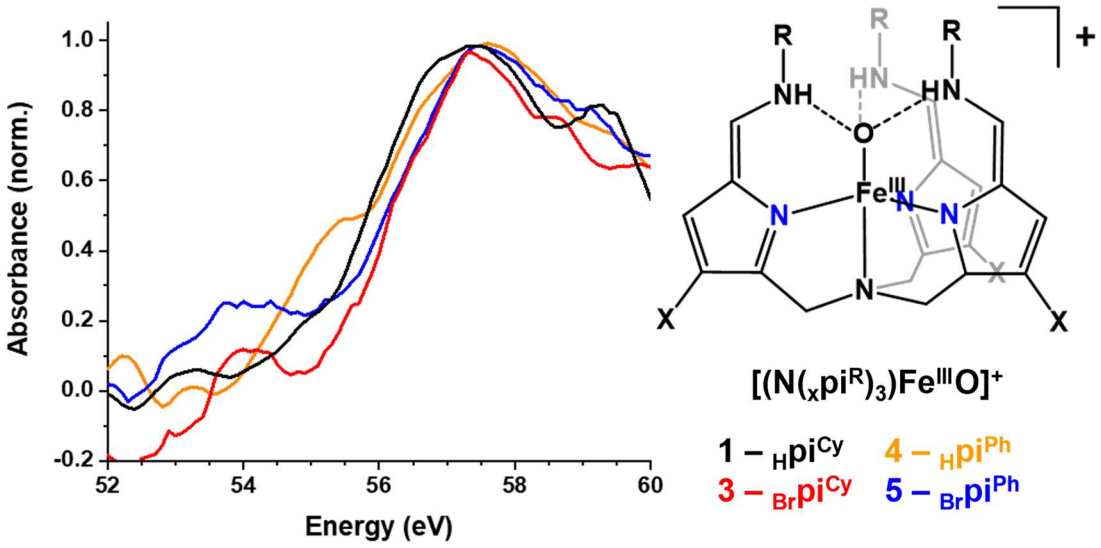

Figure 4.3 $M_{2,3}$-edge spectra of the iron(III)-oxo complexes in the tripodal ligand variants (**1**, black; **3**, red; **4**, orange; **5**, blue).

peak structure, with peak energies at 54.5 and 57.5 eV, as expected based on prior magnetic susceptibility characterization[12] and past work with high-spin Fe(II) systems,[29] indicative of the oxidation state decrease. However, the signal to noise ratio was low for complex **2** due to the anticipated lower intensity (given fewer available vacancies in the 3d orbital manifold). Challenges with developing homogeneous thin films of the iron(II)-hydroxides and low intensity signals realized that initial $M_{2,3}$-edge investigations of ligand modification effects at the iron center was used with the more amenable iron(III)-oxos.

$M_{2,3}$-edge spectra of the iron(III)-oxos **1** & **3-5** ([$(N(_{Br}afa^{Cy})_3)Fe^{III}O$]OTf – **3**, [$(N(afa^{Ph})_3)Fe^{III}O$]$BAr^F$ – **4**; [$(N(_{Br}afa^{Ph})_3)Fe^{III}O$] BAr^F – **5**) are shown in Figure 4.3. Samples were prepared by spincasting 1-3 drops of a filtered, concentrated solution of the target complex in dichloromethane onto a 100 nm Si_3N_4 substrate and confirmed by UV-Vis spectroscopy for sample identity. As seen in complex **1**, complexes **3-5** give a small pre-peak and single broad peak at higher energies, as expected for high-spin iron(III) centers. There is an increase in the pre-peak intensity in swap ping to the brominated ligand (**3** & **5**), and there is a minor blueshift (~0.2 eV)

of the main peak for the iron(III)-oxos for the modified ligand variants (**3-5**) in comparison to the iron(III)-oxo in the unmodified scaffold (**1**), corresponding to the expected energy increase from the calculated LUMO destabilization[23] in the iron 3d orbital manifold. These changes are relatively minor. It may be that the strength of the axial oxo-ligand dominates over ligand effects of the backbone ligand variants in the electronic structure of the iron(III)-oxo species, as in the tetrapodal system we observe distinct changes in the electronic structure that are primarily axial ligand-based from electronic characterization (see Chapter 3). Unpublished work in the Fout group has found that oxyanion reactivity with the iron(II)-bistriflate species of the ligand variants shows that the brominated ligand gives a more electrophilic iron center, which may make the metal center a better binder for oxyanion substrates to coordinate and thus improving reactivity; the increased pre-peak feature of the Fe $M_{2,3}$-edge and minor blueshift in the main edge in the brominated iron(III)-oxos **3** and **5** indicate this. Unpublished data investigating similar EWG modifications of iron(III) porphyrin species have also observed similar minor edge shifts with dramatic differences in photocatalysis. While there is a minor blueshift of the main peak energy in the phenyl group, it has been shown in more recent, unpublished work that the capping group of the tripodal ligand primarily affected reactivity through steric effects, as bulkier groups such as mesityl (Mes) and diisopropylphenyl (DIPP), not necessarily electronic effects. Identifying electronic effects from modifications of the primary and secondary coordination sphere of the iron tripodal ligand scaffold may be better observed with a weaker axial ligand such as a halide (e.g. Cl), though challenges with homogeneous thin film sample preparation precluded investigations of these species by $M_{2,3}$-edge XUV spectroscopy.

To better characterize the electronic structure of the iron system, soft XAS spectroscopy was performed at the iron $L_{2,3}$-edges. The L_2- and L_3-edges are the transitions from the $2p_{1/2}$ and

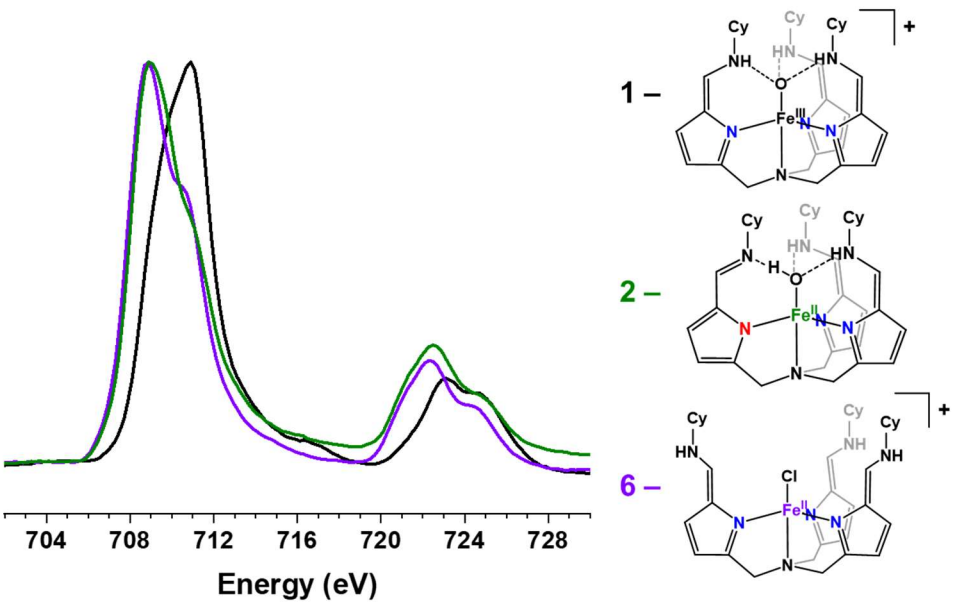

Figure 4.4 $L_{2,3}$-edge XAS spectra of the iron tripodal complexes **1** (Fe(III)-oxo, black), **2** (Fe(II)-hydroxide, green), and **6** (Fe(II)-chloride, purple).

$2p_{3/2}$ levels, respectively, to empty valence 3d orbitals. Complexity in these features arise from ligand field effects alongside 2p-3d and 3d-3d Coulomb and exchange interactions,[33] so can provide featureful spectra and insight into metal electronic states. $L_{2,3}$-edge spectra of select iron(II) or iron(III) species (Fig. 4.4) in the unmodified tripodal ligand scaffold showed only minor differences between the iron(II) chloride ([$(N(afa^{Cy})_3)Fe^{II}Cl$]OTf, **6**) and hydroxide (**2**) species. These minor differences likely arise from minor variations in ligand-metal orbital mixing, given the change in the axial ligand and variation of the ligand backbone in both spheres by the different ratio of pi to afa tautomeric arms and lack of hydrogen-bond donations to the axial chloride in complex **6**. The iron(III)-oxo complex **1** shows a 2.1 eV and 0.6-0.7 eV blue shift in the L_3- and L_2-edge, respectively, in comparison to the iron(II) species as expected for the oxidation state increase at the iron center. Unfortunately, the other known iron(III) tripodal species[24] were too unstable for sample collection. Fitting of these iron L-edges using CTM4XAS[34,3536] is ongoing but challenging due to the lower symmetry ($D_{3h}/C_{3v}/C_{2v}$) leading to an underdefined system of equations for deriving the crystal field parameters;[3738] initial treatment of the species in weak

octahedral (O_h) fields (Fig. 4.8A & B), as has been done prior for qualitative fitting of L- and M-edge XAS, proved insufficient to describe the features of the L-edge spectra. More success at examining paramagnetic electronic structure of these iron species has been achieved using other techniques, such as EPR and Mössbauer, which have been published elsewhere.[24]

4.3 $M_{2,3}$- and $L_{2,3}$-edge XAS of trigonal bipyramidal manganese complexes

The analogous manganese tripodal systems with the unmodified $N(pi^{Cy})_3$ ligand were also investigated by electronic absorption spectroscopy. The manganese tripodal system has shown similar activity to the iron tripodal system towards oxyanion reduction and O_2 activation and can access analogous Mn(II)-hydroxides and Mn(III)-oxo species.[22] The similarity of the manganese and iron system was thought to assist in determining the electronic structures of the species.

The $M_{2,3}$-edge spectra of the manganese(II) hydroxide $(N(afa^{Cy})_2(pi^{Cy}))Mn^{II}OH$ (**7**) and manganese(III)-oxo $[(N(afa^{Cy})_3)Mn^{III}O]OTf$ (**8**) in the unmodified tripodal ligand framework are shown in Figure 4.5. Complex **7** gave a broad single peak at 50.9 eV with a minor pre-peak at ~48.5 eV, corresponding to high-spin Mn(II) center. This signal shows the same peak structure as

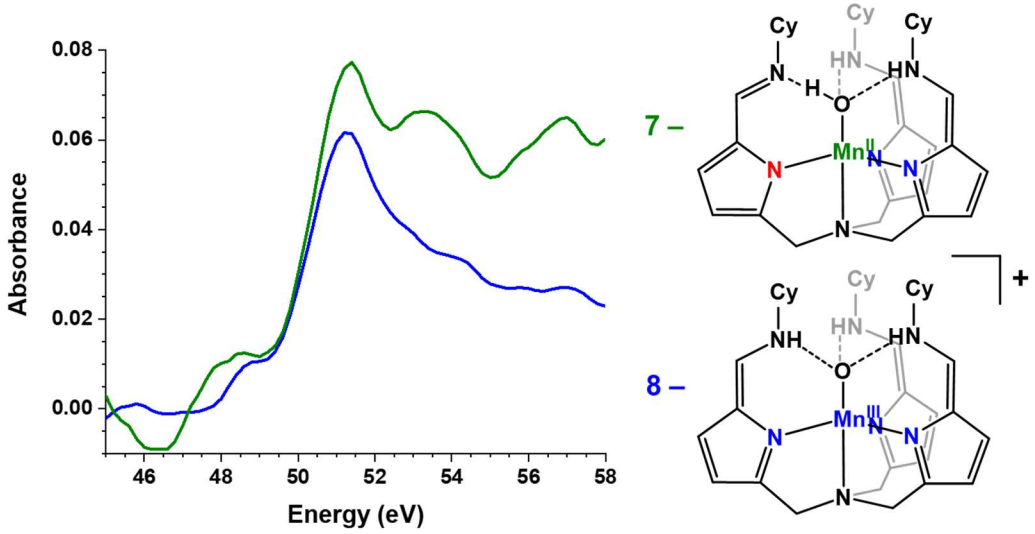

Figure 4.5 $M_{2,3}$-edge spectra of manganese(II)-hydroxo **7** and manganese(III)-oxo **8.**

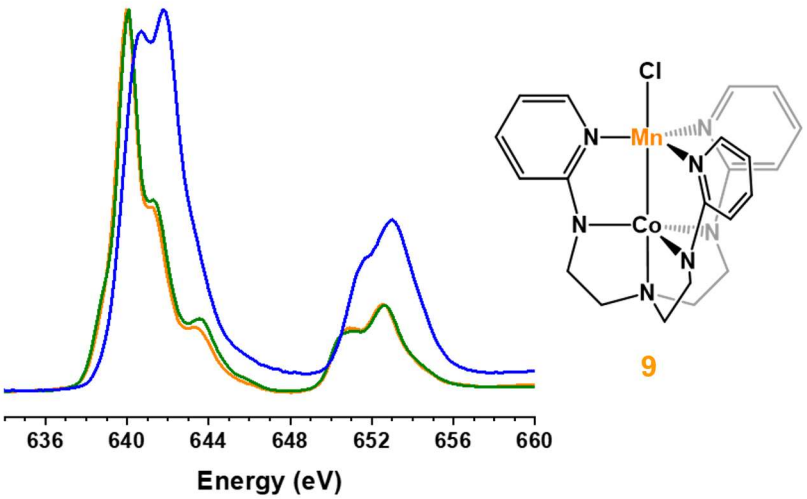

Figure 4.6 $L_{2,3}$-edge spectra of complex **7** (green), **8** (blue) and **9** (orange) with the structure of bimetallic the structure of bimetallic complex **8** shown on the right.

the high spin iron(III)-oxo signals in Figure 4.4 and observed in α-Fe_2O_3,[39] as these are all high-spin d^5 systems in a similar geometric environment. However, complex **8** gave an essentially identical signal as complex **7**, corresponding a high-spin Mn(II) center and not a Mn(III) center. The similarity of the manganese signals led us to suspect that photoreduction of the manganese(III)-oxo complex. XPS of the Mn 3s orbitals (Fig. 4.9), used to assist oxidation state assignment of Mn centers,[40,41] showed similar manganese(II) oxidation states, but it was unclear solely from these data which complexes were degrading. The $L_{2,3}$-edge spectra provide some insight into the $M_{2,3}$-edge XAS and XPS observation; as the Mn $L_{2,3}$-edges are overwhelmingly dominated by Mn 3d states, these can also serve as excellent indicators of the oxidation state and coordination about manganese centers.[42] The manganese(II)-hydroxide **7** gives a qualitative high-spin, Mn(II) spectra with greatest intensity peaks at 640.1 for L_3 and 650.8 eV for L_2 (Figure 4.6, green). The manganese(III)-oxo **8** spectrum shows qualitatively matches a high-spin Mn(III) center (Fig. 4.6, blue), in agreement with published[22] Evan's method magnetic moments and EPR data of these species. However, over multiple runs, there was an observed shift in the L-edge of the Mn(III)-oxo that correspond to photoreduction of the Mn(III) center to a high-spin Mn(II) center over time. The observed signal from complex **8** in XPS and $M_{2,3}$-edge XAS is instead the

photo-reduced species, which is a high-spin Mn(II) species based on the similarity to the Mn(II)-hydroxide. Photoreduction of manganese-oxide species by X-ray beams is known.[4344] Attempts at characterizing the photoreduced species proved fruitless, as the degradation product was unable to be isolated and characterized. Initial rough fitting of the Mn $L_{2,3}$-edges of these species indicates a relatively weak ligand field in both oxidation states (Fig. 4.10 & 4.11A), either with O_h or D_{3h}, with current fitting ongoing using D_{3h} parameters, but the same challenges in fitting these trigonal bipyramidal metal centers persist.

4.4 $M_{2,3}$- and $L_{2,3}$-edge XAS of trigonal bipyramidal cobalt systems

The cobalt $L_{2,3}$-edge spectra were also collected of the cobalt(II) bistriflate complex $[(N(afa^{Cy})_3)Co^{II}OTf]OTf$ (**11**, see Fig. 4.7 for structure) for referencing for a bimetallic system[45] developed by the Lu Group (U. Minnesota) in a pseudo-trigonal bipyramidal geometry. The cobalt tripodal system, in contrast to the iron and manganese systems, has only the cobalt(II)-triflate, -X_3^-,[26] and hydroxide species and shows little to no known small molecule activation. Only in recent unpublished work was a diamagnetic cobalt(III)-bromate species observed, but only showed

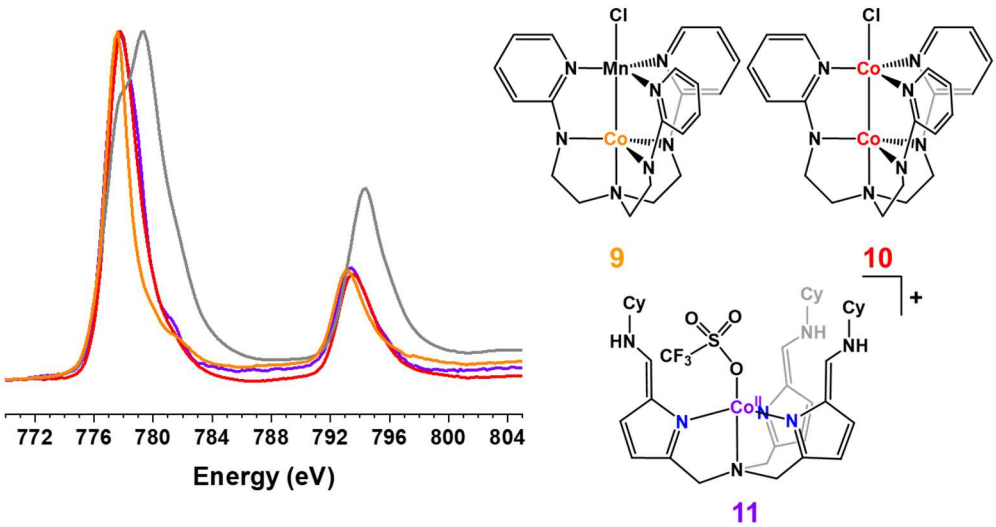

Figure 4.7 $L_{2,3}$-edge XAS spectra of bimetallic complexes **9** (CoMn, orange) and **10** (CoCo, red) along with the tripodal $[(N(afa^{Cy})_3)Co^{II}OTf]OTf$ (**11**, purple); grey is the reference compound Co_3O_4.

coordination of the oxyanion and not reduction as see in the manganese and iron systems. However, there was interest in using a cobalt(II) tripodal complex as references for comparison with a bimetallic cobalt-manganese scaffold. These bimetallic CoM tripodal species (M = Mn – **9**, Co - **10**; Fig. 4.7 for structures) show interesting photodynamics involving metal-metal interactions, particularly for the CoMn system (**9**), but identifying the electronic state of the individual metal centers in the ground states without sufficient reference compounds can be challenging.[38] The $L_{2,3}$-edge spectra of the cobalt complexes are shown in Figure 4.7. Qualitatively, all the tripodal cobalt species, both mono-cobalt and bimetallic, are very similar to each other. Both the L_3 and L_2 edges each appear as a primarily single peak, with the L_3 edge having weak transitions at slightly higher energies. Complexes **9-11** nearly neatly overlay with each other and have similar $L_{2,3}$-edge positions, with only minor differentiations apparent in the higher-energy weak features in L_3 (~781 eV). This likely arises for the different ligand-metal orbital hybridization between the different ligand scaffolds.

There is significant hybridization between the metal-metal orbitals of the bimetallic system,[38] complicating the analysis as calculating XAS transitions now must account for the hybridized transition such as [Co np + MnCo np] → [Co 3d + MnCo 3d]. Having the mono-cobalt species in a similar tripodal ligand scaffold assists in the qualitative assignment of the identity of the oxidation state of the cobalt center, as it indicates the cobalt centers of the bimetallic species **9** and **10** can be described as high-spin Co(II) (Fig. 4.7). Likewise, similar assignment can be made with the CoMn tripodal complex compared to the mono-Mn(II/III) system; the manganese center of the bimetallic complex **9** can be best described qualitatively as high-spin Mn(II) (Fig. 4.6, orange), neatly aligning with the mono-metallic Mn(II)-hydroxide complex.

However, these spectra are similarly challenging to fit quantitatively. Qualitative fitting of the edges can be achieved using either weak field O_h parameter, where 10Dq ~0.5-0.7 for both Co and Mn centers (Fig. 4.10), or with weak field D_{3h} parameters (Fig. 4.11) best fit from the $L_{2,3}$-edge spectra or from Huckel theory extracted from *ab initio* calculations as described by unpublished work by Zhang & Ryland.[37,38] However, these parameters are not consistent with each other, with different geometries and crystal field parameters giving similar spectral fit. High-spin metal complexes with weak field trigonal bipyramidal ligand scaffolds give very similar XAS spectra,[37,38] making it challenging to quantitatively simulate them without sufficient reference complexes for comparison. Even in varying a weak octahedral ligand field for a metal(II) center (M = Mn, Fe, Co), the L_2 and L_3 edges are very similar (see Fig. 4.8, 4.12-13). However, qualitative fits of the weak ligand field are possible and can still provide insight into the oxidation and spin-state of the metal center with sufficient comparison complexes as shown.

While perhaps frustrating for the authors of this work, these results showcase the power of minor changes through ligand backbone modification or weak axial interactions in the electronic structure of the metal center leading to distinct changes in activity. Future XAS investigations of these or similar weak-field trigonal bipyramidal systems should endeavor to combine these studies with other electronic characterizations, such as EPR, magnetic susceptibility, and Mössbauer; excellent computational calculation accounting for hybridization and charge-transfer effects, amongst other potential interactions; and with a broad range of reference compounds to ensure appropriate qualitative and quantitative assignment.

4.5 Conclusions

Investigating the electronic structures of bio-inspired catalysts and intermediates is important for providing insight into their performance and understanding metalloenzymatic active

sites. X-ray absorptions spectroscopies at the metal center edges, such as $L_{2,3}$- and $M_{2,3}$-edge, can provide direct information about the oxidation state, spin-state, and coordination about the metal center. An effort to characterize a series of bio-inspired iron, manganese, and cobalt trigonal bipyramidal at the $M_{2,3}$-edges in the XUV energy region or in the higher energy region at the $L_{2,3}$-edge. Primary sphere modifications of the tripodal ligand scaffold showed minor effects on the iron $M_{2,3}$-edge, while secondary sphere capping group changes resulted in no resolvable effect. While the manganese(III)-oxo showed photoreduction in the $M_{2,3}$ -edge and XPS data, $L_{2,3}$-edge of the manganese system. L-edge data of series of mono- and bi-metallic tripodal species with at least one cobalt was collected, allowing for qualitative examination, and attempted qualitative fitting to determine oxidation and spin state. The trigonal bipyramidal ligand field and the even lower symmetry of the reference tripodal complexes, however, made these spectra challenging to quantitatively fit due to the underdefined system of equations for deriving the crystal field parameters.

Acknowledgements: Initial $M_{2,3}$-edge XUV data collection was with assistance from Vura-Weis group alumni Drs. Kori Sye, Ryan Ash, Yusef Shari'ati, Aastha Sharma, Kris Benke, and Liz Ryland; L-edge XAS spectra were graciously collected by Dr. Orhan Kizilkaya (LSU CAMD) and analyzed in collaboration with Dr. Liz Ryland & Dr. Kaili Zhang. XPS data were collected with assistance from Dr. Richard Haasch. We thank the Lu group (U. Minnesota) for providing the bimetallic species **9** and **10**.

4.6 Experimental

General Experimental Considerations. Solvents were dried and deoxygenated on a Glass Contour System (SG Water USA, Nashua, NH) and stored over 4 Å molecular sieves purchased

from Strem following literature procedure prior to use. All complexes were prepared and characterized according to literature procedures[12,21,23,45] under a dinitrogen atmosphere in a drybox.

Physical Measurements. X-ray photoelectron (XPS) spectroscopic data were recorded on a Kratos Axis ULTRA XPS spectrometer, with samples prepared as thin films on gold-coated silicon substrate. $M_{2,3}$-edge absorption spectroscopy samples were generally prepared by spin-coating from a filtered, concentrated solution on either 50 nm or 100 nm silicon nitride substrate to form homogeneous thin films. Air sensitive samples (tripodal metal(II) species and bimetallic complexes) were prepared and stored in a drybox under dinitrogen atmosphere. The broadband extreme ultraviolet (XUV) probe pulse was generated by high-harmonic generation using a tabletop instrument developed by the Vura-Weis group and described in prior publications.[27,28] In short, a Ti:sapphire laser (800 nm, 4 mJ, 35 fs, 1 kHz) is focused into a semi-infinite gas cell with either argon (45 torr) or neon (80 torr) gas. The strong electromagnetic field at the focal point ionizes the gas, accelerates the free electrons, and drives them back into the ionized atoms. This generates a ~20fs XUV pulse (35-100 eV). A Si mirror followed by a 200 nm Al foil block residual IR light. After passing through the sample, the light is dispersed by a grating onto an array CCD. The spectrometer resolution was 0.3-0.4 eV FWHM based on Xe^+ atomic absorption lines.

$L_{2,3}$-edge absorption spectroscopy samples were prepared as powders spread on non-resonant tape, and data were recorded in total electron yield at Louisiana State University Center for Advanced Microstructures and Devices (LSU CAMD). References for energy calibration of the $L_{2,3}$-edge data for the appropriate metal edge were α-Fe_2O_3,[46] Mn_2O_3,[47,48] and the mixed spinel Co_3O_4.[49,50]

Multiplet calculations to simulate the L-edge spectra were performed using CTM4XAS.[35–37] Slater integrals were set at 80% of the atomic values unless otherwise noted. Individual

transitions were broadened with Lorentzians of 0.2 and 0.4 eV around the L_3 and L_2-edge regions, respectively, and convoluted with a 0.2 eV Gaussian broadening, respectively. These broadening procedures compensated for both the inherent line width due to the lifetime of the final state and the beamline resolution.

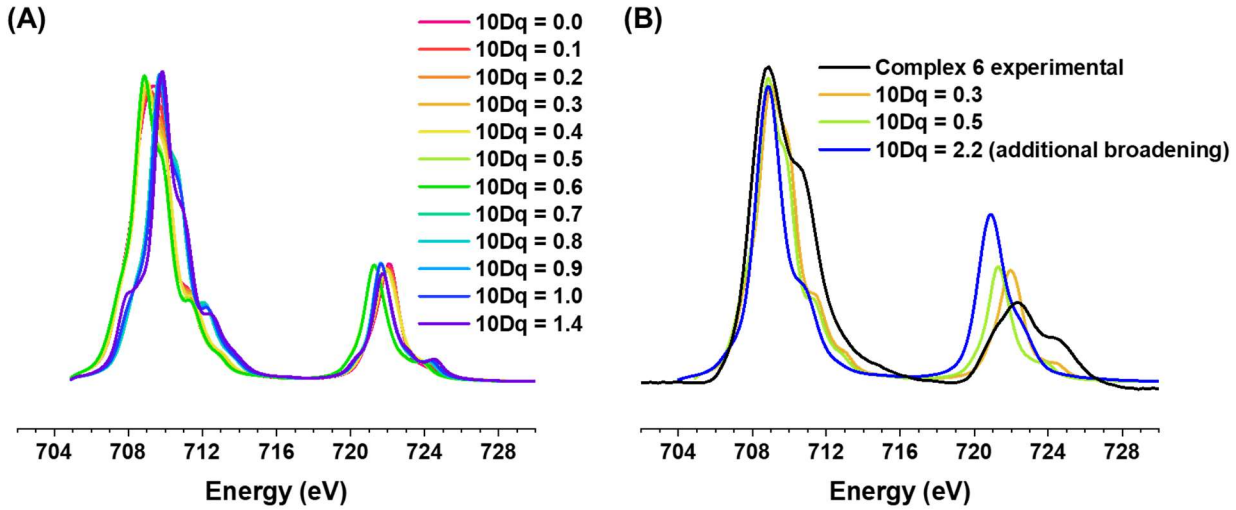

Figure 4.8 (A) CTM4XAS $L_{2,3}$-edge calculations of a O_h Fe(II) system with various 10Dq parameters; (B) example overlay of experimental $L_{2,3}$-edge data of complex **6** (black) with select "best" examples of using weak field O_h parameters in L-edge multiplet calculations, showing the poorness of the calculated fits to the experimental data with both weak O_h field (yellow, 10Dq = 0.3; green, 10Dq = 0.5) and even broadened strong O_h field (blue, 10Dq = 2.2 with Lorentzian broadening set to 0.5 for both and Gaussian set to 0.4).

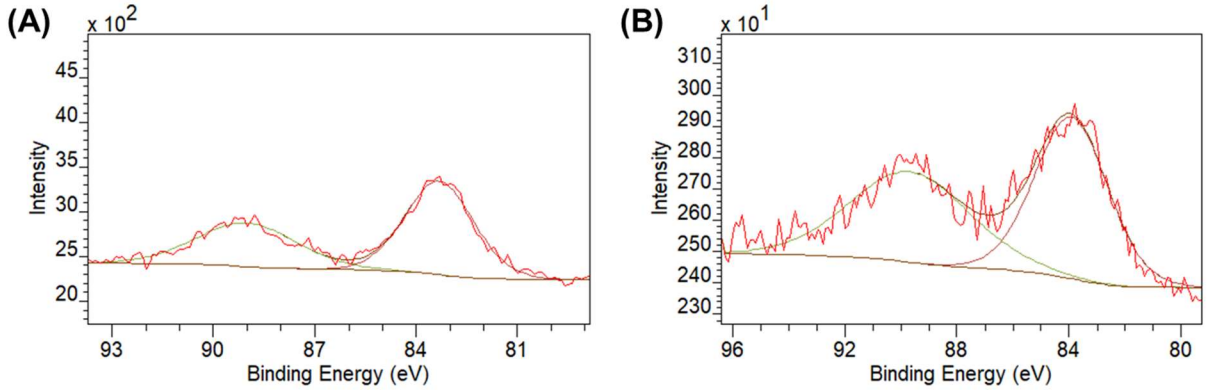

Figure 4.9 XPS of Mn 3s binding energies for complexes **7** (A, 5.7 eV difference) and photoreduced-**8** (B, 5.8 eV difference); the 5.7-5.8 eV difference between the two 3s peaks corresponds to an Mn(II) oxidation state[40,41,51,52] as expected from $M_{2,3}$-edge XAS.

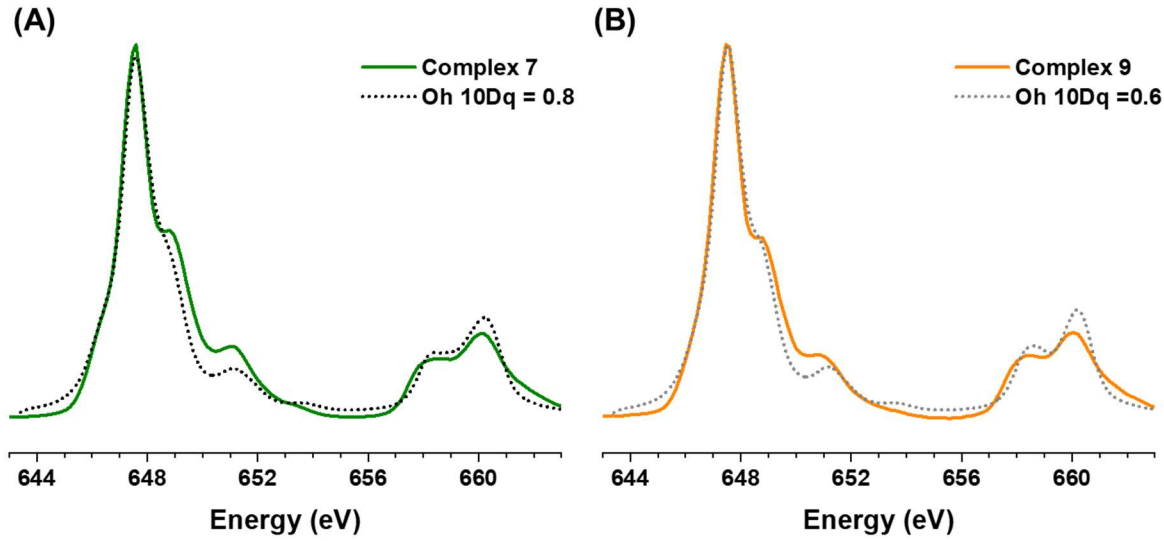

Figure 4.10 CTM4XAS $L_{2,3}$-edge XAS of Mn(II) O_h field with 10Dq =0.8 (A) and 0.6 (B) at SOC 107% as grey dotted traces with the corresponding experimental data for complexes **7** (A) and **9** (B) overlayed for comparison.

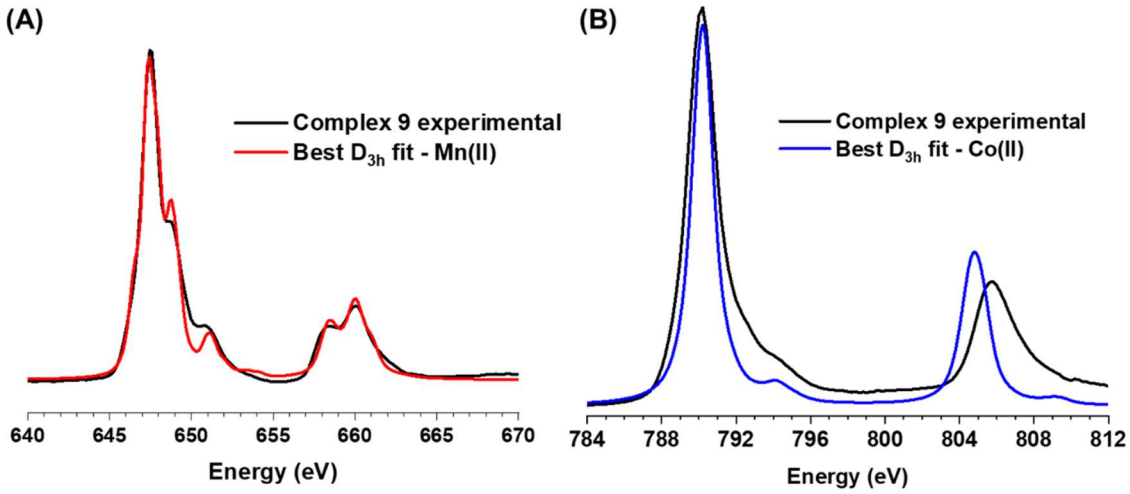

Figure 4.11 CTM4XAS $L_{2,3}$-edge XAS of complex **9** at the high-spin manganese(II) (A) and cobalt(II) (B) centers with crystal field parameters and with metal-metal mixing determined from best D_{3h} fit and $M_{2,3}$-edge fits from references 36 & 37); the experimental data of **8** is overlayed in black.

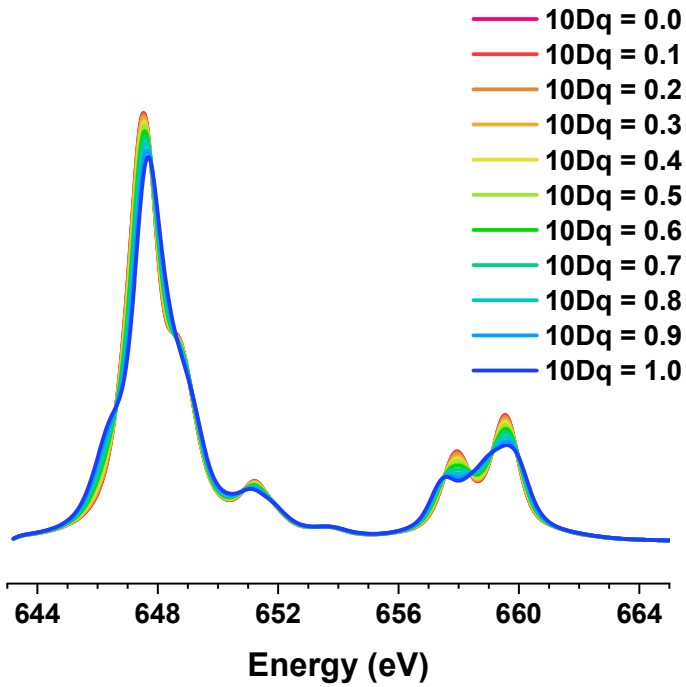

Figure 4.12 – CTM4XAS $L_{2,3}$-edge calculations of a high-spin O_h Mn(II) system with various weak field 10Dq parameters, showing gradual minor changes in edge intensities and peak transitions.

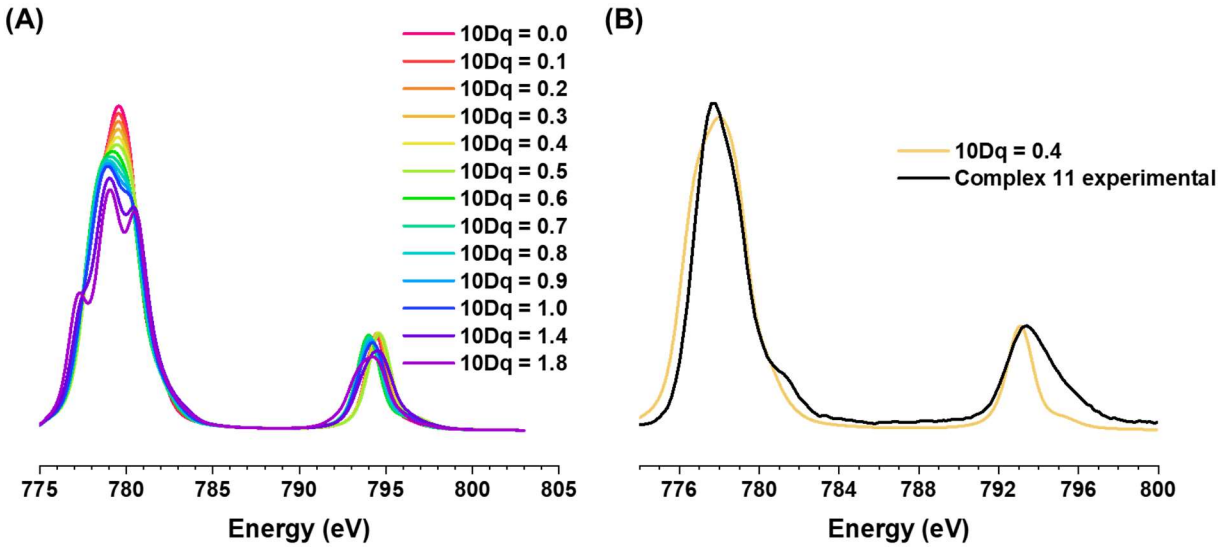

Figure 4.13 (A) CTM4XAS $L_{2,3}$-edge calculations of an Oh Co(II) system with various 10Dq parameters; (B) overlay example with experimental $L_{2,3}$-edge data of complex 11 with "best" O_h calculated CTM4XAS fit with 10Dq = 0.4.

4.7 References

(1) Meunier, B.; de Visser, S. P.; Shaik, S. Mechanism of Oxidation Reactions Catalyzed by

Cytochrome P450 Enzymes. *Chem. Rev.* **2004**, *104* (9), 3947–3980.

(2) Kovaleva, E. G.; Lipscomb, J. D. Versatility of Biological Non-Heme Fe(II) Centers in Oxygen Activation Reactions. *Nat. Chem. Biol.* **2008**, *4* (3), 186–193.

(3) Wang, W.; Liang, A. D.; Lippard, S. J. Coupling Oxygen Consumption with Hydrocarbon Oxidation in Bacterial Multicomponent Monooxygenases. *Acc. Chem. Res.* **2015**, *48* (9), 2632–2639.

(4) Lieberman, R. L.; Rosenzweig, A. C. Crystal Structure of a Membrane-Bound Metalloenzyme That Catalyses the Biological Oxidation of Methane. *Nature* **2005**, *434* (7030), 177–182.

(5) Guo, M.; Corona, T.; Ray, K.; Nam, W. Heme and Nonheme High-Valent Iron and Manganese Oxo Cores in Biological and Abiological Oxidation Reactions. *ACS Cent. Sci.* **2019**, *5* (1), 13–28.

(6) Srnec, M.; Wong, S. D.; Matthews, M. L.; Krebs, C.; Bollinger, J. M.; Solomon, E. I. Electronic Structure of the Ferryl Intermediate in the α-Ketoglutarate Dependent Non-Heme Iron Halogenase SyrB2: Contributions to H Atom Abstraction Reactivity. *J. Am. Chem. Soc.* **2016**, *138* (15), 5110–5122.

(7) Blasiak, L. C.; Vaillancourt, F. H.; Walsh, C. T.; Drennan, C. L. Crystal Structure of the Non-Haem Iron Halogenase SyrB2 in Syringomycin Biosynthesis. *Nature* **2006**, *440* (7082), 368–371.

(8) Youngblut, M. D.; Tsai, C. L.; Clark, I. C.; Carlson, H. K.; Maglaqui, A. P.; Gau-Pan, P. S.; Redford, S. A.; Wong, A.; Tainer, J. A.; Coates, J. D. Perchlorate Reductase Is Distinguished by Active Site Aromatic Gate Residues. *J. Biol. Chem.* **2016**, *291* (17), 9190–9202.

(9) Einsle, O.; Messerschmidt, A.; Huber, R.; Kroneck, P. M. H.; Neese, F. Mechanism of the Six-Electron Reduction of Nitrite to Ammonia by Cytochrome c Nitrite Reductase. *J. Am. Chem. Soc.* **2002**, *124* (39), 11737–11745.

(10) Shook, R. L.; Borovik, A. S. Role of the Secondary Coordination Sphere in Metal-Mediated Dioxygen Activation. *Inorg. Chem.* **2010**, *49* (8), 3646–3660.

(11) Hosseinzadeh, P.; Lu, Y. Design and Fine-Tuning Redox Potentials of Metalloproteins Involved in Electron Transfer in Bioenergetics. *Biochim. Biophys. Acta - Bioenerg.* **2016**, *1857* (5), 557–581.

(12) Matson, E. M.; Bertke, J. A.; Fout, A. R. Isolation of Iron(II) Aqua and Hydroxyl Complexes Featuring a Tripodal H-Bond Donor and Acceptor Ligand. *Inorg. Chem.* **2014**, *53* (9), 4450–4458.

(13) Lucas, R. L.; Zart, M. K.; Mukherjee, J.; Sorrell, T. N.; Powell, D. R.; Borovik, A. S. A Modular Approach toward Regulating the Secondary Coordination Sphere of Metal Ions: Differential Dioxygen Activation Assisted by Intramolecular Hydrogen Bonds. *J. Am. Chem. Soc.* **2006**, *128* (3), 15476–15489.

(14) Widger, L. R.; Davies, C. G.; Yang, T.; Siegler, M. A.; Troeppner, O.; Jameson, G. N. L.;

Ivanović-Burmazović, I.; Goldberg, D. P. Dramatically Accelerated Selective Oxygen-Atom Transfer by a Nonheme Iron(IV)-Oxo Complex: Tuning of the First and Second Coordination Spheres. *J. Am. Chem. Soc.* **2014**, *136* (7), 2699–2702.

(15) MacBeth, C. E.; Golombek, A. P.; Young, V. G.; Yang, C.; Kuczera, K.; Hendrich, M. P.; Borovik, A. S. O 2 Activation by Nonheme Iron Complexes: A Monomeric Fe(III)-Oxo Complex Derived From O 2. *Science (80-.).* **2000**, *289* (5481), 938–941.

(16) Lacy, D. C.; Gupta, R.; Stone, K. L.; Greaves, J.; Ziller, J. W.; Hendrich, M. P.; Borovik, A. S. Formation, Structure, and EPR Detection of a High Spin FeIV-Oxo Species Derived from Either an FeIII-Oxo or FeIII-OH Complex. *J. Am. Chem. Soc.* **2010**, *132* (35), 12188–12190.

(17) Rohde, J.-U.; In, J.-H.; Lim, M. H.; Brennessel, W. W.; Bukowski, M. R.; Stubna, A.; Münck, E.; Nam, W.; Que, L. Crystallographic and Spectroscopic Characterization of a Nonheme Fe(IV)=O Complex. *Science (80-.).* **2003**, *299* (5609), 1037–1039.

(18) Hong, S.; Sutherlin, K. D.; Park, J.; Kwon, E.; Siegler, M. A.; Solomon, E. I.; Nam, W. Crystallographic and Spectroscopic Characterization and Reactivities of a Mononuclear Non-Haem Iron(III)-Superoxo Complex. *Nat. Commun.* **2014**, *5*.

(19) Matson, E.; Park, Y.; Fout, A. Facile Nitrite Reduction in a Non-Heme Iron System: Formation of an Iron (III)-Oxo. *J. Am. Chem. Soc.* **2014**, *136* (Iii), 17398.

(20) Ford, C. L.; Park, Y. J.; Matson, E. M.; Gordon, Z.; Fout, A. R. A Bioinspired Iron Catalyst for Nitrate and Perchlorate Reduction. *Science (80).* **2016**, *354* (6313), 741–743.

(21) Matson, E. M.; Park, Y. J.; Fout, A. R. Facile Nitrite Reduction in a Non-Heme Iron System: Formation of an Iron(III)-Oxo. *J. Am. Chem. Soc.* **2014**, *136* (50), 17398–17401.

(22) Park, Y. J.; Matson, E. M.; Nilges, M. J.; Fout, A. R. Exploring Mn–O Bonding in the Context of an Electronically Flexible Secondary Coordination Sphere: Synthesis of a Mn(III)–Oxo. *Chem. Commun.* **2015**, *51* (25), 5310–5313.

(23) Gordon, Z.; Drummond, M. J.; Matson, E. M.; Bogart, J. A.; Schelter, E. J.; Lord, R. L.; Fout, A. R. Tuning the Fe(II/III) Redox Potential in Nonheme Fe(II)–Hydroxo Complexes through Primary and Secondary Coordination Sphere Modifications. *Inorg. Chem.* **2017**, *56* (9), 4852–4863.

(24) Gordon, Z.; Miller, T. J.; Leahy, C. A.; Matson, E. M.; Burgess, M.; Drummond, M. J.; Popescu, C. V.; Smith, C. M.; Lord, R. L.; Rodríguez-López, J.; Fout, A. R. Characterization of Terminal Iron(III)-Oxo and Iron(III)-Hydroxo Complexes Derived from O2 Activation. *Inorg. Chem.* **2019**, *58* (23), 15801–15811.

(25) Drummond, M. J.; Miller, T. J.; Ford, C. L.; Fout, A. R. Catalytic Perchlorate Reduction Using Iron: Mechanistic Insights and Improved Catalyst Turnover. *ACS Catal.* **2020**, *10* (5), 3175–3182.

(26) Matson, E. M.; Park, Y. J.; Bertke, J. a.; Fout, A. R. Synthesis and Characterization of M(II) (M = Mn, Fe and Co) Azafulvene Complexes and Their X_3^- Derivatives. *Dalt. Trans.* **2015**, *44* (22), 10377–10384.

(27) Zhang, K.; Lin, M. F.; Ryland, E. S.; Verkamp, M. A.; Benke, K.; De Groot, F. M. F.; Girolami, G. S.; Vura-Weis, J. Shrinking the Synchrotron: Tabletop Extreme Ultraviolet Absorption of Transition-Metal Complexes. *J. Phys. Chem. Lett.* **2016**, *7* (17), 3383–3387.

(28) Ryland, E. S.; Lin, M.-F.; Verkamp, M. A.; Zhang, K.; Benke, K.; Carlson, M.; Vura-Weis, J. Tabletop Femtosecond M-Edge X-Ray Absorption Near-Edge Structure of FeTPPCl: Metalloporphyrin Photophysics from the Perspective of the Metal. *J. Am. Chem. Soc.* **2018**, *140* (13), 4691–4696.

(29) Zhang, K.; Ash, R.; Girolami, G. S.; Vura-Weis, J. Tracking the Metal-Centered Triplet in Photoinduced Spin Crossover of Fe(Phen)32+ with Tabletop Femtosecond M-Edge X-Ray Absorption Near-Edge Structure Spectroscopy. *J. Am. Chem. Soc.* **2019**, *141* (43), 17180–17188.

(30) Ash, R.; Zhang, K.; Vura-Weis, J. Photoinduced Valence Tautomerism of a Cobalt-Dioxolene Complex Revealed with Femtosecond M-Edge XANES. *J. Chem. Phys.* **2019**, *151* (10), 104201.

(31) Shari'Ati, Y.; Vura-Weis, J. Ballistic Δ: S = 2 Intersystem Crossing in a Cobalt Cubane Following Ligand-Field Excitation Probed by Extreme Ultraviolet Spectroscopy. *Phys. Chem. Chem. Phys.* **2021**, *23* (47), 26990–26996.

(32) Shari'ati, Y.; Vura-Weis, J. Polymer Thin Films as Universal Substrates for Extreme Ultraviolet Absorption Spectroscopy of Molecular Transition Metal Complexes. *J. Synchrotron Radiat.* **2021**, *28* (6), 1850–1857.

(33) Grush, M. M.; Chen, J.; Stemmler, T. L.; George, S. J.; Ralston, C. Y.; Stibrany, R. T.; Gelasco, A.; Christou, G.; Gorun, S. M.; Penner-Hahn, J. E.; Cramer, S. P. Manganese L-Edge X-Ray Absorption Spectroscopy of Manganese Catalase from Lactobacillus Plantarum and Mixed Valence Manganese Complexes. *J. Am. Chem. Soc.* **1996**, *118* (1), 65–69.

(34) Delgado-Jaime, M. U.; Zhang, K.; Vura-Weis, J.; De Groot, F. M. F. CTM4DOC: Electronic Structure Analysis from X-Ray Spectroscopy. *J. Synchrotron Radiat.* **2016**, *23*, 1264–1271.

(35) Zhang, K.; Girolami, G. S.; Vura-Weis, J. Improved Charge Transfer Multiplet Method to Simulate M- and L-Edge X-Ray Absorption Spectra of Metal-Centered Excited States. *J. Synchrotron Radiat.* **2018**, *25* (5), 1600–1608.

(36) Stavitski, E.; de Groot, F. M. F. The CTM4XAS Program for EELS and XAS Spectral Shape Analysis of Transition Metal L Edges. *Micron* **2010**, *41* (7), 687–694.

(37) Zhang, K. The Femtosecond M-Edge Approach to the Photodynamics of Iron(II) Complexes, University of Illinois at Urbana-Champaign, 2019.

(38) Ryland, E. S. Ultrafast Photophysics of Transition Metal Coordination Complexes Studied with Femtosecond Extreme Ultraviolet Transient Absorption Spectroscopy, University of Illinois at Urbana-Champaign, 2019.

(39) Vura-Weis, J.; Jiang, C. M.; Liu, C.; Gao, H.; Lucas, J. M.; De Groot, F. M. F.; Yang, P.; Alivisatos, A. P.; Leone, S. R. Femtosecond M2,3-Edge Spectroscopy of Transition-Metal

Oxides: Photoinduced Oxidation State Change in α-Fe2O3. *J. Phys. Chem. Lett.* **2013**, *4* (21), 3667–3671.

(40) Fujiwara, M.; Matsushita, T. Characterization of Manganese Complexes. *J. Electron Spectros. Relat. Phenomena* **1995**, *74*, 201–206.

(41) Nelson, A. J.; Reynolds, J. G.; Roos, J. W. Core-Level Satellites and Outer Core-Level Multiplet Splitting in Mn Model Compounds. *J. Vac. Sci. Technol. A Vacuum, Surfaces, Film.* **2000**, *18* (4), 1072–1076.

(42) Gilbert, B.; Frazer, B. H.; Belz, A.; Conrad, P. G.; Nealson, K. H.; Haskel, D.; Lang, J. C.; Srajer, G.; De Stasio, G. Multiple Scattering Calculations of Bonding and X-Ray Absorption Spectroscopy of Manganese Oxides. *J. Phys. Chem. A* **2003**, *107* (16), 2839.

(43) Grabolle, M.; Haumann, M.; Müller, C.; Liebisch, P.; Dau, H. Rapid Loss of Structural Motifs in the Manganese Complex of Oxygenic Photosynthesis by X-Ray Irradiation at 10-300 K. *J. Biol. Chem.* **2006**, *281* (8), 4580–4588.

(44) Dubois, L.; Jacquamet, L.; Pécaut, J.; Latour, J. M. X-Ray Photoreduction of a Di(μ-Oxo)MnIIIMnIV Complex Occurs at Temperatures as Low as 20 K. *Chem. Commun.* **2006**, No. 43, 4521–4523.

(45) Tereniak, S. J.; Carlson, R. K.; Clouston, L. J.; Young, V. G.; Bill, E.; Maurice, R.; Chen, Y. S.; Kim, H. J.; Gagliardi, L.; Lu, C. C. Role of the Metal in the Bonding and Properties of Bimetallic Complexes Involving Manganese, Iron, and Cobalt. *J. Am. Chem. Soc.* **2014**, *136* (5), 1842–1855.

(46) Schedel-Niedrig, T.; Weiss, W.; Schlögl, R. Electronic Structure of Ultrathin Ordered Iron Oxide Films Grown onto Pt(111). *Phys. Rev. B* **1995**, *52* (24), 17449–17460.

(47) Gilbert, B.; Frazer, B. H.; Belz, A.; Conrad, P. G.; Nealson, K. H.; Haskel, D.; Lang, J. C.; Srajer, G.; De Stasio, G. Multiple Scattering Calculations of Bonding and X-Ray Absorption Spectroscopy of Manganese Oxides. *J. Phys. Chem. A* **2003**, *107* (16), 2839.

(48) Kurata, H.; Colliex, C. Electron-Energy-Loss Core-Edge Structures in Manganese Oxides. *Phys. Rev. B* **1993**, *48* (4), 2102–2108.

(49) Hibberd, A. M.; Doan, H. Q.; Glass, E. N.; De Groot, F. M. F.; Hill, C. L.; Cuk, T. Co Polyoxometalates and a Co3O4 Thin Film Investigated by L-Edge X-Ray Absorption Spectroscopy. *J. Phys. Chem. C* **2015**, *119* (8), 4173–4179.

(50) Van Oversteeg, C. H. M.; Doan, H. Q.; De Groot, F. M. F.; Cuk, T. In Situ X-Ray Absorption Spectroscopy of Transition Metal Based Water Oxidation Catalysts. *Chem. Soc. Rev.* **2017**, *46* (1), 102–125.

(51) Ilton, E. S.; Post, J. E.; Heaney, P. J.; Ling, F. T.; Kerisit, S. N. XPS Determination of Mn Oxidation States in Mn (Hydr)Oxides. *Appl. Surf. Sci.* **2016**, *366*, 475–485.

(52) Junta, J. L.; Hochella, M. F. Manganese (II) Oxidation at Mineral Surfaces: A Microscopic and Spectroscopic Study. *Geochim. Cosmochim. Acta* **1994**, *58* (22), 4985–4999.

Chapter 5: Extreme ultraviolet spectroscopy of third row transition metal coordination complexes

5.1 3rd row transition metals as catalysts and photosensitizers

While there is an increasing drive to develop earth-abundant metal catalytic processes, precious metals still generally dominate as catalytic centers in key organic reactions and processes.[1–11] 3rd row transition metal coordination complexes are particularly ubiquitous photocatalysts and sensitizers.[1,9,11–27] They generally have strong molar absorptivity (~10,000 $M^{-1}cm^{-1}$) in the UV-Vis spectral region, allowing for excitation at accessible single wavelengths or ambient light sources. Common ligand scaffolds, such as bipyridine (bpy) and 2-phenylpyridine (ppy), for these species are modifiable through ligand exchange or substitutions at select positions, allowing for easy tuning of the photoproperties and dynamics.[16,18,20,28,29] Their excited state redox potentials of the photoinduced states, generally triplet excited states, are well-suited for transferring electrons or energy in a variety of transformations.[1,11,22,30,31] Finally, these triplet states are generally long-lived (ns-μs)[17,18,20] due to the forbidden transition to return to the singlet ground

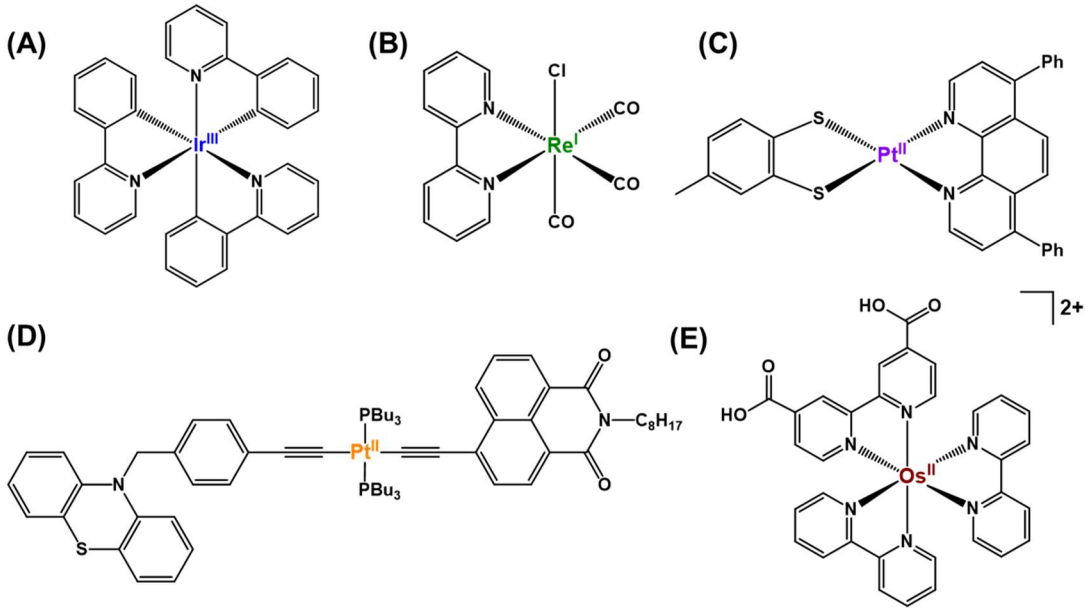

Figure 5.1 Select examples of 3rd row transition metal coordination complexes in photoactivated catalysis and sensitization processes.

state, allowing for sufficient time to transfer the needed electron or energy into the desired process. The strong spin-orbit couplings (SOC) of these 3rd row metals facilitate efficient intersystem crossing (ISC) between singlet and triplet states, which can give high quantum emission yields from the triplet state. Common examples of photoactivated 3rd row transition metal complexes include cyclometalated octahedral iridium(III) complexes such as iridium tris(2-phenylpyridine) ($Ir^{III}(ppy)_3$) (Fig. 5.1A),[32] rhenium bipyridyls (Fig. 5.1B),[33,34] square planar platinum(II) complexes such as platinum diimine dithiolates[35] (Fig. 5.1C) and platinum acetylides[17,36,37] (Fig. 5.1D),[14,17,38] and osmium(II) polypyridyl complexes (Fig. 5.1E).[39,40]

X-ray absorption spectroscopy (XAS) has been shown to be a powerful technique for understanding electronic dynamics and processes at the metal center directly. For 3rd row metals, this has primarily focused on the L_3 and L_2-edges (10-12 keV), which are the transitions of an electron from the $2p_{3/2}$ and $2p_{1/2}$ core orbitals to the valence 5d orbitals, respectively. In the past decades, recent technical advances towards development and implementation of time-resolved x-ray absorption near-edge spectroscopy (XANES) and extended x-ray absorption fine structure (EXAFS) have improved the use of transient XAS as a method for investigating the electronic and structural changes of photoactivated 3rd row transition metal compounds.[41–43] For example, time-resolved L_3 XANES and EXAFS have been used to study the photodynamics of platinum(II) dimers such as $[Pt_2(P_2O_5H_2)_4]^{4-}$ [44] and $[Pt(NDI\text{-}ppy)(\mu\text{-}Ph_2Pz)]_2$[45] in the solution phase and osmium polypyridyl complexes.[39] Iridium photosensitizers such as $Ir^{III}(ppy)_3$[43,46] and $[Ir^{III}(ppy)_2(bpy)]^+$ [47] have also recently been studied using transient $L_{2,3}$-edge XANES. However, transient XAS at the $L_{2,3}$-edges of these species are primarily limited to looking at only late dynamics or long-lived excited states, as recent synchrotron time resolution has generally been limited to the tens or hundreds of picoseconds (ps).[41,43,47] This is insufficient for looking at early photodynamics (<10

ps) or short-lived excited states within these time frames such as relaxation dynamics and intersystem crossings (ISC).[16,17,48]

5.2 Extreme Ultraviolet (XUV) Spectroscopy of 3rd Row Metals

Table-top extreme ultraviolet (XUV) spectroscopy has been shown to be a powerful technique for probing the $M_{2,3}$-edge of 1st row transition metal coordination complexes in the 40-100 eV energy range and their early and ultrafast photodynamics.[42,49–53] The Vura-Weis group uses an in-house instrument with high-harmonic generation (HHG)[49] for generating XUV pulses to probe these $M_{2,3}$-edges. The $M_{2,3}$-edge is sensitive to oxidation state, ligand field, and spin-state, providing key insight into changes at the metal center directly.[54] With XUV spectroscopy, the Vura-Weis group and others have successfully examined the structures and ultrafast photodynamics of various 1st row transition metal catalysts, such as nickel & iron porphyrins[55,56] and spin-crossover iron & cobalt systems.[55,57,58]

However, the XUV energy region is not limited to just 1st row transition metals centers. The XUV energy region also contains the $O_{2,3}$- and $N_{6,7}$-edges of the mid- to late-3rd row transition metals; the $O_{2,3}$-edge corresponds to the 5p to valence [5d6s] orbitals transition, while the $N_{6,7}$-edge comes from the 4f to valence [5d6s] orbital transition. Prior work has examined metallic samples or atomic vapors of 3rd row transition metals in the XUV region.[59–61] Sonntag, Kunz, and coworkers first performed systematic acquisition of the 40-200 eV region for metallic 2nd and 3rd row transition metals in the 1960s, observing the suite of edges that included proposed $O_{2,3}$- and $N_{6,7}$-edges between 40-120 eV for tungsten through gold (Fig. 5.2A).[61,62] Later studies using the dual laser-produced plasma (DLP) technique more closely examined plasmonic vapors of platinum and tungsten (Fig. 5.2B), identifying specific transitions and interactions observed for the $O_{2,3}$ and $N_{6,7}$-edges and examining correlation and relativistic effects.[63,64] More recent work has examined

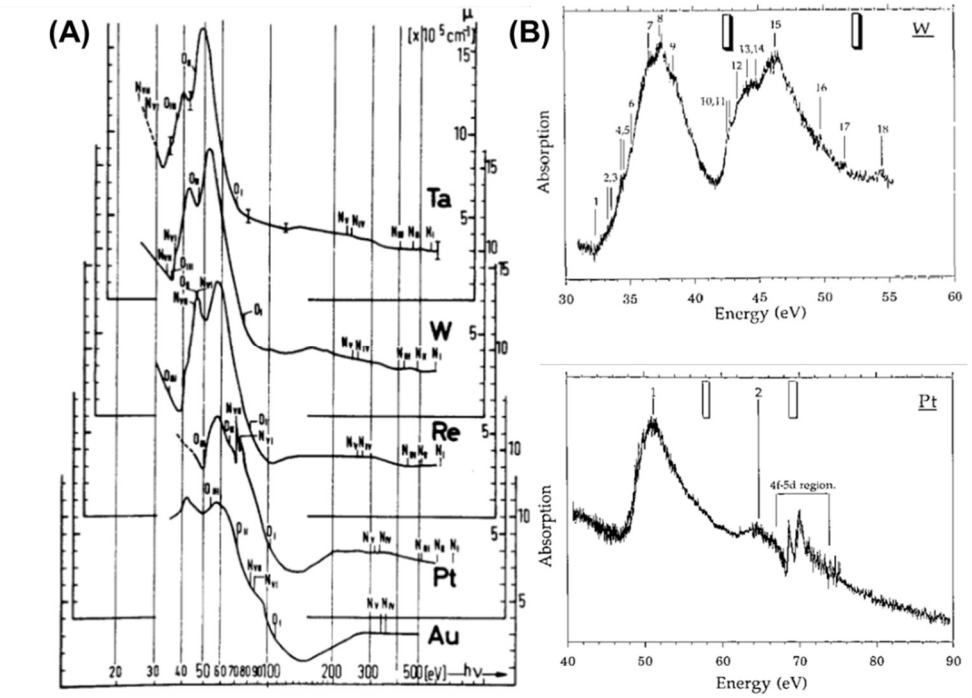

Figure 5.2 (A) 20-200 eV XUV spectra of metallic 3rd row metal samples from reference 62; (B) XUV of plasmonic W (top) and Pt (bottom) vapors showing O-edges and N-edges from reference 63.

the photo absorption spectra of gold[60] and iridium[65] in the XUV region towards calculating and fitting the transitions, finding the edges were dominated by a great number of lines from 4f-to-[5d,6d] and 5p-to-[5d,6 s] transitions. However, these studies only contain atomic and free ion cases at these XUV edges and were generally restricted to plasma-based generation of the free ions.

There are very few published cases of 3rd row metal coordination complexes examined at these edges; for example, Leone and coworkers recently used transient XUV to examine carrier dynamics in WS_2.[66] Prior work indicated there are many interacting resonances from the various excitation and relaxation processes that may broaden resonances.[59,63,64,67] Additionally, there were also limited methods for generating XUV photons up until recent technical advances in free-electron lasers and HHG that allowed for convenient, accessible XUV pulse generation.[42,49]

Herein, we describe recent efforts in developing an experimental and theoretical understanding of the $O_{2,3}$- and $N_{6,7}$-edges of 3rd row transition metal coordination complexes using

XUV spectroscopy. We characterized several Pt and Ir complexes in the solid state, identifying initial trends in the edge based on ligand field changes in iridium complexes. Furthermore, we performed transient O_3- & $N_{6,7}$-edge XANES on $Ir^{III}(ppy)_3$ as a proof-of-concept experiment, showing that metal-based excited state dynamics can be tracked at this edge akin to synchrotron-based transient L-edge XANES. This provides a foundation for future studies examining the ground electronic states and dynamics of late 3rd row metal species using XUV spectroscopy.

5.3 Ground state $O_{2,3}$- and $N_{6,7}$-edges of Pt & Ir coordination complexes

Prior work provided some guidance on potential targets and crystal field effects on the $O_{2,3}$- and $N_{6,7}$-edges for 3rd row complexes. We chose platinum and iridium coordination complexes as the initial targets for XUV spectroscopy as these are not only popular catalysts and photosensitizers, but their $O_{2,3}$- and $N_{6,7}$-edges are both well within the available XUV energy range of our instrument (40-90 eV, see Fig. 5.2).[62–65] $L_{2,3}$-edge studies of 3rd row metal complexes have primarily indicated that the valence orbitals can be considered as primarily 5d orbital character instead of mixed [5d6s] character,[39,44,68] so we simplified initial analysis to primarily focus on transitions to valence 5d orbitals. An additional factor affecting transitions for 3rd row metals is that stronger spin-orbit coupling is present compared to 1st row metals, and consideration should be given to jj-coupling instead of simply Russel-Saunders (LS) coupling. Additionally, in certain cases, the crystal field or SOC may outweigh the other in affecting the orbital manifold. For example, in certain iridium(IV) oxides (iridates) the crystal field predominates over SOC effects, resulting in large, nonstatistical branching ratios where j_{eff} dominates over conventional *S* terms.[69–73] A further consideration for the $N_{6,7}$-edges in particular is that given that the 5d orbitals are much more extensive than the 4f orbitals, they will interact more strongly with coordinating ligands, resulting in larger crystal-field parameters for the 5d orbital manifold than the 4f core orbitals. For

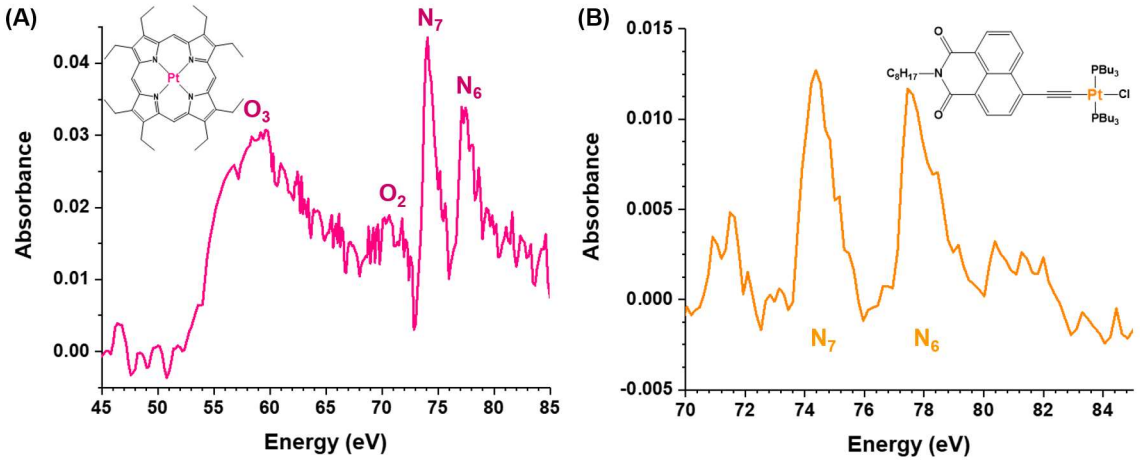

Figure 5.3 XUV spectrum of $Pt^{II}OEP$ (A, pink) from 45-85 eV and $(PBu_3)ClPt^{II}NAP$ (B, orange) from 70-85 eV, with the structure and the observed $O_{2,3}$- and $N_{6,7}$-edges labeled.

the $4f^n$ orbitals, the crystal-field is a small perturbation from $4f^{n-1}5d$, comparable with the Coulomb interaction, and dominates the spectra.[67] We thus expect that changes at the edge positions to be primarily controlled by changes in the 5d-orbital manifold, such as oxidation state and ligand field, but spin-orbit splitting in the 4f orbitals will give rise to a consistent SOC-defined split between the N_6 and N_7 edges. Preliminary calculations using a modified version of CTM4XAS performed by Grant Barton (Vura-Weis group) in collaboration with Frank de Groot also suggest that the intensity ratio between the N_6 and N_7 edges may also change with covalency.

The $O_{2,3}$- and $N_{6,7}$-edges of a key example platinum complex, platinum(II) octaethylporphyrin ($Pt^{II}OEP$) are shown in Figure 5.3A. The O_3-edge appear as a broad feature, with a rise starting at 53 eV and at lower energy relative to the $N_{6,7}$-edge. The O_2-edge appears as a weak broad feature at ~71 eV; this is a forbidden transition, but mixing within the orbital manifold allows for it to appear as a weak band. The $N_{6,7}$-edges appear at higher energy (73-80 eV) than both O-edges as a lower intensity doublet-like feature at 74.1 (N_7) and 77.4 eV (N_6). The ~3.3 eV split between N-edges arises from spin-orbit coupling (SOC) induced by the heavy metal center and is consistent with free ion XUV examples and observed $4f_{7/2}/4f_{5/2}$ binding energy in

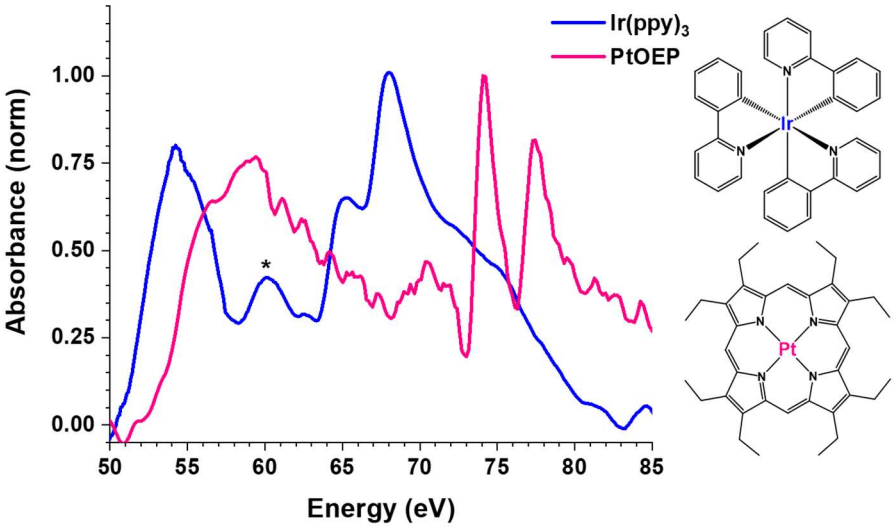

Figure 5.4 XUV $O_{2,3}$- and $N_{6,7}$-edges spectral overlay of $Pt^{II}OEP$ (pink) and $Ir^{III}(ppy)_3$ (blue); * = harmonic artifact.

XPS.[74,75] This split is always consistent regardless of oxidation or ligand field as it derives from the metal's intrinsic spin orbit coupling. While there has been some success with acquiring $N_{6,7}$-edge measurements of other platinum samples (see Fig. 5.3B with example), these have been overwhelmingly with platinum(II) square planar complexes with similar ligand scaffolds, though samples of platinum(II) and platinum(III) dimers (provided to us by the Castellano group) have been attempted but have been low signal (Fig. 5.12). Current efforts are targeting other platinum systems with significant changes in the ligand scaffold, oxidation state, and ligand field to determine the effect these have on the observed edges.

Iridium complexes have proved more amenable for sample preparation, and these iridium species will provide insight into what we might expect to see in the platinum complexes. Akin to platinum, iridium complexes similarly have O- and N-edges where the O_3-edge appears as a lower energy broad feature and the $N_{6,7}$-edges as a set of doublet-like peaks at higher energy. However, some key differences are present compared to platinum, using iridium(III) tris(2-phenylpyridine) ($Ir^{III}(ppy)_3$) as an example (Figure 5.4). First, the O_3- and $N_{6,7}$-edges are shifted downfield in

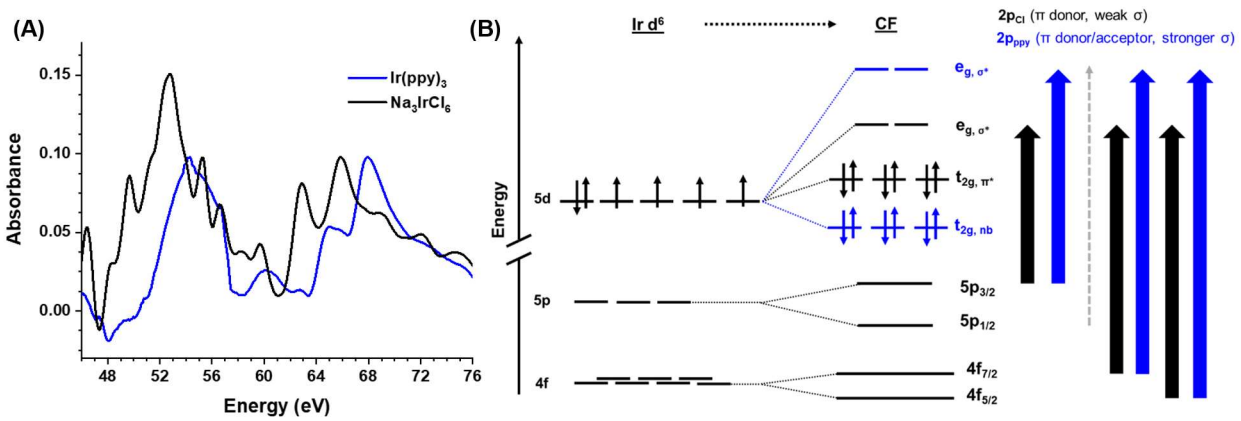

Figure 5.5 (A) XUV spectral overlay of $Ir^{III}(ppy)_3$ (blue) and $Na_3Ir^{III}Cl_6$ (black); (B) simplified orbital manifold diagram of an iridium d^6 species with introduction of an octahedral crystal field with different ligand strengths for $Ir^{III}(ppy)_3$ (in blue) and $Na_3Ir^{III}Cl_6$ (black).

energy from platinum, as iridium has a lower effective nuclear charge (Z) than platinum and the core electrons will thus have a lower binding energy. The two edges are also closer to each other, as there is crossover of the 4f and 5p levels across the 3rd row transition metals (implications for spectral analysis discussed in more details below).

Significant edge shifts occur in the O and N-edges of iridium between different ligand field strengths. In comparing $Na_3Ir^{III}Cl_6$ with $Ir^{III}(ppy)_3$, there are approximately 2 eV blueshifts in both the O- and N-edges when going from $Ir^{III}Cl_6^{3-}$ to $Ir^{III}(ppy)_3$ (Fig. 5.5A). This can be attributed to the stronger ligand field of the latter complex. Cl^- is a much weaker sigma donor compared to 2-phenylpyridine's N_{py} and C^-; the ppy ligand will result in higher energies for the empty d-orbitals compared to the chloride ligand and is consistent with the significant blue edge shift for both edges (Fig. 5.5B). Similar shifts based on ligand field strengths have also been noted at the L-edges for 3rd row metals; for example, in a recent work examining platinum macrocyclic compounds, exchanging weaker field ligands (porphyrin, chloride) for stronger field ligands (corrole, pyridine, alkyl) in octahedral Pt^{IV} compounds resulted in a 0.4 eV blue shift of the Pt L_3-edge that was confirmed by DFT to arise from the corresponding shift in the d-orbital manifold due to the strengthened ligand interactions.[76] While the shift observed between the iridium(III) species is

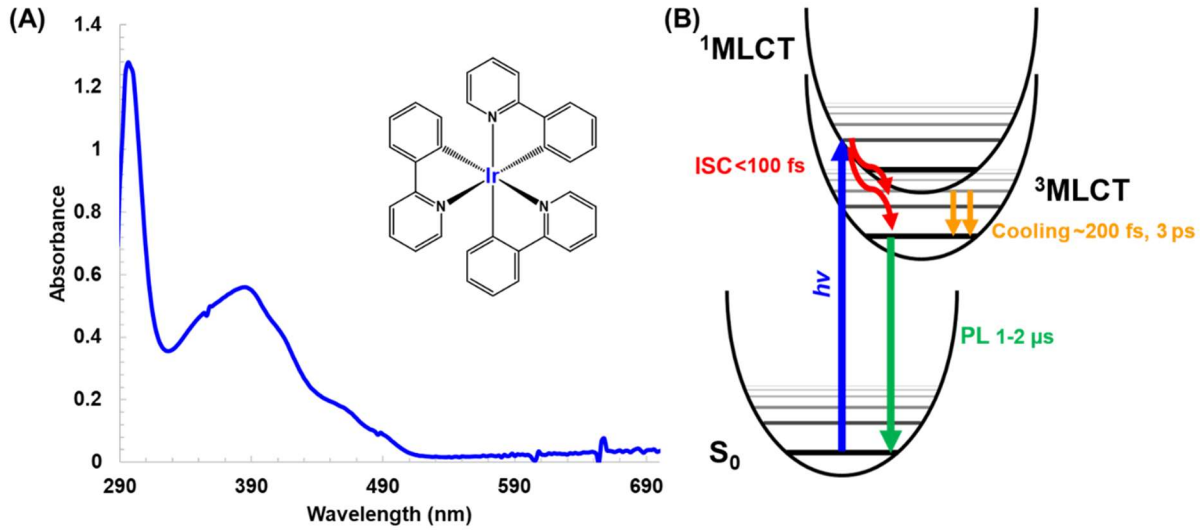

Figure 5.6 (A) UV-Vis of $Ir^{III}(ppy)_3$ thermally deposited on glass coverslip with overlaid structure; (B) simplified Jablonski diagram of $Ir^{III}(ppy)_3$ photodynamics from ^{1}MLCT excitation.

higher, this can be attributed to the more dramatic ligand field strength difference of six chloride ligands and three bidentate 2-phenylpyridine ligands. This shows that $O_{2,3}$- and $N_{6,7}$-edges can be used to track changes in ligand field on the metal center and provides support for changes in the 5d valence orbital manifold will result in changes at the XUV edges.

5.4 Transient $N_{6,7}$-edge XUV spectroscopy of $Ir^{III}(ppy)_3$

To determine whether we could track the photodynamics of these 3rd row metals with the XUV energy region, we pursued transient XANES spectroscopy of a "proof-of-concept" complex. $Ir^{III}(ppy)_3$ was chosen for its well-studied photodynamics,[16,77–81] applicability as a photosensitizer and catalyst in organic transformations,[1,11,16,29,41] and amenability to thermal deposition for sample preparation. Examining the UV-Vis spectrum of $Ir^{III}(ppy)_3$ (Fig. 5.6A), three main band ranges are present: one less than 300 nm that correspond to allowed, singlet π-π* transitions from the 2-phenylpyridine ligand, a broad band centered at 375 nm that corresponds to an allowed singlet metal-to-ligand charge transfer (^{1}MLCT, ^{1}d-π*) transition, and lower intensity ^{3}MLCT bands are clustered between 430-500nm.[32,77,82] Prior studies have found that for $Ir^{III}(ppy)_3$, the lowest excited

state is a triplet metal-to-ligand charge transfer (^{3}MLCT) involving occupied Ir 5d and unoccupied ppy-π^* orbitals, and similarly the emitting triplet state is a mixture of ^{3}MLCT substates close in energy with an ambient emission decay time of ~1.5-2 μs.[77,80] Literature optical transient absorption (OTA) and photoluminescence studies have shown $Ir^{III}(ppy)_3$ to have relatively simple photodynamics (Figure 5.6B): a 400 nm pump excites into the ^{1}MLCT state, which rapidly (less than 70-100 fs) undergoes intersystem crossing (ISC) to the ^{3}MLCT state manifold; this triplet state will undergo different vibrational cooling processes on the order of 200 fs to 5 ps before slowly relax back down to the singlet ground state over several microseconds.[16,17,31,32,43,77,78,82–89] While transient $L_{2,3}$-edge XANES of $Ir^{III}(ppy)_3$ have been performed in prior work, the authors primarily focused on identifying and tracking the emitting triplet state rather than the early photodynamics.[43,46]

The static O_3- and $N_{6,7}$-edge XUV spectrum of $Ir^{III}(ppy)_3$ shown in Figure 5.4 indicates the expected broad O_3-edge centered at 56 eV and the $N_{7,6}$-edges at 64.7 & 67.7 eV. The chosen focus for these initial transient experiments was the $N_{6,7}$-edges, with later transient experiments focused on the O_3-edge (*vide infra*). Due to the respective energies of the edges, these required different sets of HHG conditions to achieve sufficient flux at each O- and N-edges, detailed in the experimental section. Transient $N_{6,7}$-edge XANES was performed on $Ir^{III}(ppy)_3$ using 400 nm excitation, with an excitation fraction of ~14%. Both time zero (t_0) and the instrument response function (IRF) of 90 fs were independently measured by transient $M_{2,3}$-edge XANES of α-Fe_2O_3. Figure 5.7 shows averaged spectral slices at select delay times from -250 fs to 75 ps overlayed on the $N_{6,7}$-edge of $Ir^{III}(ppy)_3$. Upon excitation, bleach features appear at 64.5 and 67.5 eV along with a positive feature at 60.1 eV, with an additional weak positive feature centered at 70 eV. Within 1 ps these features have reached their maxima and start to decay. By 10 ps, all these features have

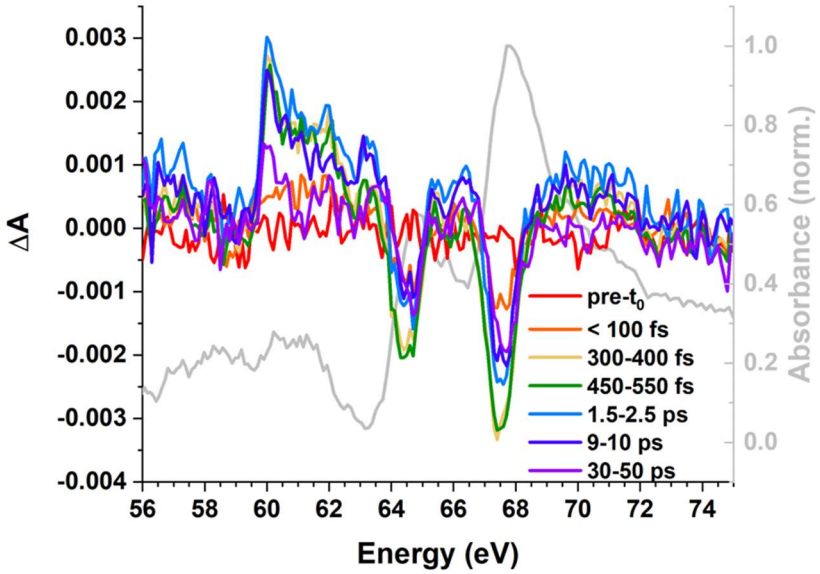

Figure 5.7 Select averaged time slices of transient $N_{6,7}$-edge XANES of $Ir^{III}(ppy)_3$ (400 nm excitation), with the ground $N_{6,7}$-edge XUV spectrum overlayed in grey.

flattened and remain so through the later delay times (up to 50 ps in Fig. 5.7 and to 100 ps in an older unaveraged data set).

The positive feature at 60.1 eV arises from the creation of a hole in the valence 5d orbital upon formation of the $^{1/3}$MLCT excited state, which can be now accessed from the electron being excited from the core orbitals by the XUV pulse. Given several options for potential 5d orbital manifolds, we considered two main possibilities that consider both O_h ligand field splitting and spin-orbit coupling laid out in Figure 5.8: (A) results in the created vacancy in the split t_{2g} set of orbitals having J = 5/2 character,[46] while (B) gives an effective J = ½ character observed in some iridium(IV) centers.[71] While it is possible to have a simpler manifold only considering an octahedral ligand field (as we have done up to this point), an earlier transient L-edge XAS of $Ir^{III}(ppy)_3$[43,46] has shown a similar positive, lower-energy excited state feature at the L_3-edge ($2p_{3/2}$ → 5d) but not at the L_2-edge ($2p_{1/2}$ → 5d). If no spin-orbit coupling were in place and differences in the d-orbit manifold just arose from strong crystal field (Fig. 5.8A), the expected MLCT states would be an S = ½ state (Ir(IV), d^5) and the vacancy would be in the t_{2g} set, which has mixed J =

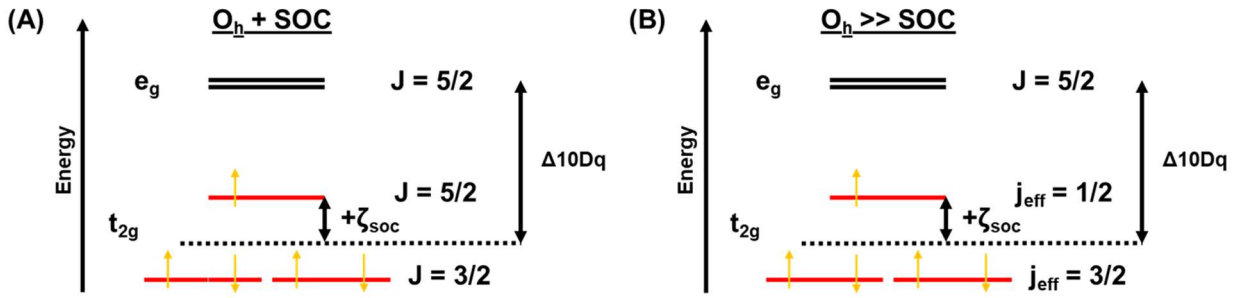

Figure 5.8 Potential 5d orbital manifolds for an Ir(IV) d^5 center in the MLCT excited state of $Ir^{III}(ppy)_3$. (A) 5d manifold with octahedral crystal field splitting and spin-orbit coupling; (B) 5d manifold where the octahedral field is much greater than SOC, resulting in an unusual jeff = ½ ground state seen in certain iridates.

5/2 and 3/2 character. Both L_2 ($2p_{1/2} \rightarrow 5d_{3/2}$) and L_3 ($2p_{3/2} \rightarrow 5d_{3/2,5/2}$) transitions would be allowed processes and result in new positive transient features at both edges; as there is only a new positive transition in the L_3 edge, both the ligand field and spin-orbit coupling effects must be considered.

As mentioned earlier, it is possible in cubic/octahedral iridium(IV) centers, particularly in iridates, to have strong octahedral ligand fields with SOC such that this results in an effective J = ½ ground state and thus the new 5d vacancy having j_{eff} = ½ character (Fig. 5.8B).[71] This would result in a transient positive excited state feature at the L_3-edge ($2p_{3/2} \rightarrow 5d_{1/2}$) but not at the L_2-edge . However, if both crystal field and SOC effects are in play, the resultant d-orbital manifold would display different multiplet splitting and J-values (Fig. 5.8A), where the vacancy is now best described as having J = 5/2 character.[71] This would still only result a positive excited state feature at the L_3-edge ($2p_{3/2} \rightarrow 5d_{5/2}$) but not the L_2-edge.

In the case of the XUV edges, the potential sources for the positive excited state absorption are transitions to the 5d orbital vacancy from $5p_{3/2}$, $4f_{7/2}$, or $4f_{5/2}$. Given that this vacancy is at lower energy regardless of J-value, it is unlikely that the positive feature arises from the $5p_{3/2}$ orbital transition, as that should be less than 53 eV (the start of the rise of the O_3-edge). We can now

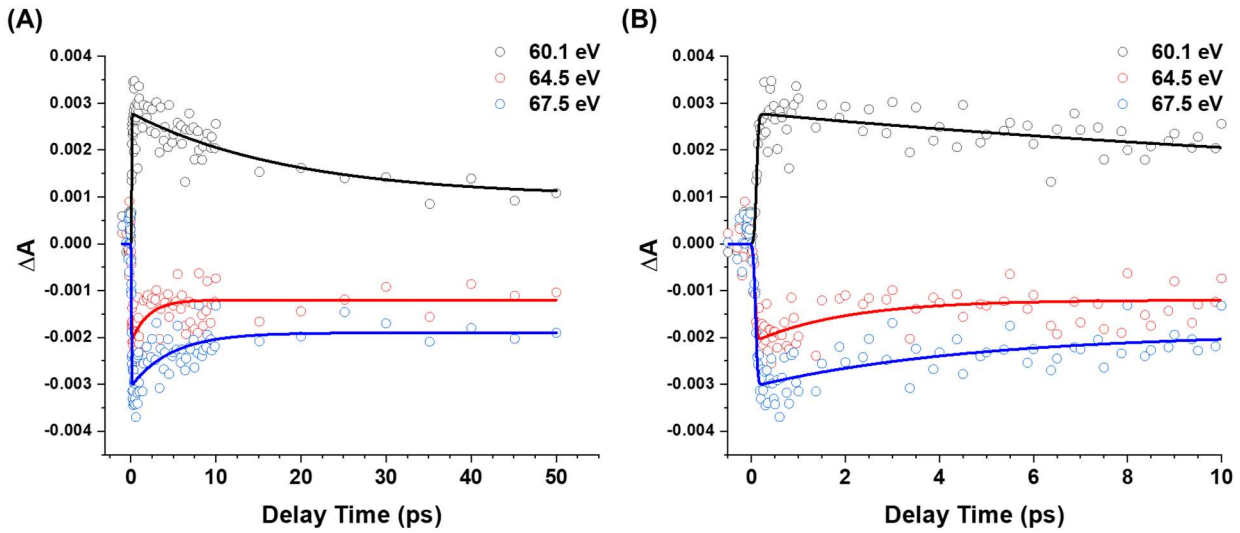

Figure 5.9 Kinetic analysis of transient $N_{6,7}$-edge features with 400 nm MLCT excitation of $Ir^{III}(ppy)_3$ out to (A) 50 ps and (B) 10 ps time delays; experimental data is indicated by the open circles while the kinetic fit is given as the solid line.

compare the J-values of the remaining 4f orbitals to the potential d-orbital vacancies. If the 5d-orbital manifold regime falls under LF >> SOC and thus the vacancy is $5d_{jeff = ½}$, then transitions from both sets of the 4f orbitals will be forbidden and thus no lower-energy positive feature should arise from the MLCT Ir(IV) states. However, given that a lower energy excited state absorption occurs, the 5d orbital manifold can likely be best described by the remaining option, where both crystal field and spin-orbit coupling are accounted for and the 5d vacancy has J = 5/2 character (Figure 5.8A). This means this positive excited state feature can be attributed from transitions of core $4f_{7/2}$ and $4f_{5/2}$ electrons into the vacancy in the split 5d t_{2g} orbitals in the ^{3}MLCT excited state. The energy difference of ~5.6 eV between the transient positive feature and the static N-edges are in line with the prior transient $L_{2,3}$-edge XANES work, where a 5.64 eV difference was observed.

Single-energy kinetic analysis at three key features (60.1 eV absorption, and 64.5 & 67.5 eV bleaches) were undertaken, and the traces are shown in Figure 5.9. Unfortunately, due to low signal-to-noise for the weak 70 eV absorption, reliable kinetic analysis could not be completed. For the three features tracked, each could be fit as a mono-exponential decay with a shelf, with the

Table 5.1 Parameters used in kinetic analysis at the transient $N_{6,7}$-edge features of $Ir^{III}(ppy)_3$

Energy (eV)	τ (ps)	Shelf (mA)
60.1	19 ± 3	+ 1.0
64.5	2.0 ± 0.7	- 1.2
67.5	4.8 ± 0.9	- 1.9

decay lifetimes and shelves tabulated in Table 5.1. Given the 90 fs IRF, we do not observe the initial ^{1}MLCT excited state after excitation as ISC occurs in 70-100 fs.[32,88] The features and fitted kinetic components thus solely arise from the ^{3}MLCT manifold and relaxation dynamics within or from this manifold. The bleach features have similar decay lifetimes at ~3-4 ps, while the positive absorption feature at 60.1 eV s has a longer decay lifetime of ~19 ps. While there is equilibration between the triplet substates within the ^{3}MLCT manifold and , this is only on the order of ~200 fs,[89] which is too short for either lifetimes observed in these data. The difference in lifetimes between these two types of features indicates that they could be coupling to relaxation modes, such as geometric relaxation of the ^{3}MLCT excited state from a "hot" state to the "cooled" state through different vibrational modes potentially coupled separately to the 5d e_g and t_{2g}- type orbitals. Prior computational work has shown an elongation of the Ir-C_{ppy}/N_{ppy} bonds in the ^{3}MLCT state compared to the ground state $Ir^{III}(ppy)_3$,[78] indicating a geometric distortion in the triplet state that could be coupled to two different vibrational modes. Transient optical and luminescence absorption of $Ir^{III}(ppy)_3$ in THF also observed a slow decay with a ~3 ps lifetime which was assigned to vibrational cooling to the surrounding matrix.[82,85,87,89,90] While this likely correspond to the 3-4 ps lifetime of the single decay component of the bleach features, this is too short to correspond the positive absorption feature decay component lifetime of ~19 ps. Computational calculations by Justin Malme (Vura-Weis group) are underway to identify potential candidates for vibrational modes in this triplet state to assist in identifying the source of these relaxation dynamics. Finally, the shelves to fit all three features are required due to the final observed excited state living

much longer than the latest timepoint collected (50 ps); this is unsurprising, given that the ^{3}MLCT excited state lifetime occurs on the order of at least one microsecond,[32,82,89,90] several orders of magnitude longer than our latest time delay.

Overall, transient iridium $N_{6,7}$-edge of $Ir^{III}(ppy)_3$ using XUV spectroscopy is in excellent agreement with literature optical and L_3-edge XAS photodynamics. We were able to assign the transient features to the long-lived ^{3}MLCT excited state and observe early relaxation dynamics in this state, observing a new excited state decay not observed in the prior optical or luminescence experiments.[82,89,90] Current computational calculations are ongoing to identify the source of the two different relaxation decays into the long-lived ^{3}MLCT excited state, potentially from different vibrational modes related to geometric changes in the excited state.

5.5 Transient O_3-edge XUV spectroscopy of $Ir^{III}(ppy)_3$

Following up on the $N_{6,7}$-edge experiments, we performed transient O_3-edge XANES of $Ir^{III}(ppy)_3$ to determine if different dynamics or information are obtained with this edge for the complex. We anticipated that the O_3-edge would provide similar dynamics to the $N_{6,7}$-edge but may furnish additional insight due to the 5p core orbital potentially coupling to different vibrational modes. Both time zero (t_0) and the instrument response function (IRF) of 123 fs were independently measured by transient XANES of PbI_2 at the iodine $N_{4,5}$-edge due to the argon gas used as the HHG medium in generating sufficient flux at the lower energy range (< 56 eV). Figure 5.7 shows averaged spectral slices at select delay times from -250 fs to 100 ps overlayed on the static O_3-edge of $Ir^{III}(ppy)_3$. Upon excitation, a positive feature centered at 48.3 eV appears, along with minor bleach features below 43 eV and weaker higher energy features between 50-57 eV. Within 1 ps these features have reached their maxima and start to decay. By 10 ps, all these features have flattened out and are still present at the maximum 100 ps range used.

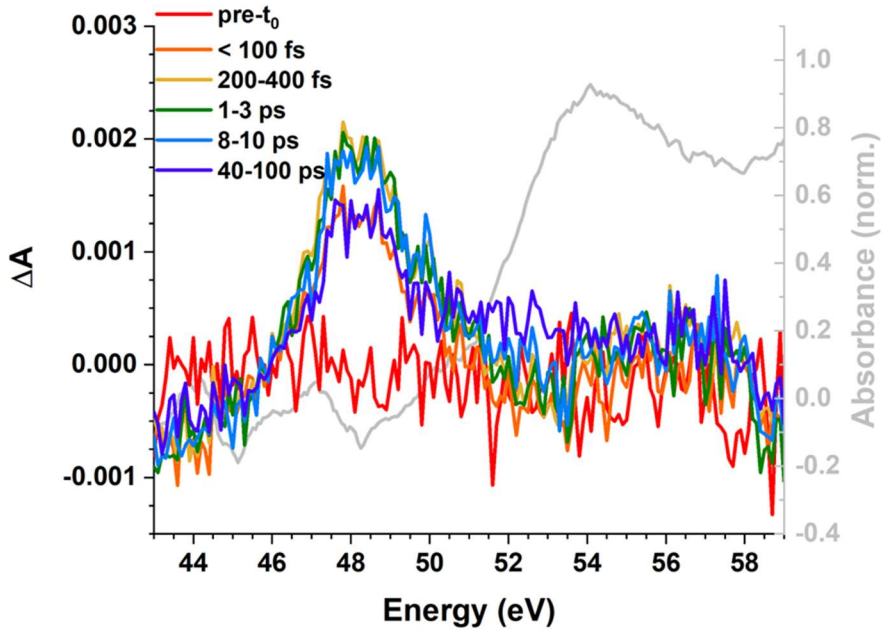

Figure 5.10 Select averaged time slices of transient O_3-edge XANES of $Ir^{III}(ppy)_3$ with 400 nm excitation, with the static O_3-edge spectrum overlaid in grey.

Analysis of the observed features for the O_3-edge XANES generally indicate similar dynamics as the transient $N_{6,7}$-edge XANES. The transient positive feature appears ~5-6 eV lower energy compared to the static O_3-edge akin to the transient positive feature, indicative that this feature also arises from the generated 5d t_{2g} hole in the MLCT states. There is not a distinct bleach feature for the O_3-edge, likely arising from distribution of the depletion over the broad O_3-edge in the GS convoluted with potential blue shift of the O_3-edge in the oxidized excited state. There may be a weak bleach feature and weak positive feature (see Figure 5.14 for a 2D transient O_3-edge plot at early delay times) at ~53.5 eV and 54-57 eV, respectively, but further data collection and averaging are required for sufficient signal-to-noise to confirm these features. The low energy bleach feature is attributed to increased ligand photoionization, which has been seen before in prior work in our group.

Single energy kinetic analysis of the positive feature at 48.3 eV, and the trace is shown in Figure 5.11. This was fitted to a mono-exponential decay with a long-time shelf like in the transient

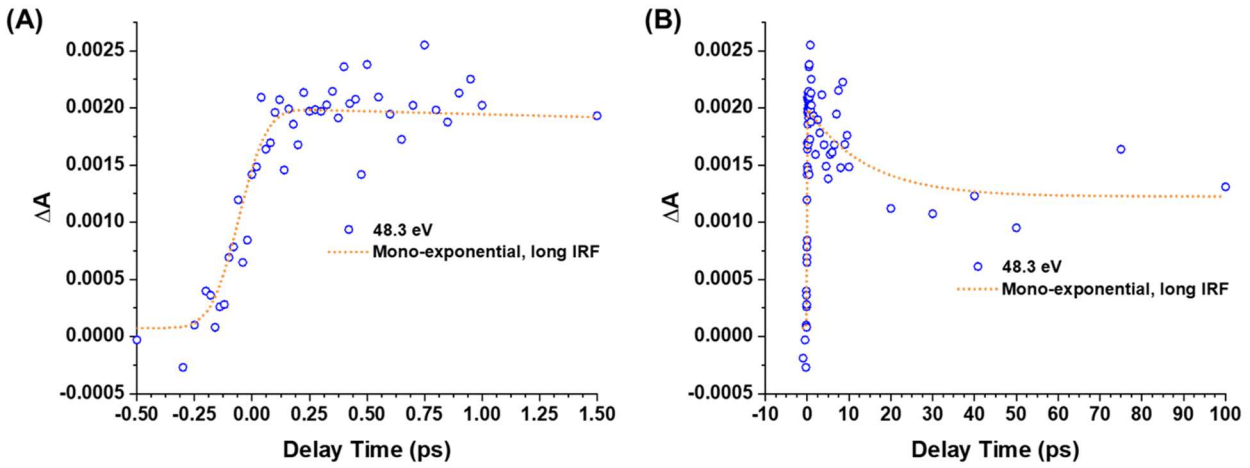

Figure 5.11 Kinetic analysis of the transient O_3-edge feature at 48.3 eV with 400 nm MLCT excitation of $Ir^{III}(ppy)_3$ out to (A) 1.5 ps and (B) 100 ps time delays; experimental data is indicated by the open circles while the mono-exponential kinetic fit with a long IRF is given as the dotted line (see Fig. 5.15 for comparisons to other potential kinetic fits).

$N_{6,7}$-edge XANES; however, this required a longer IRF of ~240 fs (Table 5.2), as the experimental IRF did not match the (see Figure 5.15 for comparisons). A sequential bi-exponential decay using the experimental IRF of 123 fs was attempted to fit the kinetic data (tabulated in Table 5.3), but the earlier short time component has a lifetime on the order of the experimental IRF and a standard error nearly as large as the lifetime itself. This suggested while there is potentially an early, short-lived feature on a similar timescale as the ~120 fs IRF, this is convoluted with the IRF rise and will need to be extracted. This led us to primarily analyze the kinetic data using the mono-exponential decay function. The kinetic of the transient O_3-edge positive feature match well to the transient $N_{6,7}$-edge positive feature, with the O_3-edge ~14 ps decay component within error of the $N_{6,7}$-edge decay component. The similar late kinetics for these positive features indicates that either the O_3-edge or $N_{6,7}$-edge could be used to track the photodynamics of $Ir^{III}(ppy)_3$ or similar iridium photosensitizers.

However, the potential presence of an early, short-lived feature by transient O_3-edge XANES that is not present in transient $N_{6,7}$-edge XANES points to potential differences between

Table 5.2 Parameters used in the mono-exponential kinetic fit at 48.3 eV in the transient O_3-edge XANES of $Ir^{III}(ppy)_3$

Fit	IRF (fs)	τ_2 (ps)	Shelf (mA)
Mono-component	245	14 ± 6	+ 1.2

the edges' observed dynamics. Time-resolved optical and photoluminescence studies indicate that ISC occurs in less than 70-100 fs,[82,85,87,89,90] which is much faster than either experimental IRF in this work and thus likely not the potential early feature observed. ^{3}MLCT substate population redistribution and intramolecular vibrational redistribution (IVR) for $Ir^{III}(ppy)_3$ has been found to be on the order of 150-200 fs based on time-resolved photoluminescence.[77,78,82,85,87,89–91] Given that the main difference between the O_3- and $N_{6,7}$-edges are the starting core orbitals, it is likely that the potential short-lived state involves changes in iridium 5p orbital interactions, such as metal-ligand bond length elongation facilitated by vibrational relaxation, in this state.

Overall, these results show that transient O_3-edge XANES can be used to track excited state dynamics of $Ir^{III}(ppy)_3$ and is generally in agreement with the earlier transient $N_{6,7}$-edge XANES. An additional short-lived state, likely arising from IVR, may be present by transient O_3-edge XANES not present in the analogous $N_{6,7}$-edge experiments, suggesting that different information about the excited state manifold could potentially be extracted by looking at the different XUV edges. Current and future work are focused on collecting more data at the O_3-edge to confirm the presence of this possible early short-lived state and examine other precious metal photosensitizers and catalysts as described *vide infra*.

5.6 Discussions on implications for current and future directions

Iridium & platinum have shown success, but other 3rd row metals of interest also have measurable $O_{2,3}$- and $N_{6,7}$-edges within accessible XUV energies. For example, osmium(II) complexes are known photosensitizers[39,92–94] and have received recent interest as near-IR

photoredox catalysts[40,95] and as potential phototherapy agents[96] in cancer treatment. Using our typical Ar and Ne gas for HHG XUV pulse generation, any edges below 40 eV would not be observable due to insufficient flux, so it expected that the $N_{6,7}$-edge of tantalum-based coordination complexes and both $O_{2,3}$- and $N_{6,7}$-edges of hafnium complexes may be too low to observe; however, unpublished work from our group has use krypton gas to achieve flux lower than 40 eV, so this may allow for us to examine these edges as Leone and coworkers recently did in WS_2 (30-45 eV).[66] Similarly, any edges above 90 eV would be inaccessible, such as gold's 4f-(6,7)d transitions at 110-120 eV; a new beamline under construction in the Vura-Weis lab aims to access the 90-200 eV XUV region and thus allow observations of these higher-energy features.

Within the current available energy range, 3rd row metal coordination complexes based on tantalum through gold (elements 73-39) could be measured with a potential caveat. As describe previously, lower *Z* 3rd row metals such as Ta and W have the $O_{2,3}$- and $N_{6,7}$-edge energies reversed. The 4f binding energy increases more quickly than the 5p binding energy with increasing Z and ionization, resulting in the observed edge flip with the crossover at rhenium.[65] As the "crossover" element, Re has the 4f and 5p binding energies at similar energies, resulting in overlapping transitions from these orbitals to the valence ones as observed in the metallic/free ion form (see Fig. 5.2A). This convolution of the $O_{2,3}$- and $N_{6,7}$-edges will likely prove incredibly challenging to fit without sufficient Re-based samples for comparison and computational calculations to ensure appropriate assignments of transitions.

The sensitivity of the O_3- and $N_{6,7}$-edges in the XUV region show promise for investigating the photophysics and dynamics of platinum- or iridium-based systems and likely other 3rd row metal systems. The sensitivity of the edges to ligand field strength indicates that changes in the edge features could be observed with changing the geometry and the oxidation state similar to

those observed at the higher energy $L_{2,3}$-edges (e.g. blueshift with increased oxidation[97,98]), with current studies ongoing to confirm this. We are expanding this technique out to other systems where the metal contribution to the photodynamics is unclear, such as platinum donor-bridge-acceptor systems where $(PBu_3)ClPt^{II}NAP$ functioning as reference for a system where there is potential MLCT photoexcitation.[99] This technique may also provide an accessible in-house, tabletop method for targeting separate metal edges in duo-metal catalysis with a 3rd row metal photosensitizer and another metal chemical catalyst, such as an iridium(III) photosensitizer paired with a nickel or copper catalyst as seen with several organic transformations.[1] Alternatively, the O_3- and $N_{6,7}$-edges could be coupled to different dynamics at the metal center of solid state materials, allowing for multiple probes with the same experiments akin to recent transient XUV of perovskites[100,101] and WS_2.[66]

Given that ligand substitution and modifications are a crucial method for tuning the photoproperties of precious earth metal sensitizers,[21,29,31] XUV spectroscopy may provide a useful spectroscopic handle for interrogating ligand substitution effects on metal-centered photodynamics and electronic structure at the O_3- and $N_{6,7}$-edges of these species. Spin-orbit coupling must also be accounted for when analyzing these spectra. For example, the N_7- and N_6-edges will always be separated into its spin orbit components by a particular energy for each 3rd row metal (3.35 eV Pt, 3.2 eV Ir) due the intrinsic spin-orbit coupling of the metal 4f orbitals. The metal 5d spin-orbit coupling component will affect the d-orbital manifold and thus which transitions will be allowed; for example, the transient $N_{6,7}$-edge spectra would have different allowed transitions based on the strength of the crystal field parameters and spin-orbit coupling, as described *vide supra*. This may provide a spectroscopic handle for investigating spin-orbit coupling effects in these heavy metals, such as the unusual $j_{eff} = ½$ ground state of iridates.[72,73,102]

5.7 Conclusion

3rd row transition metals are ubiquitous catalysts and photosensitizers, and there is interest in using transient XAS spectroscopy to complement OTA to provide insight into metal- and ligand-based dynamics and processes. L-edge efforts are hampered by insufficient time resolution to examine early or ultrafast dynamics. XUV spectroscopy targets the O and $N_{6,7}$-edges of 3rd row metals and could provide a useful handle on examining ultrafast dynamics in these systems. We examined several platinum(II) and iridium(III) coordination complexes at their $O_{2,3}$- and $N_{6,7}$-edges using XUV, providing initial insights into the effect of ligand field on the edges. We successfully performed transient $N_{6,7}$-edge and O_3-edge XANES on $Ir^{III}(ppy)_3$, where we identified the formation of the ^{3}MLCT excited state and observed early relaxation dynamics. This showed that we can track metal-based photodynamics at an XUV edge for 3rd row metal coordination complexes. Implications on the utility of $O_{2,3}$- and $N_{6,7}$-edge XUV spectroscopy with other 3rd row transition metal complexes were also discussed. Current and future efforts on this project are focused on characterizing more Pt and Ir complexes for static comparisons and expanding transient experiments to other 3rd row metal systems to investigate their metal-based photodynamics.

Acknowledgements: We thank Grant Barton (Vura-Weis group) and Dr. Frank de Groot for helpful discussion of ligand field multiplet theory and Justin Malme for computational assistance. We also thank the Weinstein group and Castellano group (NCSU) for generously providing $(PBu_3)ClPt^{II}NAP$ and $[Pt^{II}_2(ppy)_2(pyt)_2]$, respectively.

5.8 Experimental

General Methods. Iridium(III) tris(2-pheynylpyridine), platinum(II) octaethylporphyrin, and sodium hexachloroiridate(III) were purchased from Sigma Aldrich. $(PBu_3)ClPt^{II}NAP$ was

synthesized according to literature.[99] $[Pt^{II}_2(ppy)_2(pyt)_2]$ was synthesized according to literature procedure. All other materials were purchased through commercial suppliers.[103] Thin film samples were prepared in through sublimation using a house-build thermal evaporator, drop or spuncast onto 100 nm Si_3N_4 substrate, or through embedment into a polymer film as described in prior work; specific details are given below. Static UV-Vis spectra were acquired to confirm sample identity and to check for degradation pre- and post-experiments.

Sample Preparation. $Ir^{III}(ppy)_3$ samples (~114nm thickness) were deposited onto 50 and 100 nm Si_3N_4 membranes using the thermal evaporator and stored in the dark underneath dinitrogen atmosphere in a drybox. $Na_3Ir^{III}Cl_6$ samples were prepared by taking a concentrated, filtered solution of the target complex in dimethylformamide and drop-casting (2 drops) onto 100 nm Si_3N_4 membranes. $Pt^{II}OEP$ samples (~70nm thickness) were deposited onto 100 nm Si_3N_4 membranes using the thermal evaporator and stored in the dark. $(PBu_3)ClPt^{II}NAP$ samples were prepared through embedment in polymer films:[104] a concentrated, filtered solution of the complex in dichloromethane was added to a solution of 3% PS in DCM in a 3:1 ratio. 2-3 drops (~50-100 uL) were deposited onto a cleaned glasscover slip and slipcasted using another glasscover slip. The resultant embedded polymer films were allowed to dry before delamination from the glass and placement onto a sample frame. These samples were stored in the dark. $[Pt^{II}_2(ppy)_2(pyt)_2]$ samples were prepared by spin-casting a concentrated, filtered solution of the complex in toluene (2 drops) onto 100 nm Si_3N_4 membranes.

Static XUV Spectroscopy. The tabletop XUV probe was generated through the process of high-harmonic generation (HHG) as described in prior works.[51,54] A schematic of the house-built tabletop XUV instrument is provided in Scheme 5.1 from reference 51. In brief, the 1 kHz, 35 fs, 800 nm pulse of the NIR driving laser is focused into a semi-infinite gas containing approximately

100 Torr of neon or 45 torr of argon to generate approximately 20 fs XUV pulses in the energy range from 40-90 eV. The residual NIR pulses were filtered using a 100 nm thick Al foil or 50 nm Al/300 nm Zr, accessing 40-75 eV or 60-90 eV respectively, and creating a flux of 10^7 photons per pulse at the sample position. The spectrometer resolution is measured using the absorption lines of Kr^+ and Xe^+ and averaged ~0.35 eV FWHM for these experiments. All experiments are performed under high vacuum (10^{-7}-10^{-3} torr) as the XUV photons are absorbed by ambient air.

Transient XUV Spectroscopy. The tabletop XUV probe was generated through the process of high-harmonic generation (HHG) as described in prior work.[51] The 1 kHz, 35 fs, 800 nm pulse of the NIR driving laser is focused into a semi-infinite gas containing approximately 100 Torr of neon or 49.1 torr of argon gas to generate approximately 20 fs XUV pulses in the energy range from 55-80 eV or 35-60 eV, respectively. The residual NIR pulses were filtered using a 100 nm (Ne) or 200 nm (Ar) thick Al foil and creating a flux of ~10^5 photons per pulse at 64.7 eV (Ne) or 53.5 (Ar) at the sample position. The spectrometer resolution is measured using the absorption lines of Kr^+ and Xe^+ and averaged ~0.4 eV (Ne) and 0.33 eV (Ar) FWHM for these experiments. A secondary output from the same laser source was aligned to a delay stage and sent through an α-BBO crystal to generate the 400 nm, ~50 fs pump pulse via second harmonic generation. Transient absorption of a thin film of Fe_2O_3 is used to determine t_0 position and the instrument response function (IRF) of 90 fs FWHM for Ne, while PbI_2 was used for Ar conditions to determine t_0 position and the IRF of 123 fs FWHM. The pump fluence of 1.7 mJ/cm^2 at 400 nm for Ne conditions corresponds to an average excitation fraction of 14% per iridium center, while 1.1 mJ/cm^2 at 400 nm for Ar conditions corresponds to an average excitation fraction of 9% per iridium center. To further avoid sample damage during transient data collection, samples are raster scanned, gas cooled using N_2, and regularly checked for damage by static XUV.

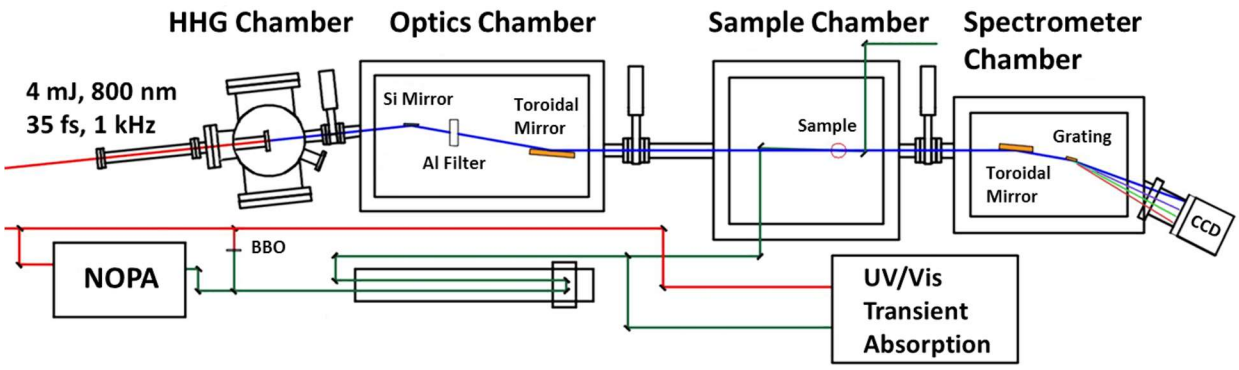

Scheme 5.1 HHG XUV instrumentation set-up from reference 51.

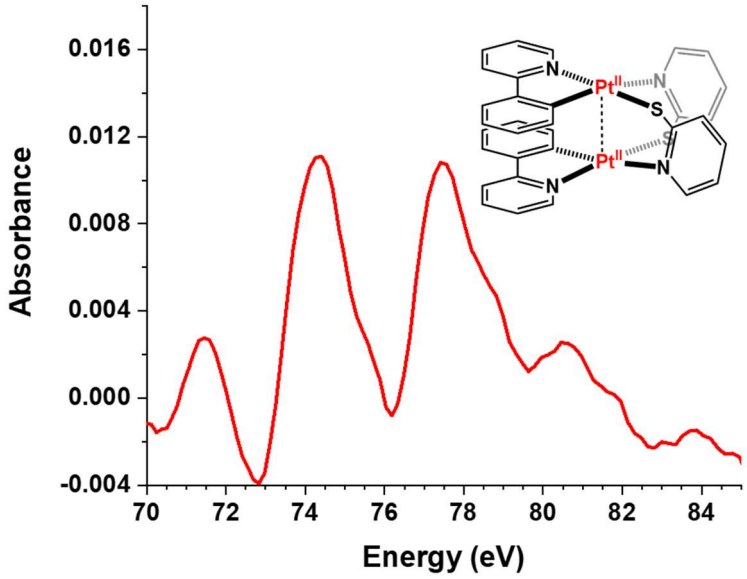

Figure 5.12 $N_{6,7}$-edge XUV spectrum of the platinum(II) dimer $[Pt^{II}_2(ppy)_2(pyt)_2]$.

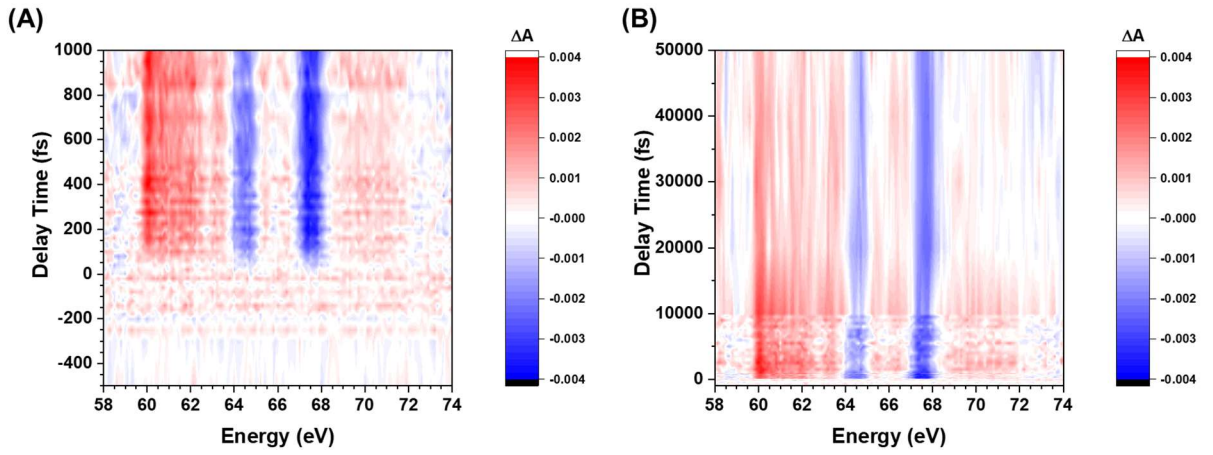

Figure 5.13 2D plot of transient $N_{6,7}$-edge XANES of $Ir^{III}(ppy)_3$ with 400 nm excitation at short (A) and long (B) delay times.

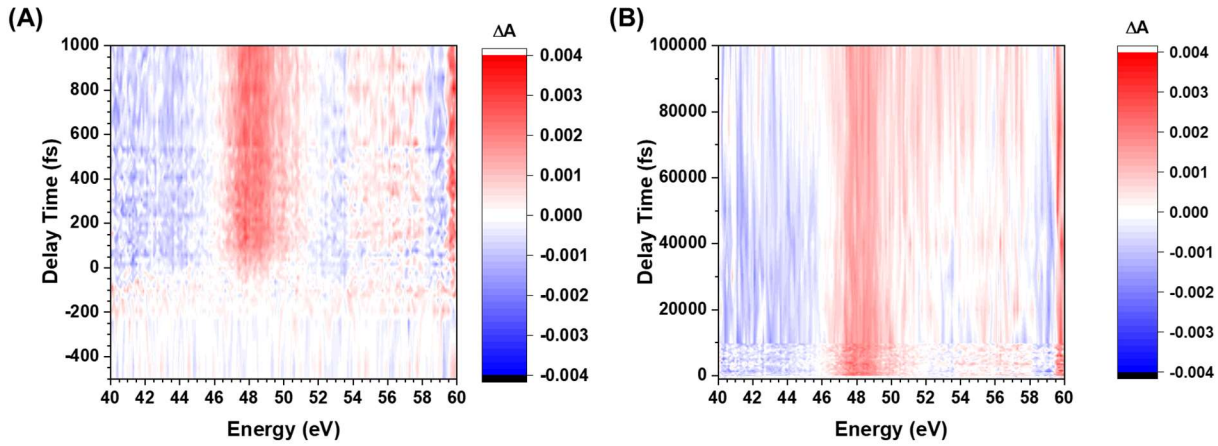

Figure 5.14 2D plot of transient O_3-edge XANES of $Ir^{III}(ppy)_3$ with 400 nm excitation at short (A) and long (B) delay times.

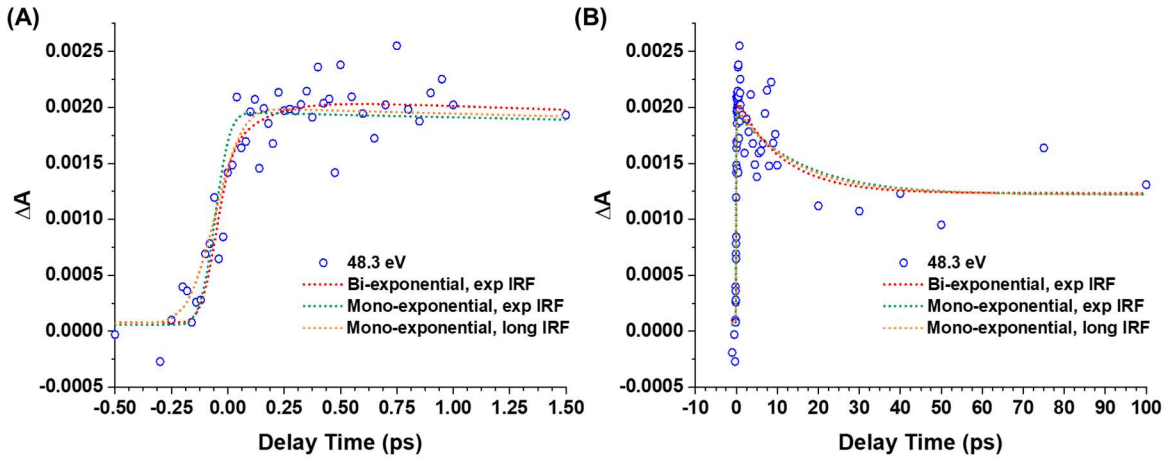

Figure 5.15 Kinetic analysis of the transient O_3-edge feature at 48.3 eV with 400 nm MLCT excitation of $Ir^{III}(ppy)_3$ out to (A) 1.5 ps and (B) 100 ps time delays; experimental data is indicated by the open circles. The bi-exponential sequential decay fit with the experimental 123 fs IRF is given as the red dotted line, the mono-exponential kinetic fit with the experimental IRF is given as the green dotted line, and the mono-exponential kinetic fit with the "long" IRF (245 fs) is given as the yellow dotted line.

Table 5.3 Parameters used in the mono- and sequential bi-exponential decay kinetic analysis at 48.3 eV for transient O_3-edge XANES of $Ir^{III}(ppy)_3$ with 400 nm MLCT excitation

Fit	IRF (fs)	τ_1 (ps)	τ_2 (ps)	Shelf (mA)
Mono-component	123 (set)	-	16 ± 8	+ 1.2
Mono-component	245	-	14 ± 6	+ 1.2
Bi-component (seq.)	123 (set)	0.16 ± 0.11	11 ± 3	+ 1.2

5.9 References

(1) Chan, A. Y.; Perry, I. B.; Bissonnette, N. B.; Buksh, B. F.; Edwards, G. A.; Frye, L. I.; Garry, O. L.; Lavagnino, M. N.; Li, B. X.; Liang, Y.; Mao, E.; Millet, A.; Oakley, J. V.; Reed, N. L.; Sakai, H. A.; Seath, C. P.; MacMillan, D. W. C. Metallaphotoredox: The Merger of Photoredox and Transition Metal Catalysis. *Chem. Rev.* **2022**, *122* (2), 1485–1542.

(2) Hoque, M. E.; Hassan, M. M. M.; Chattopadhyay, B. Remarkably Efficient Iridium

Catalysts for Directed C(Sp2)-H and C(Sp3)-H Borylation of Diverse Classes of Substrates. *J. Am. Chem. Soc.* **2021**, *143* (13), 5022–5037.

(3) Windle, C. D.; Perutz, R. N. Advances in Molecular Photocatalytic and Electrocatalytic CO 2 Reduction. *Coord. Chem. Rev.* **2012**, *256* (21–22), 2562–2570.

(4) Maity, B.; Zhu, C.; Rueping, M.; Cavallo, L. Mechanistic Understanding of Arylation vs Alkylation of Aliphatic Csp3-H Bonds by Decatungstate-Nickel Catalysis. *ACS Catal.* **2021**, *11* (22), 13973–13982.

(5) Freyschlag, C. G.; Madix, R. J. Precious Metal Magic: Catalytic Wizardry. *Mater. Today* **2011**, *14* (4), 134–142.

(6) Fürstner, A. Gold and Platinum Catalysis—a Convenient Tool for Generating Molecular Complexity. *Chem. Soc. Rev.* **2009**, *38* (11), 3208–3221.

(7) Schrock, R. R.; Hoveyda, A. H. Molybdenum and Tungsten Imido Alkylidene Complexes as Efficient Olefin-Metathesis Catalysts. *Angew. Chemie - Int. Ed.* **2003**, *42* (38), 4592–4633.

(8) Cadu, A.; Andersson, P. G. Iridium Catalysis: Application of Asymmetric Reductive Hydrogenation. *Dalt. Trans.* **2013**, *42* (40), 14345–14356.

(9) Huo, H.; Shen, X.; Wang, C.; Zhang, L.; Röse, P.; Chen, L. A.; Harms, K.; Marsch, M.; Hilt, G.; Meggers, E. Asymmetric Photoredox Transition-Metal Catalysis Activated by Visible Light. *Nature* **2014**, *515* (7525), 100–103.

(10) Meister, T. K.; Riener, K.; Gigler, P.; Stohrer, J.; Herrmann, W. A.; Kühn, F. E. Platinum Catalysis Revisited-Unraveling Principles of Catalytic Olefin Hydrosilylation. *ACS Catal.* **2016**, *6* (2), 1274–1284.

(11) Cannalire, R.; Pelliccia, S.; Sancineto, L.; Novellino, E.; Tron, G. C.; Giustiniano, M. Visible Light Photocatalysis in the Late-Stage Functionalization of Pharmaceutically Relevant Compounds. *Chem. Soc. Rev.* **2021**, *50* (2), 866–897.

(12) Joe, C. L.; Doyle, A. G. Direct Acylation of C(Sp3)-H Bonds Enabled by Nickel and Photoredox Catalysis. *Angew. Chemie - Int. Ed.* **2016**, *55* (12), 4040–4043.

(13) Huo, H.; Wang, C.; Harms, K.; Meggers, E. Enantioselective, Catalytic Trichloromethylation through Visible-Light-Activated Photoredox Catalysis with a Chiral Iridium Complex. *J. Am. Chem. Soc.* **2015**, *137* (30), 9551–9554.

(14) Xu, H.; Chen, R.; Sun, Q.; Lai, W.; Su, Q.; Huang, W.; Liu, X. Recent Progress in Metal-Organic Complexes for Optoelectronic Applications. *Chem. Soc. Rev.* **2014**, *43* (10), 3259–3302.

(15) Stennett, E. M. S.; Ciuba, M. A.; Levitus, M. Photophysical Processes in Single Molecule Organic Fluorescent Probes. *Chem. Soc. Rev.* **2014**, *43* (4), 1057–1075.

(16) Gildea, L. F.; Williams, J. A. G. *Iridium and Platinum Complexes for OLEDs*; Woodhead Publishing Limited, 2013.

(17) Lees, A. J.; Long, C. *Photophysics of Organometallics*; Springer US: New York, NY,

2010; Vol. 29.

(18) Yersin, H. *Highly Efficient OLEDs with Phosphorescent Materials*, 1st ed.; WILEY-VCH Verlag GmbH & Co. KGaA, 2008.

(19) Kunkely, H.; Vogler, A. Water Splitting by Light with Osmocene as Photocatalyst. *Angew. Chemie - Int. Ed.* **2009**, *48* (9), 1685–1687.

(20) Lowry, M. S.; Bernhard, S. Synthetically Tailored Excited States: Phosphorescent, Cyclometalated Iridium(III) Complexes and Their Applications. *Chem. - A Eur. J.* **2006**, *12* (31), 7970–7977.

(21) Chapman, S. J.; Swords, W. B.; Le, C. M.; Guzei, I. A.; Toste, F. D.; Yoon, T. P. Cooperative Stereoinduction in Asymmetric Photocatalysis. *J. Am. Chem. Soc.* **2022**, *144* (9), 4206–4213.

(22) Genzink, M. J.; Kidd, J. B.; Swords, W. B.; Yoon, T. P. Chiral Photocatalyst Structures in Asymmetric Photochemical Synthesis. *Chem. Rev.* **2022**, *122* (2), 1654–1716.

(23) Crisenza, G. E. M.; Faraone, A.; Gandolfo, E.; Mazzarella, D.; Melchiorre, P. Catalytic Asymmetric C–C Cross-Couplings Enabled by Photoexcitation. *Nat. Chem.* **2021**, *13* (6), 575–580.

(24) He, J.; Bai, Z. Q.; Yuan, P. F.; Wu, L. Z.; Liu, Q. Highly Efficient Iridium-Based Photosensitizers for Thia-Paternò-Büchi Reaction and Aza-Photocyclization. *ACS Catal.* **2021**, *11* (1), 446–455.

(25) Zhang, X.; Qin, J.; Huang, X.; Meggers, E. One-Pot Sequential Photoredox Chemistry and Asymmetric Transfer Hydrogenation with a Single Catalyst. *European J. Org. Chem.* **2018**, *2018* (4), 571–577.

(26) Vara, B. A.; Patel, N. R.; Molander, G. A. O-Benzyl Xanthate Esters under Ni/Photoredox Dual Catalysis: Selective Radical Generation and Csp3-Csp2 Cross-Coupling. *ACS Catal.* **2017**, *7* (6), 3955–3959.

(27) Zhang, X.; MacMillan, D. W. C. Alcohols as Latent Coupling Fragments for Metallaphotoredox Catalysis: Sp3-Sp2 Cross-Coupling of Oxalates with Aryl Halides. *J. Am. Chem. Soc.* **2016**, *138* (42), 13862–13865.

(28) Diluzio, S.; Connell, T. U.; Mdluli, V.; Kowalewski, J. F.; Bernhard, S. Understanding Ir(III) Photocatalyst Structure-Activity Relationships: A Highly Parallelized Study of Light-Driven Metal Reduction Processes. *J. Am. Chem. Soc.* **2022**, *144* (3), 1431–1444.

(29) Evans, R. C.; Douglas, P.; Winscom, C. J. Coordination Complexes Exhibiting Room-Temperature Phosphorescence: Evaluation of Their Suitability as Triplet Emitters in Organic Light Emitting Diodes. *Coord. Chem. Rev.* **2006**, *250* (15–16), 2093–2126.

(30) Gawelda, W.; Johnson, M.; De Groot, F. M. F.; Abela, R.; Bressler, C.; Chergui, M. Electronic and Molecular Structure of Photoexcited [RuII(Bpy) 3]2+ Probed by Picosecond X-Ray Absorption Spectroscopy. *J. Am. Chem. Soc.* **2006**, *128* (15), 5001–5009.

(31) Monti, F.; Baschieri, A.; Sambri, L.; Armaroli, N. Excited-State Engineering in Heteroleptic Ionic Iridium(III) Complexes. *Acc. Chem. Res.* **2021**, *54* (6), 1492–1505.

(32) Ichimura, K.; Kobayashi, T.; King, K. A.; Watts, R. J. Excited-State Absorption Spectroscopy of Otho-Metalated Ir(III) Complexes. *J. Phys. Chem.* **1987**, *91* (24), 6104–6106.

(33) Kiefer, L. M.; King, J. T.; Kubarych, K. J. Dynamics of Rhenium Photocatalysts Revealed through Ultrafast Multidimensional Spectroscopy. *Acc. Chem. Res.* **2015**, *48* (4), 1123–1130.

(34) Cannizzo, A.; Blanco-Rodríguez, A. M.; Nahhas, A. El; Šebera, J.; Záliš, S.; Vlček, A.; Chergui, M. Femtosecond Fluorescence and Intersystem Crossing in Rhenium(I) Carbonyl-Bipyridine Complexes. *J. Am. Chem. Soc.* **2008**, *130* (28), 8967–8974.

(35) Cummings, S. D.; Eisenberg, R. Tuning the Excited-State Properties of Platnum(II) Diimine Dithiolate Complexes. *J. Am. Chem. Soc.* **1996**, *118* (8), 1949–1960.

(36) Delor, M.; Keane, T.; Scattergood, P. A.; Sazanovich, I. V.; Greetham, G. M.; Towrie, M.; Meijer, A. J. H. M.; Weinstein, J. A. On the Mechanism of Vibrational Control of Light-Induced Charge Transfer in Donor-Bridge-Acceptor Assemblies. *Nat. Chem.* **2015**, *7* (9), 689–695.

(37) Liu, Y.; Jiang, S.; Glusac, K.; Powell, D. H.; Anderson, D. F.; Schanze, K. S. Photophysics of Monodisperse Platinum-Acetylide Oligomers: Delocalization in the Singlet and Triplet Excited States. *J. Am. Chem. Soc.* **2002**, *124* (42), 12412–12413.

(38) Archer, S.; Weinstein, J. A. Charge-Separated Excited States in Platinum(II) Chromophores: Photophysics, Formation, Stabilization and Utilization in Solar Energy Conversion. *Coord. Chem. Rev.* **2012**, *256* (21–22), 2530–2561.

(39) Zhang, X.; Canton, S. E.; Smolentsev, G.; Wallentin, C. J.; Liu, Y.; Kong, Q.; Attenkofer, K.; Stickrath, A. B.; Mara, M. W.; Chen, L. X.; Wärnmark, K.; Sundström, V. Highly Accurate Excited-State Structure of [Os(Bpy)2dcbpy] 2+ Determined by X-Ray Transient Absorption Spectroscopy. *J. Am. Chem. Soc.* **2014**, *136* (24), 8804–8809.

(40) Dröge, F.; Noakes, F. F.; Archer, S. A.; Sreedharan, S.; Raza, A.; Robertson, C. C.; Macneil, S.; Haycock, J. W.; Carson, H.; Meijer, A. J. H. M.; Smythe, C. G. W.; Bernardino De La Serna, J.; Dietzek-Ivanšić, B.; Thomas, J. A. A Dinuclear Osmium(II) Complex Near-Infrared Nanoscopy Probe for Nuclear DNA. *J. Am. Chem. Soc.* **2021**, *143* (48), 20442–20453.

(41) Vogt, M.; Smolentsev, G. Time-Resolved X-Ray Spectroscopy to Study Luminophores with Relevance for OLEDs. *ChemPhotoChem* **2022**, e202100180.

(42) Kraus, P. M.; Zürch, M.; Cushing, S. K.; Neumark, D. M.; Leone, S. R. The Ultrafast X-Ray Spectroscopic Revolution in Chemical Dynamics. *Nat. Rev. Chem.* **2018**, *2* (6), 82–94.

(43) Göries, D.; Dicke, B.; Roedig, P.; Stübe, N.; Meyer, J.; Galler, A.; Gawelda, W.; Britz, A.; Geßler, P.; Sotoudi Namin, H.; Beckmann, A.; Schlie, M.; Warmer, M.; Naumova, M.; Bressler, C.; Rübhausen, M.; Weckert, E.; Meents, A. Time-Resolved Pump and Probe x-

Ray Absorption Fine Structure Spectroscopy at Beamline P11 at PETRA III. *Rev. Sci. Instrum.* **2016**, *87* (5).

(44) Van Der Veen, R. M.; Milne, C. J.; Nahhas, A. El; Lima, F. A.; Pham, V. T.; Best, J.; Weinstein, J. A.; Borca, C. N.; Abela, R.; Bressler, C.; Chergui, M. Structural Determination of a Photoehemieally Active Diplatinum Molecule by Time-Resolved EXAFS Spectroscopy. *Angew. Chemie - Int. Ed.* **2009**, *48* (15), 2711–2714.

(45) Weingartz, N. P.; Mara, M. W.; Roy, S.; Hong, J.; Chakraborty, A.; Brown-Xu, S. E.; Phelan, B. T.; Castellano, F. N.; Chen, L. X. Excited-State Bond Contraction and Charge Migration in a Platinum Dimer Complex Characterized by X-Ray and Optical Transient Absorption Spectroscopy. *J. Phys. Chem. A* **2021**, *125* (40), 8891–8898.

(46) Göries, D. Photoinduced Charge Transfer in a Transition Metal Complex Investigated by Time-Resolved X-Ray Absorption Fine Structure Spectroscopy: Setup and Experiment., Universit¨at Hamburg, 2014.

(47) Britz, A.; Bokarev, S. I.; Assefa, T. A.; Bajnóczi, È. G.; Németh, Z.; Vankó, G.; Rockstroh, N.; Junge, H.; Beller, M.; Doumy, G.; March, A. M.; Southworth, S. H.; Lochbrunner, S.; Kühn, O.; Bressler, C.; Gawelda, W. Site-Selective Real-Time Observation of Bimolecular Electron Transfer in a Photocatalytic System Using L-Edge X-Ray Absorption Spectroscopy**. *ChemPhysChem* **2021**, *22* (7), 693–700.

(48) Smolentsev, G.; Sundström, V. Time-Resolved X-Ray Absorption Spectroscopy for the Study of Molecular Systems Relevant for Artificial Photosynthesis. *Coord. Chem. Rev.* **2015**, *304–305*, 117–132.

(49) Scutelnic, V.; Leone, S. R. Elucidation of Molecular Dynamics by Extreme Ultraviolet and Soft X-Ray Transient-Absorption Spectroscopy. *ACS Symp. Ser.* **2021**, *1398*, 1–14.

(50) Cirri, A.; Husek, J.; Biswas, S.; Baker, L. R. Achieving Surface Sensitivity in Ultrafast XUV Spectroscopy: M2,3-Edge Reflection-Absorption of Transition Metal Oxides. *J. Phys. Chem. C* **2017**, *121* (29), 15861–15869.

(51) Ryland, E. S.; Lin, M.-F.; Verkamp, M. A.; Zhang, K.; Benke, K.; Carlson, M.; Vura-Weis, J. Tabletop Femtosecond M-Edge X-Ray Absorption Near-Edge Structure of FeTPPCl: Metalloporphyrin Photophysics from the Perspective of the Metal. *J. Am. Chem. Soc.* **2018**, *140* (13), 4691–4696.

(52) Vura-Weis, J.; Jiang, C. M.; Liu, C.; Gao, H.; Lucas, J. M.; De Groot, F. M. F.; Yang, P.; Alivisatos, A. P.; Leone, S. R. Femtosecond M2,3-Edge Spectroscopy of Transition-Metal Oxides: Photoinduced Oxidation State Change in α-Fe2O3. *J. Phys. Chem. Lett.* **2013**, *4* (21), 3667–3671.

(53) Geneaux, R.; Marroux, H. J. B.; Guggenmos, A.; Neumark, D. M.; Leone, S. R. Transient Absorption Spectroscopy Using High Harmonic Generation: A Review of Ultrafast X-Ray Dynamics in Molecules and Solids. *Philos. Trans. R. Soc. A Math. Phys. Eng. Sci.* **2019**, *377* (2145), 20170463.

(54) Zhang, K.; Lin, M. F.; Ryland, E. S.; Verkamp, M. A.; Benke, K.; De Groot, F. M. F.; Girolami, G. S.; Vura-Weis, J. Shrinking the Synchrotron: Tabletop Extreme Ultraviolet

Absorption of Transition-Metal Complexes. *J. Phys. Chem. Lett.* **2016**, *7* (17), 3383–3387.

(55) Zhang, K.; Ash, R.; Girolami, G. S.; Vura-Weis, J. Tracking the Metal-Centered Triplet in Photoinduced Spin Crossover of Fe(Phen)32+ with Tabletop Femtosecond M-Edge X-Ray Absorption Near-Edge Structure Spectroscopy. *J. Am. Chem. Soc.* **2019**, *141* (43), 17180–17188.

(56) Ryland, E. S.; Zhang, K.; Vura-Weis, J. Sub-100 Fs Intersystem Crossing to a Metal-Centered Triplet in Ni(II)OEP Observed with M-Edge XANES. *J. Phys. Chem. A* **2019**, *123* (25), 5214–5222.

(57) Ash, R.; Zhang, K.; Vura-Weis, J. Photoinduced Valence Tautomerism of a Cobalt-Dioxolene Complex Revealed with Femtosecond M-Edge XANES. *J. Chem. Phys.* **2019**, *151* (10), 104201.

(58) Shari'Ati, Y.; Vura-Weis, J. Ballistic Δ: S = 2 Intersystem Crossing in a Cobalt Cubane Following Ligand-Field Excitation Probed by Extreme Ultraviolet Spectroscopy. *Phys. Chem. Chem. Phys.* **2021**, *23* (47), 26990–26996.

(59) Kennedy, E. T.; Costello, J. T.; Mosnier, J. P.; Van Kampen, P. VUV/EUV Ionising Radiation and Atoms and Ions: Dual Laser Plasma Investigations. *Radiat. Phys. Chem.* **2004**, *70* (1–3), 291–321.

(60) Su, M. G.; Dong, C. Z.; Murphy, N.; O'Sullivan, G. Analysis of the Xuv Photoabsorption Spectrum of Au2+, Au3+, and Au4+. *Phys. Rev. A - At. Mol. Opt. Phys.* **2009**, *79* (4), 1–8.

(61) Dietz, R. E.; McRae, E. G.; Weaver, J. H. Core-Electron Excitation Edges in Metallic Ni, Cu, Pt, and Au. *Phys. Rev. B* **1980**, *21* (6), 2229–2247.

(62) Haensel, R.; Radler, K.; Sonntag, B.; Kunz, C. Optical Absorption Measurements of Tantalum, Tungsten, Rhenium and Platinum in the Extreme Ultraviolet. *Solid State Commun.* **1969**, *7* (20), 1495–1497.

(63) Costello, J. T.; Kennedy, E. T.; Sonntagi, B. F.; Cromer, C. L. Xuv Photoabsorption of Laser-Generated w and Pt Vapours. *J. Phys. B At. Mol. Opt. Phys.* **1991**, *24* (24), 5063–5069.

(64) Sladeczek, P.; Martins, M.; Richter, M.; Selbmann, K. H.; Zimmermann, P. Photoionization Experiments on Atomic Pt in the Range 40-90 Ev. *J. Phys. B At. Mol. Opt. Phys.* **1994**, *27* (18), 4123–4131.

(65) Martins, M.; Sladeczek, P.; Tiedtke, K.; Zimmermann, P. Vacuum Ultraviolet Photoionization of the 5d Elements in the Region of the 5p and 4f Excitation. *Eur. Phys. J. D - At. Mol. Opt. Phys.* **1998**, *1* (1), 47–52.

(66) Chang, H. T.; Guggenmos, A.; Chen, C. T.; Oh, J.; Géneaux, R.; Chuang, Y. De; Schwartzberg, A. M.; Aloni, S.; Neumark, D. M.; Leone, S. R. Coupled Valence Carrier and Core-Exciton Dynamics in WS2 Probed by Few-Femtosecond Extreme Ultraviolet Transient Absorption Spectroscopy. *Phys. Rev. B* **2021**, *104* (6), 1–14.

(67) Reid, M. F. *Electronic Structure and Transition Intensities in Rare-Earth Materials*; Christchurch, NZ, 2014.

(68) El Nahhas, A.; Van Der Veen, R. M.; Penfold, T. J.; Pham, V. T.; Lima, F. A.; Abela, R.; Blanco-Rodriguez, A. M.; Záliš, S.; Vlček, A.; Tavernelli, I.; Rothlisberger, U.; Milne, C. J.; Chergui, M. X-Ray Absorption Spectroscopy of Ground and Excited Rhenium-Carbonyl- Diimine Complexes: Evidence for a Two-Center Electron Transfer. *J. Phys. Chem. A* **2013**, *117* (2), 361–369.

(69) Clancy, J. P.; Chen, N.; Kim, C. Y.; Chen, W. F.; Plumb, K. W.; Jeon, B. C.; Noh, T. W.; Kim, Y.-J. Spin-Orbit Coupling in Iridium-Based 5d Compounds Probed by x-Ray Absorption Spectroscopy. *Phys. Rev. B* **2012**, *86* (19), 195131.

(70) Laguna-Marco, M. A.; Kayser, P.; Alonso, J. A.; Martínez-Lope, M. J.; Van Veenendaal, M.; Choi, Y.; Haskel, D. Electronic Structure, Local Magnetism, and Spin-Orbit Effects of Ir(IV)-, Ir(V)-, and Ir(VI)-Based Compounds. *Phys. Rev. B - Condens. Matter Mater. Phys.* **2015**, *91* (21), 1–9.

(71) Martins, C.; Aichhorn, M.; Biermann, S. Coulomb Correlations in 4d and 5d Oxides from First Principles - Or How Spin-Orbit Materials Choose Their Effective Orbital Degeneracies. *J. Phys. Condens. Matter* **2017**, *29* (26).

(72) Kim, B. J.; Ohsumi, H.; Komesu, T.; Sakai, S.; Morita, T.; Takagi, H.; Arima, T. Phase-Sensitive Observation of a Spin-Orbital Mott State in Sr 2 IrO 4. *Science (80-.).* **2009**, *323* (5919), 1329–1332.

(73) Kim, B. J.; Jin, H.; Moon, S. J.; Kim, J. Y.; Park, B. G.; Leem, C. S.; Yu, J.; Noh, T. W.; Kim, C.; Oh, S. J.; Park, J. H.; Durairaj, V.; Cao, G.; Rotenberg, E. Novel Jeff=1/2 Mott State Induced by Relativistic Spin-Orbit Coupling in Sr2IrO4. *Phys. Rev. Lett.* **2008**, *101* (7), 1–4.

(74) Zhu, Z.; Tao, F.; Zheng, F.; Chang, R.; Li, Y.; Heinke, L.; Liu, Z.; Salmeron, M.; Somorjai, G. A. Formation of Nanometer-Sized Surface Platinum Oxide Clusters on a Stepped Pt(557) Single Crystal Surface Induced by Oxygen: A High-Pressure STM and Ambient-Pressure XPS Study. *Nano Lett.* **2012**, *12* (3), 1491–1497.

(75) Shyu, J. Z.; Otto, K. Identification of Platinum Phases on γ-Alumina by XPS. *Appl. Surf. Sci.* **1988**, *32* (1–2), 246–252.

(76) Matson, B. D.; Thomas, K. E.; Alemayehu, A. B.; Ghosh, A.; Sarangi, R. X-Ray Absorption Spectroscopy of Exemplary Platinum Porphyrin and Corrole Derivatives: Metal-: Versus Ligand-Centered Oxidation. *RSC Adv.* **2021**, *11* (51), 32269–32274.

(77) Hofbeck, T.; Yersin, H. The Triplet State of Fac-Ir(Ppy)3. *Inorg. Chem.* **2010**, *49* (20), 9290–9299.

(78) Kleinschmidt, M.; Van Wüllen, C.; Marian, C. M. Intersystem-Crossing and Phosphorescence Rates in Fac-IrIII(Ppy)3: A Theoretical Study Involving Multi-Reference Configuration Interaction Wavefunctions. *J. Chem. Phys.* **2015**, *142* (9).

(79) Nemirow, C.; Fine, J.; Lu, Z.; Diri, K.; Krylov, A. I.; Wittig, C. Photoionization of Tris(2-Phenylpyridine)Iridium. *Mol. Phys.* **2012**, *110* (15–16), 1893–1908.

(80) Fine, J.; Diri, K.; Krylov, A. I.; Nemirow, C.; Lu, Z.; Wittig, C. Electronic Structure of Tris(2-Phenylpyridine)Iridium: Electronically Excited and Ionized States. *Mol. Phys.*

2012, *110* (15–16), 1849–1862.

(81) Adachi, C.; Baldo, M. A.; Forrest, S. R.; Thompson, M. E. High-Efficiency Organic Electrophosphorescent Devices with Tris(2-Phenylpyridine)Iridium Doped into Electron-Transporting Materials. *Appl. Phys. Lett.* **2000**, *77* (6), 904–906.

(82) Holzer, W.; Penzkofer, A.; Tsuboi, T. Absorption and Emission Spectroscopic Characterization of Ir(Ppy) 3. *Chem. Phys.* **2005**, *308* (1–2), 93–102.

(83) Hedley, G. J.; Ruseckas, A.; Liu, Z.; Lo, S. C.; Burn, P. L.; Samuel, I. D. W. Iridium Metal Complexes as an Unambiguous Probe of Intramolecular Vibrational Redistribution. *J. Am. Chem. Soc.* **2008**, *130* (36), 11842–11843.

(84) Hedley, G. J. Ultrafast Photophysics of Iridium Complexes, University of St. Andrews, 2012.

(85) Messina, F.; Pomarico, E.; Silatani, M.; Baranoff, E.; Chergui, M. Ligand-Centred Fluorescence and Electronic Relaxation Cascade at Vibrational Time Scales in Transition-Metal Complexes. *J. Phys. Chem. Lett.* **2015**, *6* (22), 4475–4480.

(86) Hedley, G. J.; Ruseckas, A.; Samuel, I. D. W. Ultrafast Intersystem Crossing in a Red Phosphorescent Indium Complex. *J. Phys. Chem. A* **2009**, *113* (1), 2–4.

(87) Hedley, G. J.; Ruseckas, A.; Samuel, I. D. W. Vibrational Energy Flow Controls Internal Conversion in a Transition Metal Complex. *J. Phys. Chem. A* **2010**, *114* (34), 8961–8968.

(88) Tang, K. C.; Liu, K. L.; Chen, I. C. Rapid Intersystem Crossing in Highly Phosphorescent Iridium Complexes. *Chem. Phys. Lett.* **2004**, *386* (4–6), 437–441.

(89) Hedley, G. J.; Ruseckas, A.; Samuel, I. D. W. Ultrafast Luminescence in Ir(Ppy)3. *Chem. Phys. Lett.* **2008**, *450* (4–6), 292–296.

(90) Finkenzeller, W. J.; Yersin, H. Emission of Ir(Ppy)3. Temperature Dependence, Decay Dynamics, and Magnetic Field Properties. *Chem. Phys. Lett.* **2003**, *377* (3–4), 299–305.

(91) Smolentsev, G.; Van Vliet, K. M.; Azzaroli, N.; Van Bokhoven, J. A.; Brouwer, A. M.; De Bruin, B.; Nachtegaal, M.; Tromp, M. Pump-Probe XAS Investigation of the Triplet State of an Ir Photosensitizer with Chromenopyridinone Ligands. *Photochem. Photobiol. Sci.* **2018**, *17* (7), 896–902.

(92) Demas, J. N.; Taylor, D. G. On the "Intersystem Crossing" Yields in Ruthenium(II) and Osmium(II) Photosensitizers. *Inorg. Chem.* **1979**, *18* (11), 3177–3179.

(93) Matsubara, T.; Bergkamp, M.; Ford, P. C. Photochemistry of Osmium(II) Ammine Complexes. The Dinitrogen Species Dinitrogenpentaammineosmium(2+) and Cis-(Bis)(Dinitrogen)Tetraammineosmium(2+). *Inorg. Chem.* **1978**, *17* (6), 1604–1607.

(94) Demas, J. N.; Harris, E. W.; Flynn, C. M.; Diemente, D. Luminescent Osmium(II) and Iridium(III) Complexes as Photosensitizers. *J. Am. Chem. Soc.* **1975**, *97* (13), 3838–3839.

(95) Ravetz, B. D.; Tay, N. E. S.; Joe, C. L.; Sezen-Edmonds, M.; Schmidt, M. A.; Tan, Y.; Janey, J. M.; Eastgate, M. D.; Rovis, T. Development of a Platform for Near-Infrared Photoredox Catalysis. *ACS Cent. Sci.* **2020**, *6* (11), 2053–2059.

(96) Roque, J. A.; Barrett, P. C.; Cole, H. D.; Lifshits, L. M.; Shi, G.; Monro, S.; Von Dohlen, D.; Kim, S.; Russo, N.; Deep, G.; Cameron, C. G.; Alberto, M. E.; McFarland, S. A. Breaking the Barrier: An Osmium Photosensitizer with Unprecedented Hypoxic Phototoxicity for Real World Photodynamic Therapy. *Chem. Sci.* **2020**, *11* (36), 9784–9806.

(97) Jayarathne, U.; Chandrasekaran, P.; Greene, A. F.; Mague, J. T.; Debeer, S.; Lancaster, K. M.; Sproules, S.; Donahue, J. P. X-Ray Absorption Spectroscopy Systematics at the Tungsten L-Edge. *Inorg. Chem.* **2014**, *53* (16), 8230–8241.

(98) Hoffman, A. S.; Sokaras, D.; Zhang, S.; Debefve, L. M.; Fang, C. Y.; Gallo, A.; Kroll, T.; Dixon, D. A.; Bare, S. R.; Gates, B. C. High-Energy-Resolution X-Ray Absorption Spectroscopy for Identification of Reactive Surface Species on Supported Single-Site Iridium Catalysts. *Chem. - A Eur. J.* **2017**, *23* (59), 14760–14768.

(99) Scattergood, P. A.; Delor, M.; Sazanovich, I. V.; Bouganov, O. V.; Tikhomirov, S. A.; Stasheuski, A. S.; Parker, A. W.; Greetham, G. M.; Towrie, M.; Davies, E. S.; Meijer, A. J. H. M.; Weinstein, J. A. Electron Transfer Dynamics and Excited State Branching in a Charge-Transfer Platinum(Ii) Donor-Bridge-Acceptor Assembly. *Dalt. Trans.* **2014**, *43* (47), 17677–17693.

(100) Lin, M.; Verkamp, M. A.; Leveillee, J.; Ryland, E. S.; Benke, K.; Zhang, K.; Weninger, C.; Shen, X.; Li, R.; Fritz, D.; Bergmann, U.; Wang, X.; Schleife, A.; Vura-Weis, J. Carrier-Specific Femtosecond XUV Transient Absorption of PbI 2 Reveals Ultrafast Nonradiative Recombination. *J. Phys. Chem. C* **2017**, *121* (50), 27886–27893.

(101) Verkamp, M.; Leveillee, J.; Sharma, A.; Lin, M. F.; Schleife, A.; Vura-Weis, J. Carrier-Specific Hot Phonon Bottleneck in CH3NH3PbI3Revealed by Femtosecond XUV Absorption. *J. Am. Chem. Soc.* **2021**, *143* (48), 20176–20182.

(102) Takayama, T.; Yaresko, A.; Matsumoto, A.; Nuss, J.; Ishii, K.; Yoshida, M.; Mizuki, J.; Takagi, H. Spin-Orbit Coupling Induced Semi-Metallic State in the 1/3 Hole-Doped Hyper-Kagome Na3Ir3O8. *Sci. Rep.* **2014**, *4*, 1–6.

(103) Koshiyama, T.; Omura, A.; Kato, M. Redox-Controlled Luminescence of a Cyclometalated Dinuclear Platinum Complex Bridged with Pyridine-2-Thiolate Ions. *Chem. Lett.* **2004**, *33* (10), 1386–1387.

(104) Shari'ati, Y.; Vura-Weis, J. Polymer Thin Films as Universal Substrates for Extreme Ultraviolet Absorption Spectroscopy of Molecular Transition Metal Complexes. *J. Synchrotron Radiat.* **2021**, *28* (6), 1850–1857.